# *Mineralia Slovaca*

**www.geology.sk/mineralia**

# Obsah – Content

**COVER:**
Seabed polymetallic nodules in the area of Clarion-Clipperton Fracture Zone in eastern Pacific. Central background picture: Colour-shade bathymetric map of the H22 exploration block in the IOM exploration area. This picture is placed on representative EPMA BSE image of analysed polymetallic nodules. Upper image: Cross-section of the sedimentary cover along the profile 707_2 in the H22_NE exploitable block. Bottom-left image: Simplified scheme of nodule natural cracking process due to cement growth. Bottom-right image: Location of the EPMA spot data at the Fe–Mn–10x(Ni + Co + Cu) ternary plot; classification of the micronodules is after Bonatti et al. (1972). This topic is presented in the article by Baláž in this issue (on pages 95–118).

**OBÁLKA:**
Hlbokomorské polymetalické konkrécie v oblasti zlomového pásma Clarion-Clipperton vo východnom Pacifiku. Centrálny obrázok (v pozadí): Farebná batymetrická mapa prieskumného bloku H22 v prieskumnom území IOM. Tento obrázok je umiestnený na reprezentatívnej EPMA BSE snímke analyzovaných polymetalických konkrécií. Horný obrázok: Rez vrstvami sedimentárneho pokryvu pozdĺž profilu 707_2 vo využiteľnom bloku H22_NE. Obrázok vľavo dole: Zjednodušená schéma prirodzenej deštrukcie (praskania) konkrécií v dôsledku rastu/kryštalizácie tmeliaceho materiálu trhlín. Obrázok vpravo dole: Lokalizácia meraných bodov EPMA na trojstrannom grafe Fe – Mn – 10x (Ni + Co + Cu); klasifikácia mikrokonkrécií podľa Bonattiho et al. (1972). Problematika je prezentovaná v článku Baláža v tomto čísle časopisu (na stranách 95 – 118).

# Results of the second phase of deep-sea polymetallic nodules geological survey in Interoceanmetal Joint Organization licence area (2016–2021)

PETER BALÁŽ

Interoceanmetal Joint Organization, Szczecin, Poland

**Abstract:** The exploration rights of the Interoceanmetal Joint Organization for exploration of polymetallic nodules (PMN) are granted from 29 March 2001 to an area located within the Clarion-Clipperton Zone (CCZ) in the eastern central Pacific Ocean. Exploration area covers 75,000 km$^2$ and consists of two sectors (B1 and B2). The B2 sector comprises four exploration blocks (H11, H22, H33 and H44). The most prospective area, selected for detailed research, is marked as H22_NE exploitable block and delineated within the H22 exploration block. The article presents results of geological survey, based mostly on the data collected during the second phase of exploration in the licence area (2016–2021, extension of the contract). Results are based on IOM's expeditions and relevant analytical work. During the IOM-2018 expedition high resolution bathymetric survey of H11, H22, H33 and H44 exploration blocks was carried out. The IOM-2019 expedition provided a new set of the data obtained using the distance methods (side-scan sonar, profiler) and contact methods (box-corer and gravity corer) in H22_NE exploitable block, H33 exploration block and preliminary delineated Preservation Reference Zone. The study was focused on analytical work based on sediment and nodule analyses of samples in H22 exploration block and H22_NE exploitation block. New estimation of mineral resources in B2 sector was caried out using the geostatistical method of ordinary block kriging with Yamamoto correction. The polymetallic nodule resources have been classified within the Inferred, Indicated and Measured Resources categories of the CRIRSCO classification system.

**Key words:** deep sea exploration, seabed minerals, polymetallic nodules, Clarion-Clipperton Zone

**Graphical abstract**

BSE image of the analysed polymetallic nodule
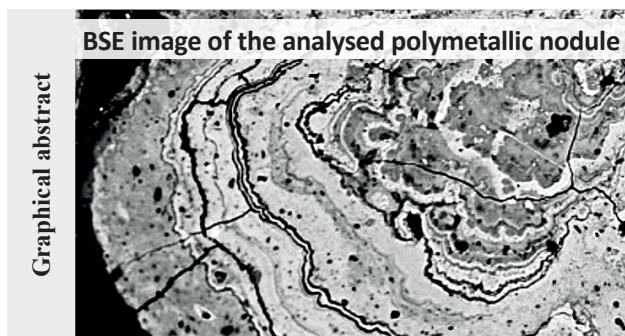
**Highlights**

- Detailed multibeam bathymetry mapping of 4 exploration blocks (H11, H22, H33, H44).
- Chemical, geochemical and mineralogical analysis of sediments and nodules in H22_NE block.
- Assessment of the ability to determine polymetallic nodule abundance based on seabed photography.
- New resource estimate, including identification of Measured Resources (CRIRSCO classification system).

## Introduction

The exploration rights of the Interoceanmetal Joint Organization are granted from 29 March 2001 to an area located within the Clarion-Clipperton Zone (CCZ) in the eastern central Pacific Ocean. All activities related to exploration of minerals in the CCZ (the Area – the seabed and ocean floor beyond the limits of national jurisdiction) come under the United Nations Convention on the Law of the Sea (1982), the Agreement relating to the implementation of Part XI of the Convention (1994) as well as Regulations on Prospecting and Exploration for Polymetallic Nodules in the Area – regulations established by the International Seabed Authority (ISA). The ISA issues legal documents regulating the conduct of research and the future use of the seabed.

As of 2021, ISA has entered into 19 contracts for exploration for polymetallic nodules (PMN) in the Clarion-Clipperton Fracture Zone, Central Indian Ocean Basin and Western Pacific Ocean. Besides that, there were 7 contracts for exploration for polymetallic sulphides in the South West Indian Ridge, Central Indian Ridge and the Mid-Atlantic Ridge and 5 contracts for exploration for cobalt-rich crusts in the Western Pacific Ocean (ISA, 09/2021).

Adjacent properties (common borders) to the IOM exploration area belong to 4 organizations – NORI (Nauru), OMS (Singapore), BGR (Germany) and BMJ (Jamaica) (Fig. 1). The BMJ exploration area was delineated in April 2021 and reflects generally increased interest in deep sea mineral exploration in the area that has emerged during the past decade. 11 out of a total 19 exploration contracts has been signed in the 2011–2021 period.
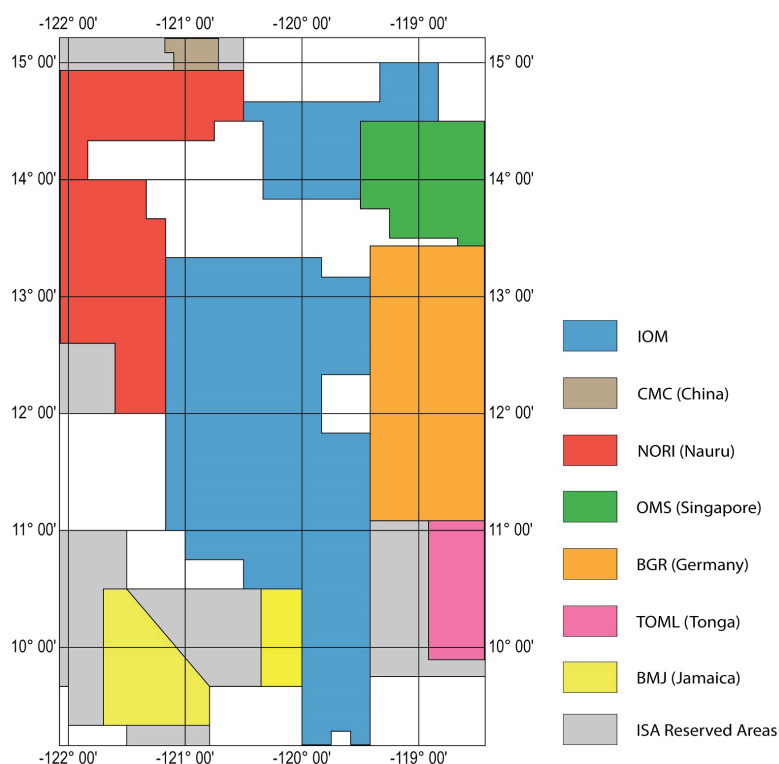
**Fig. 1.** Outlines of the IOM exploration area and adjacent properties in the Clarion-Clipperton Zone (ISA, 2021).

the PRZ in its license area is imposed on the contractor by the ISA. Delineation of the PRZ in the IOM exploration area is preliminary and the final location is being considered.

**Tab. 1**

IOM's Exploration area (sectors and blocks). Areas are calculated in UTM map projection coordinate system.

| Exploration area | Area [km²] |
|---|---|
| B1 sector | 11 952 |
| B2 sector | 63 234 |
|     H11 exploration block | 5 390 |
|     H22 exploration block | 4 151 |
|         H22_NE exploitable block | 957 |
|     H33 exploration block | 4 008 |
|     H44 exploration block | 1 919 |
|     PRZ (preliminary) | 2 626 |
| **Total** | **75 186** |

The IOM's contract for exploration of polymetallic nodules was granted for 15 years and provides the contractor security of tenure and exclusive right to explore for polymetallic nodules in the exploration area, as well as to move to a contract for exploitation. Regulations for exploitation of mineral resources in the Area are under the development process by the ISA. In 2016, the contract was extended for the following 5 years. A summary of the results of the geological survey of the first phase (2001–2016) was published recently (Baláž, 2021).

In addition to geological survey, IOM is engaged in research into the technology of mining and processing of deep-sea polymetallic nodules, as well as environmental research.

**Location**

The IOM exploration area covers app. 75,000 km² of the eastern part of the CCZ and consists of two sectors, B1 and B2. In B2 sector there are four exploration blocks (H11, H22, H33, H44) and preliminary delineated Preservation Reference Zone (Tab. 1, Fig. 2). Within the H22 exploration block the H22_NE exploitable block was delineated. Preservation Reference Zone (PRZ) is an area in which no mining shall occur to ensure representative and stable biota of the seabed in order to assess any changes of the marine environment. The obligation of establishing

**Survey methodology**

Before the signing of the exploration contract between the ISA and IOM in 2001, 21 research expeditions were carried out to the CCZ area, mainly focused on regional research. In the first phase of the contract (2001–2016), 4 expeditions were organized. In the second phase (2016–2021, the extension of the contract) there were 2 expeditions. The work was carried out in accordance with the program approved by the ISA. The study included a geological survey focused on determination of PMN abundance, nodule coverage, determination of metal content and chemical composition of PMNs, as well as study of seabed sediments, their geotechnical properties. During the expeditions basic oceanographic, meteorological and environmental data were collected. During the extension period 2 expeditions were carried out (2018 and 2019):

*IOM-2018*

– high resolution bathymetric mapping of selected parts of the IOM exploration area – H11, H22, H33 and H44 exploration blocks (15 609 km² in total),
– H11       5,400 km²    (1 : 100 000 scale),
– H22       3,201 km²    (1 : 100 000),
– H33       3,970 km²    (1 : 100 000),
– H44       1,920 km²    (1 : 100 000),
– H22_NE    1,118 km²    (1 : 50 000).

**Fig. 2.** IOM exploration area (B1 and B2 – sectors, H11, H22, H33, H44 – exploration blocks, H22_NE – exploitable block, PRZ – Preservation Reference Zone).

– Geoacoustic profiling          313.54 km
– Photo-video profiling          418.14 km
– Sample retrieval with a box corer
  32 launch-raising operations
– Sample retrieval with a gravity corer
  4 launch-raising operations

As a part of the IOM-2019 expedition, geoacoustic survey (geoacoustic profiling with side-scan sonar) was used for detailed mapping of the seabed, obtaining the acoustic bottom profile to a depth of about 100 m. Photo and video profiling provided information for the analysis of bottom nodule coverage (individual images of the bottom) and the identification of zones with the occurrence of PMN, as well as the identification of obstacles to potential mining. Two types of seabed sampling systems were applied during the expeditions: sampling of PMN and sediments using a box-corer device; and sediment sampling using a gravity-corer device. Basic work and measurements requiring immediate sample processing were performed on board of the research vessel during the shipment.

## Results

After individual expeditions, the results of the survey were summarized in reports on geological and environmental research, in semi-annual reports for the meetings of the IOM Council, as well as in annual reports for the ISA. The overview and results of the survey work are summarized in technical reports (Baláž et al., 2019; Zarzecki et al., 2021).

The presented results provide additional information to the data presented earlier (Baláž, 2021), relevant for updating the resources estimate in the B2 sector. The collected data are used for planning of the IOM polymetallic nodules project – potential exploitation and processing of raw materials, environmental impact assessment, economic assumptions and feasibility of the project.

### Seabed topography

The bathymetric survey was carried out according to the design profile scheme. Exploration blocks H11, H22, H33 and H44 were mapped at scale 1 : 100 000. A system of parallel profiles has been used, to ensure 80 % overlap of adjacent profiles. The distance between profiles was 9 km. Exploitable block N22_NE was mapped at scale 1 : 50 000. A system of parallel profiles has been used, to ensure 100 % overlap of adjacent profiles. The distance between the profiles was 4.3 km. This provides detailed information for the area selected for initial mining phases.

A set of charts were prepared for each block, including the colour-shade chart (Fig. 3), the bathymetric chart with

Multibeam bathymetry was used to measure depth and map the bottom morphology using multibeam echo sounder, providing information on the character of the seabed based on the intensity of the reflected signal (backscatter). Work was carried out in exploration blocks H11, H22, H33 and H44. A detailed survey was carried out in the H22_NE exploitable block.

*IOM-2019*

IOM conducted an at-sea exploration in selected parts of the exploration area (H22_NE exploitable block, H33 exploration block and Preservation Reference Zone).

**Fig. 3.** Colour-shade chart of the H22 exploration block.

contours, the contours chart, the gradient chart, the chart of slopes of the sea-bottom exceeding 7° as well as the chart of amplitudes of the backscattered signal.

### Lithology and stratigraphy

*The structure of the sedimentary cover of the H22 exploration block*

The study of the structure of the sedimentary cover of exploration block H22 is based on the interpretation of hydroacoustic profile 707_2. The total length of the profile is 57,159 m. It is a continuation of the hydroacoustic profile No. 707, passing from the south from the H11 exploration block. The profile is oriented from SW to NE, azimuth 65° (Fig. 4).

Hydroacoustic complex A is subdivided into sub-complexes A1 and A2, where A1 includes cover clay and siliceous-clayey sediments and A2 clay sediments – red deep-sea clays, radiolarian clays, possibly with zeolites. The acoustic boundaries between A1 and A2 are discontinuous and are clearly manifested only in those sections where clay-ore crusts with increased strength characteristics are found in the upper part of red deep-sea clays, which are a good acoustic marker. Complex B represents calcareous clays, an interbedding of nanofossil limestones and radiolarian clays, complex

C represents layer of nanofossil limestones and complex F represents basement, composed of tholeiitic basalt (Fig. 5). A study shows that the maximum thickness of the sedimentary cover in the full section is 92 m at the 17.2 km picket. Thickness of particular hydroacoustic complexes: A1 – 6.5 m, A2 – 11 m, B – 39.3 m, C – 35.2 m (Dreiseitl, 2018).
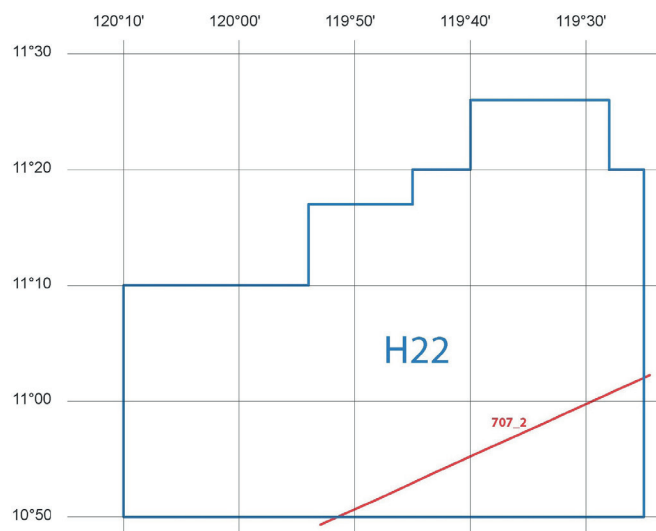


**Fig. 4.** Position of the 707_2 profile in the H22 exploration block (red line).

**Fig. 5.** Maximum section of the sedimentary cover (92 m) along profile 707_2 in the area of station 3 505 (16.3 kg/m², depth 4 332 m) (Dreiseitl, 2018).



In several places of the profile, bottom sediments are missing and basement rocks in the form of cliffs and/or volcanic edifices emerge. Near the outcrops, the thickness of bottom sediments is considerably reduced.

*Physical and strength properties of bottom sediments in H22 exploration block*

Determination of the physical and strength properties of bottom sediments was carried out at 50 sampling stations collected in expeditions until 2014. The sampling depth was determined by the possibility of taking samples of undisturbed composition and not exceeding 0.44 m.

Determination of the moisture and soil density was carried out on 125 samples. The test of penetration resistance, vane shear strength and the residual strength of sediment was performed on 98 samples. The following parameters were calculated: parameters of dry unit weight, porosity, porosity factor and bulk density, and the over-consolidation ratio.

Figure 6 presents the water content and density values of the two observed types of bottom sediments, evalua-

ted in an on-board laboratory. The difference between the siliceous varieties of bottom sediments (blue points) and non-siliceous red pelagic clays (red points) can be observed, confirming their different engineering-geological properties. The bottom sediment samples, selected for engineering and geological studies, were analysed in two ways (Dreiseitl, 2018):
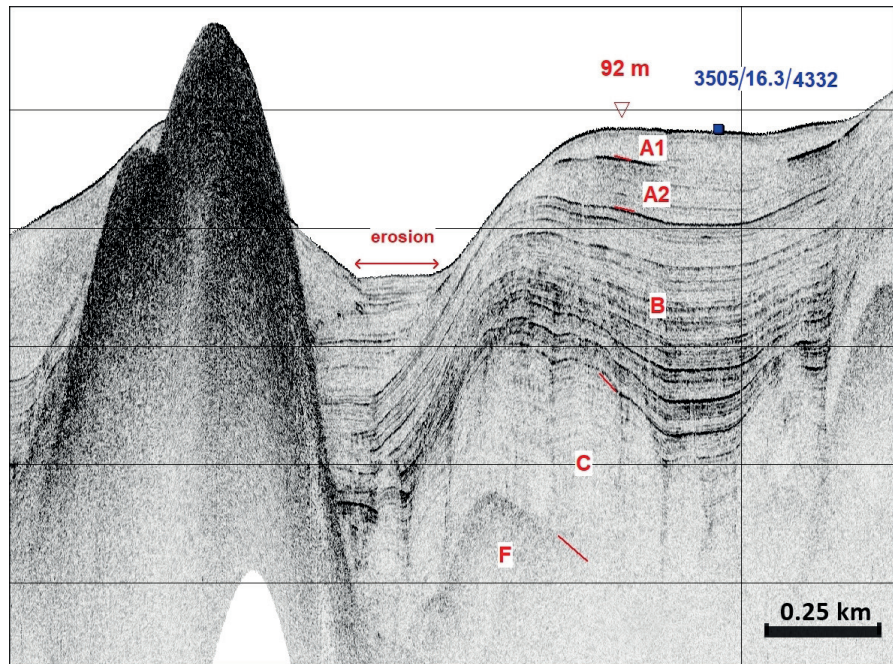
– according to the type of bottom sediments,
– according to the depth of sampling intervals.

The types of bottom sediment (Dreiseitl, 2018):

*Siliceous clay silt with an increased content of diatoms* (SILETM), with amorphous silica content exceeding 20 %, analysed on samples drawn from depth 2 to 30 cm. In the case of a GAL sample (geochemically active layer, 0–7 cm), which is of semi-liquid state, determination of the strength properties was impossible.
*Siliceous clay* (SIL) with amorphous silica ranging from 10–20 %, is the most common sediment type in the H22 exploration block. They are found at the depths from 2 to 30 cm.
*Slightly siliceous clay* (SLSIL) with amorphous silica ranging from 5–10 %, can be found in the depths ranging from 10 to 30 cm.
*Red pelagic clay* (RPC) is charac-
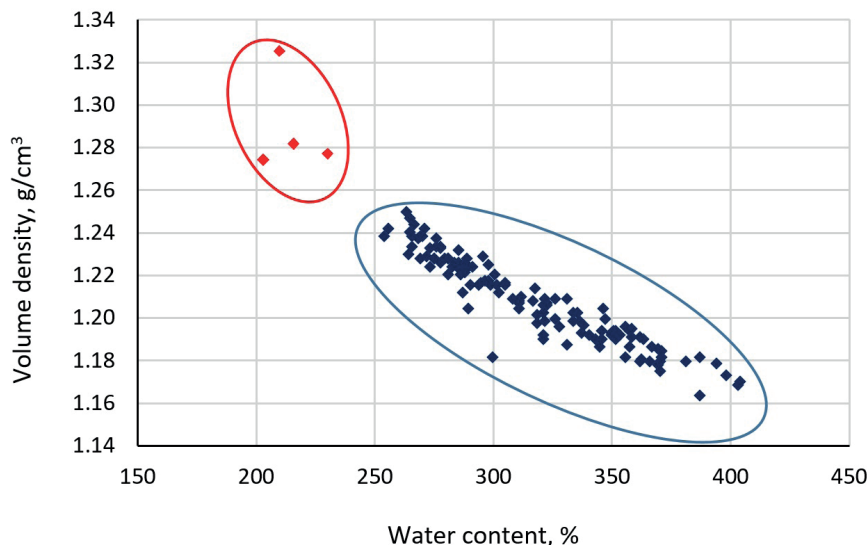


**Fig. 6.** Distribution of siliceous (blue area) and non-siliceous (red area) types of the sediments, according to soil volume density and water content (Dreiseitl, 2018).

terized by an amorphous silica content less than 5 %. They were found in depth interval 8 to 44 cm.

The mean values for the physical and strength properties of different types of bottom sediments in the H22 exploration block are given in Tab. 2

The depth intervals analysed:

0–7 cm     – geochemically active layer (GAL),
8–20 cm    – the predominant sampling interval was 10–15 cm,
25–32 cm   – predominant sampling interval was 25–30 cm,
> 32 cm.

The mean values for the physical and strength properties according to the depth of sampling intervals in the H22 exploration block are given in Tab. 3.

Variability of the water content and the sediment density, together with the depth, is shown in Fig. 7 (the deeper the sediment is deposited, the denser it is – a result of squeezing sea water from the pore space). The highest water content was measured in the GAL sediments (range 0–7 cm), which are in direct contact with seawater and, accordingly, these precipitates are characterized by low density.

Based on the strength analysis of the particular bottom sediments in the exploration block H22 at the depth interval of 8–20 cm (prevailing sampling interval of 10–15 cm) a map of strength properties in a scale 1 : 400,000 was prepared. An interval of 8–20 cm includes the first underlying layer at all stations. The second underlying layer, usually at the 25–30 cm interval, is not disclosed at all stations. The average strength of bottom sediments of

**Tab. 2**

The mean values for the physical and strength properties of different types of bottom sediments in the H22 exploration block (Dreiseitl, 2018).

| Sediment type | Number of tests | Water content [%] | Density [g/cm³] | Dry unit weight [g/cm³] | Porosity [%] | Porosity factor | Bulk density [g/cm³] | Number of tests | Penetrtation resistance [kPa] | Shear strength [kPa] | Residual strength [kPa] | Overconsolidation ratio |
|---|---|---|---|---|---|---|---|---|---|---|---|---|
| **SIL (ETM)** | 19 | 347 | 1.19 | 0.27 | 90 | 9.24 | 2.73 | 15 | 2.0 | 2.7 | 1.4 | 2.2 |
| **SIL** | 86 | 319 | 1.21 | 0.29 | 89 | 8.55 | 2.75 | 64 | 4.1 | 4.2 | 1.7 | 2.5 |
| **SLSIL** | 15 | 274 | 1.23 | 0.33 | 88 | 7.40 | 2.77 | 16 | 7.9 | 7.0 | 2.5 | 2.8 |
| **RPC** | 5 | 226 | 1.28 | 0.39 | 86 | 6.40 | 2.90 | 3 | 22.3 | 12.9 | 4.0 | 3.3 |

**Tab. 3**

The mean values of the physical and strength properties of bottom sediments according to sampling depths in the H22 exploration block (Dreiseitl, 2018).

| Sampling interval [cm] | Number of tests | Water content [%] | Density [g/cm³] | Dry unit weight [g/cm³] | Porosity [%] | Porosity factor | Bulk density [g/cm³] | Number of tests | Penetrtation resistance [kPa] | Shear strength [kPa] | Residual strength [kPa] | Overconsolidation ratio |
|---|---|---|---|---|---|---|---|---|---|---|---|---|
| **0–7** | 29 | 359 | 1.19 | 0.26 | 91 | 9.71 | 2.77 | 0 | – | – | – | – |
| **8–20** | 47 | 310 | 1.21 | 0.30 | 89 | 8.26 | 2.73 | 50 | 3.9 | 4.0 | 1.7 | 2.4 |
| **25–32** | 47 | 292 | 1.22 | 0.31 | 89 | 7.88 | 2.77 | 48 | 6.1 | 5.3 | 2.0 | 2.7 |
| **> 32** | 2 | 243 | 1.26 | 0.37 | 87 | 6.65 | 2.80 | 0 | – | – | – | – |
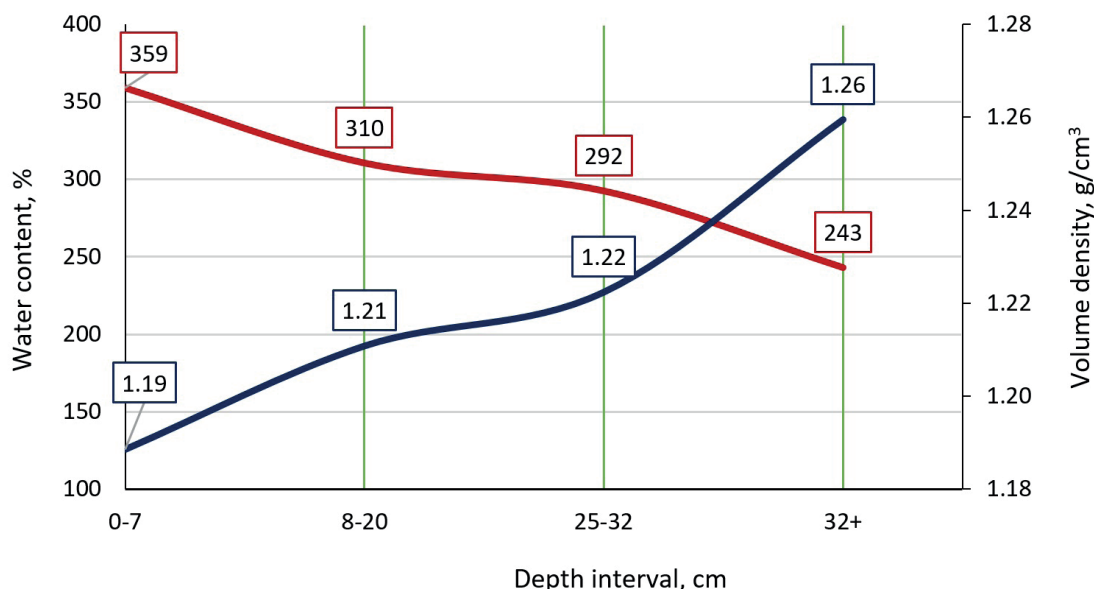
**Fig. 7.** Vertical variability of water content (red line) and density (blue line) of the bottom sediments in the H22 exploration block (Dreiseitl, 2018).

the second layer (5.3 kPa), exceeds the average strength of the first layer (4.0 kPa).

*Geochemical properties of bottom sediments in H22 exploration block*

The active pH reaction and the redox potential Eh are the main geochemical indicators of bottom sediments, which can be used to study the processes of oxidation and/or hydration. The measurement results (191 pairs) for the sampling intervals shown in Tab. 4, belong to the bottom sediments of GAL and all three known siliceous varieties: siliceous clayey silt, slightly siliceous clayey silt, and ethmodiscus silt. Both in the values of the active reaction of the medium and the redox potential of bottom

sediments in relation to the depths of sampling, as well as to the depths of the ocean (Fig. 8), no anomalies were observed. Values of Eh < 400 mV were generally not observed in the study area, except for 4 values of Eh in the interval 300–400 mV (red points in Fig. 8). The range of pH variability is 7.10–7.80, which characterizes the environment from weakly alkaline (7.50–7.80) to neutral (7.00–7.50). The range of Eh variability does not exceed (without taking into account 4 extreme values) 160 mV.

Red pelagic clays were identified at 6 sampling stations, where 7 data pairs were obtained. The range of pH variability is 7.33–7.59, which characterizes the environment as neutral. All Eh values are > 400 mV and the range of variability reaches 190 mV (Dreiseitl, 2018).

**Tab. 4**

Active reaction and redox potential of siliceous clayey silts of H22 exploration block (Med – medium value, Max – maximal value, Min – minimal value) (Dreiseitl, 2018).

| Sampling depth [cm] | Number of asurement pairs | pH | | | Eh [mV] | | |
|---|---|---|---|---|---|---|---|
| | | Med | Max | Min | Med | Max | Min |
| 0–3 (GAL) | 49 | 7.48 | 7.60 | 7.21 | 473 | 553 | 402 |
| 3–5 (GAL) | 14 | 7.44 | 7.56 | 7.23 | 481 | 551 | 437 |
| 5–10 (GAL) | 10 | 7.42 | 7.51 | 7.30 | 470 | 501 | 420 |
| 10–15 | 50 | 7.42 | 7.62 | 7.10 | 484 | 565 | 415 |
| 25–30 | 47 | 7.45 | 7.80 | 7.12 | 468 | 553 | 403 |
| > 30 | 21 | 7.37 | 7.72 | 7.24 | 484 | 517 | 422 |
| | **191** | | | | | | |

## pH

## Eh [mV]
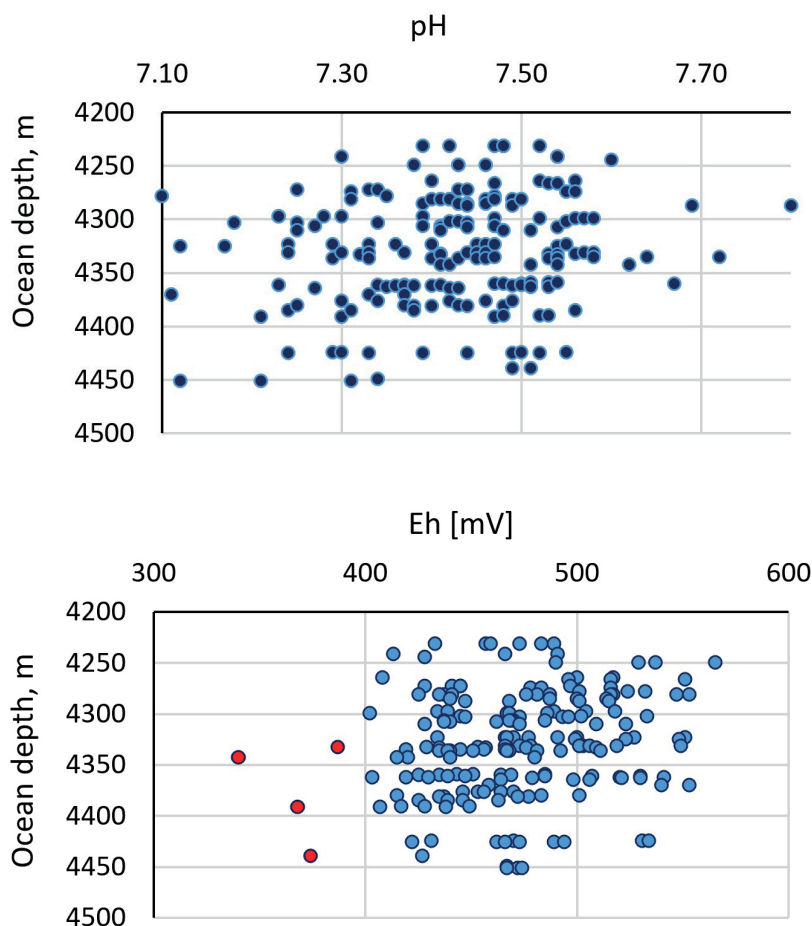
**Fig. 8.** Distribution of pH and Eh values of bottom sediments in geologically active layer (GAL) over the ocean depth in the H22 exploration block (Dreiseitl, 2018).

*Selected metal contents of bottom sediments in H22 exploration block*

Determination of 9 metal contents (Fe, Mn, Ni, Cu, Co, Zn, Pb, Cd and As) was carried out in the on-board laboratory at 65 samples, representing 23 stations (IOM-2014 cruise). Samples were taken in three depth intervals

(0–5, 10–15 and 25 + cm). In siliceous sediments, manganese (5 582 to 2 020 ppm) and nickel (228 to 112 ppm) content decreases with depth, iron content (4.57 to 4.90 %) increases with depth. Regularities were not found for the rest of metals (Cu 337 to 466 ppm, Co 47 to 65 ppm, Zn 140 to 146 ppm). The higher content of all elements is associated with the presence of micronodules in the sediment, as well as ore material near the crusts, which are often concentrated in the top layer of red pelagic clays (Dreiseitl, 2018).

More detailed analyses of chemical composition of bottom sediments were carried out in stationary (land) laboratory (Tab. 5). Samples from the same intervals of depth were used (0–5, 10–15 and 25+ cm). The total average content of rare earth elements in sediments (REE – 14 elements from La to Lu, without Sc and Y) is 277 mg/kg, which is approximately 2 times less than that in nodules. Red pelagic clays represent the sediments with the most abundance of metals (Dreiseitl, 2018).

In bottom sediments (without distinguishing individual sediment types), basic metals have an increased content in interval 0–5 cm, due to the presence of micronodules, as well as in interval more than 25 cm, which signals the proximity of layer of red pelagic clays and the presence of ore crusts on its top. Interval 10–15 cm is influenced by recent sedimentation, which is manifested by an increased content of amorphous silica and decreased content of metals. In the red pelagic clays, there is also an increased content of rare earth elements (in some samples reaching values over 300 ppm).

**Tab. 5**

Average values of selected metal contents of bottom sediments by sampling depths (SIL = siliceous sediments, value in brackets = number of analysed samples) (Dreiseitl, 2018, modified).

| Sediment type / Sampling interval [cm] | % | | ppm | | | | | | |
|---|---|---|---|---|---|---|---|---|---|
| | Fe | Mn | Ni | Cu | Co | Zn | Pb | Cd | As |
| SIL [0–5] | 4.50 (10) | 0.46 (10) | 159 (11) | 349 (11) | 63 (11) | 126 (11) | 18 (11) | 0.22 (11) | 7.17 (11) |
| SIL [10–15] | 4.58 (10) | 0.32 (10) | 109 (11) | 299 (11) | 52 (11) | 121 (11) | 19 (11) | 0.12 (11) | 5.76 (11) |
| SIL [25–30] | 4.75 (11) | 0.57 (11) | 198 (12) | 476 (12) | 96 (12) | 136 (12) | 23 (12) | 0.23 (12) | 6.91 (12) |
| Red pelagic clays [11–44] | 5.63 (3) | 2.05 (3) | 508 (4) | 944 (4) | 224 (4) | 187 (4) | 31 (4) | 0.60 (4) | 9.02 (4) |

### Selected metal contents in sediments of H22_NE exploitation block

In total, 60 samples were analysed. The mean Fe content (4.42 + 0.90 %) is higher than those of Mn (0.40 + 0.33 %). The mean Mn/Fe ratio is 0.08. The Mn and Fe contents increased with depth, the increase in some cases being related to the formation of diagenetic micronodules. Among metals other than Mn and Fe, dominant were Cu and Ni. The mean Cu and Ni contents were 388.3 + 101.5 ppm and 141.0 + 73.4 ppm, respectively. The content of Cu, Ni, Co, Zn and Pb were gradually increasing with depth. The As and Cd contents were low, with means of 8.4 + 3.0 ppm and 0.14 + 0.13 ppm, respectively. The mean ∑REE content was 285.8 + 127.9 ppm, with LREEs dominating over HREE. Among the REEs, the highest contents were shown by Y, Ce, Nd and La. Like those of other metals, the REE contents were gradually increasing with depth, the increase being particularly pronounced (to more than 400–500 ppm) below 40–50 cm. In contrast, the ∑REE content in GAL and below was fairly uniform (Maciąg et al., 2021).

The gradual increase in the contents of all metals, including REEs, with depth (Fig. 9) has to be regarded as associated with diagenetic processes which are particularly intensive below 30–40 cm in the sediment (Maciąg and Zawadzki, 2019; Zawadzki et al., 2020).

### Grain size analysis of sediments in H22_NE exploitation block

The sediment in most samples was mostly slightly plastic, slightly to moderately sticky, slightly hard, and mottled. Few samples showed the sediment to be non-plastic or soft as well as gelatinous or brittle. Traces of bioturbation were found in 58 out of the 90 samples examined. An increased amount of micronodules, nodule remains and some unidentifiable biogenic remnants or intraclasts were observed in 15 samples.

None of the samples showed the presence of $CaCO_3$, as tested with 10 % HCl. The absence of carbonates in the form of calcite or aragonite was additionally confirmed by the XRD analysis.

The sediments examined represented sandy silts, clayey silts and silts. Several samples were inhomogeneous enough to be classified as sand-silt-clay (Fig. 10). The sediments examined were generally very poorly and poorly sorted. The low amounts of very fine gravel and very coarse
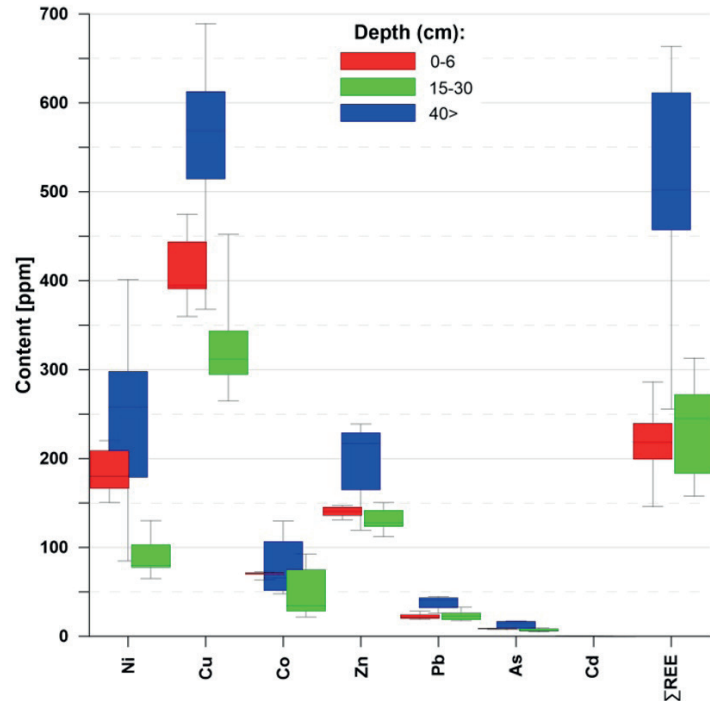


**Fig. 9.** Box-and-whiskers plots of depth-related variability in contents of selected metals. Whiskers indicate the minimum and maximum values; boxes show the lower (25 %) and upper (75 %) quartile of the data (Maciąg et al., 2020).
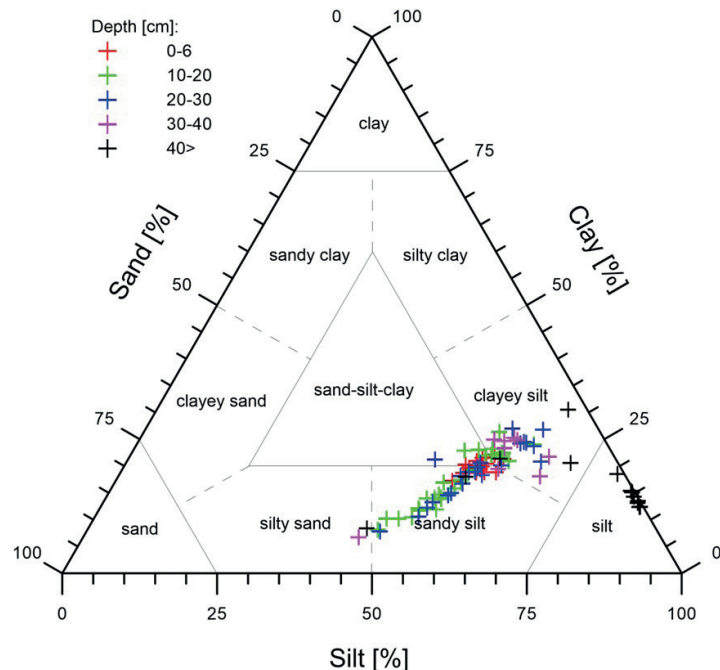


**Fig. 10.** The Shepard (1954) ternary diagram indicating the dominance of sandy silts, clayey silts, silts and a mixed group of sand-silt-clay (Maciąg et al., 2020)

sand subfractions found can be related to the presence of polymetallic nodule fragments or micronodules. The clay fraction content varied from 6.71 to 30.55 %, increasing with depth in the sediment.

The mean grain size varies from 6.99 to 47.00 μm (4.41–7.16 Φ), with a mean of 18.48 μm + 8.08 μm (5.88 Φ). Sorting varied from 2.23 to 6.63 μm, with a mean of 4.05 μm. Skewness varied from –0.43 to 0.20 (Maciąg et al., 2020).

### *Amorphous silica content in sediments of H22_NE exploitation block*

The UV-VIS analyses showed elevated contents of biogenic silica (amorphous siliceous phase represented by opal-A), which was also indicated by the XRD analyses (Maciąg et al., 2020). The biogenic $SiO_2$ contents were found to vary within 9.28–39.04 % (mean of 22.51 + 6.02 %). These values are about 12 to 15 % lower than the XRD data; however, they do not include other amorphous mineral phases such as volcanic glass or allophanes (Maciąg et al., 2011). Additionally, the XRD analyses of the amorphous phase carried a higher potential error, related mainly to the underestimation of the diffractogram background (Kowalska, 2014).

The amorphous silica content was observed to decrease with increasing depth in the sediment, the clay mineral contents increasing with depth (Fig. 11). Particularly distinct was the increase in the smectite content with depth in the sediment. The illite content increased only within 15–30 (35) cm, usually decreasing below that level. All those changes are associated with the chemical decomposition of biosilica or volcanic glass and their transformation to new mineral phases, such as smectite (Zawadzki et al., 2020).

*Total carbon (TC), total nitrogen (TN), total sulphur (TS), total organic carbon (TOC), and total inorganic carbon (TIC) contents in sediments of H22_NE exploitation block*

As shown by the analyses of biogenic components, the total carbon

(TC) contents were low (0.101–0.680 %; mean of 0.352 + 0.146 %). The carbon species were dominated by organic carbon (TOC), the contents of which were observed to vary within 0.068–0.582 % (mean of 0.332 + 0.170 %). The total inorganic carbon (TIC) contents were extremely low (< 0.147 %), as additionally confirmed by the lack of sediment reaction with HCl (see above) and no trace of carbonate minerals revealed by XRD. The total nitrogen (TN) contents were very low (0.016–0.118 %; mean of 0.073 + 0.026 %). Compared to TN, the contents of total sulphur (TS) and total phosphorus (TP) contents were higher (0.216–0.956 %; mean of 0.503 + 0.15 % and 0.066–0.435 %; mean of 0.136 + 0.088 %, respectively).

The TC and TOC contents were observed to gradually decrease with depth; a similar pattern was seen in the TN and TS contents. An opposite behaviour was detected in the TP contents which were increasing with depth (Fig. 11). The decreasing contents of most biogenic components with depth is typical and associated with oxygen consumption during denitrification and desulphurization (Volz et al., 2018). The increase in the phosphorus content below 40 cm should be regarded as strongly associated with increasing contents of ∑REE (Maciąg et al., 2020).

### *XRD analyses*

The sediment samples analysed showed a relatively low variability of their mineral components (Maciąg et al., 2020). The bulk X-ray diffraction analysis revealed domination of two major component groups: (i) amor-
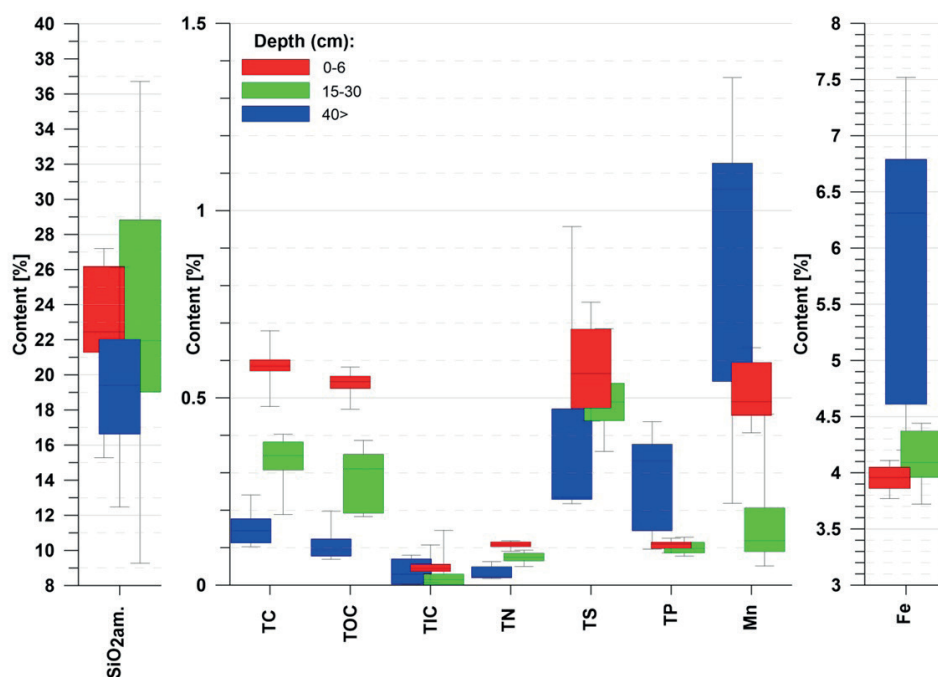


**Fig. 11.** Box-and-whiskers plots of depth-related variability in contents of biogenic components (including amorphous biosilica) as well as Mn and Fe. Whiskers indicate the minimum and maximum values; boxes show the lower (25 %) and upper (75 %) quartile of the data (Maciąg et al., 2020).
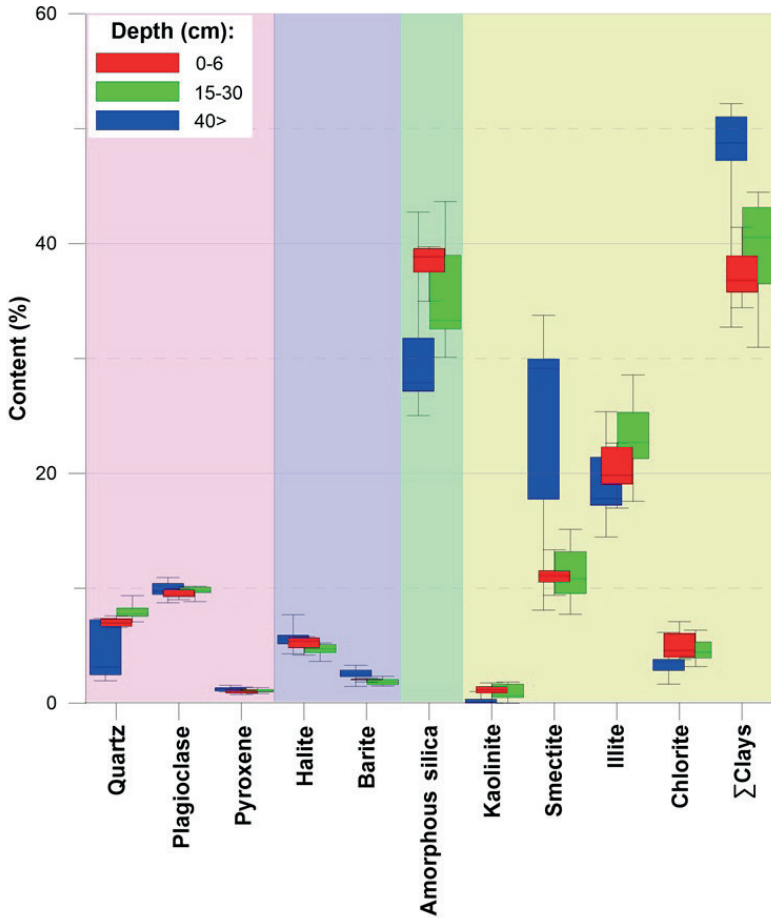
**Fig. 12.** Box-and-whiskers plots showing the depth-related variability in contents of the minerals identified. Whiskers indicate the minimum and maximum values; the boxes show the lower (25 %) and upper (75 %) quartile of the data (Maciąg et al., 2020).

*SEM/EDX analyses*

The scanning electron microscopy (SEM) photographs were taken and energy-dispersive X-ray (EDX) micro-geochemical analyses were conducted, 103 photographs were taken and 137 EDX analyses were performed. A total of 45 slurried samples were selected based on a macroscopic description, grain size analysis, bulk geochemistry and XRD results (Maciąg, 2021).

The sediments analysed showed the presence of a large variety of mineral and biogenic components as well as various debris. Generally, the contents of those components varied little in all the profiles analysed, the variability being partially related to burial-associated degradation and diagenesis of sediments.

Biogenic components were dominated by siliceous radiolarian skeletons, with lower amounts of sponge spicules and a minor presence of diatom frustules. The amount of siliceous bioclasts usually decreased with depth in the sediment; morphological preservation of the bioclasts declined with depth in the sediment, and contrasted with the best-preserved structures found in the GAL. The siliceous bioclasts, particularly radiolarians, showed traces of corrosion and alteration, evidenced by overgrowths of initial clay minerals.

phous biogenic silica represented by opal-A, and (ii) clay minerals. Their contents varied within 25.01–47.67 % and 25.86–52.16 %, respectively. The mean contents of amorphous silica and clay minerals were 35.32 % + 5.56 % and 40.06 + 6.26 %, respectively. The clay minerals were dominated by illite (I) and smectite (S), with mean contents of 20.67 % and 14.32 %, respectively. The mean I/S ratio was 1.75 + 0.63. The chlorite content varied within 1.64–7.10 % (mean of 4.32 % + 1.13 %). Kaolinite occurred in trace amounts only, up to 1.89 %, and usually below 1 % (Fig. 12). The allogenic detrital components were dominated by plagioclases and quartz, with ranges of 8.60 to 11.05 % and 1.93–9.41 %, respectively and the mean contents of 9.71 % + 0.55 % and 6.67 % + 1.92 %, respectively. In addition, pyroxenes were detected, usually in trace amounts (up to 1.54 %, and usually below 1 %). Diagenetic minerals featured halite (3.15–7.68 %; mean of 5.08 % + 0.80 %) and barite (1.44–3.28 %; mean of 2.05 + 0.41 %).



**Fig. 13.** Classification of the micronodules analyzed (N = 35) after Bonatti et al. (1972), with modifications (Maciąg, 2021).

Increased contents of bioapatite were observed below the depths of 40–50 cm in the sediment (cores 3632T and 3633T), indicating a relatively low substitution with alkali and alkaline metals, Mn-Fe impurities or Cl. One grain showed the presence of more than 5 % ΣREE. Some apatites were of magmatic rather biogenic origin, as evidenced by increased F contents.

A few samples from below 40 cm in the core showed increased contents of authigenic barite. Additionally, cores 3632T and 3633T showed the presence of zeolites, particularly within 60–110 cm of core depth. Interestingly, although the zeolites indicated Ba impurities, no barite was identified in those samples with increased zeolite contents.

The Mn-micronodules analysed were of a typical diagenetic-hydrogenetic origin (Fe contents very low or below EDX detection limits) and showed increased contents of Ni and Cu (4–8 %); in a few cases, traces of Co and Zn were revealed (Fig. 13). Organic burrows showed coatings enriched with Mn-oxyhydroxides, suggesting the processes of bio-irrigation and bio-oxidation.

The allogenic debris components were represented by minor plagioclases (anorthite-labradorite series) as well as by altered amphiboles and pyroxenes. The absence of detrital quartz grains suggests their presence within the fine pelitic fraction. In a few cases, volcanic glass was identified (e.g. among zeolites identified in cores 3632T and 3633T) (Maciąg, 2021).

**Polymetallic nodules**

*Mineral composition*

The detailed mineralogical and microgeochemical characteristics of polymetallic nodules collected during IOM-2014 and IOM-2019 expeditions from IOM exploration area (H22_NE exploitable block) were studied (Skowronek et al., 2021). The data were applied for the delimitation of nodule growth generations and estimation of the growth ratios (back-stripping using the Co-chronometer method). The applied methods included bulk X-ray powder diffraction (XRD) and electron probe microanalysis (EPMA), providing information about Mn-Fe minerals and clays composing nodules, as well as the geochemical zonation of the growth generations.

The analysed samples are generally dominated by todorokite/buserite, with a lesser amount of birnessite and traces of vernadite. Additionally, the samples indicated the presence of Fe-rich clay minerals (potentially nontronite and Fe-smectite) and mixtures of quartz, barite, zeolites (potentially Na-phillipsite), apatite, and barite (Tab. 6).

The analysed nodules were mostly diagenetic (Mn/Fe > 5), with less influence on the hydrogenous processes, dominated by the presence of 10-Å phyllomanganates represented by todorokite/buserite, additionally mixed with birnessite and vernadite. The specific lithotype (intranodulith), being an integral part of polymetallic nodules, de-

**Tab. 6**

Mineral compositions of the selected polymetallic nodule samples from the H22 exploration block, as determined by XRD. The amount of minerals is shown semi-quantitatively based on the results of the peak comparisons and integration: ++++ dominating < 50 %, +++ 50–30 %, ++ 30–10 %, + 10–5 %, and (+) traces < 5 % (Skowronek et al., 2021).

| Sample | Type | Todorokite/ Busserite | Birnessite | Vernadite | Clays | Barite | Apatite | Zeolites | Quartz |
|--------|------|------|------|------|------|------|------|------|------|
| 3529 | D | +++ | ++ | (+) | + | (+) | ++ | + | (+) |
| 3535 | D | +++ | +++ | (+) | + | (+) | + | + | (+) |
| 3537A | D-HD | +++ | + | (+) | ++ | (+) | (+) | ++ | + |
| 3537B | D-HD | +++ | ++ | (+) | ++ | (+) | + | – | + |
| 3542 | H | +++ | ++ | (+) | ++ | (+) | + | ++ | (+) |
| 3602 | D | ++++ | ++ | (+) | – | (+) | (+) | + | (+) |
| 3603 | D | +++ | ++ | (+) | ++ | (+) | (+) | + | + |
| 3604 | D | ++++ | ++ | (+) | + | (+) | (+) | + | (+) |
| 3605 | D | +++ | +++ | (+) | ++ | + | – | – | – |
| 3613 | HD | +++ | ++ | (+) | ++ | (+) | ++ | + | (+) |
| 3614 | H-HD | ++++ | ++ | (+) | + | (+) | – | ++ | (+) |
| 3615 | H-HD | ++ | ++ | (+) | ++ | (+) | – | +++ | (+) |

veloped as a result of the secondary diagenetic processes of lithification and the cementation of Fe-rich clays (potentially nontronite and Fe-rich smectite), barite, zeolites (Na-phillipsite), bioapatite, biogenic remnants, and detrital material, occurs in holes, microcaverns, and open fractures in between ore colloforms. The contents of å(Ni, Cu, and Co) varied from 1.54 to 3.06 wt %. Several remnants of siliceous microorganisms (radiolarians and diatoms) were found to form pseudomorphs. The applied Co-chronometer method indicated that the nodules' age is mainly Middle Pliocene to Middle Pleistocene, and the growth rates are typical of diagenetic and mixed hydrogenetic-diagenetic (HD) processes. Additionally, few nodules showed suboxic conditions of nucleation. Growth processes in the eastern part of the CCZ deposit might have been induced with the Plio-Pleistocene changes in the paleooceanographic conditions related to the deglaciation of the Northern Hemisphere.

The analysed polymetallic nodules consist of a core concentrically overgrown by laminae (microlayers) and areas of lithified detrital materials. The core, the laminae, and the detrital material were considered separately. The core is composed of either fragments of ancient nodules (here, Mn-Fe laminae are clearly visible) or fragments of rocks (an absence of laminae). The growth structures (laminae) overgrowing the core developed as colloforms composed of precipitated Mn-rich oxyhydroxides, mainly Ni–Cu-rich todorokite/10-Å phyllomanganates (buserite) and birnessite (Fig. 5a–d). The number of laminae composed of vernadite is relatively low (Fig. 14).

The results of the spot EPMA evidenced the nonuniform distribution of the metals in the nodules. Several of the measurement points were characterized by high concentrations of Mn in relation to Fe and were assigned to the traditionally defined diagenetic morphotype (Mn/Fe ratio > 5). The measurements typical for hydrogenetic or mixed (hydrogenetic-diagenetic-biogenous) morphotypes, i.e., depleted in Mn in comparison to the diagenetic morphotype, were less frequent (Fig. 15). The elevated contents of Fe (plots near the Fe edge) measured for nearly 30 points in all the analysed nodules were associated with the intercalation of the clay minerals and other components of detrital origin (enriched with Si, Al, or alkali-alkaline metals).

In general, regardless of the internal differentiation of the nodules, the mean Mn and Fe contents varied from 19.6 to 38.9 wt % and from 3.2 to 8.3 wt %, respectively. The mean Mn/Fe ratio was 5.37. Among the other economic metals, Ni and Cu dominated, with their mean contents varying from 0.60 to 1.52 wt % and 0.64 to 1.42 wt %, respectively. The mean EPMA contents of Ni and Cu were 1.15 and 1.08 wt %, respectively. The Co concentration varied from 0.06 to 0.31 wt %, averaging 0.20 wt %. The hydrogenetic and mixed hydrogenetic-diagenetic nodules showed lower contents of å(Cu, Ni, and Co) compared to the diagenetic nodules, with concentrations varying from 1.54 to 2.07 wt %. Additionally, low contents of Zn were identified (mean = 0.14 wt %, varying from 0.07 to 0.19 wt %), as well as Pb, As, Cr, and V (Skowronek et al., 2021).

Polymetallic nodules collected in the IOM licence area (H22-NE expoitation block) showed complex internal textures reflecting multistage nucleation affected by potential changes in the paleoproductivity and surface temperatures



**(a)**



**(b)**
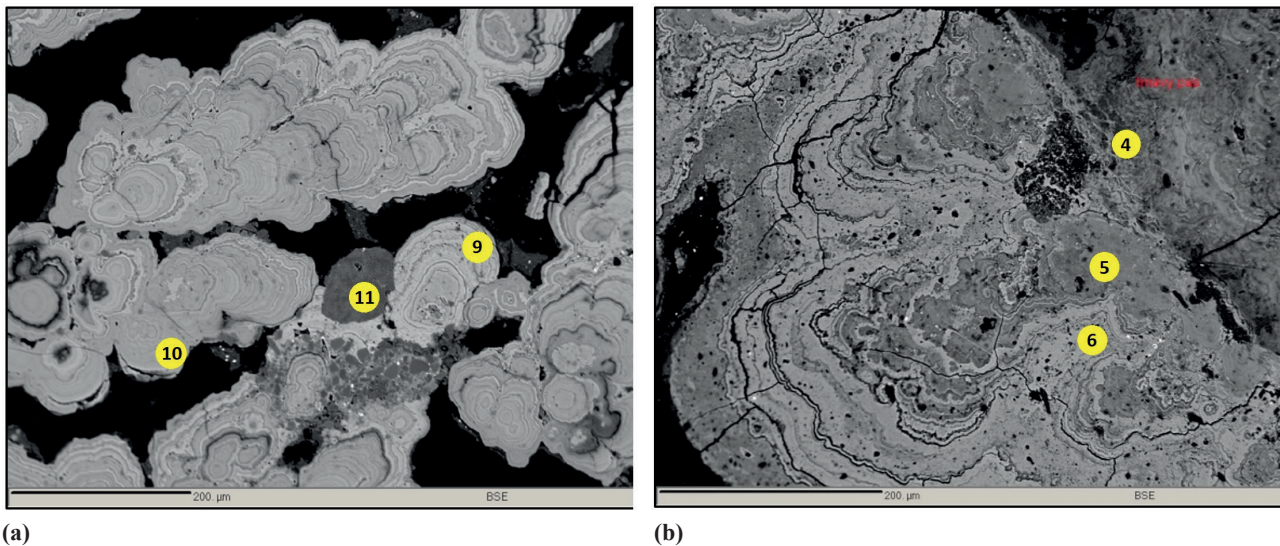
**Fig. 14.** Representative EPMA BSE images of the analysed polymetallic nodules. Sample 3642: (a) massive bright and well-developed colloforms composed of pure Mn oxyhydroxides enriched with Ni and Cu (9,10); no. 11 is an intraclast of Fe-rich clay minerals. Sample 3602: (b) typical Mn-rich diagenetic colloforms enriched with metals (5,6) and bordering a zone of veinlets and Fe-rich clay aggregates (4) (Skowronek et al., 2021).
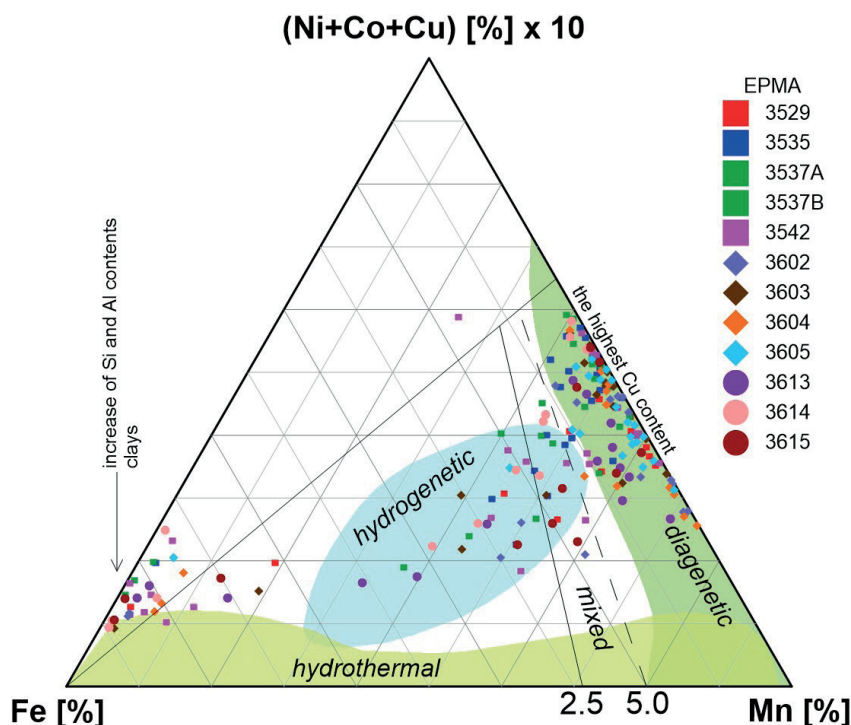
**Fig. 15.** Location of the EPMA spot data at the Fe–Mn-10 [å(Ni, Co, and Cu)] ternary plot; 2.5–5.0 = Mn/Fe ratio (reference [63] with further modifications). Coloring identifying major genetic types of analysed colloforms (Skowronek et al., 2021).

occurring during the Late Pliocene-to-Middle Pleistocene (Plio-Pleistocene) postglacial transition. Most of the analysed samples showed distinctive diagenetic features evidenced by relatively high growth rates (> 5 mm/Myr), increased Ni + Cu + Co contents (> 4 wt %), and admixtures of Fe-rich clays or barite.

The polymetallic nodules located in the nearest vicinity to underwater volcanic-shaped areas usually showed higher inputs of the hydrogenic components (slow growth rates, increased amount of Fe, and the presence of vernadite) compared to the nodules collected in relatively flat, streaked, and meridian-oriented blocks of the seafloor.

Intranodulith was proposed as a term describing the specific lithotype that is the integral part of polymetallic nodules, which developed as a result of the secondary diagenetic processes of lithification and cementation of
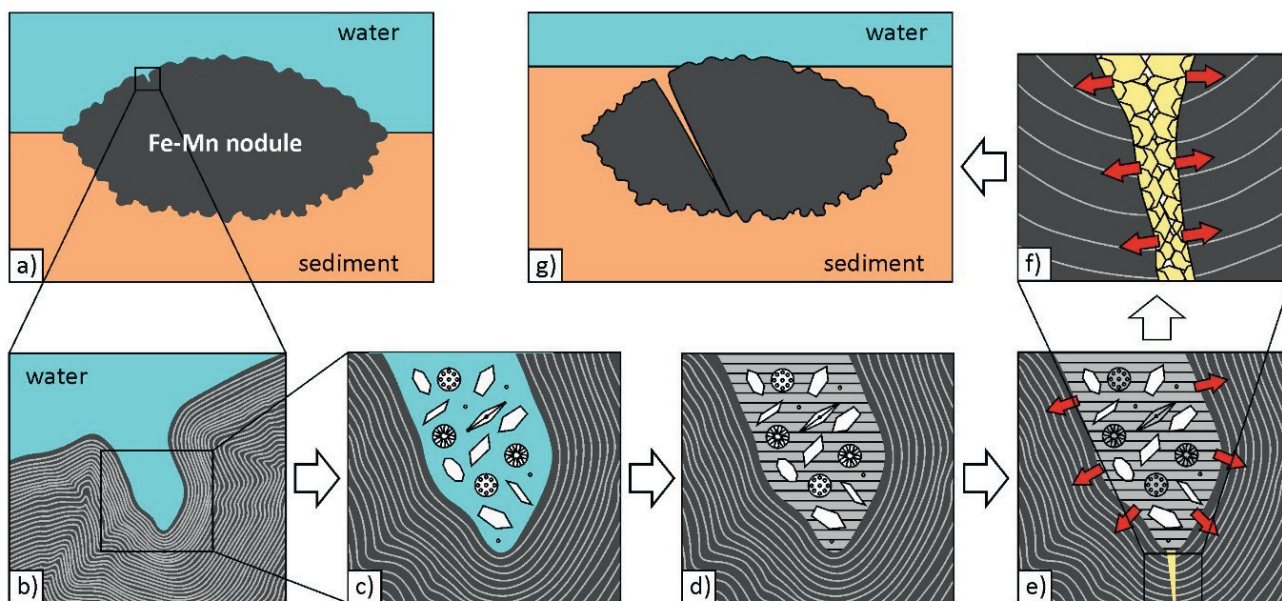


**Fig. 16.** Simplified scheme of nodule cracking due to cement growth: (a–g) the steps of the cracking process from a solid (a) to a broken nodule (g). Nodule crack caused by internal tension in the vein created by crystal growth inside the intranodulith. Red arrows indicate internal tension forces (Skowronek et al., 2021).

trapped detrital materials within holes, microcaverns, or open fractures in between ore colloforms.

A hypothesis of nodule cracking on the seafloor being caused by internal tension in the vein created by crystal growth was proposed (Fig. 16). An increase in the volume during the diagenetic lithification of the sediments trapped in cavities between colloforms (intranodulith) might have been responsible for the initial impulse that ultimately led to cracks of the Mn-Fe nodules. The further growth of the cement crystals within the initial fissure led to their additional extension, which could have ultimately caused the breakage of the nodules directly at the seafloor, being evidenced, e.g., in seabed photos or photo profiles. This secondary diagenetic process can cause the disintegration of the whole nodule without the influence of any external factors – the nodule disintegrates "by itself" (Skowronek et al., 2021).

*Chemical composition*

The reference sample of the polymetallic nodules was prepared. Homogeneity was determined by XRF analysis taken from different places of the homogenized material in the mixing container. The mixing process was repeatedly formed until the standard deviations for Mn, Fe, Si, Al, Ni, Cu, Mg and Cl under 0.23, 0.06, 0.1, 0.04, 0.03, 0.03, 0.15 and 0.06, respectively were achieved. In total, 50 g of the homogenized reference material was prepared (Vu et al., 2020).

The reference contains 95 % of the particles with the particle size under 45 μm and its humidity is in the range from 1.6 to 2.1 %. The average chemical composition of the reference for the main metals is listed in Tab. 7. The chemical composition of the main metals was calculated from the results provided by 5 laboratories. The obtained results show that laboratories using the wet method (FAAS, ICP-MS, ICP-AES) provided almost identical results for analysis of the main metals. Spectroscopic methods (XRS, XRF) provide either higher or lower metal content for Mn, Ni and Cu.

**Tab. 7**

Average content of main metals in the reference material [wt %] (Vu et al., 2020).

|  | Mn | Fe | Ni | Cu | Co | Mo | Zn | Pb | P |
|---|---|---|---|---|---|---|---|---|---|
| **Average** | 30.817 | 5.385 | 1.313 | 1.305 | 0.165 | 0.080 | 0.153 | 0.026 | 0.150 |
| **Min** | 29.660 | 4.930 | 1.030 | 1.060 | 0.130 | 0.060 | 0.130 | 0.022 | 0.136 |
| **Max** | 32.600 | 5.790 | 1.510 | 1.550 | 0.200 | 0.130 | 0.170 | 0.029 | 0.162 |
| **St. Dev.** | 1.048 | 0.292 | 0.161 | 0.160 | 0.023 | 0.034 | 0.014 | 0.003 | 0.011 |
| **RSD [%]** | 0.035 | 0.054 | 0.122 | 0.123 | 0.137 | 0.421 | 0.089 | 0.129 | 0.072 |

Main metals of H22_NE exploitable block were studied by AAS and XRF methods. Comparison of the results of both methods is shown in Tab. 8.

**Tab. 8**

The chemical composition of nodules (base metals) in H22_NE exploitable block, determined by the AAS and XRF methods (Vu et al., 2020).

| n = 20 | Mn [%] | Fe [%] | Ni [%] | Cu [%] | Co [%] | Zn [%] | Mo [%] | Pb [%] | Mn/ Fe ratio | ΣNi, Cu, Co [%] |
|---|---|---|---|---|---|---|---|---|---|---|
| **AAS** | 26.99 | 5.78 | 1.27 | 1.20 | 0.18 | 0.15 | 0.05 | 0.03 | 4.85 | 2.65 |
| **XRF** | 30.10 | 6.07 | 1.33 | 1.27 | 0.20 | 0.15 | 0.07 | 0.03 | 5.14 | 2.81 |

In H22_NE exploitable block, chemical analyses of nodules were performed at 20 boxcorer stations. Comparison of the mean values of the metal contents from the laboratories of UCHT, Prague, Czech Republic (Vu et al., 2020) and SGIDŠ, Spišská Nová Ves, Slovakia (Mackových and Lučivjanský, 2020) are presented in Tab. 9. The coefficient of variation for each of the metals does not exceed 20 %, which means that the obtained data are homogeneous. Using the Mn/Fe module, as well as the productivity index ΣNi, Cu, Co, the nodule genotype was associated with each station (sample).

**Tab. 9**

Mean values of the contents of basic metals from the laboratories of the UCHT and SGIDŠ (20 stations of the H22_NE block).

| n = 20 | Mn [%] | Fe [%] | Ni [%] | Cu [%] | Co [%] | Zn [%] | Mo [%] | Pb [%] | Mn/ Fe ratio | ΣNi, Cu, Co [%] |
|---|---|---|---|---|---|---|---|---|---|---|
| **UCHT** | 26.99 | 5.78 | 1.27 | 1.20 | 0.18 | 0.15 | 0.05 | 0.03 | 4.85 | 2.65 |
| **SGIDŠ** | 31.34 | 6.15 | 1.06 | 1.05 | 0.15 | 0.13 | 0.06 | 0.02 | 5.31 | 2.27 |

Tab. 10 presents the contents of 14 rare earth elements (without scandium and yttrium) in 20 nodule samples collected in the H22_NE exploitable block.

Chemical composition of nodules at particular stations allowed to determine genotypes within sampled blocks (H22_NE, PRZ and H33). Among samples, collected during expedition IOM-2019, diagenetic nodules occur at 18 stations, hydrogenetic at 5 stations and mixed type at 5 stations. Buried nodules were found at 11 box core stations. The results were added to those, which have been obtained during former expeditions.

**Tab. 10**

Mean values of REEs contents from the laboratories of the UCHT and SGIDŠ (20 stations of the H22_NE block).

| n = 20 | La | Ce | Pr | Nd | Sm | Eu | Gd | Tb | Dy | Ho | Er | Tm | Yb | Lu |
|--------|-----|-----|------|-----|------|------|------|------|------|------|------|------|------|------|
| | LREEs [ppm] | | | | | | | HREEs [ppm] | | | | | | |
| **UCHT** | 96.5 | 235 | 28.7 | 125 | 32.0 | 8.46 | 29.8 | 4.81 | 24.9 | 4.82 | 13.3 | 1.89 | 12.4 | 1.88 |
| **SGIDŠ** | 82.3 | 191 | 29.7 | 115 | 28.3 | 7.68 | 23.2 | 5.17 | 26.2 | 4.52 | 11.4 | 2.08 | 11.9 | 1.72 |

*Geotechnical properties*

The basic physical properties, which have to be determined on board immediately after the nodules are retrieved from the boxcorer or dredge samplers, are water content and bulk density (volumetric density). In addition, some other properties, such as dry nodule density (the drying takes place 72 hours at 105 °C), porosity, void ratio, and specific nodule density are calculated. Natural water content (ore based water content, $w_n$) is the ratio of the mass of evaporated water to the mass of wet nodule specimen. While the water content (w) and the natural water content (wn) analysis, the salt content in the sea water present in the nodule pores, assumed as M = 35 ‰, needs to be taken into account. Basic physical parameters of PMN investigated by IOM during the contract period are presented in Tab. 11.

*Nodule blanketing in H22 exploration block and H22_NE exploitable block*

Nodule blanketing (rate of sediment coverage, dimensionless coefficient) by the sediment is a characteristic feature of the entire IOM exploration area. Blanketing coefficient is calculated as the ratio of template coverage to seabed image coverage. If there is no sediment cover,

the coefficient is 1. According to analysis of 76 samples (values of template and seabed photo) the mean value of blanketing coefficient for exploration block H22 is 1.3 (Zarzecki et al., 2021). H22_NE exploitable block average blanketing coefficient was calculated on 40 samples and represents value 1.3 as well (IOM, 2021).

Wet nodule abundance (kg/m²) and nodule coverage (based on seabed photo in %) of 20 samples obtained during the IOM-2019 expedition were assessed. The positive correlation appears to be fairly strong (coefficient of determination $R^2 = 0.66$), giving evidence of similar level of nodule blanketing within the particular ore bodies (Fig. 17). It is clearly seen at the chart that about 50 % of nodule coverage on seabed photos corresponds to 14–20 kg/m² in boxcorer. Furthermore, if nodule coverage exceeds 60 %, nodule abundance about 20 kg/m² can be anticipated (Zarzecki et al., 2021).

*Use of seafloor photographs for resources estimation*

The main objective of the study (Mucha et al., 2020) was to assess the ability to determine polymetallic nodule abundance based on seafloor photography in the H22 exploration block of the IOM area. The assessment of the nodule abundance (APN) requires quality photographs of

**Tab. 11**

Basic physical parameters of nodules in the IOM exploration area in respect to the cruises 2001–2019
(values in a counter: min-max, value in a denominator: mean, n = number of analysis).

| Year of the cruise | Water content, w [%] | Bulk density, ρ [g/cm³] | Dry nodule density, $ρ_d$ [g/cm³] | Porosity, n [%] | Void ratio, e | Specific nodule density, $ρ_s$ [g/cm³] | Natural water content, $w_n$ [%] |
|--------|--------|--------|--------|--------|--------|--------|--------|
| **2001** n = 227 | 38–69 **47** | 1.70–2.06 **1.95** | 1.01–1.50 **1.33** | 55–68 **60** | 1.21–2.15 **1.53** | 3.08–3.75 **3.35** | 28–41 **32** |
| **2004** n = 308 | 38–63 **48** | 1.77–2.08 **1.95** | 1.09–1.50 **1.31** | 54–69 **62** | 1.18–2.18 **1.62** | 3.13–3.65 **3.43** | 28–39 **33** |
| **2009** n = 173 | 36–57 **46** | 1.83–2.06 **1.97** | 1.18–1.51 **1.35** | 53–66 **61** | 1.14–1.96 **1.57** | 2.98–3.68 **3.46** | 27–37 **32** |
| **2014** n = 205 | 29–71 **47** | 1.77–2.27 **1.97** | 1.03–1.75 **1.34** | 46–72 **62** | 0.86–2.56 **1.62** | 3.05–3.68 **3.49** | 22–42 **32** |
| **2019** n = 92 | 40–67 **48** | 1.74–2.13 **1.99** | 1.15–1.48 **1.35** | 53–76 **63** | 1.15–3.15 **1.70** | 2.58–4.88 **3.65** | 29–40 **32** |
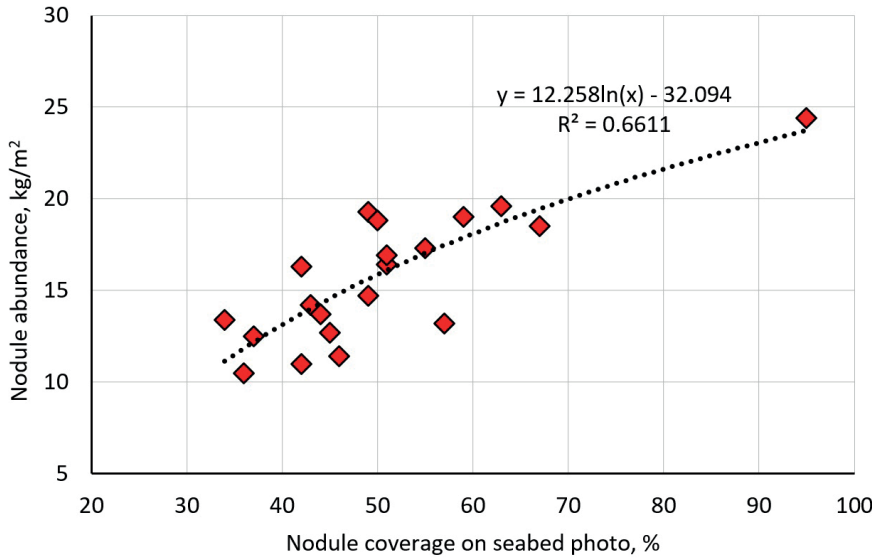
**Fig. 17.** Relation between nodule abundance and nodule coverage in H22_NE exploitable block (Zarzecki et al., 2021).

seafloor areas where the degree of covering nodules with bottom sediments is low. The measurement of the seafloor nodule coverage and basic geometrical features of the nodules: surface, long and short axes, and the number of nodules, should be carried out using well-sized images.

Out of 52 sampling sites (including photos), 37 were properly sized and used for analysis. The basic data set was insufficient to isolate large enough training and test sets (with at least 30 observations), respectively. For this reason, the cross-validation obtained is considered preliminary and requires additional verification on a bigger data set.

The created data sets, depending on the type and number of measured variables, were used to estimate the nodule abundance based on the equations of regression models. All analysed models are statistically significant at the significance level of 0.05. The accuracy of the estimation was quantified using the standard estimation error (SEE) and mean absolute estimation error (MAE).

All tested models are preliminary and require verification of their reliability based on a separate, independent and sufficiently large data set (> 30 observations). The best results were achieved with multivariate regression model using 8 variables (SEE = 2.53; MAE = 1.75):

APN [kg/m$^2$] = 0.233 · NCS[%] – 0.002 · NS +
+ 1.879 · Mean A [cm] – 2.181 · Median A [cm] +
+ 12.863 · Mean La [cm] – 0.509 · Median La [cm] –
– 21.477 · Mean Sa [cm] + 5.793 · Median Sa [cm],

where: NCS – percentage of seafloor nodule coverage, NS – number of nodules on the seafloor, Mean A – mean of nodule area, Median A – median of nodule area, Mean La – mean of long axis, Median La – median of long axes, Mean Sa – mean of short axis, Median Sa – median of short axis.

Combining measurements of the nodule abundance based on box corer data and seafloor photographs shall require the development of formulas taking into account the diverse geometrical bases of both types of data and the accuracy of determining the nodule abundance based on box corer sampling and the regression model.

Wasilewska-Błaszczyk & Mucha (2022) assessed possibilities and limitations of the use of seafloor photographs for estimating PMN resources in case study. Direct seafloor sampling is insuficient to obtain an acceptable accuracy of resource estimates in small blocks of potential deposits. This is why the results of photographic surveys of the seafloor are analysed to increase the reliability of the estimates.

A statistically significant correlation was found between the abundance of nodules and seafloor nodule coverage (quantitative variables), the nodule abundance and genetic type of nodules (ordinal variable estimated visually from photos), and between seafloor coverage with nodules and sediment coverage of nodules (ordinal variable estimated visually from photos). The correlation relationship between the seafloor nodule coverage determined manually and automatically (using computer software) was examined for the part of the data set (data from IOM-2014 expedition). A very strong linear correlation between the seafloor nodule coverage determined manually and automatically, with the correlation coefficient 0.966 (R2 = 93.3 %) was found.

Type and method of data collection (quantitative or ordinal) based on direct sampling and seafloor photographs is shown in Fig. 18. The values of the basic statistical parameters of nodule abundance (APN), seafloor coverage with nodules in the photograph (NC-S), and nodule coverage of the grid (NC-T) are summarized in Tab. 12.
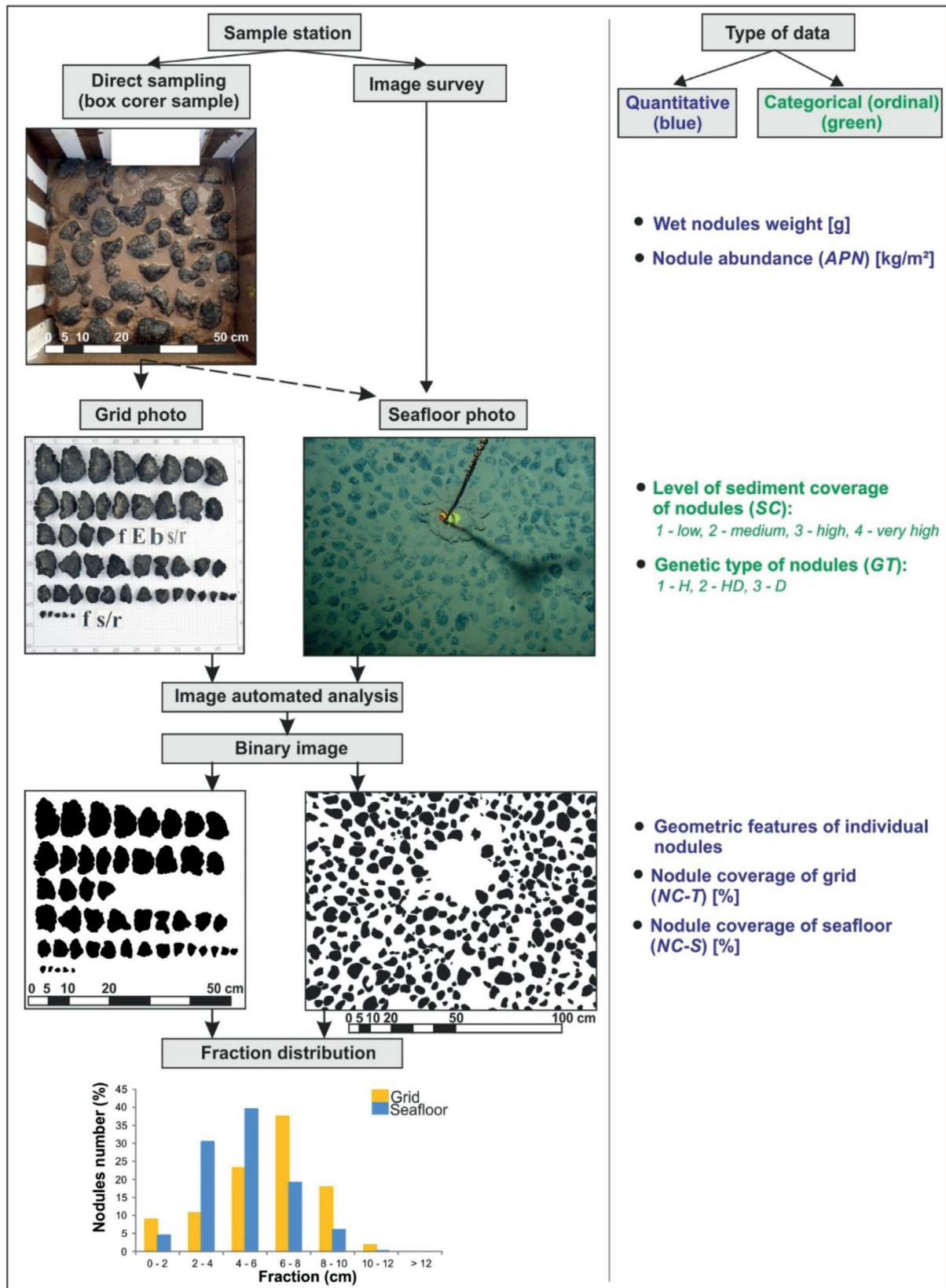
**Fig. 18.** Type and method of data collection (quantitative or ordinal) based on direct sampling and seafloor photographs (Wasilewska-Błaszczyk & Mucha, 2022).

**Tab. 12**

Statistics of nodule abundance (APN) and nodule
coverage of laboratory grid (NC-T) and seafloor (NC-S).

| Parameter | Expedition | Count | Minimum | Maximum | Arithmetic Mean | Standard Deviation | Coefficient of Variation | Skewness | Standard Skewness | Standard Curtosis |
|---|---|---|---|---|---|---|---|---|---|---|
| **APN [kg/gm²]** | 2014 | 48 | 1.5 | 19.3 | 12.5 | 4.4 | 35.3 | –0.62 | –1.76 | –0.23 |
| | 2019 | 20 | 6.9 | 23.1 | 15.9 | 4.4 | 27.9 | –0.19 | –0.35 | –0.68 |
| | 2014 + 2019 | 68 | 1.5 | 23.1 | 13.5 | 4.6 | 34.4 | –0.38 | –1.29 | –0.10 |
| **NC-T [%]** | 2014 | 48 | 5.2 | 63.2 | 41.4 | 12.5 | 30.1 | –1.08 | –3.04 | 2.02 |
| | 2019 | 20 | 24.0 | 70.0 | 55.0 | 10.7 | 19.4 | –1.03 | –1.88 | 2.18 |
| | 2014 + 2019 | 68 | 5.2 | 70.0 | 45.4 | 13.4 | 29.6 | –0.80 | –2.70 | 1.87 |
| **NC-S [%]** | 2014 | 48 | 7.0 | 72.0 | 37.9 | 13.3 | 35.1 | –0.37 | –1.06 | 0.56 |
| | 2019 | 20 | 18.0 | 59.0 | 43.3 | 10.3 | 23.7 | –1.00 | –1.82 | 1.02 |
| | 2014 + 2019 | 68 | 7.0 | 72.0 | 39.5 | 12.6 | 32.0 | –0.56 | –1.89 | 0.77 |

To estimate the nodule abundance at seafloor photographic stations where no samples were collected, statistical methods of multiple regression can be used, including general linear models, taking into account both – quantitative variable (percentage of seafloor nodule coverage) and categorized ordinal variables (degree of seafloor coverage with sediments, genetic type of nodules). Preliminary multiple regression analysis aimed at estimating nodule resources as a function of the percentage coverage of the seafloor with nodules, visual assessment of the coverage with bottom sediments (performed by a geologist experienced in the photographic evaluations), and the genetic type of nodules yielded promising results.

It should be noted that, contrary to expectations, the expansion of box corer dataset by adding a large amount of photographic data does not lead to a radical improvement of the accuracy of resources estimations. This is due to the very unfavorable linear distribution of photographic sites located only along the photo profiles, which is also reflected in the very uneven data distribution in individual smaller blocks (future mining fields). A significant accuracy improvement of PN resources estimations may be expected after taking the additional seafloor photographs along the lines perpendicular to the courses of the current photo profiles. Such opportunity is provided by the autonomous underwater vehicles (AUV). The additional exploration of the PN deposit will also be of great importance to evaluation of local variability and continuity of nodules abundance (Mucha & Wasilewska-Błaszczyk, 2022).

**Estimation of resources**

Current resources estimation is based on data collected during scientific expeditions carried out by IOM. So far, four reports using geostatistical data analysis have been prepared (2007, 2011, 2015 and 2020) and two validations performed by the Competent Person (2016 and 2020). The current state is shown in Tab. 13. The resource validation was carried out in accordance with the CRIRSCO directives (Committee for Mineral Reserves International Reporting Standards) and Annex V of the Recommendations for the guidance of contractors on the content, format and structure of annual reports (ISBA/21/LTC/15): Reporting standard of the International Seabed Authority for Mineral Exploration Results Assessments, Mineral Resources and Mineral Reserves (Szamałek, 2020). The effective date for the estimate is August 2020. No mineral reserves were estimated at this stage of the project development.

New estimation of mineral resources in B2 sector was caried out using the geostatistical method of ordinary block kriging with Yamamoto correction. Estimates of resources and abundance of nodules and metals were carried out in square elementary blocks with a side of 500 m using kriging and co-kriging (Fig. 19). The estimates used 8 nearest sampling stations, two from each quadrant (quarters) into which the circular data search zone was divided. The center of the circular data search zone coincides with the center of the elementary block. In the calculation procedure, isotropic models of variograms, cross-variograms,

**Tab. 13**

Mineral resource estimate of wet polymetallic nodules in the IOM Exploration Area. Cut-off 10 kg/m²
of wet nodules – without volcanoes, seabed areas free of nodules and areas sloped over 7°. Note: Sector B2 includes
exploration blocks H11, H22, H33, H44 and exploitable block H22_NE
(Mucha & Wasilewska, 2007; Shanov et al., 2007; Mucha & Wasilewska-Błaszczyk, 2020; Szamałek, 2020).

| Mineral Resource Classification | Mean Abundance [kg/m²] | Mn [%] | Ni [%] | Cu [%] | Co [%] | Zn [%] | REE [ppm] | Resources Wet [Mt] |
|---|---|---|---|---|---|---|---|---|
| Measured (H22_NE block) | 14.60 | 29.19 | 1.31 | 1.25 | 0.18 | 0.15 | 713 | 12.2 |
| Measured Total | | | | | | | | 12.2 |
| Indicated (H11 + H22 blocks) | 12.40 | 31.37 | 1.30 | 1.29 | 0.16 | 0.16 | – | 77.0 |
| Indicated Total | | | | | | | | 77.0 |
| Inferred (B1 sector) | 13.40 | 27.80 | 1.20 | 0.90 | 0.20 | – | – | 62.6 |
| Inferred (H33 block) | 12.00 | 32.35 | 1.41 | 1.20 | 0.18 | 0.15 | – | 21.8 |
| Inferred (H44 block) | 11.50 | 30.71 | 1.32 | 1.19 | 0.19 | 0.14 | – | 13.6 |
| Inferred (B2 sector other) | 11.59 | 30.90 | 1.32 | 1.21 | 0.18 | 0.15 | – | 85.3 |
| Inferred Total | | | | | | | | 183.3 |
| Grand Total | | | | | | | | 272.5 |
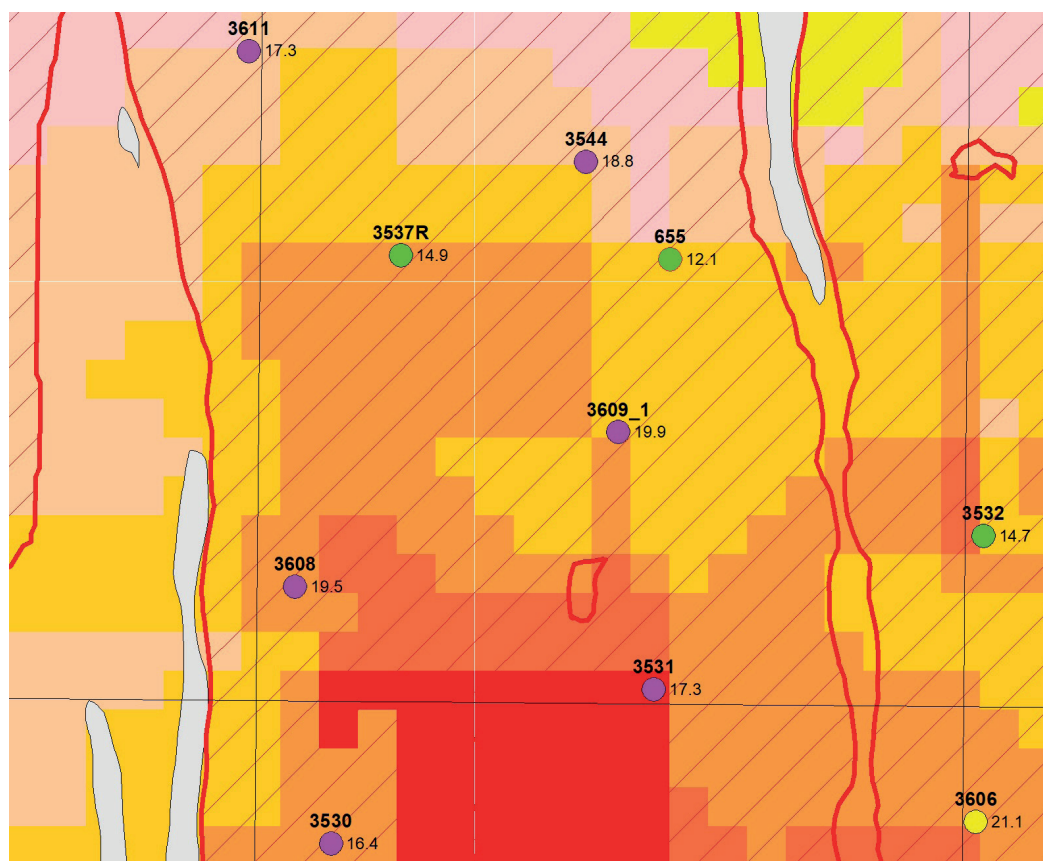


**Fig. 19.** Section from the most promising area of nodule abundance in H22_NE exploitable block. Grey areas represent seafloor with slope more than 7°, hatched areas represent ore bodies (Mucha & Wasilewska-Błaszczyk, 2020).

covariance and cross-co-variance were used. The total resources of polymetallic nodules of the exploration blocks and ore fields (ore bodies), for different values of maximal the ocean-floor slopes, were obtained by summation of resources estimated for elementary blocks.

The accuracy of resource estimation in blocks H11 + H22 and in block H22_NE is high as evidenced by small, standard kriging errors in the range of 3–6 %. The resources of nodules in blocks H33 and H44, expressed by standard errors from the 8–12 % range, were estimated with much lower accuracy. The different size of errors is the result of the different density of the bottom sampling in individual blocks.

The dependency of the tonnage of nodules and mean abundances in relation to the minimum abundance of wet nodules in B2 Sector is shown in Fig. 20.

## Conclusions

Research work in the second phase of the deposit exploration included processing of data collected during the IOM-2019 expedition and combined with data sets from previous sampling campaigns (2001–2014). The analytical work was based on sediment and nodule analyses of samples from the H22 exploration block and the H22_NE exploitation block. The structure of the sedimentary cover of the H22 exploration block, grain size analysis, mineral analysis, physical, strength, geochemical and geotechnical properties of bottom sediments and nodules were studied. Chemical composition and the contents of all main metals, including REEs, were analysed. Continued work on use of seafloor photographs for resources estimation.

IOM has sufficient samples of adequate quality and authenticity to define Inferred, Indicated and Measured Mineral Resources. The effective date for the estimate is August 2020. Mineral Resources were estimated at various nodule abundance cut-offs. Selected base scenario is an abundance cut-off of 10 kg/m$^2$ (in wet condition). Metals of value are manganese, nickel, cobalt, copper, zinc and REEs. Other metals of potential value (Mo, Fe, Li) have not been estimated, but in the future, based on processing technology development, they could provide added value to the project.

Measured Resources in exploitation block H22_NE and Indicated Resources in exploration blocks H11 and H22 were

selected for the Pre-feasibility Study. Future activities of IOM will focus on a detailed survey of selected blocks and increasing the category of resources, alternatively reserves. Geological data, together with other data obtained during the technological research of mining and processing methods, as well as environmental research represent the basis for the commercial model of deposit utilization. Legal framework for mining and environmental
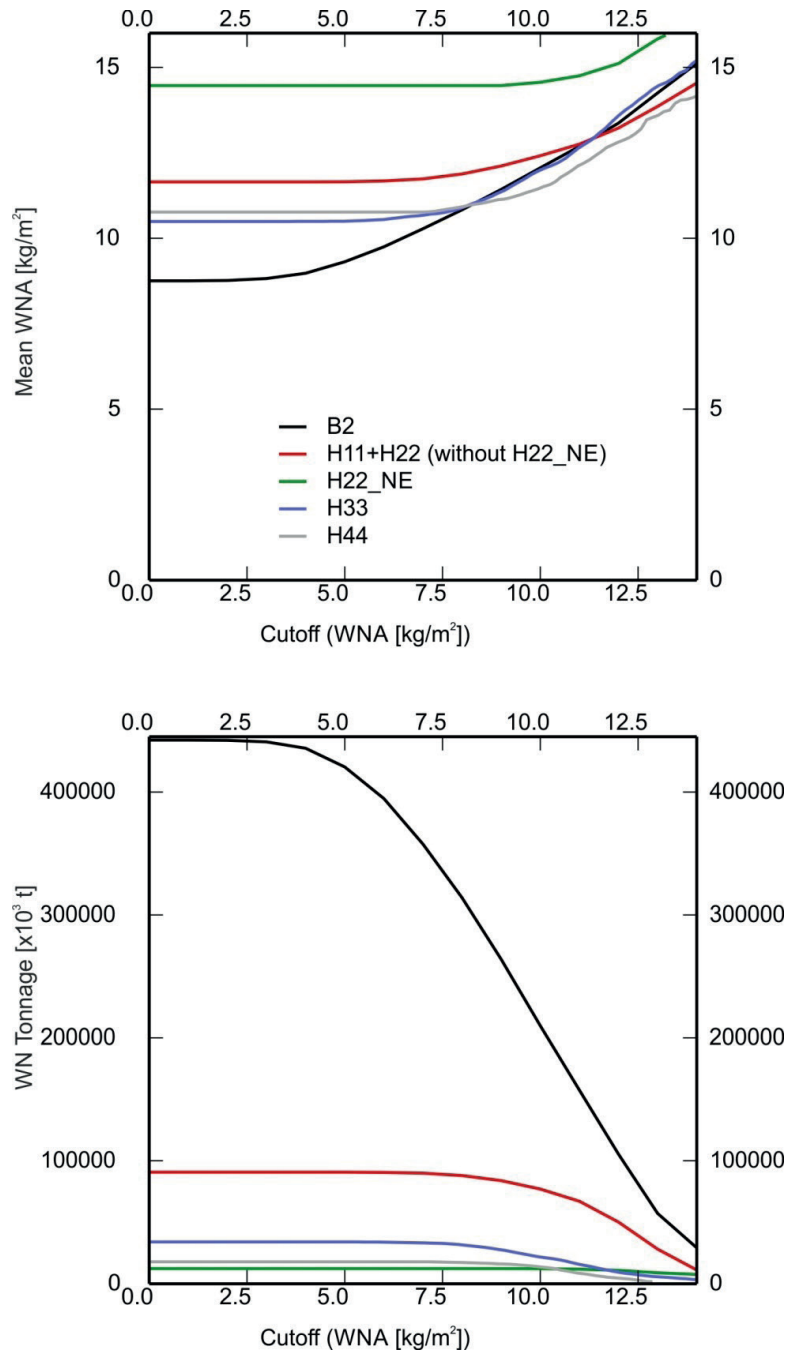


**Fig. 20.** Graph of the dependence of the average abundance of wet nodules (top) and the tonnage of wet nodules (bottom) on the cut-off value of the abundance of wet nodules (WNA); seabed slope ≤ 7° (Mucha & Wasilewska-Błaszczyk, 2020).

regulations, as a fundamental condition for future deep sea mining activities, is under the development by the ISA.

## References

Baláž, P., Dreiseitl, I., Abramowski, T., Shiryaev, B., Cabello, M. & Mianowicz, K., 2019: Preliminary Economic Assessment Technical Report – IOM Polymetallic Nodules Project in CCZ, Pacific Ocean. *IOM Internal Report. Szczecin, IOM.*

Baláž, P., 2021: Results of the first phase of the deep-sea polymetallic nodules geological survey in the Interoceanmetal Joint Organization licence area (2001–2016). *Miner. Slov., 53, 1, 3–36.*

Dreiseitl, I., 2018: Otchet o kompleksnych geologo-ekologiceskich issledovanijach, vypolnennych v rejse IOM-2014 (in Russian language). *IOM Internal Report.*

IOM Report on Activities of the Interoceanmetal Joint Organization (IOM) in 2021 submitted in fulfilment of the Contract for Exploration concluded with the International Seabed Authority. *IOM Internal Report. Szczecin, 29 p.*

ISA, 09/2021: International Seabed Authority, Exploration Contracts (https://www.isa.org.jm/exploration-contracts).

ISA, 2021: International Seabed Authority, Polymetallic Nodules Exploration Areas (https://www.isa.org.jm/polymetallic-nodules-exploration-areas-clarion-clipperton-fracture-zone).

ISBA/21/LTC/15, 2015: International Seabed Authority, Recommendations for the guidance of contractors on the content, format and structure of annual reports (https://www.isa.org.jm/document/isba21ltc15).

Kowalska, S., 2014. Wyznaczanie zawartości substancji amorficznej w skałach metodą Rietvelda (XRD). *Nafta-Gaz, LXX, 10, 700–706.*

Maciąg, Ł., Kotliński, R. A. & Borówka, R. K., 2011: Lithological Variability of Siliceous Clayey Silts from IOM Area (Clarion-Clipperton Fracture Zone, East Pacific). *Gór. Geoinż., 35, 4, 243–255.*

Maciąg, Ł. & Zawadzki, D., 2019: Spatial variability and resources estimation of selected critical metals and rare earth elements in surface sediments from the Clarion-Clipperton Fracture Zone, equatorial Pacific Ocean, Interoceanmetal claim area. In: The 20th Annual Conference of the International Association for Mathematical Geosciences IAMG2019. *Pennsylvania, USA, St. College, 174–178.*

Maciąg, Ł., Zawadzki, D., Radziejewska, T., Wróbel, R., Sławińska, J., Osóch, P., Tomkowiak, J., Witkowski, J., Stachowska, Z., Januszkiewicz, A. & Tomaszewicz, A., 2020: Comprehensive analysis (chemistry, lithology, mineralogy, granulometry) of ocean floor sediments (IOM cruise 2019). Mar Ecol Consulting Teresa Radziejewska. *IOM Internal Report. Szczecin, 30 p.*

Maciąg, Ł., 2021: Comprehensive analysis (chemistry, lithology, mineralogy, granulometry) of ocean floor sediments (IOM cruise 2019), the complex SEM-EDX analyses. Mar Ecol Consulting Teresa Radziejewska. *IOM Internal Report. Szczecin, 64 p.*

Mackových, D. & Lučivjanský, P., 2020: Determination of matrix composition of polymetallic nodules on samples taken in the cruise IOM-2019. State Geological Institute of Dionýz Štúr, Geoanalytical laboratories. *IOM Internal Report. Szczecin, 21 p.*

Mucha, J. & Wasilewska, M., 2007: Estimation of polymetallic nodule resources of the IOM's exploration area and its nickel, manganese and molybdenum contents using a geostatistical method for available geological data processing (in Russian). *IOM Internal Report. Szczecin.*

Mucha, J., Wasilewska-Błaszczyk, M. & Yubko, V., 2011: Estimation of polymetallic nodule resources of and its nickel, manganese copper and cobalt contents using the geostatistical method of processing based on the IOM geological data. *IOM Internal Report. Szczecin.*

Mucha, J. & Wasilewska-Blaszczyk, M., 2020: Estimation of the Resources of Polymetallic Nodules and Contained Metals in Sector B2 and the Exploration Blocks H11 + H22, H33 and H44. *IOM Internal Report. Krakow, AGH Univ. Sci. Technol.*

Shanov, S., Boikova, A. & Radulov, A., 2007: Estimation of the resources of polymetallic nodules of the IOM exploration area and their content of copper, cobalt and zinc using a geostatistical method for processing the geological data available in IOM. *IOM Internal Report. Szczecin, 48 p.*

Skowronek, A., Maciag, Ł., Zawadzki, D., Strzelecka, A., Baláž, P., Mianowicz, K., Abramowski, T., Konečný, P. & Krawcewicz, A., 2021: Chemostratigraphic and Textural Indicators of Nucleation and Growth of Polymetallic Nodules from the Clarion-Clipperton Fracture Zone (IOM Claim Area). *Minerals, 11, 868,* https://doi.org/10.3390/min11080868.

Szamałek, K., 2020: Validation of the Estimation of Resources of Polymetallic Nodules and Metals Contained in the Nodules in the B2 Sector and Exploration Blocks H11, H22, H33 and H44 with Resource Categorization within the Seabed Exploration Area According to Agreement between IOM and the International Seabed Authority. *IOM Internal Report. Szczecin.*

Vu, H., Kristianová, E., Frýdl, T., Bastl, T., Tomaško, T. & Dvořák, P., 2020: Chemical analysis of nodule samples recovered during the IOM-2019 cruise. University of chemistry and technology, Faculty of Chemical Technology, Prague. *IOM Internal Report. Szczecin, 50 p.*

Zarzecki, D., Kołodziejczyk, M., Hendryk, M., Urbanek, M., Abramowski, T., Baláž, P., Cabello, M., Dreiseitl, I., Mianowicz, K. & Shiryaev, B., 2021: Pre-Feasibility Study Technical Report on the IOM Polymetallic Nodules Project in Clarion-Clipperton Zone. *IOM Internal Report. Szczecin, 328 p.*

Zawadzki, D., Maciąg, Ł., Abramowski, T. & McCartney, K., 2020: Fractionation Trends and Variability of Rare Earth Elements and Selected Critical Metals in Pelagic Sediment from Abyssal Basin of NE Pacific (Clarion-Clipperton Fracture Zone). *Minerals, 10, 4.*

# Výsledky druhej fázy geologického prieskumu hlbokomorských polymetalických konkrécií v prieskumnom území Spoločnej organizácie Interoceanmetal (2016 – 2021)

Prieskumné práva boli Spoločnej organizácii Interoceanmetal udelené na prieskum polymetalických konkrécií (PMN) 29. marca 2001 na území nachádzajúcom sa v zóne Clarion-Clipperton (CCZ) vo východnej časti centrálneho Tichého oceánu. Prieskumné územie má rozlohu približne 75 000 km² a pozostáva z dvoch sektorov (B1 a B2). Sektor B2 zahŕňa štyri prieskumné bloky (H11, H22, H33 a H44). Najperspektívnejšia oblasť vybraná na podrobný prieskum je označená ako H22_NE (*exploitable block*) a *je* vymedzená v rámci prieskumného bloku H22. V článku sú uvedené výsledky geologického prieskumu na základe dát získaných počas druhej fázy prieskumu (2016 – 2021, t. j. prvé predĺženie zmluvy na prieskum). Výsledky sú založené na dátach z expedícií IOM a príslušných analytických prácach. Počas expedície IOM-2018 sa uskutočnil batymetrický prieskum prieskumných blokov H11, H22, H33 a H44. Expedícia IOM-2019 poskytla nový súbor údajov získaných pomocou dištančných metód (sonár s bočným skenovaním, *profiler*) a kontaktných metód (*box-corer* a *gravity-corer*) v bloku H22_NE, prieskumnom bloku H33 a predbežne vymedzenej ochrannej referenčnej zóne (PRZ). Ochranná referenčná zóna (*Preservation Reference Zone*) je oblasť, v ktorej sa nesmie vykonávať ťažba, aby sa zabezpečila reprezentatívna biota morského dna s cieľom porovnania zmien morského prostredia s územím ťažby. Povinnosť stanoviť PRZ vo svojom prieskumnom území ukladá vykonávateľovi prieskumu ISA (*International Seabed Authority* – Medzinárodná organizácia pre morské dno).

Výsledkom batymetrických prác bol súbor nových máp povrchu morského dna vrátane vrstevnicovej mapy, mapy sklonov morského dna, ako aj mapy amplitúd spätne rozptýleného signálu (*backscatteru*). Prieskumné bloky boli zmapované v mierke 1 : 100 000, detailne mapovaný blok H22_NE v mierke 1 : 50 000. Štúdium štruktúry sedimentárneho pokryvu prieskumného bloku H22 bolo založené na interpretácii hydroakustického profilu s vymedzením jednotlivých sedimentárnych komplexov, resp. subkomplexov a bazaltového podložia.

Analytické práce boli založené na analýzach vzoriek sedimentov a konkrécií z bloku H22 a H22_NE. Skúmala sa štruktúra sedimentačného pokryvu prieskumného bloku H22, vykonala sa analýza granulometrie, minerálna analýza, fyzikálne, pevnostné, geochemické a geotechnické vlastnosti sedimentov dna a polymetalických konkrécií. Analyzovalo sa chemické zloženie a obsah všetkých hlavných kovov vrátane REE. Použité postupy zahŕňali širokú škálu analytických metód (XRD, XRS, XRF, SEM/EDX, EPMA BSE, FAAS, ICP-MS, ICP-AES). Bola navrhnutá aj hypotéza prirodzeného praskania (deštrukcie) konkrécií na morskom dne vyvolaného vnútorným napätím v žilách, iniciovaného diagenézou sedimentov v dutinách a následne rastom kryštálov v cementačnej výplni trhlín.

Pokračovali práce na využívaní fotografií morského dna na odhad zdrojov/zásob polymetalických konkrécií. Hlavným cieľom štúdia bolo posúdenie schopnosti určiť hustotu uloženia (kg/m²) konkrécií na základe analýzy fotografií morského dna v prieskumnom bloku H22. Odhad hustoty uloženia konkrécií si vyžaduje kvalitné fotografie oblastí morského dna a nízku mieru pokrytia konkrécií sedimentmi dna. Meranie základných geometrických parametrov konkrécií prebiehalo manuálne, ako aj s využitím softvéru na analýzu obrazu. Bol pripravený multivariačný regresný model na orientačný výpočet hustoty uloženia na základe geometrických parametrov konkrécií získaných z fotografii morského dna.

Výsledky prieskumu boli po jednotlivých expedíciách zhrnuté v správach o geologickom a environmentálnom výskume, v polročných správach na zasadnutia Rady IOM, ako aj vo výročných správach pre ISA. Prehľad a výsledky prieskumných prác boli zhrnuté v technických správach (Baláž et al., 2019; Zarzecki et al., 2021). Prezentované výsledky poskytujú dodatočné informácie k už skôr publikovaným údajom (Baláž, 2021), ktoré sú relevantné na aktualizáciu odhadu zdrojov v sektore B2. Získané údaje a analýzy sa využívajú pri plánovaní projektu využívania polymetalických konkrécií IOM.

Nový odhad zdrojov v sektore B2 bol vykonaný pomocou geoštatistickej metódy blokového krigingu s Yamamotovou korekciou. Zdroje polymetalických konkrécií boli zaradené do kategórií *Inferred*, *Indicated* a *Measured* podľa klasifikačného systému CRIRSCO. Súčasný odhad množstva zdrojov vychádza z údajov zhromaždených počas všetkých vedeckých expedícií. Doteraz boli vypracované štyri výpočty s použitím geoštatistickej analýzy údajov (2007, 2011, 2015 a 2020) a dve validácie vykonané kompetentnou osobou (2016 a 2020). Súčasný stav je uvedený v tab. 13. Validácia zdrojov bola vykonaná v súlade so smernicami CRIRSCO (Výbor pre medzinárodné

štandardy vykazovania zásob nerastných surovín) a ISA (ISBA/21/LTC/15: *Reporting standard of the International Seabed Authority for Mineral Exploration Results Assessments, Mineral Resources and Mineral Reserves*). Dátum účinnosti posledného výpočtu zdrojov je august 2020. V tejto fáze projektu neboli odhadnuté žiadne zásoby nerastných surovín.

Nerastné zdroje boli odhadnuté pri rôznych hraničných hodnotách hustoty uloženia konkrécií. Zvolený základný scenár používa medznú hodnotu (*cut-off*) 10 kg/m$^2$ (vo vlhkom stave). Hlavnými záujmovými kovmi sú mangán, nikel, kobalt, meď, zinok a REE. Ďalšie kovy s potenciálnou hodnotou (Mo, Fe, Li) neboli odhadnuté, ale v budúcnosti by na základe vývoja technológií spracovania mohli predstavovať pridanú hodnotu projektu.

Geologické údaje spolu s ďalšími údajmi získanými počas technologického výskumu ťažobných a spracovateľských metód, ako aj environmentálneho výskumu predstavujú základ komerčného modelu využívania ložiska. Právny rámec ťažby (vrátane environmentálnych predpisov) vypracúva ISA a je v štádiu prípravy.

# Oxidation and decomposition of stratiform SedEx sulfidic mineralization in the epidote-amphibolite facies producing cassiterite, V-rich micas, In-Sn-Ag-Sb-Pb-Bi-Zn-Fe-As-Cu-Ni-Co sulfides and Fe-Ca-Pb carbonates in situ (Bystrý potok locality,  Gemeric unit, W. Carpathians)

MARTIN RADVANEC, IVAN HOLICKÝ and STANISLAV GONDA

State Geological Institute of Dionýz Štúr, Mlynská dolina 1, Sk-817 04 Bratislava, Slovakia

**Graphical abstract**

Sedimentary exhalative - SedEx sulfidic mineralization

Cassiterite *metamorphic*
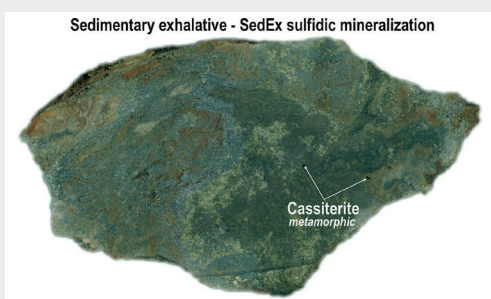
**Highlights**

- Stratigraphicaly linked Silurian C-rich phyllites with limestone lenses and Late Silurian–Devonian SedEx sulfidic mineralization were metamorphosed in Permian epidote-amphibolite facies and related chlorite-apatite zone of Variscan orogenesis.

- Limestones were transformed to hedenbergite-garnet-epidote-actinolite-chlorite-fluorapatite bearing skarn.

- The Sn-In-Fe-Ag-Pb-Bi-Ni-rich SedEx-sulfides were decomposed by fluid phase oxidation to form metamorphogenic cassiterite, V-rich micas, szomolnokite, hauchecornite, In-rich sakuraiite, Cu-Ag tetrahedrites, siderite a.o. minerals in situ.

**Abstract:** The studied area of Bystrý potok locality (Gemeric unit, W. Carpathians) is built of lenses of lydites and limestones, being a part of the graphite bearing phyllites of Silurian Holec Beds. The Holec Beds represent the bedrock of the albite-quartz bearing keratophyre (trachyte sensu IUGS classif.) sequence with stratiform SedEx (sedimentary-exhalation) sulfidic mineralization in the Gemeric Lower Paleozoic stratigraphy. This SedEx mineralization was contemporaneous with Late Silurian–Devonian keratophyre/basalt magmatism and originated at 280–340 °C from the seafloor exhalates in Lower Paleozoic rift magmatism. The Silurian-Devonian rock sequences were metamorphosed in Permian.

The limestone lenses were altered to Permian skarn in the epidote-amphibolite facies (526–546 °C, 3–6 kbar) and in related chlorite-apatite zone (420–540 °C) they consisted of garnet $Grs_{41.4-60.2}Sps_{19.8-32.8}Alm_{16.7-22.2}Adr_{0-8.5}$, hedenbergite $Wo_{44.5-50.1}Fs_{31.6-38.2}En_{12.7-20.7}$, epidote, actinolite, fluorapatite, titanite, chlorite, ankerite and siderite. The disseminated original millerite was partially replaced by hauchecornite, hauchecornite-*(Sb)* and cobaltite was formed in the silicate matrix of the skarn.

The Permian metamorphism of the epidote-amphibolite facies and the chlorite-apatite zone has also released a fluid phase rich in $O_2$, $H_2O$, $CO_2$, $H_3PO_4$, $H_2S$, HF and V from the organic matter-bearing rock (Holec Beds) into the overlying bed with keratophyres and primary stratiform SedEx sulfidic mineralization where V-rich micas, V-rich chlorite and schreyerite formed. The primary stratiform SedEx sulfidic mineralization composed predominantly of pyrite 1 less pyrrhotite, chalcopyrite, sphalerite 1, galena 1, arsenopyrite, ferrokesterite, stephanite, gudmundite, bismuthinite 1, PbBiSb-rich sulphide ($A_2B_2S_5$-type) and kobellite has been oxidized and decomposed by this fluid phase to form a new metamorphic minerals in situ. The pyrrhotite decomposed to form szomolnokite, pyrite 2, goethite and siderite. The galena 1 was partly oxidized and decomposed to anglesite and cerussite. The In-rich ferrokesterite, Sn-rich sakuraiite and In-rich sphalerite 1 oxidized, decomposed, and reacted with the fluid phase to form cassiterite, chalcopyrite, In-rich sakuraiite and sphalerite 2. The PbSbBi-rich sulfide ($A_2B_3X_6$-type), wittite, bismuthinite 2, native Bi and Se-rich galena 2 are new minerals, formed by the decomposition of original PbBiSb-rich sufhide ($A_2B_2X_5$-type), kobellite and bismuthinite 1.

Tetrahedrites 1–3 ranging from tetrahedrite-*(Fe)*, kenoargentotetrahedrite-*(Fe)* to rozhdestvenskayaite-*(Fe)* show a gradual ordering in three separate zones controlled by immiscibility gaps in the Cu-Ag substitution of tetrahedrite group. These tetrahedrites were formed by the decomposition of the original SedEx ferrokesterite, stephanite and gudmundite. The gudmundite was also commonly oxidized to form valentinite and the decomposition of ferrokesterite, galena 1 and gudmundite also produced bournonite and plumosite-like. Altogether 22 reactions illustrate the relationship between the source SedEx mineralization and the new metamorphic minerals, which have formed at the expense of the original stratiform SedEx sulfidic mineralization in situ.

The metamorphogenic fluid phase, released from the Holec Beds, has been enriched with additional elements from the stratigraphic horizon of the stratiform SedEx sulfidic mineralization and is genetically part of the Permian metamorphic-magmatic-hydrothermal (MMH) cycle (281–256 Ma).

**Key words:** metallogeny, stratiform SedEx mineralization, metamorphism, cassiterite, In and Bi sulfides, Cu-Ag tetrahedrites, Gemeric unit

## Introduction

The occurrence of stratiform sulfidic, mostly pyrite mineralization, in the valley of Bystrý potok creek, is located between the Banisko and Zlatý stôl hills in the central part of Gemeric unit, the Western Carpathians (Fig. 1). Its stratiform position has been verified by three adit levels since 1877, when four mining tariffs for the occurrence of pyrite were granted, forming the "Alžbeta" mining field (Fig. 1b). The final data on mining activities are from 1914–1917. According to mining prospecting, the mineralization has the shape of a column or a narrow lens widened conformably with the dip of beds. The lens is 20 m long, 0.81 to 2 m thick and has a depth range of about 100 m. Mineralization at the lens margin has wedged out or was tectonically cut (Kantor & Fusán, 1952; Grecula et al., 1995). A hereditary tunnel long ca 310 m was dug under the lens. There is a lack of any data about it and no mining maps have been preserved (Kantor & Fusán, 1952). Material on small heaps indicates that variable mineral assemblages have been found in the Alžbeta mining field (Kantor & Fusán, 1952; Ilavský, 1961; Drnzíková & Mandáková, 1970 in Grecula et al., 1995).

The polymetallic ore in the lens is often massive, layered (alternating layers are up to 7 cm thick with different proportions of individual sulfides), but usually a disseminated form is also present, consisting of pyrite, chalcopyrite, galena, sphalerite, pyrrhotite, arsenopyrite, marcasite, ankerite, dolomite, quartz, being accompanied by rare cassiterite, white mica similar to zinnwaldite, tetrahedrite, jamesonite, Sb-Bi sulfides, gold, apatite and muscovite (Grecula et al., 1995). For the first time in this locality, cassiterite was exactly described in Gemeric unit (Kantor & Fusán, 1952).

Metallogenesis at the Bystrý potok locality is the aim of this study. Here, metamorphogenic minerals, formed in the epidote-amphibolite facies and the related chlorite-apatite zone, have been identified in layers, bands and aggregates of the original stratiform SedEx sulfidic mineralization in-situ. These new minerals were formed by oxidation and decomposition of the original SedEx mineralization into cassiterite, valentinite, goethite, szomolnokite, anglesite, V-rich mica, V-rich chlorite, schreyerite, Fe-Mn-Pb carbonates and Ag-Sb-Pb-Bi-Zn-Sn-In-Fe-As-Cu-Ni-Co sulfides in the Permian metamorphism. Metamorphogenic ore minerals and their SedEx source mineralization are also found in the albite-quartz bearing metakeratophyre (trachyte – IUGS). The original keratophyre and SedEx mineralization formed contemporaneously with the keratophyre/basic-spilitic magmatism in the Late Silurian-Devonian rift and are stratigraphically located in the upper part of the host Holec Beds or on their surface. The Holec Beds are composed of lydites and lenses of limestones in the Silurian graphitic phyllite formation of Lower Paleozoic age (Grecula, 1982; Grecula et al., 1995, 2009, 2011). The limestone lenses therein have been altered to form a skarn consisting of garnet, hedenbergite, epidote, actinolite, chlorite and Ni-Co-As-Sb-Bi-rich sulfiides, and this mineral assemblage determines the P-T condition of the epidote-amphibolite facies in this locality.

## Geological setting and mineralogy description

The Bystrý potok study area is composed of Lower Paleozoic sequences of Betliar and Smolník formations of Gemeric Volovec Supergroup – pyroclastics, metapsammite, metakeratophyre and metapelite of the Holec Beds. Rocks are metamorphosed in greenschist and epidote-amphibolite facies or biotite zone (530–630 °C, ca 3 kbar) as a result of Permian overheating during the Variscan orogenic metamorphism in the Paleo-Gemeric domain (Fig. 1; Grecula et al., 2009, 2011). The metapelite contains an admixture of psammitic quartz as a passive component during the Variscan metamorphism (MV2; earlier designated as M1), dated from 275 to 262 Ma in the Permian. The clastic quartz of size about 0.5 cm in the pelitic matrix is the reason why this metapelite is traditionally called "porphyroid" in the literature (Fig. 1b., Radvanec et al., 2007).

The Holec Beds are composed of metapelite with the graphite admixture, lenses of lydites, crystalline limestones and rarely the dolomite bearing limestone in the Silurian Beliar Formation of graphitic phyllites of Lower Paleozoic age in the study area. In the stratigraphy of the Lower Paleozoic, the Holec Beds are underlain by keratophyre, basalt-spilite and the stratiform SedEx sulfide mineralization (Fig. 2; Grecula et al., 2009). In the Alžbeta mine field, the stratified SedEx mineralization was located in the upper part of the Holec Beds and the original limestone lenses there were metamorphosed to skarn. The course of Holec Beds with lydite, keratophyre, skarn and stratiform SedEx sulfidic mineralization is NE-SW with dip to the SE (Fig. 3; Kantor & Fusán, 1952).

The disseminated and stratiform sulfidic mineralization in the Gemeric unit was produced by sedimentary-exhalation (SedEx) process and is geotectonically related to bimodal, keratophyre and basalt-spilite magmatism in the seafloor of Late Silurian-Devonian rift (Figs. 1–2). The exhalations accompanying this magmatism have brought ore elements to the seafloor and caused crystallization of the zonal stratiform mineralization. After Devonian rift evolution, the SedEx mineralization was regionally metamorphosed mainly in the greenschists, less frequently in the biotite zone or epidote-amphibolite and amphibolite facies of Variscan orogenic MV2 metamorphism in Permian (275–262 Ma), and within subsequent Alpine orogenesis it underwent local greenschist MAp2 overprint along unroofing ApD2 shear zones (Grecula, 1982; Grecula et al., 1995, 2009, 2011; Radvanec et al., 2007; Radvanec & Grecula, 2016; Radvanec et al., 2017). For these geotectonic and metamorphic events in the Gemeric unit, the SedEx mineralization was modified in-situ to a mixture of original and new metamorphic sulfides, Sn-Pb-Zn-Cu oxides, sulfates, carbonates and other minerals, such are: pyrite, sphalerite, pyrrhotite, chalcopyrite, arsenopyrite, galena, glaucodote, cobaltite, arsenolite, claudetite, cosalite, bismuthinite, native Bi, Cu and Ag, dyscrasite, bournonite, boulangerite, jamesonite, bornite, tetrahedrite, ullma, stibnite, chalcotite, cubanite, quartz, K-feldspar, K-SO minerals, gypsum, white mica, actinolite, garnet,
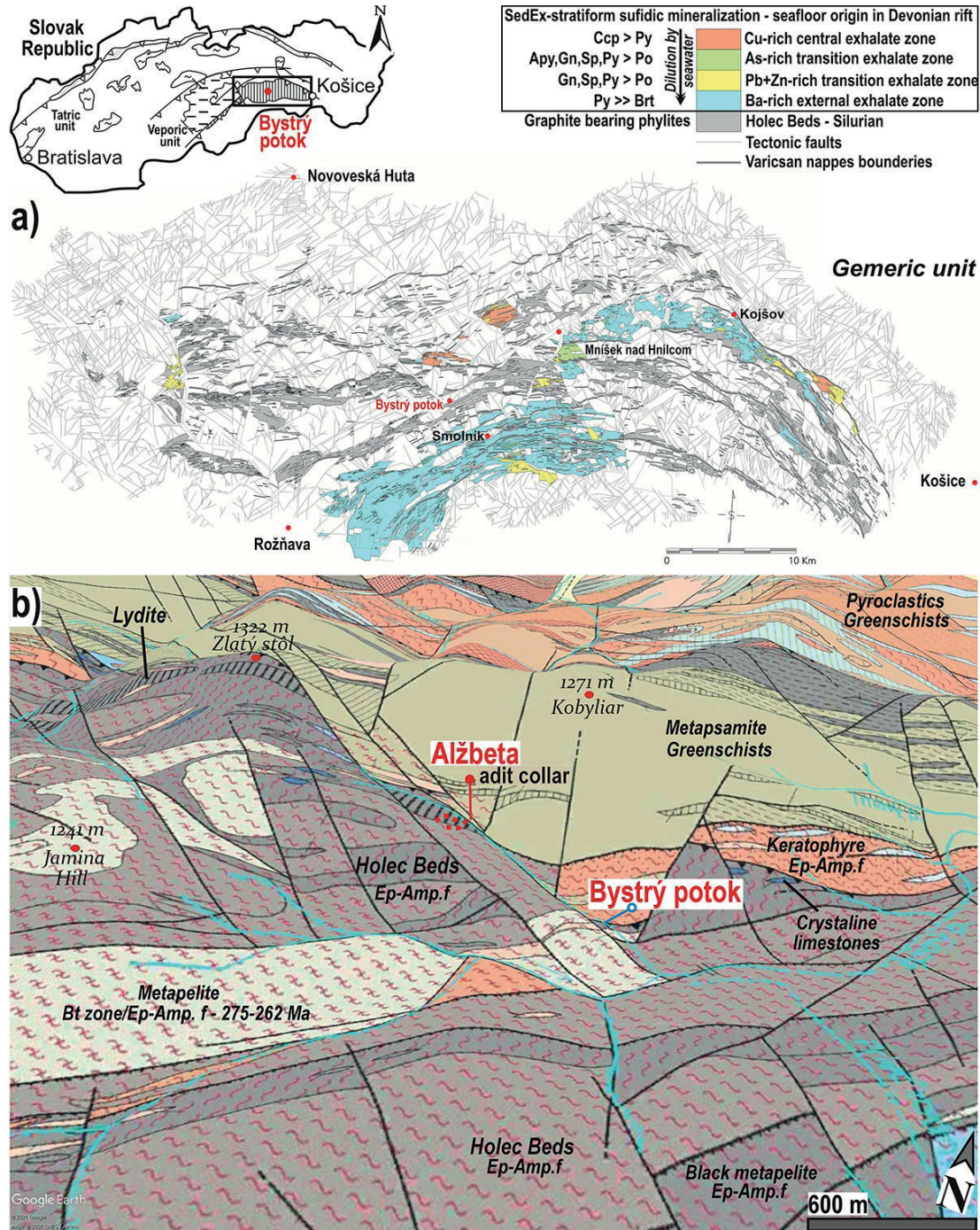
**Fig. 1.** The Smolník, Mníšek nad Hnilcom and Bystrý potok sites represent main localities of stratiform sulfidic mineralization formed by sedimentary-exhalation (SedEx) process in the Gemeric unit during Variscan riftogeneous phase VD0. The SedEx process is genetically associated with albite-quartz bearing keratophyre (trachyte sensu IUGS classif.) and basalt outflows on the seafloor at the bimodal magmatism of Late Silurian-Devonian rift. **1a** – The map of disseminated stratiform sulfidic mineralization classified from the central to external zones depending on the distance of the outflow place – i.e. where the exhalation fluids, enriched with various elements, reached the seafloor in the rift. Abbreviations: chalcopyrite (Ccp), pyrite (Py), arsenopyrite (Apy), galena (Gn), sphalerite (Sp), pyrrhotite (Po), baryte (Brt). These mineral zones were segmented during the Variscan and Alpine tectonic overprint together with the Holec Beds bedrock, being a part the Silurian Betliar Fm. This bedrock consists of crystalline limestone, sericite-graphite phyllites, graphite phyllites and lydite. **1b** – Geological map and metamorphic facies of the Bystrý potok area in a 3D model according to Grecula et al. (2009, 2011). The metapelite was metamorphosed in the Variscan MV2 Bt zone of epidote-amphibolite facies dated from 275 to 262 Ma, being a consequence of earlier collisional phase of Variscan orogeny and thermal overprint on hot line (Radvanec et al., 2007).

121

pyroxene, andesine, labradorite, epidote, chlorite, albite, cassiterite, hematite, molybdenite, sulphur, gold, anatase, rutile, apatite, fluorite, biotite, epidote, graphite, ilmenite, uraninite, scheelite, tourmaline, magnetite, topaz, zircon, baryte, talk, dolomite, ankerite, ankerite Mn, siderite, calcite, chalcocite, covellite, malachite, azurite, melanterite, chalcanthite, goethite, szomolnokite, halotrichite, jarosite, copiapite, coquimbite, voltaite, rhomboclase, epsomite, goslarite, cuprite, erythrite, cuprojarosite, kieserite, scorodite, zincite, hexahydrite, leucoxene, lepidocrocite, metavoltine and psilomelane (Bartalský et al., 1993; Grecula et al., 1995; Radvanec & Gonda, 2019). The new metamorphic association has not been clearly defined from the original stratiform SedEx mineralization in these studies, except by Radvanec & Gonda (2019).

According to the results of mineralogical, geochemical and isotope studies, exhalation zones of the SedEx mineralization were identified from central to external zones, depending on the distance of the place where the exhalations ore fluid reached the seafloor. The central Cu-rich exhalation zone was identified according to the amount and relationships of sulfides. Here, chalcopyrite predominates over pyrite. The arsenopyrite, galena, sphalerite and pyrite predominate over pyrrhotite in the transitions of As and Pb-Zn and rarely Ag-rich zones. In the external Ba-rich zone, the dilution of the exhalating fluid with seawater was significant. The disseminated pyrite predominates over rare occurred baryte in this zone (Fig. 1a). The temperature of exhaled fluids dropped from 412–320 °C in the central zone to 176 °C in the outer zone (Radvanec et al., 1993, 2004; Grecula et al., 1995).

The isotopic composition of galena from localities Smolník, Bystrý potok (Alžbeta) and Mníšek nad Hnilcom (Jalovičí hill) corresponds to the development of orogenic lead (Fig. 1). The lead isotope data for galena $^{207}Pb/^{204}Pb = 15.5$–$15.8$; $^{208}Pb/^{204}Pb = 37.6$–$38.5$; $^{206}Pb/^{204}Pb = 17.8$–$18.1$ roughly agree with their Lower Paleozoic stratigraphic age in most applied models, with respect to uranogenic leads, while model calculation based on thorogenic $^{208}Pb$ gives significantly lower model ages. This higher proportion of thorogenic lead in stratiform mineralizations can be explained by the participation of some isotopically evolved lower crustal and/or metamorphic source during the formation of volcanic rocks on the seafloor. The complex sulfidic mineralization is characterized by values $\delta^{34}S = +5$ to $15$ ‰. It is well consistent to the genetic exhalation-sedimentary model of polymetallic mineralization genetically associated with the Late Silurian-Devonian rift in Gemeric unit (Grecula, 1982; Grecula et al., 1995; Radvanec et al., 2004). The bulk chemical compositions of SedEx mineralizations and their normalized REE contents show the upper crust source for the sulfide formation and subsequent metamorphic event in the chlorite zone on the Smolník locality (Radvanec & Gonda, 2019). The localities of Smolník and Mníšek nad Hnilcom represent typical stratiform SedEx mineralization in the Lower Paleozoic complex (Bartalský et al., 1993; Radvanec et al., 1993; Grecula et al., 1995, 2009). For other less significant localities of stratiform SedEx mineralization see Grecula et al. (1995).

In the studied area of Bystrý potok, the former fluid exhalations belong to the central and transition zones and the mineralization formed from exhalations is located stratigraphically in the upper part of Silurian graphitic phyllites without accompanying basalt volcanism, which occurs significantly in the Smolník locality. The sulfides formation in the Bystrý potok locality was accompanied with the albite-quatrz bearing keratophyre, spilite-keratophyre (chlorite bearing) and its pyroclastics shows the locality as the first manifestation of the fluid smoke exhalation into the seafloor before the main basalt volcanic activity in the Lower Silurian-Devonian rift (Fig 2).

The main mineral in the Bystrý potok locality is pyrite, which predominates over other sulfides. Pyrite commonly forms spheroids, ranging in size from 0.010 to 0.035 mm, with a grain-size of approximately 0.015 mm. Their shape is spherical, rarely elliptical or less regular. The individual pyrite spheroids are usually separated from each other by sphalerite or other sulfides. If the pyrite grains are in contact during growth, a matrix of various pyrite neoblasts formed on their spherical parts of the original individuals. In the combined spheroids of pyrite and pyrrhotite, the pyrrhotite always forms a core around which a new pyrite rim is developed. The pyrite thus forms regular **pyrite rings**. Sometimes the position of pyrrhotite is eccentric, so the hook-like or atoll-shaped pyrite and/or marcasite formations around that pyrrhotite nucleus were formed. In rare cases, marcasite has been found in atoll margins in the form of fine crystalline coatings resulting from the decomposition of pyrrhotite. The core of the annular formations is also formed by the sphalerite, more rarely by galena. **Irregularly shaped pyrite** is also common around pyrite spheroids. It is usually fine-grained. The occurrence of **skeletal pyrite** is also common. It is either in the form of isolated grains or forms aggregates. The free spaces between the individual "ribs" of pyrite are filled by other sulfides, mainly sphalerite or galena (Kantor & Fusán, 1952).

Positions with a monomineralic predominance of sulfides alternate in the SedEx lens. In addition to rolling into parallel strips, the pressure deformation is locally manifested by breccia. That breccia consists of pyrite, sphalerite, pyrrhotite, galena, arsenopyrite and chalcopyrite respectively. Of these, pyrite with sphalerite predominates, while the other sulphides are minor. The grey-black fragments of brecciated ore consist of fine-grained sulfides, which are surrounded by a predominantly coarser-grained matrix of pyrrhotite, sphalerite, chalcopyrite and idiomorphic pyrite. The size of pyrrhotite ranges from 0.05 to 1.0 mm. The size of the pyrite is from 0.1 to 1.0 mm or from 0.1 to 0.2 mm and the size of sphalerite with chalcopyrite has similar dimensions. The individual segments of the breccia are enclosed in cement, formed of coarser-grained sulfides, especially in pyrrhotite, sphalerite and chalcopyrite (Kantor & Fusán, 1952). This sulfide matrix is dark, coloured from brown to black by sphalerite and pyrrhotite. Pyrite is also often present in the form of macroscopically solid clusters or there is pyrite in the form of small idiomorphic grains. The chalcopyrite often occurs in these sulfide po-

sitions and in some parts the disseminated or even more continuous veins of galena were revealed. Veins of galena were also found along the marginal parts of the ore body. In the chalcopyrite or in the mixture of "whole sulfides" the rare gold occurs having size from 0.003 to 0.012 mm.

The quartz is rare in the lens. It is either fine-grained with a sugary appearance or is coarser-grained light grey to milky white. Carbonates seldom form continuous clusters or positions in sulfides that are at most cm thick. In some places of the marginal parts of the lens, the increased concentration of white micas was found (Kantor & Fusán, 1952). The cassiterite belongs to the sulfide association. The idiomorphic cassiterite forms long prismatic crystals up to 0.4 mm. It occurs in the pyrrhotite, sphalerite, chalcopyrite and galena. Irregular small grains of cassiterite were also found in these sulfides. The cassiterite is also present in those parts, where chalcopyrite predominates in the fine-grained quartz. Here it is surrounded by white mica, by quartz and carbonates (l.c.). White mica is a common mineral, sometimes overgrown with "muscovite" and is markedly pleochroic, clear or yellowish to brownish. Its *C*-axis parts are pink-brown in colour and have a low birefringence. According to this optical characteristic, Kantor & Fusán (1952) considered this mica to be the zinnwaldite. The apatite, chlorite and feldspar often occur in the association of cassiterite, sulfides, quartz and white mica. The host rock around the ore lens is silicified and impregnated by sulfides. There are frequent inclusions of idiomorphic pyrite, accompanied by its aggregates and veins (l.c.).

## Methodology

Mineralogical and petrological data were obtained by studying samples of skarn, albite-quartz bearing metakeratophyre and samples of stratiform SedEx sulfidic mineralization from the Bystrý potok valley (Figs. 1, 2). Samples were collected from the adit at levels 2 (48° 45' 33.4" N, 20° 40' 31.6" E, Fig. 3) and 1 (dump-2; 48° 45' 33.7" N, 20° 40' 28.8" E and adit).

The relations among minerals were studied in polished thin sections. Chemical composition of minerals was determined by electron microprobe analyses (EMPA). The EMPA of minerals and their crystallization succession were obtained in the State Geological Institute of Dionýz Štúr, Department of microanalysis, Bratislava. The Cameca SX-100 electron microprobe was equipped with three spectrometers and Kevex delta IV EDS system. The natural and synthetic standards were used for calibration. Measuring conditions: acceleration voltages 15 kV and 25 kV, current 10 nA at analyses of carbonates or 20 nA at silicate analyses. The diameter of the electron beam was changed according to the type and size of minerals. Micas were measured by widened beam 7–10 μm, carbonates 10–15 μm and other minerals by 2–5 μm beam. The measurement time from 10 to 60 s was chosen aiming to achieve the required measurement accuracy of given element. Detection limit for individual elements is smaller than 0.05 wt. % with an error 2-sigma.

After study by optical microscope and subsequent measurement by microprobe, the EMPA results for all
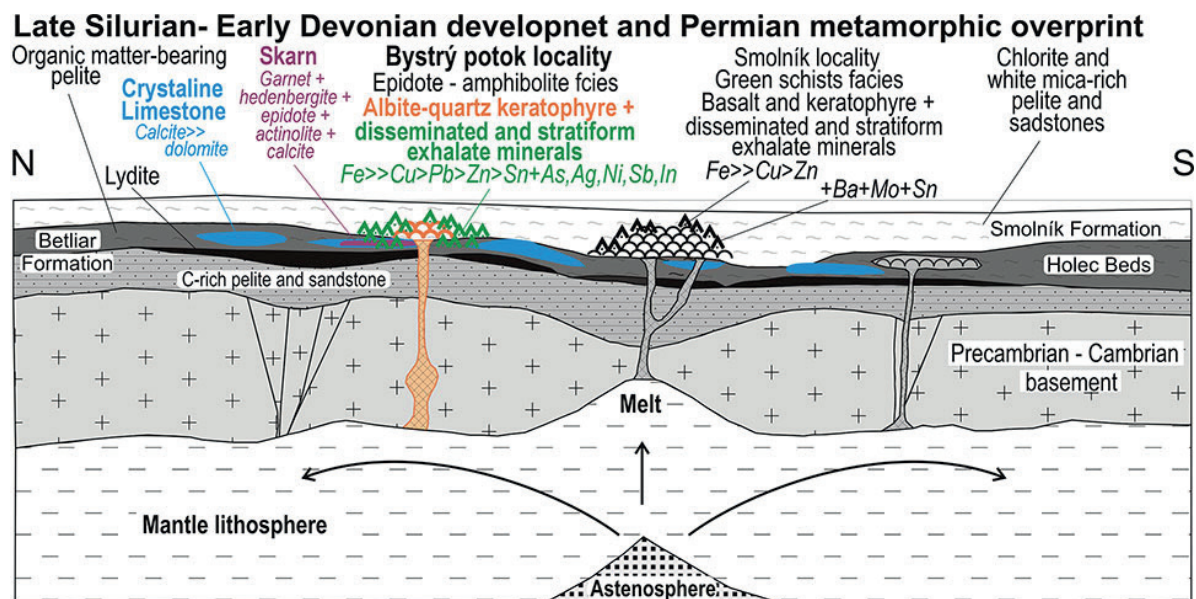


**Fig. 2.** The Late Silurian–Early Devonian development (VD0, MV0) and schematic Permian metamorphic overprint (MV2) without visualized tectonic arrangement of rocks by Variscan orogeny in Paleo-Gemeric area. The disseminated and stratiform sulfidic mineralization is formed by the sedimentary-exhalation processes (SedEx), related to the bimodal – keratophyre and basalt magmatism in the seafloor in the Late Silurian-Devonian rift. The skarn was formed in the epidote-amphibolite facies in the limestone protolith of the Holec Beds and this facies shows P-T conditions of the stratiform sulfidic mineralization overprint in the Bystrý potok area as well. The epidote-amphibolite and amphibolite facies accompanying the late (VD2, MV2) of Variscan orogeny is of Permian age in the Gemeric unit (Grecula et al., 2009, 2011). These data complement lithostratigraphic development of Gemeric unit proposed by Radvanec & Grecula (2016).

detected minerals were plotted in diagrams, triangle diagrams and in a tetrahedral projection (Figs. 5, 9, 10, 12, 17, 20 and 21). The chemical composition of the carbonates is shown in triangular diagrams between the end-members magnesite-siderite-calcite-cerussite. Chemical analyses of V-rich mica, V-rich chlorite and other minerals show the tetrahedral projection K = KfsFCaA, where the content of $V_2O_3$, $Al_2O_3$ and $Cr_2O_3$ is in the A according to the modified manual of Spear (1995). Mineral assemblages in the KAl = KfsFCA projection show the index minerals of epidote-amphibolite facies and chlorite-apatite zone (Fig. 5a). Projection of K = KfsVTiA (A = $Al_2O_3$) shows the position of V-rich muscovite-phengite and V-rich phengite-illite between the muscovite-roscoelite-illite-kaolinite end-members including projection of V-rich chlorite, schreyerite, rutile and titanite in this tetrahedral projection (Fig. 5b).

Analyses of sulfides, oxides and other minerals after recalculation to chemical formula were visualized in the individual tetrahedral projections: ZnFeCuIn, ZnFeCuSn, NiFeCoAs, NiSbFeAg, NiSbFeBi, SbFeBiPb, CuSbFeAg, CuSbFePb and CuSbFeAg, while S, O, $CO_2$ and OH contents were neglected (Figs. 17, 21). Projections of the mineral chemical formulae in each of these element systems show the relationships between the source SedEx minerals and the newly formed metamorphogenic minerals within the end-members. The interconnection of the end-members in the system of elements determines the plane in which the new metamorphogenic mineral was formed at the expense of the SedEx end-members. They are also planes of 22 empirical reactions. See text below and Figs. 5, 17, 20 and 21. The individual projections were combined to show the entire mineral crystallization system in the study area (Figs. 17, 21).

The 22 empirical reactions show reacting source minerals controlled by their chemical formulae, as well as new metamorphic mineral assemblages, also confirmed by their chemical formulae. The composition of the fluid phase has been calculated in the reactions. The relationship between the reacting source minerals in the reactions and the new mineral association is always confirmed by the BSE images (Figs. 4, 6–8, 11, 13–16, 18, 19).

Diagrams, triangle diagrams and a tetrahedron projection of the chemical composition were used for the chemical classification of sulfides rich in Pb, Bi, Sb, Cu, Ag and Fe. In figures all these sulfides are directly compared with reference mineral compositions published in the Mineralogy Database (webmineral.com; Figs. 20–21).

The summary types of formula ABX, $A_9B_2X_8$, $A_3BX_3$, $A_2BX_3$, $A_2B_2X_5$, $A_2B_3X_6$, $A_3B_3X_7$ and the term sulfides are used in this study for bournonite, plumosite-like and other sulfosalts composed of Pb, Bi, Sb, Cu, Ag, Fe and S. The contents of Ni, Co, Pb, Cu and Ag are bound in group *A*, Sb, As and Bi are in group *B*, and the position of Fe in both groups depends on whether $Fe^{3+}$ is bound together with Sb and Bi in group *B* or as $Fe^{2+}$ in group *A*. This alternative Fe binding was inferred from correlations of element contents and their substitutions in the chemical formulas. The group *X* consists of S and Se (see Tables). The chemical formulae of the tetrahedrite group were calculated according to the procedure of Biagioni et al. (2020).

In addition to familiar mineral names such as tetrahedrite, bournonite, plumosite-like, bismuthinite, kobellite, wittite, etc., the rule of gradually decreasing number of *apfu* elements in their chemical formula was applied to the names of new sulfides. The PbBiSb- and PbSbBi-rich sulfides were named according to this rule, see text below.

In the investigated locality, the same sulfides usually have two modes of occurrence, e.g. pyrite 1 and pyrite 2, etc. These generations of sulfides vary according to location and chemical composition, see text and Tables. Only two modifications of chalcopyrite have not been correctly distinguished because they have the same chemical composition, although the position of the chalcopyrites in the mineral associations is obviously different, especially according to their place of occurrence. For this reason, altogether two chalcopyrite generations are collectively referred to as chalcopyrite.

In this study, the term sakuraiite is used for Sn sakuraiite (Sn-rich sakuraiite) and In sakuraiite (In-rich sakuraiite) depending on which element predominates in the sakuraiite formula. These terms also describe the finding that In sakuraiite does not contain Sn. To compare the chemical composition with sphalerite, the chemical formulae of In and Sn sakuraiite was calculated on the basis of 2 atoms and was used in the diagrams (Figs. 9, 10; Tabs. 5, 10).

In this study, we use the traditional term keratophyre in the sense of the rock classification of Grecula et al. (2009, 2011). In addition, the term keratophyre clearly captures the geotectonic background of its origin as a product of magma differentiation on the seafloor in the Late-Silurian and Devonian rift. According to the IUGS chemical classification of volcanic rocks, it is a quartz-albite bearing trachyte metamorphosed in epidote-amphibolite facies.

## Mineralogical and petrological results

Mineralogical and petrological data were obtained studying the skarn, albite-quartz bearing metakeratophyre and disseminated and massive sulfide ore layers in the Bystrý potok locality (Figs. 1–3).

### *Garnet-clinopyroxenite skarn as a marker of P-T metamorphic conditions at the Bystrý potok locality*

The common thin layers and small lenses of garnet-pyroxenite skarn with thickness up to 10 cm occur in the **graphite** bearing phyllite formation of Holec Beds (Figs. 2–3). The garnet-pyroxenite skarn represents mostly a fine-grained green avocado coloured rock with purple garnet bearing bands. Texture of skarn is most often fibro-granoblastic, less often granoblastic and frequently banded (Fig. 4). The skarn was formed under control of late Variscan ductile overprint of south-vergent unroofing kinematics VD2 (classification sensu Németh, 2021), being initiated by Variscan post-collisional overheating and tectono-metamorphic overprint MV2 (l.c.) above hot-line in Permian (Fig. 3).

During the gradual evolution of skarn, the limestone protolith was firstly changed by the Late Silurian-Devonian exhalations related to the formation of SedEx mineralization. This fluid SedEx alteration produced

**chalcopyrite** $CuFeS$, **galena 1** $PbS$ and **cobaltite 1** $(Co_{0.91}Ni_{0.07}Fe_{0.05})_{1.03}As_{0.95}S$ as disseminated mineralization in **calcite** $CaCO_3$ matrix of limestone. Inclusions around 1 μm of galena 1 often occur in the cobaltite 1. The size of chalcopyrite reaches 120 μm, galena 1 around 5 μm and cobaltite 1 up to 20 μm. Only **millerite** $(Ni_{0.99}Co_{0.01})S$ of this SedEx mineralization forms aggregates up to 700 μm in size and these aggregates enclose chalcopyrite, galena 1 and the remnants of calcite (Fig. 4d). In limestones small layers and lenses, the calcite was locally accompanied by **dolomite** $Ca_{0.96-1}(Mg_{0.76-0.84}Fe_{0.14-0.2}Mn_{0.06-0.07})(CO_3)_2$ (Figs. 4c, 5, 11f and 12a).

After formation of disseminated SedEx mineralization, the calcite and locally dolomite bearing matrix of former limestone was metamorphosed and transformed into the skarn. The skarn finally composes of homogeneous **garnet** $Grs_{41.4-60.2}Sps_{19.8-32.8}Alm_{16.7-22.2}Adr_{0-8.5}$ usually from 50 to 500 μm in size, **hedenbergite** $Wo_{44.5-50.1}Fs_{31.6-38.2}En_{12.7-20.7}$ where MnO ranges from 1.49 to 6.07 wt. %, **epidote** Ps = 0.2–0.4, **actinolite**, **fluorapatite** $Ca_5(PO_4)_3F$, **titanite** $Ca_{1.03}Ti_{0.82}Al_{0.17}Fe_{0.04}Si_{1.02}O_{4.8}F_{0.2}$, **quartz**, **zircon** and remnants of calcite. Short veins of **pyrochroite** and **Mn-rich calcite** $Ca_{0.84-0.89}Mn_{0.09-0.12}Fe_{0.01-0.03}CO_3$ fill cracks in that mineral assemblage (Fig. 4b).

Projection of these minerals in the tetrahedron KAl = KfsFCA shows their relationship typical for epidote-amphibolite facies, which metasomatically formed the epidote-hedenbergite-grossular/almandine-actinolite-chlorite bearing skarn assemblage at a temperature range of 500–600 °C at approximately 2–7 kbar (Spear, 1995; Radvanec et al., 2017) and/or a calculated temperature of 526–546 °C at P = 3–6 kbar according to garnet-clinopyroxene geothermometer (Ravna, 2000; Fig. 5a). The input analyses for the garnet-clinopyroxene geothermometer of Ravna (2000) are given in Table 2. The obtained skarn P-T conditions are in good agreement with the epidote-amphibolite fa-

cies conditions found in the wider vicinity of the Bystrý potok locality (Fig. 1b; Grecula et al., 2009). The identical pyroxene, garnet, amphibole, epidote and plagioclase skarns containing magnetite, hematite and sulfides were also formed at the same temperature around 570 °C and by the same process of alteration of original limestone lenses in the Holec Beds on the Trochánka, Javor and Gondárska lúka localities. These skarns also originated in the Variscan orogeny (Faryad & Peterec, 1987).

Determination of the P-T conditions of the epidote-amphibolite facies is crucial in the study of the metamorphism of the Late Silurian–Devonian SedEx disseminated mineralization at the Bystrý potok locality.

Under P-T conditions of the epidote-amphibolite facies a new generation of sulfides has originated in the skarn. In silicates matrix of skarn the irregularly zoned **Ni-rich cobaltite 2** $(Co_{0.73}Ni_{0.22}Fe_{0.05})_1As_{0.97}S_{1.03}$ – $(Co_{0.82}Ni_{0.12}Fe_{0.07})_{1.01}As_{0.96}S_{1.03}$ with a size 20–40 μm was formed and the millerite was partly replaced by **hauchecornite** and by **hauchecornite-(Sb)** (Fig. 4d-e). This hauchecornite grain is zoned having Bi-rich parts of $(Ni_{8.56}Co_{0.38}Fe_{0.05})_{8.99}(Bi_{1.34}Sb_{0.47}Fe_{0.24})_{2.05}S_{7.95}$, Sb/Bi-rich $(Ni_{8.40}Co_{0.53}Fe_{0.05})_{8.98}(Sb_{1.44}Bi_{0.42}Fe_{0.17})_{2.03}S_{7.98}$ and Sb-rich



**Fig. 3.** The occurrence and relationship of stratiform SedEx sulfidic mineralization, albite and quartz bearing metakeratophyre and the skarn in the host Holec Beds found in the 2nd level of the Alžbeta adit in the Bystrý potok locality. The Holec Beds consist of sericite-graphite phyllites, lydite and limestone as a protolith of garnet-hedenbergite-epidote-actinolite bearing skarn. The rock sequence in this locality manifests late Variscan ductile overprint (MV2 metamorphism, in previous papers signed as M1; Radvanec & Gonda, 2019) of south-vergent unroofing kinematics VD2, being initiated by Variscan post-collisional overheating and tectono-metamorphic overprint MV2 above hot-line in Permian. It produced anticline setting and resulting south-vergent unroofing in this locality. Later Paleo-Alpine north-vergent thrusting ApD1 and south-vergent unroofing ApD2 are manifested by brittle-ductile secondary foliation and cleavage. Regional shearing during Neo-Alpine AnD3 phase produced sinistral Transgemeric shear zone trending ENE-WSW, which rotated CCW earlier foliation planes of VD2, ApD1 and ApD2 to direction of shear zone (present general dip is 154/68). Classification of orogenic and metamorphic phases sensu Németh (2021). Photo: Miloš Greisel
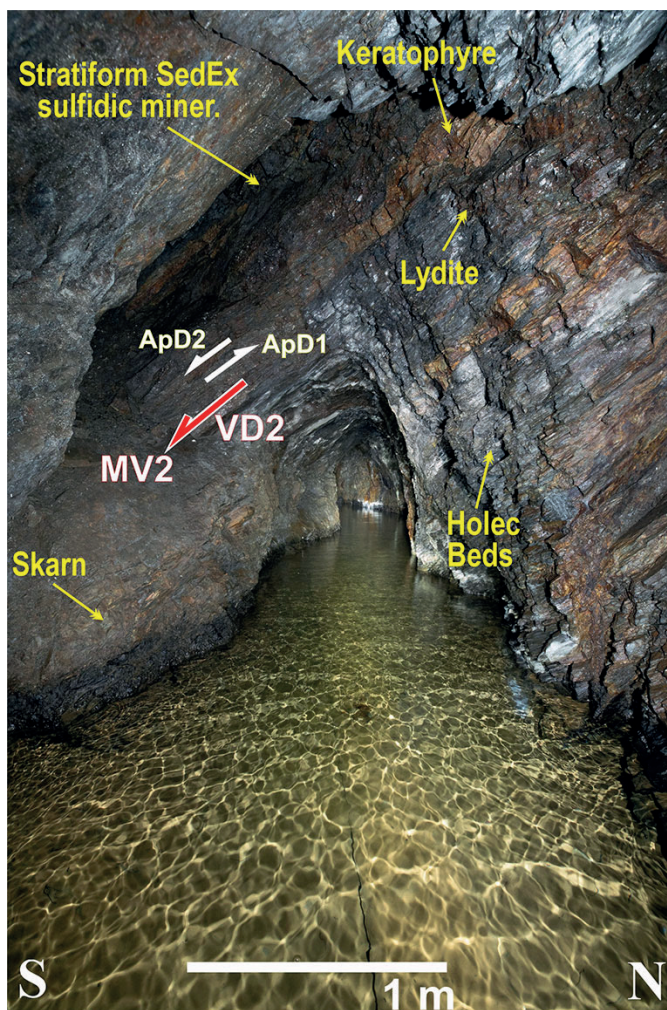
$(Ni_{8.23}Co_{0.50}Fe_{0.25})_{8.98}(Sb_{1.70}Fe_{0.14}Bi_{0.08})_{1.92}S_{8.09}$ part respectively. The Fe *(apfu)* is significantly bound in group B with Bi and Sb in these chemical formulae. The Sb* = (Sb + Fe³⁺)/(Sb + Bi + Fe³⁺) ratios therein range from 0.34 to 0.96 showing the variable influence of SbFe³⁺S (gudmundite), $Bi_2S_3$ (bismuthinite) and/or native Bi molecules during the replacemnet of millerite to form zonal hauchecornite (Fig. 4d–e, Tab. 1). The formation of zonal hauchecornite is described by reactions 1, 2 and its formation is visualized in NiSbBiFe tetrahedron between millerite, gudmundite and bismuthinite/native Bi end-members. The SedEx processes produced those reacting source minerals for the formation of new hauchecornite (Fig. 21).

$18NiS + FeSbS + Bi_2S_3 + 6H_2O \rightarrow$
Millerite    Gudmundite  Bismuthinite

$$Ni_9(SbBiFe)_2S_8 + Ni_9(BiSbFe)_2S_8 + 6H_2S + 3O_2 \quad (1)$$
Hauchecornite-(*Sb*)    Hauchecornite

$18NiS + FeSbS + 2Bi + 3H_2O \rightarrow$
Millerite    Gudmundite Bi native

$$Ni_9(SbBiFe)_2S_8 + Ni_9(BiSbFe)_2S_8 + 3H_2S + 3O \quad (2)$$
Hauchecornite-*(Sb)*    Hauchecornite
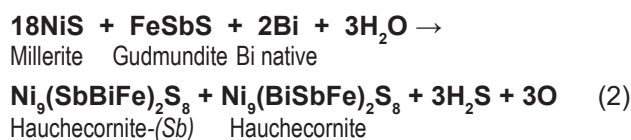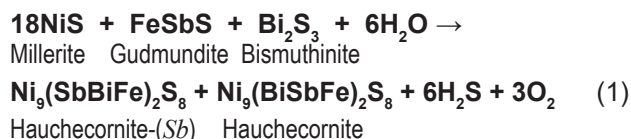
Further details on gudmundite, bismuthinite 1 and the native Bi formation are given in the text below.

In the skarn, the fluorapatite is accompanied by garnet, epidote, hedenbergite and actinolite, representing the major and indexed minerals formed during the replacement of former limestone in the beginning of epidote-amphibolite facies (Fig. 4). The homogeneous grains of fluorapatite do not contain any admixture of other elements and its chemical formula is close to end-member $Ca_5(PO_4)_3F$ (Tab. 2). In different localities of Gemeric unit the same pure fluorapatite in assemblage with tourmaline, biotite, phengitic muscovite, margarite, topaz, stilpnomelane, chlorite, quartz, fluorite, ankerite, dolomite, kutnohorite, rhodochrosite, siderite, magnesite, allanite, U-rich and In-rich minerals, columbite, cassiterite, molybdenite, goyazite and sulfides occur. In all these localities from greisen in direct contact with Permian S-type granite through skarns and veins in granite exocontacts to U-SedEx surface mineralization, the fluorapatite does not contain any admixture of other elements, however it was formed in different P-T conditions of the Permian hydrothermal mineralization. The assemblage where the fluorapatite occurs with phengitic muscovite and chlorite, was named the chlorite-apatite zone and the temperature range 420–540 °C of this zone has a regional enlargement in the Permian hydrothermal mineralization of Gemeric unit (Radvanec & Gonda, 2019, 2020).

The origin of the studied fluorapatite is conditioned by the existence of calcite lenses in the organic-bearing sediments of the Holec Beds, where limestone/calcite in the epidote-amphibolite facies reacted with a fluid phase containing $H_3PO_4$ and HF to form fluorapatite according to reaction 3.

$5CaCO_3 + 3H_3PO_4 + HF \rightarrow$
Limestone    P-F bearing fluid phase

$$Ca_5(PO_4)_3F + 5H_2O + 5CO_2 \quad (3)$$
Apatite
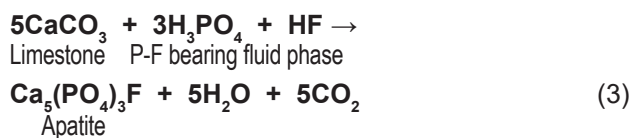
The position of fluorapatite enclosed in garnet, epidote and actinolite indicates its formation probably in the prograde zone of epidote-amphibolite facies (Figs. 4, 5a). However, it is irrelevant to consider the prograde and/or retrograde state of the chlorite-apatite zone in the study area, because the temperature range of 500–600 °C or 526–546 °C of the epidote-amphibolite facies and the temperature range of 420–540 °C of the chlorite-apatite zone partially overlap, indicating the chlorite-apatite zone as part of the epidote-amphibolite facies.

### Texture of polymetallic mineralization

The mineralization of the Bystrý potok locality consists mainly of the basic and original stratiform SedEx-sulfidic mineralization and the new mineralization formed by the in-situ epidote-amphibolite facies and/or by the chlorite-apatite zone overprint. The mineral texture has a fine-grained form up to 1 mm in grain size generally. In this complex mineralization, the sulfide clusters of galena, sphalerite, pyrite, pyrrhotite, chalcopyrite and arsenopyrite predominate over the aggregates and individual disseminated grains of these sulfides. The disseminated form is usually present in graphite bearing phyllites, albite-quartz bearing metakeratophyre and in the skarn. The massive part of mineralization is formed of spots and pseudo-layers coloured brown, yellow and/or they are black. The galena bearing parts have a silver metallic luster and are matt grey to matt black. Spots of dolomite, ankerite, siderite, fluorapatite, chlorite and quartz up to 2 cm in size are enclosed in the sulfide mass. The phengitic V-rich mica has euhedric shape and the individual cassiterites have a hypidiomorphic shape and remnants of SedEx sulfides are always enclosed in this cassiterite aggregate. Both of these minerals reach about 1 mm in the sulfide matrix. The complex mineralization shows that sulfides stratification or layering was formed by the exhalations on the seafloor and also shows the subsequent ductile deformation acting in the epidote-amphibolite and chlorite-apatite zone (Fig. 6).

### The original mineral assemblage of the stratiform SedEx mineralization

Sulfide aggregates, accompanied with chlorite with various Fe contents and rarely by quartz, represent a common composition of the SedEx mineralization originated from seafloor exhalations in the Late Silurian-Devonian rift. The original SedEx chlorites are classified according to the daphnite-ripidolite-pycnochlorite series and also the Si = 7.01–7.92 *(apfu)* with Fe²⁺ + Fe³⁺ = 5.01–5.84 bearing chlorite was found (Tab. 2). In addition to sulfides, quartz and chlorites, the allanite-*(Ce)*, monazite, thorite and rutile also occur in the volcanic part of former albite-quartz bearing keratophyre. If exhalations
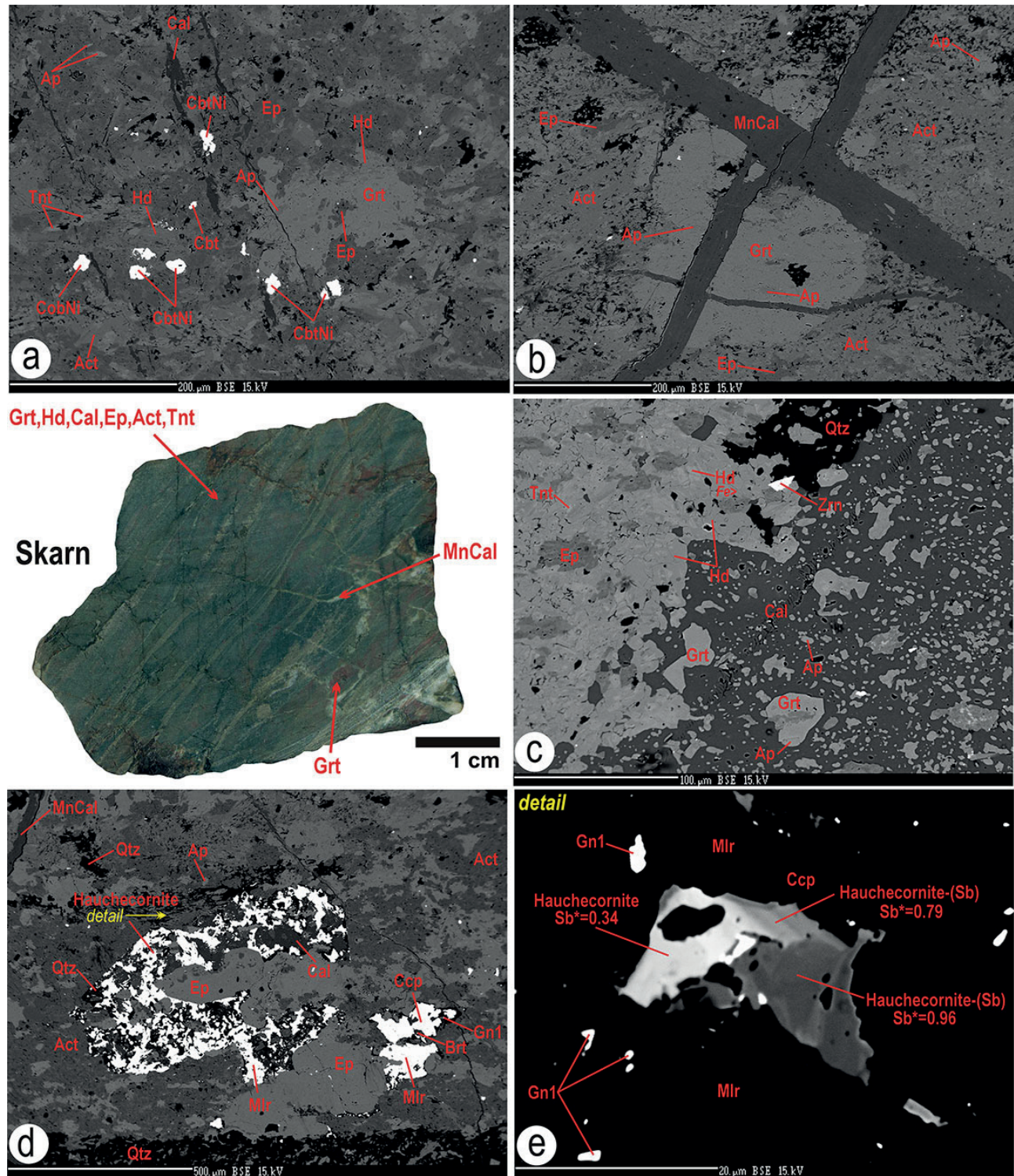
**Fig. 4.** The skarn minerals were formed in the Permian MV2 epidote-amphibolite facies metamorphism from the limestone protolith of the Holec Beds. *a* – The Ni-rich cobaltite (CbtNi) and cobaltite (Cbt) in the matrix composed by garnet (Grt), hedenbergite (Hd), epidote (Ep), titanite (Tnt), fluorapatite (Ap) and actinolite (Act). *b* – Mn-rich calcite (MnCal) short veins crosscut the matrix of garnet, epidote, actinolite and fluorapatite. *c* – The relationship of former limestone-calcite (Cal) and skarn minerals: quartz (Qtz), zircon (Zrn), garnet, epidote, titanite, hedenbergite. *d* – Aggregates of millerite (Mlr), zonal hauchecornite and chalcopyrite in the matrix of epidote, actinolite, fluorapatite, quartz, calcite, Mn calcite and baryte (Brt). *e* – Detail in figure *(d)*. Zonal aggregate of hauchecornite, hauchecornite-*(Sb)* and chalcopyrite (Ccp) in millerite with inclusions of galena 1 (Gn1); Sb* = (Sb + Fe$^{3+}$)/(Sb + Bi + Fe$^{3+}$). BSE images of mineral assemblages.
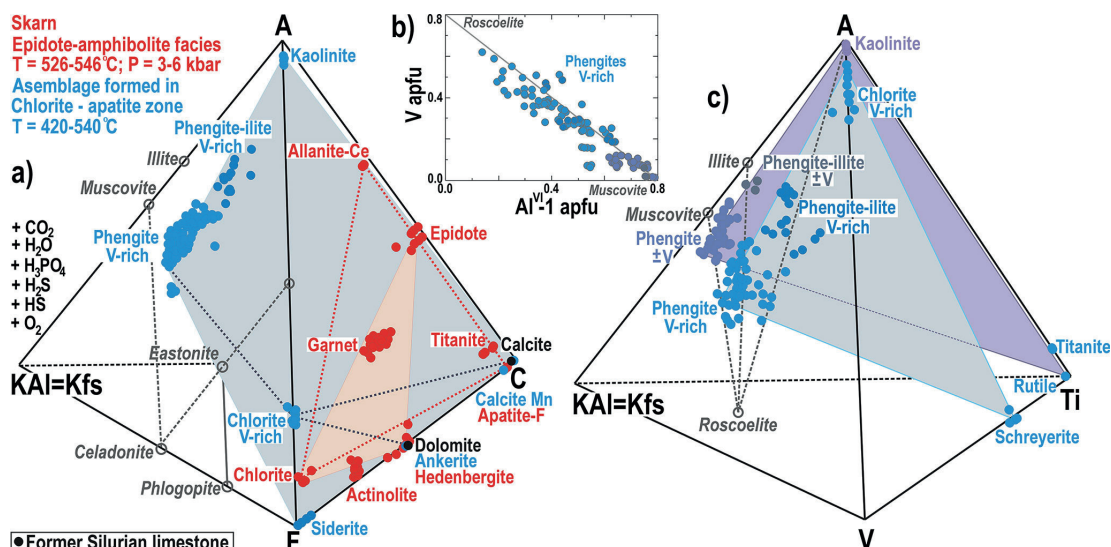
**Fig. 5.** *a* – Tetrahedral phase diagram KA1 = KfsFCAl shows projections of skarn minerals (red) and the chlorite-apatite zone mineral assemblage (blue) that formed in-situ in the SedEx stratiform sulfide mineralization. The compositional plane between chlorite, garnet, hedenbergite, amphibolite and epidote completely classifies the epidote-amphibolite facies according to the metamorphic facies classification criteria (Spear, 1995; Ravna, 2000). The calcite and dolomite (black) are remnants of Silurian limestones protolith, stratigraphically located in the Holec Beds from which the skarn was formed MV2 epidote-amphibolite facies. *b* – V-rich micas (phengites) projection and substitution V = Al$^{VI}$ in plot V versus Al$^{VI}$-1 *(apfu)* based on 12 (O). *c* – Tetrahedral phase diagram for the KA1 = KfsVTiA system shows the positions of V-rich mica varieties, V-rich chlorite, kaolinite, schreyerite and titanite were formed by the chlorite-apatite zone.

were spilled into the limestone environment, the SedEx mineralization also includes remnants of calcite and dolomite (Figs. 4c, 11d–f, 13f and 14d).

Much of the SedEx mineralization typically consists of a mixture of monomineral and sulfide aggregates and the various coexisting sulfides are invariably enclosed within the host large sulfide (Figs. 6, 8). The **pyrite 1** $Fe_{1.01}S_{1.98-1.99}$ (Fe/S = 0.51) aggregate (1st pyrite generation) usually encloses **galena 1** $Pb_{0.97}Zn_{0.02}S$, **chalcopyrite** $(CuFe)S_2$, **pyrrhotite** FeS without admixtures of other elements (Fig 8a, 19b–c). Pyrite 1 and pyrrhotite contain Au up to 0.013 wt. % (Tab. 3). The pyrite 1 coexists with BiPb-rich sulfide, whose chemical formula is close to **kobellite** $Pb_{20.18-20.19}Cu_{2.07-2.22}Fe_{1.23-1.35}Ag_{0.61-0.62}Zn_{0.04}Cd_{0.06}Bi_{26.14}Sb_{4.76-4.77}(Se_{0.21-0.24}S_{69.53-69.57})$ with a ratio of Sb/(Sb + Bi) = 0.15 (Tab. 4). This kobellite contains inclusions of **native Bi** $(Bi_{0.85}Sb_{0.05}Fe_{0.05}Pb_{0.02}S_{0.04})$ and together with pyrite 1 is enclosed in an **albite** matrix which is a part of the keratophyre (Fig. 19a). In the albite matrix and in pyrrhotite aggregate with **quartz** the rounded remnants of **PbBiSb-rich sulfide** $(Pb_{1.44-1.48}Fe_{0.23-0.35}Cu_{0.11-0.33}Ag_{0.03-0.04})_2(Bi_{1.19-1.30}Sb_{0.77-0.97})_2(Se_{0-0.19}S_{4.91-4.94})_5$ were found. The size of this PbBiSb-rich sulfide ($A_2B_2S_5$ type) ranges up to 60 μm (Figs. 19c–d, Tab. 4). Several mm large remnants of **stephanite** $Ag_{4.80-5.01}Sb_{0.95-1.02}Fe_{0.01-0.08}Cu_{0-0.18}In_{0.01}S_{3.97-3.99}$ occur with coexisting galena 1 in the quartz matrix and stephanite was also found in the **gudmundite** $Fe^{3+}_{0.98-1.03}Sb_{0.99-1}S_{0.98-1.01}$ (Figs. 18a, c–d, Tab. 3). The always corroded gudmundite is usually associated with the galena 1 and chalcopyrite in the quartz matrix as well (Fig. 18a, e–f). In the gudmundite the Fe atoms are surrounded by 3 Sb atoms and 3 S atoms at the points of an irregular tetrahedron, where the Fe

atom is packed between a large Sb atom and a small S atom. The ordinary gudmundite "crystal", in common with other members of the arsenopyrite group is actually a twinned composite simulating a single orthorhombic individual (Buerger, 1939). Therefore, the Fe atom in the chemical formula of gudmundite and also arsenopyrite binds as $Fe^{3+}$ (http://webmin.mindat.org/). Unlike the corroded gudmundite, the **arsenopyrite** $(Fe^{3+}As_{0.97})S_{1.02}$ is stable and occurs together with chalcopyrite, pyrite 1, pyrrhotite and sphalerite 1 or else arsenopyrite is enclosed in galena 1 or sphalerite 1. Arsenopyrite usually forms momomineral aggregates and bands up to 1 cm thick in the SedEx mineralization (Figs. 6d, 8c, 14d; Tab. 3). Rare **bismuthinite 1** $(Bi_{1.78}Fe_{0.22})_2(Se_{0.01}S_{2.94})_{2.95}$ up to 20 μm in the size occurs as an inclusion usually in pyrite 1, pyrrhotite or in galena 1 (Fig. 8a). A number of its analysed grains consistently show a chemical composition with a uniform Fe content of approximately 0.22 *apfu*. The bismutinite 1 shows a Bi content of 1.78 *apfu*, giving a sum of Bi + Fe = 2, and where Bi is substitued by Fe, indicating a form of $Fe^{3+}$ bond in its chemical formula, as in the gudmundite and arsenopyrite (Tab. 4).

The assemblage of pyrrhotite, chalcopyrite, chlorite, quartz, pyrite 1 and **sphalerite 1** $(Zn_{0.70-0.85}Fe_{0.11-0.16}Cu_{0.01-0.08}In_{0.01-0.08})S$ is usually present in the host galena 1 aggregates. However the sphalerite 1 in this association also formed monomineral pseudo-layers, bands and/or spots up to 5 cm thick (Fig. 6 and 8c–f). In that massive sphalerite 1, the indium content ranges irregularly from 0.61 to 8.78 wt. % and Cu from 0.33 to 4.68 (Figs. 15, 16a–b, Tab. 5). The indium content (up to 0.1 *apfu*) progressively correlates with Cu (up to 0.1 *apfu*) and the
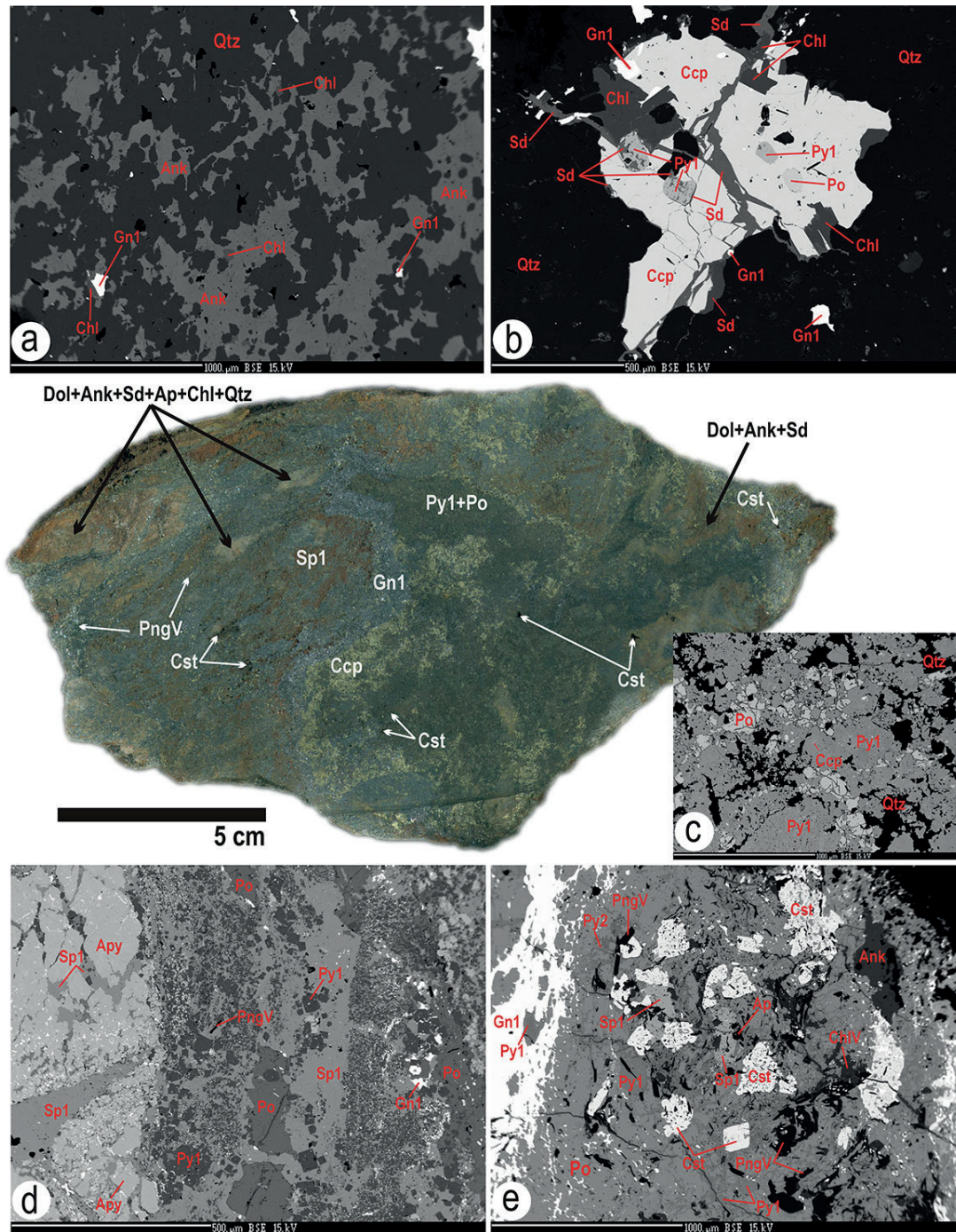
**Fig. 6.** The massive part of fine-grained mineralization in the Bystrý potok locality consists mainly of the basic VD0 stratiform SedEx sulfidic mineralization and new mineralization formed in-situ by the MV2 epidote-amphibolite facies and by chlorite-apatite zone. That complex mineralization is a mixture of galena 1 (Gn1), sphalerite 1 (Sp1), pyrite 1 (Py1), pyrrhotite (Po), chalcopyrite (Ccp), arsenopyrite (Apy) together with spots containing the dolomite (Dol), ankerite (Ank), siderite (Sd), fluorapatite (Ap), chlorite (Chl) and quartz (Qtz). The cassiterite (Cst) and euhedral V-rich mica (PngV) form disseminated grains and/or aggregates in the matrix of former SedEx sulfides. **a** – Ankerite, chlorite, quartz represent common assemblage in carbonates bearing spots. **b** – An aggregate of chalcopyrite in a matrix of quartz, chlorite, siderite and galena 1 encloses pyrite 1 and pyrrhotite inclusions. The inclusions of unstable pyrite 1 partially decomposed into siderite, and the siderite fills cracks in the chalcopyrite aggregate. **c** – The SedEx mineralization especially represents pyrite 1 with chalcopyrite inclusions, less pyrrhotite and quartz. **d** – The sphalerite 1 bearing part contains pyrite 1, pyrrhotite, arsenopyrite, V-rich mica (PngV), and galena 1. **e** – The cassiterite aggregates formed in assemblage of V-rich mica, fluorapatite, V-rich chlorite (ChlV), ankerite, pyrite 1, pyrite 2 (Py2), sphalerite 1, pyrrhotite and galena 1. Cassiterite always cemented the original SedEx sulfides. BSE images of mineral assemblages.
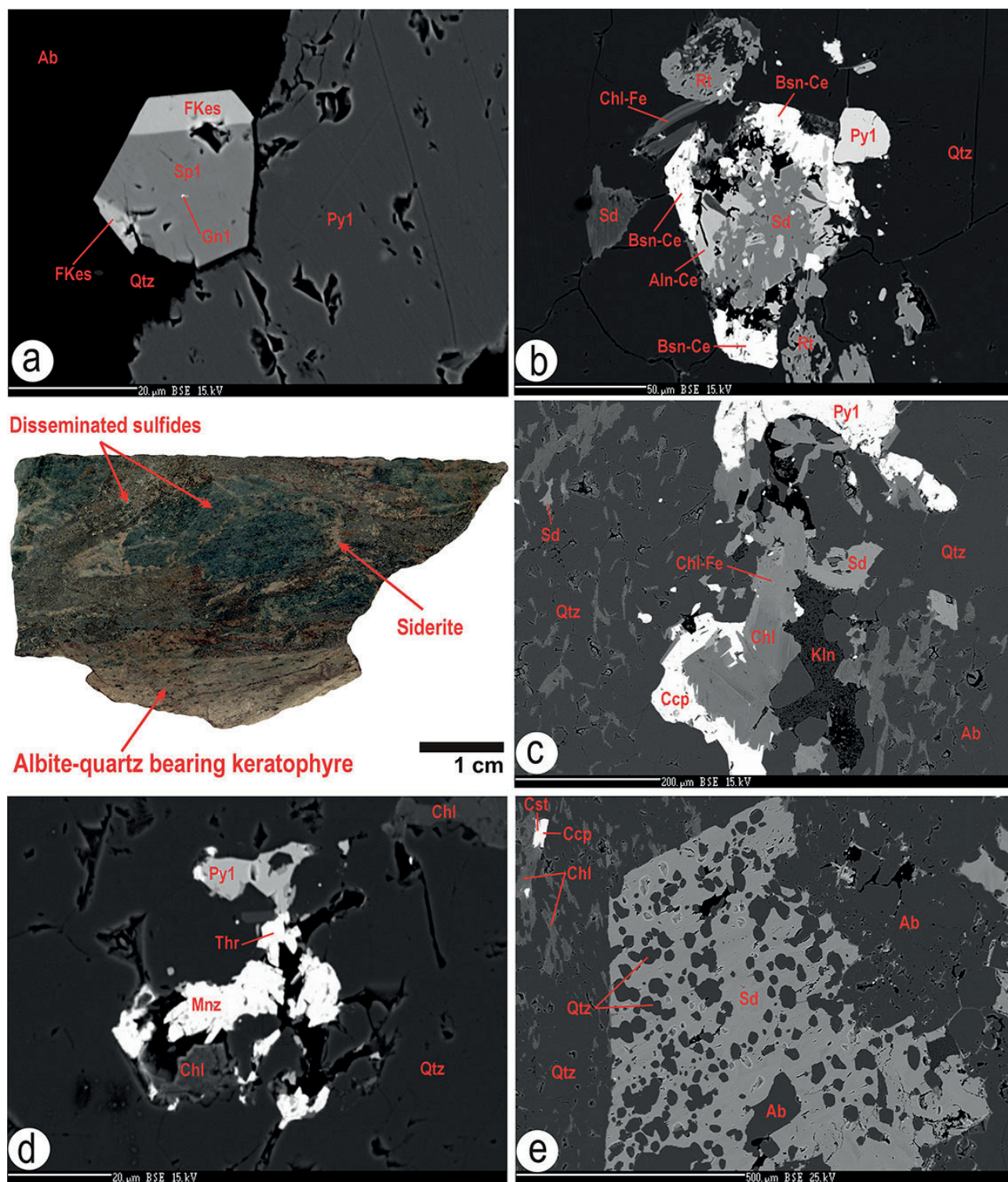
**Fig. 7.** Albite-quartz bearing metakeratophyre with disseminated SedEx sulfides and newly formed siderite, bastnäsite-*Ce* cassiterite in chlorite-apatite zone. *a* – The SedEx ferrokesterite (FKes), sphalerite 1 (Sp1), galena 1 (Gn1), quartz (Qtz) and pyrite 1 (Py1) in the albite part of metakeratophyre. *b* – Aggregate composed by Fe-rich chlorite (Chl-Fe), rutile (Rt), siderite (Sd), pyrite 1 (Py1) and the allanite-*Ce* (Aln-Ce) is replaced by bastnäsite-*Ce* (Bsn-Ce) in the quartz part of metakeratophyre. *c* – The relationship of siderite, Fe-rich chlorite, kaolinite (Kln), pyrite 1 and chalcopyrite (Ccp) in albite-quartz bearing matrix. *d* – Rare monazite (Mnz) and thorite (Thr) in the quartz, chlorite and pyrite 1 matrix. *e* – Siderite encloses albite (Ab) and quartz and their relationship to the albite-quartz bearing matrix with cassiterite (Cst) and chalcopyrite. BSE images of mineral assemblages.

sum of Cu + In also progressively correlates with Fe, however the Fe content has a negative trend with Zn, indicating a coupled (CuInFe) ↔ Zn substitution in the sphalerite 1. The chemical formula of sphalerite 1 shows the presence of roquesite ($CuInS_2$) molecule ranging from 1 to 15.6 mol. % and/or ishiharaite (CuFeInZn)S molecule presence according to the (CuInFe) ↔ Zn substitution (Fig. 9). Therefore, the Zn content of sphalerite 1 ranges from 0.7 to 1 *apfu* and this range is used for the term sphalerite in this study (Fig. 9d, 10e–f, Tab. 5).

Aggregates and massive SedEx parts of sphalerite 1 include galena 1 and arsenopyrite. That massive form of sphalerite 1 always includes homogeneous **ferrokesterite** ($Cu_{1.76-1.96}Fe_{0.88-0.96}Zn_{0.16-0.52}Sn_{0.88-0.92})_4S_4$ less often **In-rich ferrokesterite** ($Cu_{1.72-1.96}Fe_{0.68-1.08}Zn_{0.12-0.52}Sn_{0.84-1.04}In_{0.04-0.16})_4S_4$ where indium content ranges from 0.54 to 4.38 wt. % and **Sn-rich sakuraiite** ($Cu_{0.6-1.72}Fe_{0.6-0.92}Zn_{0.60-2.48}Sn_{0.28-0.84}In_{0-0.20})_4S_4$ with variable indium content from 0 to 6.02 wt. % (Figs. 8c and 15, Tab. 5). According to the obtained EMPA data, the contents of Cu, Fe, Zn, Sn ± In in the ferrokesterite – Sn sakuraiite – sphalerite 1 series are variable and can be evaluated according to the binary chemical plots in Fig. 10. The positive correlation between Cu versus Sn, Cu versus Fe and Cu+Sn versus Fe was found. The negative correlation is shown by Fe versus Zn and the chaotic correlation is between In versus Sn in the ferrokesterite – Sn sakuraiite – sphalerite 1 series. In these sulfide series, the incorporation of elements is following the Cu + Sn + Fe versus Zn substitution scheme. This substitution trend (CuFeSn) ↔ Zn is valid for ferrokesterite/In-rich ferrokesterite, Sn sakuraiite and it also applies for the coexisting sphalerite 1, if sphalerite 1 very rarely contains Sn (Fig. 10). By comparing the host In-rich sphalerite 1 and the coexisting inclusions of ferrokesterite and Sn sakuraiite, it can be concluded that the In and Sn content did not mix and/or was mixed only locally during the crystallization of sulfides from SedEx exhales on the seafloor. Only In-rich ferrokesterite and Sn sakuraiite contain sporadic amounts of In up to 0.04 *apfu* (Fig. 10a).

Coexisting stannite/ferrokesterite group and sphalerite are considered by many authors to be a reliable geothermometer and in this study it is used to estimate precipitation temperature of described phases. Using the equation of Nakamura & Shima (1982) on the partitioning of Fe and Zn between the sphalerite 1 and ferrokesterite, data were obtained to estimate the temperature of their formation on the seafloor. In sphalerite 1 the ratio Fe/Zn ranges from 0.14 to 0.21 and in ferrokesterite from 1.48 to 4.87. The log of these ratios range from –0.69 to –087 in sphalerite 1 and from 0.17 to 0.81 in ferrokesterite (Tab. 5). Using log ($XFeS/XZnS$) sphalerite versus log ($XCu_2FeSnS_4/XCu_2ZnSnS_4$) stannite, Nakamura & Shima (1982) proposed equations and temperature lines between coexisting sphalerite and stannite group. According to these data, ore-forming temperatures were obtained for the Bystrý potok locality from 280 to 340 °C. This temperature result fits well between the exhaled fluid temperature ranges from 412–320 °C in the central zone and to 176 °C in the outer zone, and this temperature is well related to the transition zone of the exhales from which SedEx mineralization formed on the seafloor (Radvanec et al., 1993, 2004; Grecula et al., 1995).

The above stratiform SedEx sulphides are the source mineralization that gave rise to the metamorphogenic minerals in the epidote-amphibolite facies or chlorite-apatite zone.

### Decomposition and oxidation of stratiform SedEx mineralization in the epidote-amphibolite facies and related chlorite-apatite zone in situ

The original stratiform SedEx mineralization was metamorphosed in the epidote-amphibolite facies (500–600 °C, resp. 526–546 °C; see discussion in earlier chapter about garnet-clinopyroxenite skarn) and the chlorite-apatite zone (420–540 °C) in situ, causing the formation of skarn and indexed chlorite with apatite in the Bystrý potok locality (Fig. 5a). Like the Holec Beds including skarn and lydite also the SedEx mineralization is an integral part of the tectonic plan formed under control of late Variscan ductile overprint of south-vergent unroofing kinematics VD2, being initiated by Variscan post-collisional overheating and tectono-metamorphic overprint MV2 above hot-line in Permian (Fig. 3). Under the control of this tectono-metamorphic overprint the unstable SedEx minerals in the above temperature ranges have oxidized and decomposed by interaction with the fluid phase.

### Decomposition of pyrrhotite, pyrite 1 and galena 1 by oxidation and dolomite replacement

Pyrrhotite and especially pyrite 1 are the basic minerals formed by SedEx processes. They were oxidized and decomposed in interaction with $H_2O$, $O_2$, $H_2S$ and $CO_2$ bearing fluid phase to form **szomolnokite** $Fe_{1.1}S_{0.97}O_4 \cdot H_2O$, **pyrite 2** $Fe_{0.98}S_{2.02}$, **goethite** FeO(OH) and **siderite** $Fe_{0.83-0.98}Ca_{0.01-0.10}Mg_{0-0.03}Mn_{0.01-0.04}CO_3$. At the beginning of the gradual oxidation, szomolnokite and pyrite 2 formed at the expense of pyrrhotite according to reactions 4–5. The resulting szomolnokite fills the place of the former pyrrhotite and the ring around the szomolnokite forms a coexisting pyrite 2. In pyrite 2, the Fe content (45.58 wt. %) is lower and the S content (53.82) is higher compared to pyrite 1, and also the ratio Fe/S = 0.49 is lower compared to the value of 0.51 in the pyrite 1 (Tab. 3). The next oxidation step caused the formation of goethite and siderite on the pyrite 2 showing the complex and gradual decomposition of former pyrrhotite (Figs. 11a–b). In summary, the pyrrhotite bearing spots were alternatively decomposed once into szomolnokite or into szomolnokite and pyrite 2 or into szomolnokite, pyrite 2 and siderite or into szomolnokite, pyrite 2, goethite and siderite or sometimes only siderite according to reactions 6–8 (Figs. 11a–c, 13c, 14b). Macroscopically, this transformation is reflected in the samples as dark brown to black between the pyrite and chalcopyrite.

$$FeS \ + \ H_2O \ + \ 2O_2 \ \rightarrow FeSO_4 \cdot H_2O \qquad (4)$$
Pyrrhotite                  Szomolnokite
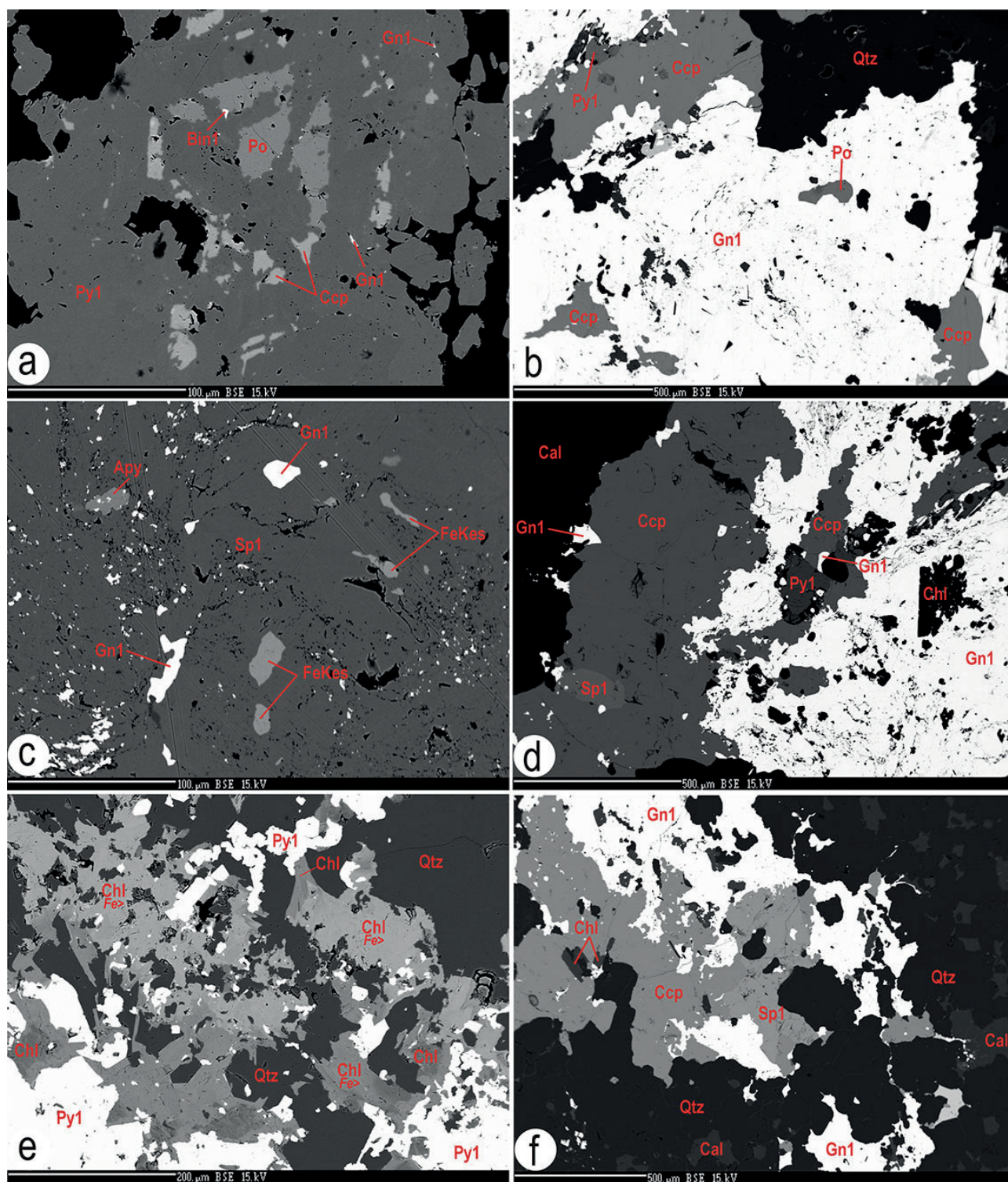
**Fig. 8.** The common composition and structure of stratiform SedEx sulfidic mineralization, which formed from seafloor exhalates in the Late Silurian-Devonian rift. *a* – Pyrite 1 (Py1) closes pyrrhotite (Po), chalcopyrite (Ccp), galena 1 (Gn) and bismuthinite 1 (Bin1). *b* – Pyrite 1, chalcopyrite, pyrrhotite, galena 1 and quartz (Qtz) mass assemblages. *c* – Inclusions of galena 1, arsenopyrite (Apy), ferrokesterite (FKes) in the host sphalerite 1 (Sp1). *d* – Calcite (Cal), chalcopyrite, sphalerite 1, pyrite 1, chlorite (Chl) and galena 1 assemblage. *e* – The relationship of pyrite 1, quartz (Qtz), Fe-rich chlorite (Chl, Fe >) and chlorite. *f* – Calcite, sphalerite 1, chalcopyrite, chlorite, galena 1and quartz assemblage. BSE images of mineral assemblages.

**2FeS + H₂S + 5O → FeSO₄. H₂O + FeS₂** (5)
Pyrrhotite                    Szomolnokite      Pyrite 2

**3FeS + H₂O + CO₂ + 5O →**
Pyrrhotite
**FeSO₄. H₂O + FeS₂ + FeCO₃** (6)
Szomolnokite    Pyrite 2    Siderite

**4FeS + 2H₂O + CO₂ + 3O₂ →**
Pyrrhotite
**FeSO₄. H₂O + FeS₂ + FeO(OH) + FeCO₃ + HS** (7)
Szomolnokite    Pyrite 2    Goethite    Siderite

**FeS +H₂O + CO₂ → FeCO₃ + H₂S** (8)
Pyrrhotite                    Siderite
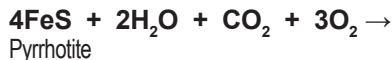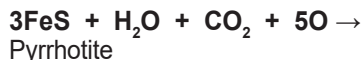
In contrast to the pyrrhotite, the pyrite 1 is more stable phase in P-T conditions of chlorite-apatite zone. Pyrite 1 was only partially decomposed by oxidation to form siderite or goethite according to reactions 9 and 10 (Figs. 6b, 11a–b, 13b and 13f).

**FeS₂ + 2H₂O + CO₂ → FeCO₃ + 2H₂S + 0.5O₂** (9)
Pyrite 1                    Siderite

**FeS₂ + 3H₂O + HS → FeO(OH) + 3H₂S + 0.5O₂** (10)
Pyrite 1                    Goethite

Dolomite, as the remnant of Silurian limestones in the SedEx mineralization, was gradually replaced by **ankerite**

$Ca_{0.98-1}(Fe_{0.24-0.50}Mg_{0.48-0.66}Mn_{0.04-0.10})(CO_3)_2$, goethite and finally by the siderite according to the reaction 11 (Figs. 11d, f and 13f).

**MgCa(CO₃)₂ + 3FeS + 4H₂O + CO₂ + HS →**
Dolomite          Pyrrhotite
**FeO(OH) + FeCa(CO₃)₂ +**
Goethite          Ankerite
**+ FeCO₃ + 0.5O₂ + 4H₂S + Mg⁺** (11)
Siderite                    in Chlorite
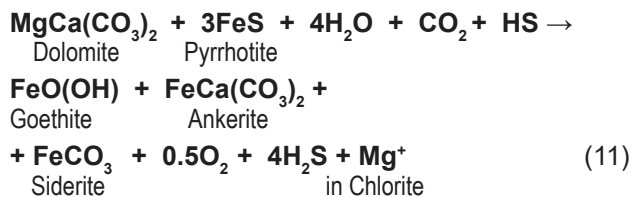
Galena 1 aggregates were oxidized and decomposed to **anglesite** $Pb_{0.89}Bi_{0.07}SO_4$ and **cerussite** $PbCO_3$. Anglesite and cerussite partially replaced the margin of host galena 1 and/or replaced galena 1 around the cracks in it according to reaction 12 (Figs. 11c and 14d, Tab. 6, 7).

**2PbS + H₂O + CO₂ + 2O₂ →**
Galena 1
**PbSO₄ + PbCO₃ + H₂S** (12)
Anglesite    Cerrusite
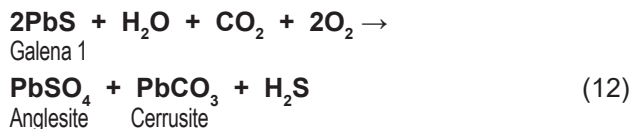
### V-rich micas, V-rich chlorite and schreyerite formation

Euhedral and prismatic **V-rich micas** up to 2 mm in size and **V-rich chlorites** crystallized omnidirectionally in various sulfide aggregates. These micas and chlorite were found along with the coexisting fluorapatite and cassiterite, although their main occurrences are in the galena 1, dolomite, allanite-*(Ce)* and pyrite 1 aggregates
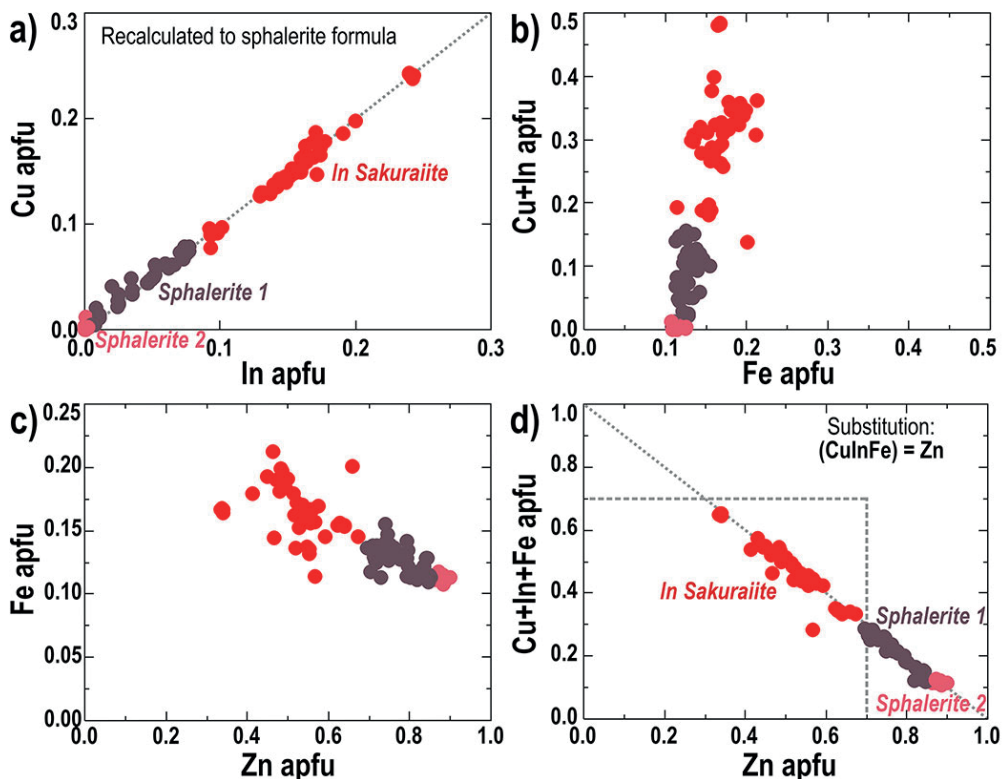


**Fig. 9.** Binary plots showing chemical composition *(apfu)* of In-rich sphalerite 1, In-rich sakuraiite and sphalerite 2: **a** – Cu *vs.* In; **b** – Cu + In *vs.* Fe; **c** –Fe *vs.* Zn; and **d** – Cu + In + Fe *vs.* Zn. The In-rich sphalerite 1 was formed by the SedEx exhales in Late Silurian – Devonian rift. The In-rich sakuraiite and sphalerite 2 were formed by the oxidation and decomposition of In-rich sphalerite 1 in the Permian chlorite-apatite zone according to reaction 16, see text.

(Figs. 13 and 14b). The optical characteristics of V-rich micas are close to zinnwaldite and the individual V-rich micas are zonal. The core of the prismatic grain is usually **V-rich muscovite-phengite** and the rim forms **V-rich phengite-illite** however their intergrowth were also found. V-rich chlorite forms the outer rim of V-rich mica but separate accumulations of V-rich chlorite were found as well (Fig. 6e, 13d–f, 14b, 15a). The $V_2O_3$ content ranges from 0.47 to 10.05 wt. % in V-rich muscovite-phengite, in the V-rich phengite-illite ranges from 1.18 to 9.35 and in V-rich chlorite from 0.72 to 2.46. In V-rich micas the variable $Cr_2O_3$ content reaches up to 3.11 wt. % (Tab. 9).

The chemical classifications of V-rich micas in K = KfsFCA projection, where A = $(Al^{Total}+V)/2-(K/2)$ shows their general position in mineral content assemblages formed by the chlorite-apatite zone near the end-members of muscovite and illite with affinity to kaolinite (Fig. 5a, Tab. 9). The chemical formulas of V-rich micas show V = $Al^{VI}$ –1 substitution in the range up to 0.8 apfu between

muscovite and roscoelite end-member (Fig. 5b). The roscoelite $KV_2AlSi_3O_{10}(OH)_2$ represents vanadium analogue of muscovite where V = $Al^{VI}$ (Fleet, 2003). In the projection K = KfsVTiA, where A = $Al^{Total}/2-(K/2)$, two modes of V-rich micas were found. The low vanadium content up to 0.12 *apfu* in the phengite and phengite-illite classifies this mica near the muscovite and illite end-member, and this low-vanadium mica is coexistent with kaolinite, titanite, and rutile. The V-rich mica with vanadium content ranging from 0.16 to 0.62 *apfu* coexists with V-rich chlorite and Ti-V-rich oxide (Fig. 5c). That oxide ($V_{1.15}Fe^{3+}_{0.5}Cr_{0.21}Mn^{3+}_{0.08}Sc_{0.04}Al_{0.02})_2(Ti_{2.63}Sr_{0.13}U_{0.09}Pb_{0.07}Sn_{0.03}Zn_{0.03}Si_{0.01}Mg_{0.01})_3O_9(OH)_{0.5}$ is **schreyerite** close, belongs to the schreyerite group containing (OH) and has a varied association of elements according to its stoichiometry (Tab. 8). The schreyerite reaches a size of 30 μm and occurs with chalcopyrite, galena 1, V-rich mica and szomolnokite (Fig. 13c).
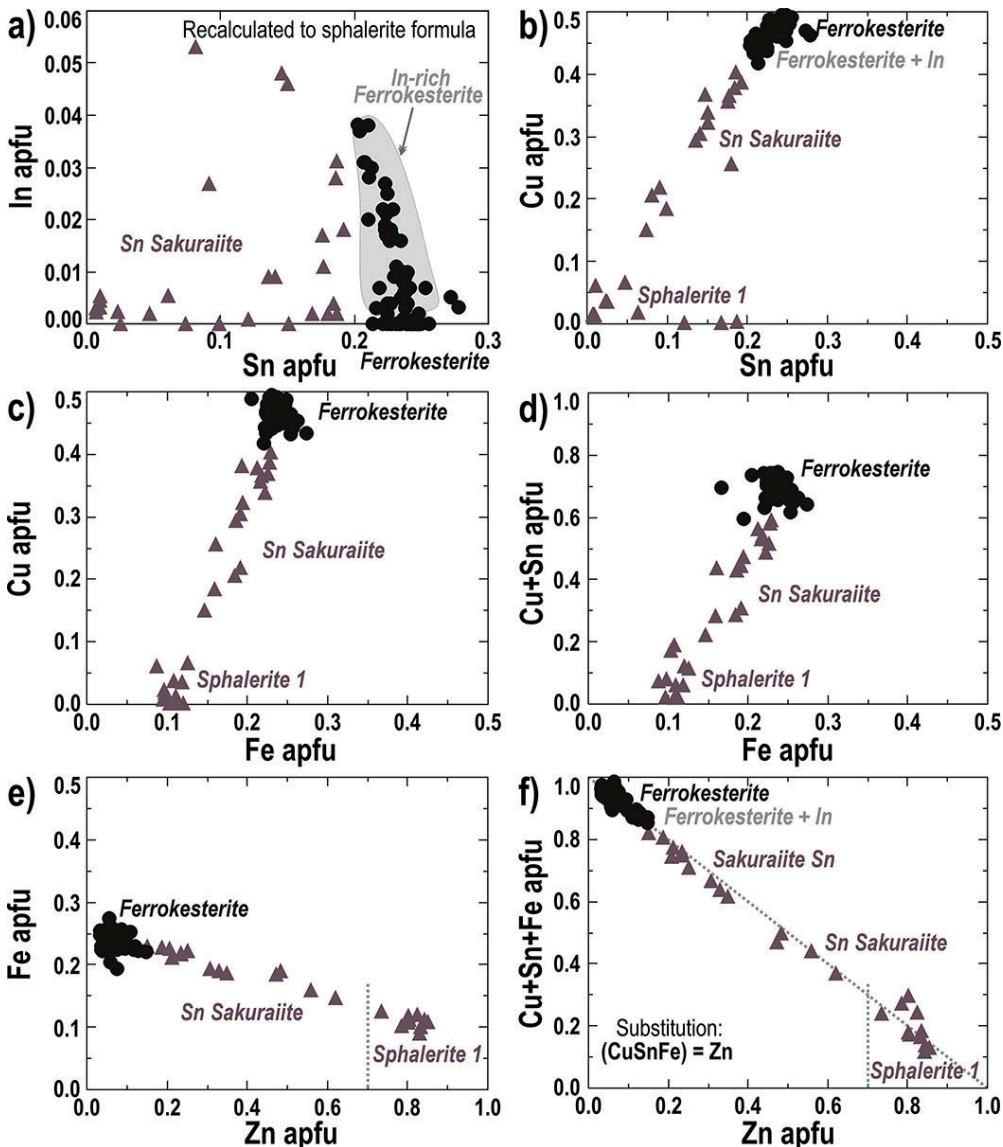


**Fig. 10.** Binary diagrams showing the chemical compositions of ferrokesterite, Sn-rich sakuraiite and sphalerite 1 formed from SedEx exhalates in the Late Silurian-Devonian rift. **(a)** In *vs*. Sn; **(b)** Cu *vs*. Sn; **(c)** Cu *vs*. Fe; **(d)** Cu + Sn *vs*. Fe; **(e)** Fe *vs*. Zn; and **(f)** Cu + Sn + Fe *vs*. Zn.

The EMPA data of V-rich micas show that their total contents range from 93.89 to 100.08 wt. % including $H_2O$ and often K-deficient. Some V-rich micas appear to be mica phases with A2M structure and their total contents range around 100 wt. % including $H_2O$ (Tab. 8). Other K-deficient analyses with total contents below 99 wt. % indicate $H_2O$ enrichment of V-rich micas and they represent therefore likely the interlayer-deficient micas. Such a mica is also roscoelite with a total content of 93 to 95.44 wt. % (Fleet, 2003). The roscoelite and vanadium muscovite are associated with remobilization of vanadium from black shales and mafic rocks (Fleet, 2003). The V-rich micas studied compare well with the vanadium- and Cr-bearing phengite (containing up to 6.93 wt. % $V_2O_3$ and 1.52 wt. % $Cr_2O_3$) found in quartz-rich graphitic black shales (Morad, 1990).

In the Bystrý potok locality the sources of vanadium for V-rich mica, V-rich chlorite and schreyerite formations are from graphite-bearing phyllites of Holec Beds, where in the epidote-amphibolite facies and in the chlorite-apatite zone, the vanadium was released from the organic-rich layer during the conversion of the organic matter to graphite. Round graphite often occurs enclosed in fluorapatite and in galena 1 (Fig.16e). In the fluid phase of the chlorite-apatite zone, vanadium was transported and subsequently bound in close proximity to its source, and the binding of vanadium well explains the occurrence of V-rich micas, V-rich chlorite, and schreyerite in the studied mineralization, which lithostratigraphically overlies the source of the vanadium from the underlying Holec Beds (Fig. 2). However, the varied elements composition of the schreyerite shows mobilization of not only of V but also Cr, Fe, Mn, Sr, Sc and U from the underlying Holec Beds into the SedEx stratiform mineralization.

### Cassiterite formation

**Cassiterite** $SnO_2$ forms individual, usually hypidiomorphic grains or aggregates as a common oxide formed at the expense of SedEx mineralization in situ (Figs. 6e, 14 and 15). Its chemical composition shows a simple $SnO_2$ content without the addition of other elements. It is typical for the composition of cassiterites in all localities of the Gemeric unit (Radvanec & Gonda, 2019; Tab. 8). Cassiterite aggregates enclose pyrrhotite, pyrite 1, fluorapatite and galena 1 and/or chalcopyrite or arsenopyrite, depending on spot where the cassiterite aggregate originated in the host SedEx mineralization. The occurrence of coexisting V-rich mica, fluorapatite and xenotime-*(Y)* in the cassiterite is also variable. Some cassiterite grains or aggregates contain them, others are devoid of them (Fig. 14). The formation of cassiterite in situ is conditioned by the occurrence, decomposition and oxidation of suitable Sn-rich source sulfides such as ferrokesterite and/or Sn sakuraiite. The ferrokesterite and Sn sakuraiite have originated by the SedEx processes and decomposed in the chlorite-apatite zone by oxidation. Figure 15 shows an unstable ferrokesterite residue surrounded by chalcopyrite, and cassiterite forms a thin ring around this chalcopyrite.

This ferrokesterite oxidation can be described by reaction 13. Alternatively, the reaction of ferrokesterite, goethite and $CO_2$ shows the formation of chalcopyrite, cassiterite and siderite according to reaction 14.

**$Cu_2FeSnS_4$ + $FeS_2$ + $2H_2O$ →**
Ferrokesterite    Pyrite 1

**$2CuFeS_2$ + $SnO_2$ + $2H_2S$**                    (13)
Chalcopyrite   Cassiterite

**$Cu_2FeSnS_4$ + $2FeO(OH)$ + $CO_2$ →**
Ferrokesterite          Goethite

**$2CuFeS_2$ + $SnO_2$ + $FeCO_3$ + $H_2O$**          (14)
Chalcopyrite  Cassiterite   Siderite
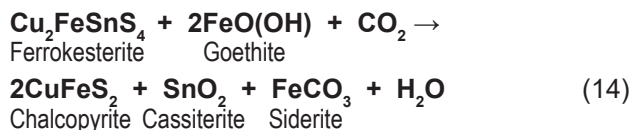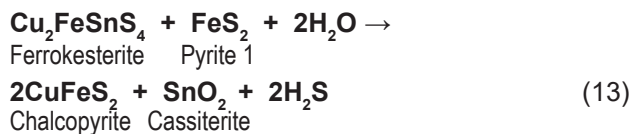
Mineralogical results show that the oxidation of ferrokesterite and Sn sakuraiite proceeds from the margin in a stepwise manner and the unreacted ferrokesterite and Sn sakuraiite residues are always oval in the host chalcopyrite (Fig. 15). When ferrokesterite and Sn sakuraiite are in direct contact with cassiterite, the chemical formula of the relics is non-stoichiometric and their analyses are a mixture of the former Sn-rich sulfide and newly formed cassiterite reaching Sn up to 41 wt. % (Fig. 15b).

### Valentinite formation

The decomposition of unstable former SedEx gudmundite caused **valentinite** $Sb_{1.99}Fe_{0.05}O_3$ and siderite formation according to the reaction 15 (Fig. 18f). Under the conditions of chlorite-apatite zone the gudmundite partly decomposed and its composition shows only $Sb_2O_3$ content except of FeO up to 0.95 wt. % (Tab. 6).

**$2FeSbS$ + $2H_2O$ + $2CO_2$ →**
Gudmundite

**$Sb_2O_3$ + $2FeCO_3$ + $2H_2S$**                   (15)
Valentinite   Siderite
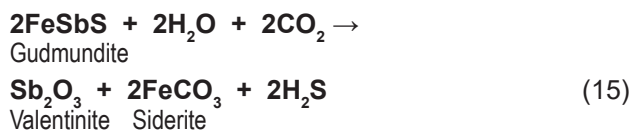
### In-rich sakuraiite formation

The **In-rich sakuraiite** ($Zn_{0.34-0.64}Fe_{0.15-0.19}Cu_{0.09-0.2}In_{0.09-024}$)$S_{0.98-1.02}$ was formed by decompositions of indium bearing sphalerite 1, ferrokesterite and Sn sakuraiite. These three carriers of In and Sn contents were formed in the SedEx mineralization and decomposed in the chlorite-apatite zone. By the thermal effect of the chlorite-apatite zone, the In-bearing sphalerite 1 decomposed into a mixture of In sakuraiite exsolution lamellae and **sphalerite 2** ($Zn_{0.89}Fe_{0.11}$)S (Fig. 16c). In addition to the lamellae, In sakuraiite also forms single grains up to 20 μm in size. These grains, usually having hypidiomorphic shape, are most commonly found at the rim of chalcopyrite, always in a quartz matrix. In sakuraiite inclusions are also rarely found in pyrite 1 cracks (Figs. 16d–f). The indium content ranges from 10.78 to 25.83 wt. % in both of these In sakuraiite modes (Tab. 10). The formation of lamellae represents the thermal decomposition of unstable sphalerite 1 in situ, but the second mode produces the partial and/or
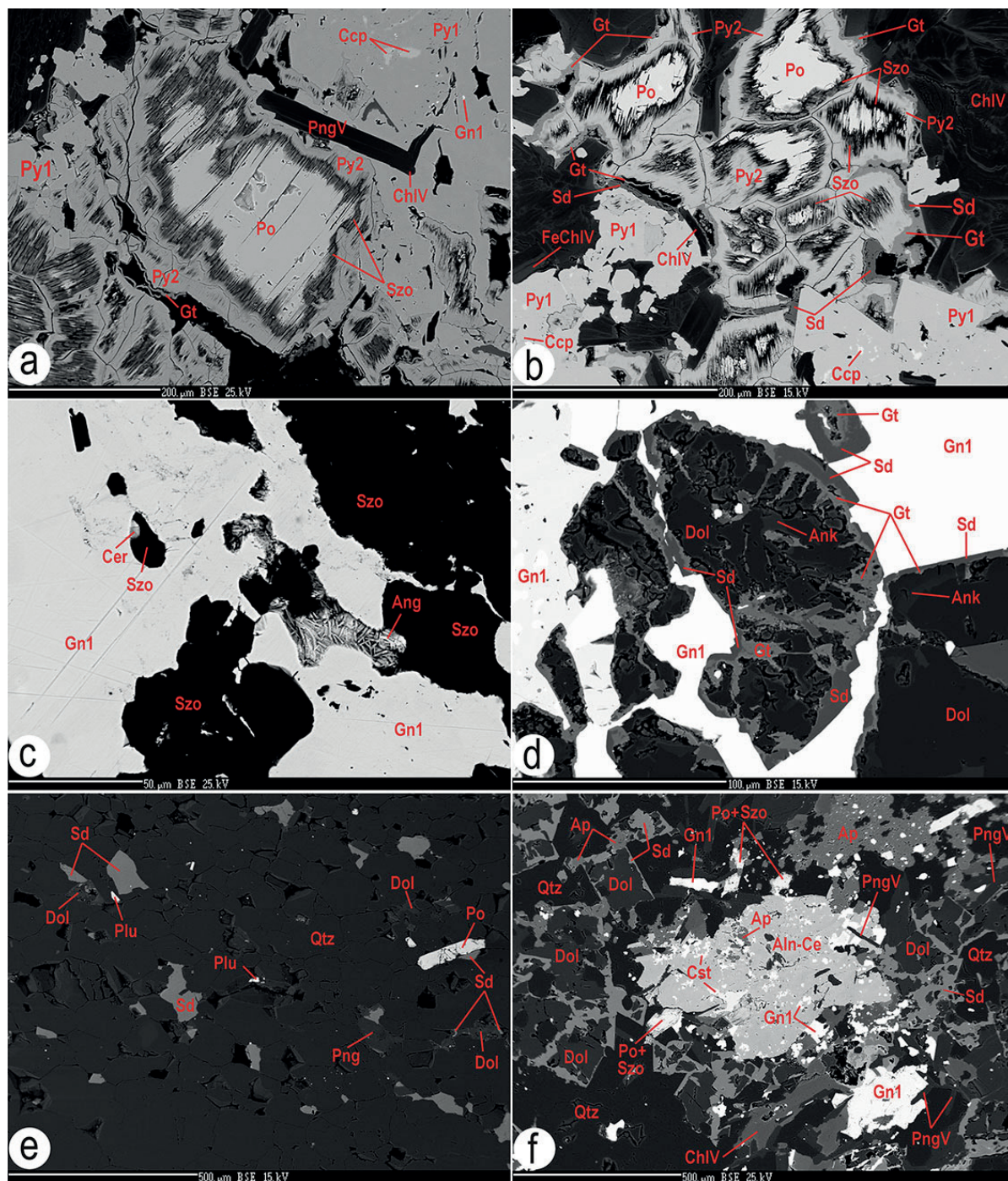
**Fig. 11.** Decomposition of the SedEx pyrrhotite (Po), galena 1 (Gn1) and pyrite 1 (Py1) by oxidation and dolomite (Dol) replacement by goethite (Gt), ankerite (Ank) and siderite (Sd) in the chlorite-apatite zone. *a* – Decomposition of pyrrhotite into szomolnokite (Szo), pyrite 2 (Py2) and goethite (Gt). Galena 1 (Gn1) and chalcopyrite (Ccp) inclusions in the host pyrite 1. The V-rich mica – phengite (PngV) and V-rich chlorite (ChlV) were formed between pyrite 1 and the pyrrhotite remnant. *b* – Gradual decomposition of the pyrrhotite aggregate by oxidation to form szomolnokite, pyrite 2, goethite and siderite according to the reaction 8, see text. The pyrite 1 contains chalcopyrite inclusions and the matrix consists of V-rich chlorite (ChlV) and V-Fe-rich chlorite (FeChlV). *c* – Galena 1 partially decomposed to form cerussite (Cer), anglesite (Ang) and pyrrhotite was completely replaced by szomolnokite. *d* – The remnant of the Silurian limestone – dolomite encloses with galena 1. The dolomite is gradually replaced by goethite, ankerite (Ank) and finally by the siderite (Sd) according to the reaction 9, see text. *e* – Dolomite and pyrrhotite remnants together with siderite and plumosite-like (Plu) formation in quartz matrix. *f* – The aggregate of allanite-*Ce* (Aln-Ce), cassiterite (Cst), fluorapatite (Ap), V-rich mica and galena 1 are found in a matrix consisting of dolomite remnants, quartz, V-rich mica, V-rich chlorite and fluorapatite. The rim of dolomite is replaced by siderite and pyrrhotite was decomposed to the szomolnokite (Po + Szo). BSE images of mineral assemglages.

complete decomposition of Sn(±In) sakuraiite and In-rich ferrokesterite by oxidation in the chlorite-apatite zone. This decomposition resulted in the indium transport by the fluid phase, away from the source minerals to form new In sakuraiite in the quartz matrix, according to reactions 16 and 17.

*Temperature of chlorite-apatite zone*

$8Zn_{0.84-0.79}Fe_{0.11-0.13}Cu_{0.023}In_{0.023}S \rightarrow$
Sphalerite 1

$(Zn_{0.45}Fe_{0.19}Cu_{0.18}In_{0.18})S + 7Zn_{0.89}Fe_{0.11}S$   (16)
In Sakuraiite – *lamellae in*     Sphalerite 2

$7(Cu_{0.34}Zn_{0.25}Fe_{0.22}Sn_{0.15}In_{0.05})S + FeS + H_2O + 0.5O_2 \rightarrow$
Sn sakuraiite          Pyrrhotite

$2(Zn_{0.43}Fe_{0.22}Cu_{0.19}In_{0.18})S +$
In sakuraiite

$+ 2CuFeS_2 + SnO_2 + (Zn_{0.90}Fe_{0.10})S + H_2S$   (17)
Chalcopyrite   Cassiterite     Sphalerite 2
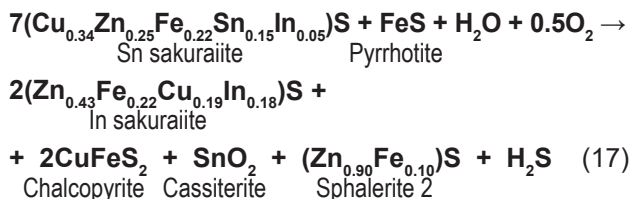
The Cu, Fe, Zn and In contents in the In sakuraiite – sphalerite 2 series are variable and can be evaluated according to binary *apfu*-chemical plots in comparison to the sphalerite 1 created in the SedEx process (Fig. 5). For this comparison, the chemical formula of In sakuraiite was calculated to ZnS-sphalerite base in accordance with the crystalline structure of sakuraiite (Kissin & Owens, 1986). In In-rich sakuraiite, the indium content progressively correlates with Cu in the ideal In = Cu function of values from 0.1 to 0.25 *apfu*. This diagram shows the progressive In = Cu correlation trend that is also the same in sphalerite 1 with In = Cu values up to 0.08 *apfu* (Fig. 9a). The finding of an identical In = Cu correlation in former sphalerite 1 and in new In sakuraiite shows the preservation of the In = Cu function from the source sphalerite 1. This inherited In = Cu correlation does not change in In sakuraiite, which was formed by the decomposition of sphalerite 1 in the chlorite-apatite zone, and quantifies the content of

the roquesite molecule ranging from 18.5 to 48.4 mol. % in In sakuraiite (Tab. 10). The sum of Cu + In *apfu* also progressively correlates with Fe, but the Fe content has a negative correlation with Zn and the coupled (CuInFe) ↔ Zn substitution was found in all samples from the source sphalerite 1 to new sphalerite 2 and In sakuraiite respectively (Fig. 9). The highest indium content in the In sakuraiite analyses is about 25.83 wt. % and their recalculation showed a more accurate arrangement of the elements in the chemical formula $(Zn,Fe)_2InCuS_4$ of that In sakuraiite based on 8 atoms.

The relationships between the source set of In-rich SedEx minerals, which are sphalerite 1, Sn sakuraiite, ferrokesterite and a newly formed association, such as sphalerite 2, In sakuraiite, cassiterite, show (CuSnFe) ↔ Zn and (CuInFe) ↔ Zn, as two independent substitution trends in the ZnFeCuSnIn system, where the composition planes between end members show reactions 13, 16 and 17. Evaluation of these independent substitutions reveals the relationship of the original (CuSnFe) ↔ Zn substitution created in Sn-rich sulfides with variable amounts of indium and the new In sakuraiite mineralization represented by the (CuInFe) ↔ Zn substitution, which originated by the decomposition of Sn-rich sulfides (± In) in the chlorite-apatite zone (Fig. 17).

### Cu/Ag-rich tetrahedrite successive formation

The formation of tetrahedrite is closely related to the increasing content of Ag from the core to the rim of the tetrahedrite grains and aggregates (Fig. 18b). Tetrahedrites are found on SedEx sulfide remnants such as gudmundite, stephanite, chalcopyrite, galena 1 and are always associated with cassiterite, V-rich mica and siderite in the quartz matrix (Fig. 18). The core of tetrahedrite aggregates consists of **tetrahedrite 1** $Cu_7Ag_3Sb_4(FeZn)_2S_{13}$, where the Ag content ranges from 15.89 to 26.97 wt. % and its mineral formula is based on 29 atoms. It is tetrahedrite-*(Fe)* with a detailed chemical formula $Cu_6(Ag_{2.68-3.51}Cu_{0.35-1.34}Fe^{3+}_{0-0.11})_{3.90-4.02}(Fe^{2+}_{1.64-1.71}Zn_{0.29-0.36})_2Sb_{3.96-4.07}S_{12.95-13.05}$
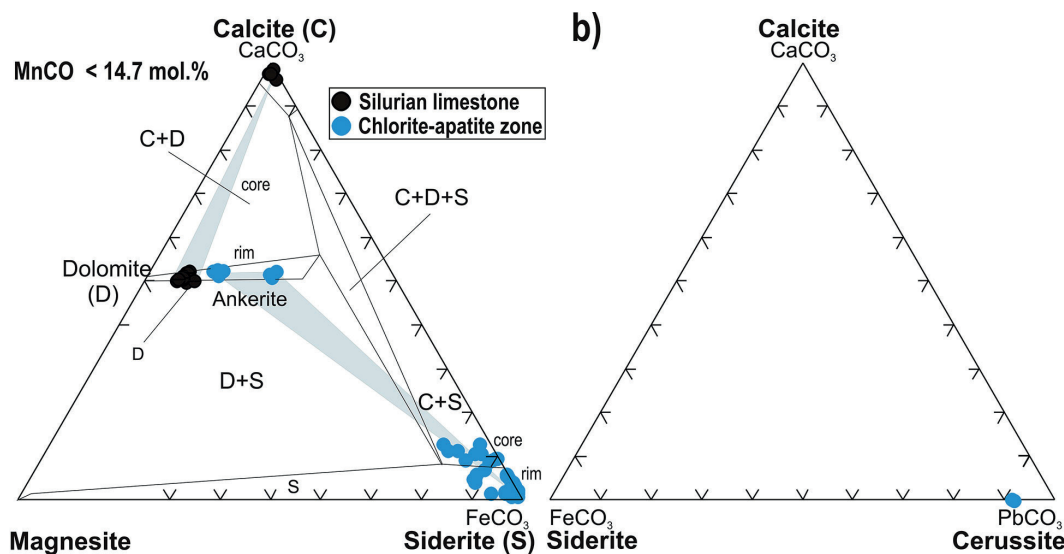
**Fig. 12.** Classification of carbonates. *a* – The triangular diagram shows the carbonate phase system and the projection of dolomite and calcite from the Silurian limestone layer of the Holec Beds. Composition of ankerite and siderite pair from the chlorite-apatite zone. *b* – Composition of cerrusite formed by the oxidation of galena 1 in the chlorite-apatite zone.
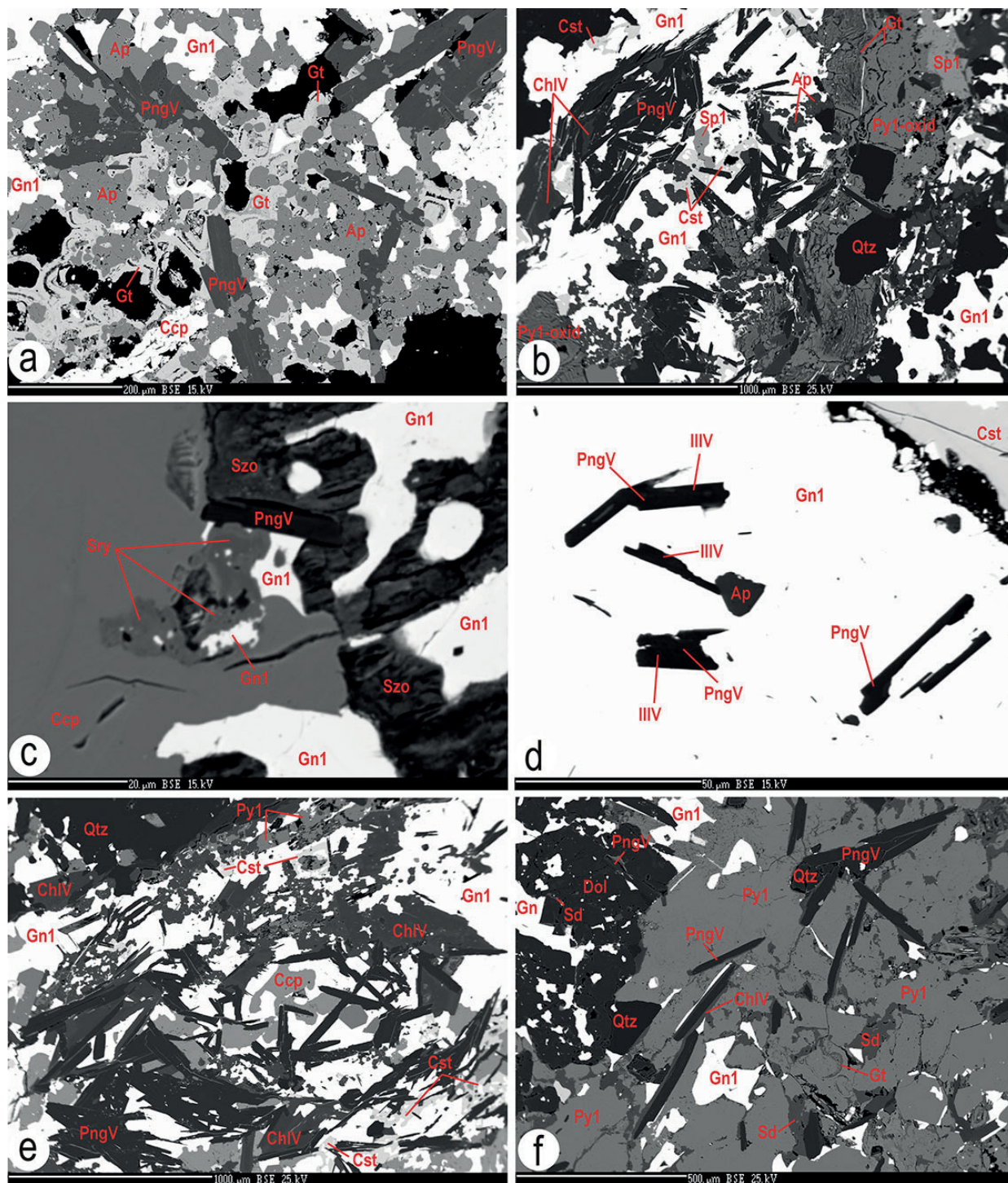
**Fig. 13.** Formation of V-rich micas (PngV), V-rich chlorite (ChlV), schreyerite and oxidation of SedEx sulfides in the chlorite-apatite zone. ***a*** – The relationship of euhedral V-rich mica, goethite (Gt), apatite (Ap) in the chalcopyrite (Ccp), quartz (Qtz) and galena 1 (Gn1) matrix. ***b*** – The aggregate consists of galena 1, oxidized pyrite 1 (Py1-oxide), goethite, V-rich mica, V-rich chlorite, fluorapatite, sphalerite 1 (Sp1) and cassiterite (Cst). ***c*** – Schreyerite (Sry) and galena 1 in host chalcopyrite (Ccp). That aggregate occurs with the contact with szomolnokite (Szo) and V-rich mica. ***d*** – The euhedral white micas are composed of V-rich muscovite-phengite and V-rich phengite-illite (IllV) and these white micas with fluorapatite and cassiterite occur in galena 1. ***e*** – The quartz, chalcopyrite, pyrite 1 (Py1), cassiterite, V-rich micas and V-rich chlorite assemblage. ***f*** – Pyrite 1 aggregate was locally decomposed to goethite and siderite (Sd) by reactions 9 and 10, see text. The V-rich mica is surrounded by V-rich chlorite, and both were precipitated with quartz in host pyrite 1 and dolomite. Galena 1 is also present in pyrite 1. Dolomite is replaced by siderite and together with galena 1 form the matrix. BSE images of mineral assemblages.

according to classification of the tetrahedrite group (Biagioni et al., 2020). The inner rim 1 is formed by **tetrahedrite 2** $Ag_5Cu_2Sb_4(FeZn)_2S_{12}$ having the Ag content from 29.05 to 31.81 wt. % and its mineral formula is based on 28 atoms and shows kenoargentotetrahedrite-*(Fe)* $(Ag_{4.93-5.44}Cu_{0.56-1.07})_6(Ag_{3.83}Fe^{3+}_{0.09-0.13})_{3.93-3.96}(Fe^{2+}_{1.76-1.78}Zn_{0.22-0.24})_2Sb_{4.01-4.07}S_{11.96-12.04}$. The outer rim 2 in contact with the matrix forms rare **tetrahedrite 3** $Ag_9CuSb_4Fe_2S_{13}$ with the highest Ag content in the range from 42.45 to 49.26 wt. % and its mineral formula is based on 29 atoms and shows rozhdestvenskayite-*(Fe)* $Ag_6(Ag_{2.27-3.21}Cu_{0.69-1.71}Fe^{3+}_{0-0.17})_{3.91-4.15}(Fe^{2+}_{1.70-1.75}Zn_{0.25-0.31})_2Sb_{4.02-4.05}S_{12.80-12.98}$. In all three formulae of tetrahedrites, the Ag *apfu* content substitutes Cu in the sum of Cu + Ag = 10, Zn substitutes $Fe^{2+}$ in the sum $Fe^{2+}$ + Zn = 2, the excess Fe above 2 is $Fe^{3+}$ and Sb content is uniformly 4 (Tab. 6).

Decomposition and oxidation in the chlorite-apatite zone of the original SedEx association of stephanite, gudmundite and ferrokesterite by the fluid phase resulted in the formation of tetrahedrite 1 to 3, cassiterite and siderite formation according to reaction 18. The increasing contents of Ag in tetrahedrite 1 to 3 from core to rim 2 in the tetrahedron projection of Ag-Sb-Fe-Cu system shows the immiscible gaps of tetrahedrites in the linear ordering of their composition and also shows the projection plane of reaction 18 between end members stephanite, gudmundite and ferrokesterite (Fig. 21).

**$Ag_5SbS_4$ + $3FeSbS$ + $3Cu_2FeSnS_4$ + $6H_2O$ + $5O$ +**
Stephanite   Gudmundite   Ferrokesterite

**+ $5CO_2$ → $Cu_6Ag_5Sb_4FeS_{13}$ + $3SnO_2$ +**
Tetrahedrite           Cassiterite

**+ $5FeCO_3$ + $6H_2S$**                (18)
Siderite
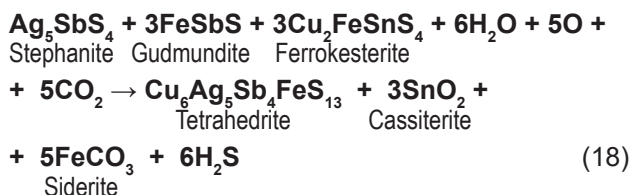
### *Bournonite and plumosite-like formation*

Irregular **bournonite** $Pb_{0.98-0.99}Cu_{0.98-0.99}Sb_{0.94-0.96}Fe_{0.05-0.06}As_{0.04}S_{2.98-2.99}$ with a size of up to 20 μm is always occurring on galena 1. Together with galena 1, it occurs in association with cassiterite and siderite in the quartz matrix (Fig. 14c). Bournonite is homogeneous, containing Fe from 0.59 to 0.65 wt. % and As from 0.64 to 0.69 wt. % (Tab. 6). Rare **plumosite-like** $Pb_{2.78}Fe_{0.06}Bi_{0.02}As_{0.08}Sb_{3.09}S_{6.96}$ in similar size and position to the bournonite also occurs in the quartz matrix along with chalcopyrite, In sakuraiite, cassiterite, galena 1 and siderite (Fig.11e). The Fe and As contents in the plumosite-like chemical formula point to its common origin with bournonite. Both were formed by oxidation and decomposition of galena 1, gudmundite, and ferrokesterite in the chlorite apatite zone according to reaction 19 (Fig. 21).

**$4PbS$ + $4FeSbS$ + $Cu_2FeSnS_4$ + $H_2O$ + $4O_2$ $3CO_2$ →**
Galena1   Gudmundite   Ferrokesterite

**$PbCuSbS_3$ + $Pb_3Sb_3S_7$ + $CuFeS_2$ + $SnO_2$ +**
Bournonite   Plumosite-like   Chalcopyrite   Cassiterite

**+ $3FeCO_3$ + $2FeO(OH)$**           (19)
Siderite           Goethite
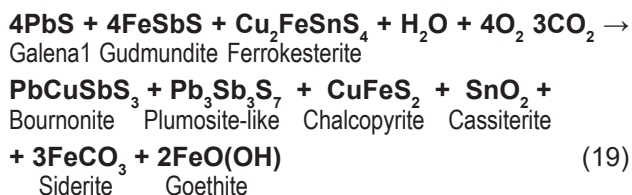
### PbSbBi-rich sufide, native Bi 2 and Se-rich galena 2 formation

The **PbSbBi-rich sulfide** $(Pb_{1.70-1.86}Cu_{0.14-0.31}Ag_{0.02-0.04})_{1.91-2.05}(Sb_{1.42-1.46}Fe^{3+}_{0.37-0.83}Bi_{0.84-1.13})_{2.95-3.09}(Se_{0-0.13}S_{5.90-5.99})_{5.95-6.08}$, in general $A_2B_3S_6$-type, **S-rich wittite** $(Bi_{3.61}Fe_{0.14}Sb_{0.07}Cu_{0.06}Ag_{0.04}Sn_{0.01})_{3.93}Pb_{3.01}(Se_{0.41}S_{8.65})_{9.06}$, **native Bi 2** $(Bi_{0.56}Sb_{0.09}Fe_{0.07}Pb_{0.08}Cu_{0.01}S_{0.19})$ and Se-rich **galena 2** $(Pb_{0.83-0.85}Fe_{0.08-0.10}Bi_{0.03-0.05}Sb_{0-0.03}Cu_{0-0.01}Ag_{0-0.01})(Se_{0.03-0.10}S_{0.90-0.99})$ are new minerals formed in chlorite-apatite zone (Fig. 19, Tab. 4). This assemblage originated from the decomposition of original PbBiSb-rich sulfide $(A_2B_2S_5$-type), kobellite and bismuthinite 1, which were formed by the SedEx process.

The original SedEx kobellite has been oxidized in the chlorite-apatite zone and its rim has partially decomposed to the native Bi 2 of size a few mm. The native Bi 2 there always contains sulphur residues up to 5.5 wt. % and varying contents of Cu, Fe, Pb and Sb up to 10 wt. %, indicating a mixture with kobellite remnant. Comparing two generations of native Bi, according to their composition, the inclusions found in the kobellite core coexist with kobellite and are free of other elements content (Fig. 19a, Tab. 4).

The original PbBiSb-rich SedEx sulfide $(A_2B_2S_5$ type) was partially decomposed and replaced by the Se-rich galena 2, bismuthinite 2 and respectively by the wittite and galena 2 that are found in albite and/or in the host pyrrhotite (Fig. 19c–d). Its decomposition is illustrated by reactions 20 and 21. The reactions plane is shown by the projection between the end-members in the Bi-Sb-Fe-Pb tetrahedron (Fig. 21). The generated wittite shows good agreement with the reference wittite and/or eclarite in the classification diagrams (Figs. 20 and 21).

**$2Pb_2BiSbS_5$ + $3H_2O$ → $Bi_2S_3$ + $4PbS$ +**
PbSbBi sulfide           Bismuthinite 2  Galena 2

**+ $Sb_2O_3$ + $3H_2S$**                (20)
Valentinite

**$4Pb_2BiSbS_5$ + $6H_2O$ → $Bi_4Pb_3S_9$ + $5PbS$ +**
PbSbBi sulfide           Wittite       Galena 2

**+ $2Sb_2O_3$ + $6H_2S$**              (21)
Valentinite
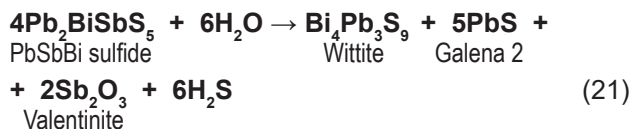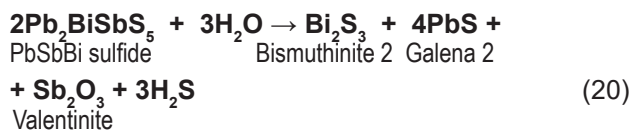
The new PbSbBi-rich sulfide $(A_2B_3X_6$-type) formed in chlorite-apatite zone up to 50 μm in size fills cracks in host pyrite 1 and chalcopyrite along with cassiterite (Fig. 19e–f). Plotting *apfu* compositions of $Fe_{total}$ versus Bi and $Fe_{total}$ versus Sb show inverse correlations and well defines the substitution Sb + $Fe^{3+}$↔Pb + Cu+ Ag at approximately the constant Bi about 1 (*apfu*) if Fe content ranges from 2 to 5 wt.% in that PbSbBi sulfide (Figs. 20 d–e; Tab. 4). In this case the chemical formula is $(Pb_{1.70-1.86}Cu_{0.14-0.31}Ag_{0.02-0.04})_{1.91-2.05}(Sb_{1.42-1.46}Fe^{3+}_{0.37-0.83})_{1.83-2.25}Bi_{0.84-1.13}(Se_{0-0.13}S_{5.90-5.99})_{5.95-6.08}$ as $A_2(B_2 + Bi)_3X_6$-type in detail. If Fe content ranges from 5 to more of 6 wt. %, the chemical formula changes to $(Pb_{1.56-1.64}Cu_{0.13-0.18}Ag_{0.02-0.03})_{1.71-1.85}$
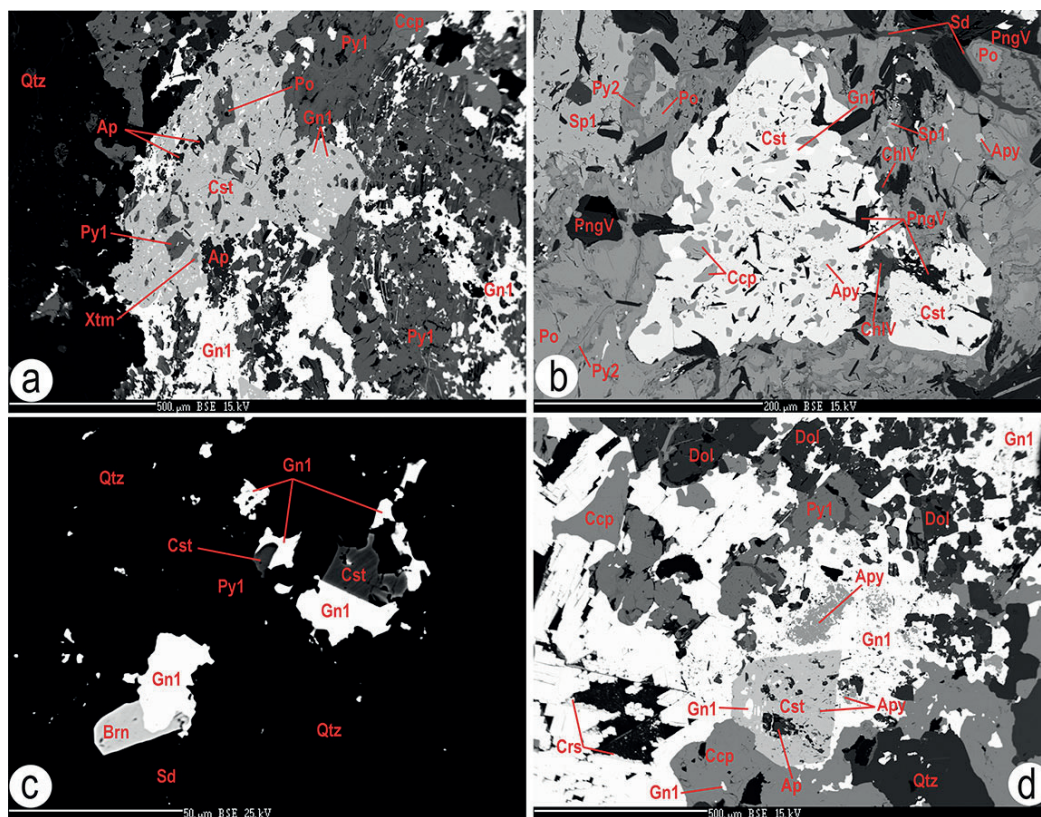
**Fig. 14. *a, b*** – Stratiform SedEx mineralization, such as galena 1 (Gn1), pyrrhotite (Po), xenotime (Xmt), pyrite 1 (Py1), chalcopyrite (Ccp), arsenopyrite (Apy), is cemented by cassiterite in aggregate, where V-rich mica-phengite (PngV), V-rich chlorite (ChlV) and fluorapatite (Ap) coexist with cassiterite. The matrix of the aggregate consists of quartz (Qtz), sphalerite (Sp1), pyrrhotite (Po), pyrite 1 and siderite (Sd). The pyrrhotite is replaced by pytite 2 (Py2). ***c*** – Galena 1 is partially replaced by bournonite (Brn) and cassiterite forming an aggregate with galena 1 in the quartz (Qtz) siderite (Sd) matrix. ***d*** – Assemblage of pyrite 1, pyrrhotite, quartz, arsenopyrite (Apy), chalcopyrite, galena 1, dolomite and hypidiomorphic cassiterite. Cassiterite closes arsenopyrite, galena 1, fluorapatite and the galena 1 rim is partially replaced by cerussite (Cer). BSE images of mineral assemglages.

$(Sb_{1.22-1.36}Bi_{0.84-0.95})_{2.06-2.31}Fe_{0.94-1.02}(Se_{0.08}S_{5.92})_6$ as $A_2(B_2 + Fe)_3X_6$-type in details. The high Fe in the chemical formula shows a depletion in $A_2$ of about 0.3 and an excess in $B_2$ of about 0.3, indicating a possible binding of the Fe content as $Fe^{2+}$ around 0.3 *apfu* in $A_2$ according to the presented $A_2B_3X_6$-type, although a substantial fraction of the Fe is bound in the form of $Fe^{2+}$ and $Fe^{3+}$ in that PbSbBi rich sulfde (Tab. 4).

In the Sb-Bi-Pb triangle diagram, the new PbSbBi-rich sulfide translates to a tintinaite-wittite/eclarite trend, but the significant influence of the gudmundite ($Fe^{3+}SbS$) molecule in its composition can be clearly seen in $(Sb + Fe_{total})$-Bi-$(Pb + Cu + Ag)$ triangle diagram and in Bi-Sb-Fe-Pb tetrahedron projection (Figs. 20a–b and 21). The formation of PbSbBi-rich sulfide can be explained by reaction 22 and the reaction plane is shown by the projection of reacted end-members in the Bi-Sb-Fe-Pb tetrahedron (Fig. 21).

**FeSbS + Bi₂S₃ + 2PbS + FeS + 2O₂ +**
Gudmundite  Bismuthinite1  Galena1  Pyrrhotite

**H₂O → Pb₂SbBiFeS₆ + Bi + FeSO₄.H₂O** (22)
PbSbBi sulfide  native  Szomolnokite
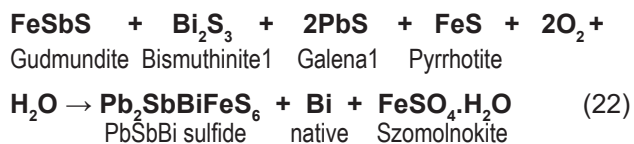
**Discussion**

In the Permian epidote-amphibolite facies and the related chlorite-apatite zone the graphite was formed from organic matter in the graphite-bearing phyllites and also skarn from limestone lenses of the Silurian Holec Beds in the Bystrý potok locality. That conversion of organic matter to graphite and limestone to garnet-hedenbergite-epidote-amphibole skarn released significant amount of $CO_2$ from the sourse organic matter and limestone into the fluid phase (Figs. 1, 2, 3, 5, 16e). During graphite and skarn formation, in addition to $CO_2$, as well $O_2$, $H_2O$ and $H_3PO_4$ were released and this fluid phase also transported V and Ca to the stratigraphically overlying Late Silurian-Devonian stratiform SedEx sulphide mineralization, where V-rich micas-phengites, fluorapatite, V-rich chlorite and rarely schreyerite formed in the original SedEx sulfide matrix (Fig. 13). Besides graphite-bearing phyllites and limestone also the lydite from the Holec Beds demonstrated to be the source of Si, P, Rb, Cu, Cr, Ni, Ba, Sc, V, Cd, Se, Ti, Si, Fe, Mg, U, Zn, Pb, Sb, Tl, Hf, HREE and $CO_2$ that were released into the fluid phase in the Permian metamorphism (Radvanec & Gonda, 2019). According to the geological map, the Holec Beds cover approximately 1/4–1/5 of the
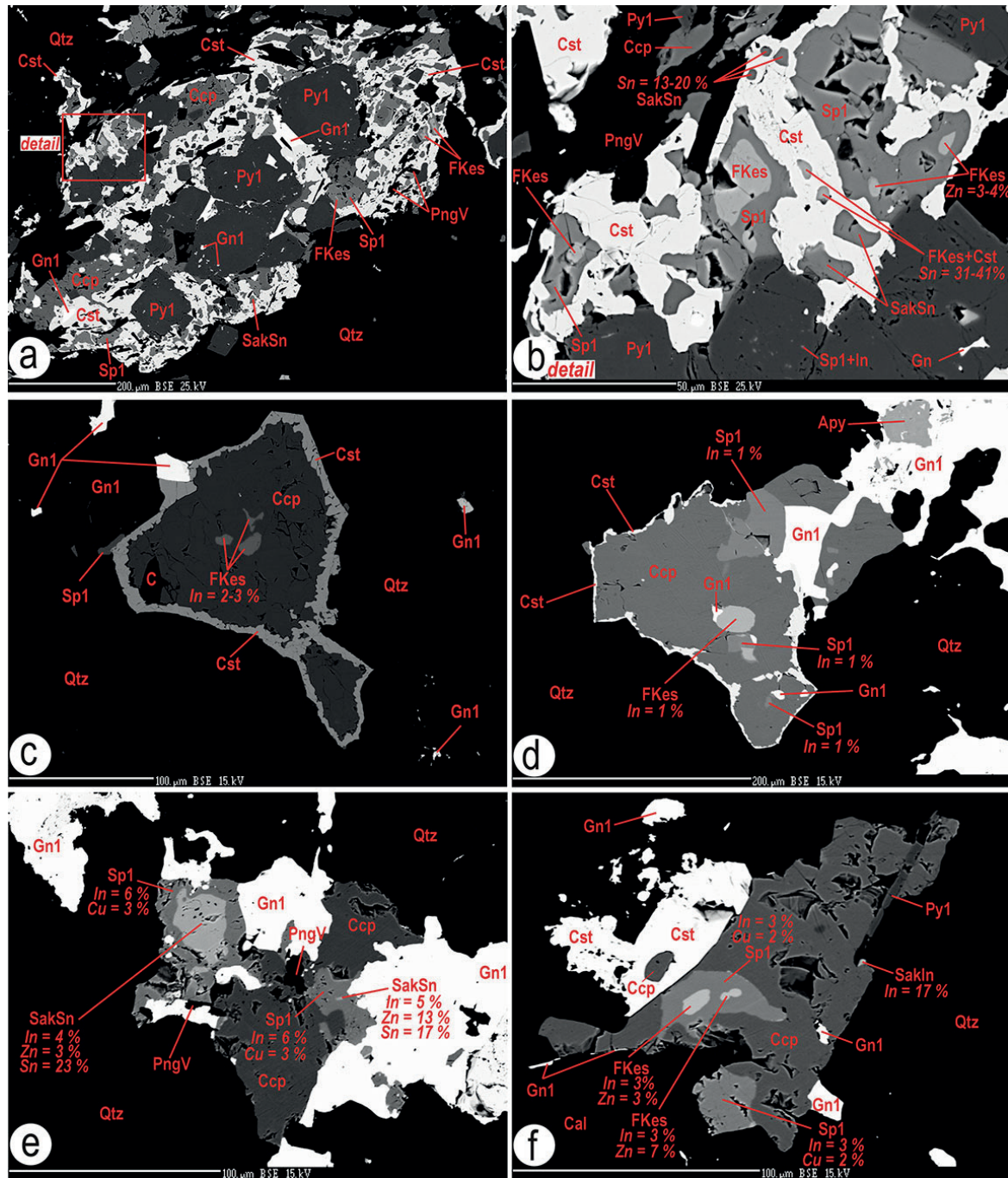
**Fig. 15.** *a* – Sulfides originated in the SedEx process, such as chalcopyrite (Ccp), pyrite 1 (Py1), galena 1 (Gn1), sphalerite 1 (Sp1), ferrokesterite (FKes), and Sn-rich sakuraiite (SakSn), are cemented by cassiterite (Cst) and V-rich mica-phengite (PngV) forming an aggregate in the quartz matrix (Qtz). *b* – The detail shows remnants of ferrokesterite and Sn-rich sakuraiite enclosed in the cassiterite aggregate. The disseminated inclusions of In-rich sphalerite 1 (Sp1 + In) and galena 1 occur in the host pyrite 1. The spots in cassiterite, where the Sn content ranges from 31 to 41 wt. % represents a mixture of unreacted ferrokesterite residues and new cassiterite (FKes + Cst). Analyses of these spots show a weak stoichiometry. *c, d* – The ferrokesterite with the In content from 1 to 3 wt. % was decomposed by oxidation to chalcopyrite and cassiterite according to the reaction 13, see text. The chalcopyrite encloses sphalerite 1, galena 1 and that chalcopyrite also contains residues of ferrokesterite and sphalerite 1 with the same content of In = 1 wt. %. Arsenopyrite (Apy) occurs in galena 1. *e* – The SedEx aggregate consists of variable Sn-rich sakuraiite, galena 1, chalcopyrite and sphalerite 1. The In content of the Sn-rich sakuraiite ranges from 4 to 6 wt. % and in sphalerite 1 the same amount of In = 6 % was found. *f* – The SedEx aggregate of Sn-rich sakuraiite, ferrokesterite, galena 1, chalcopyrite, cassiterite, pyrite 1 and sphalerite 1 in the quartz matrix with new cassiterite. The content of In = 3 wt. % is the same in ferrokesterite, Sn-rich sakuraiite and also in sphalerite 1. In-rich Sakuraiite (SakIn) was formed on the chalcopyrite. BSE images of mineral assemglages.
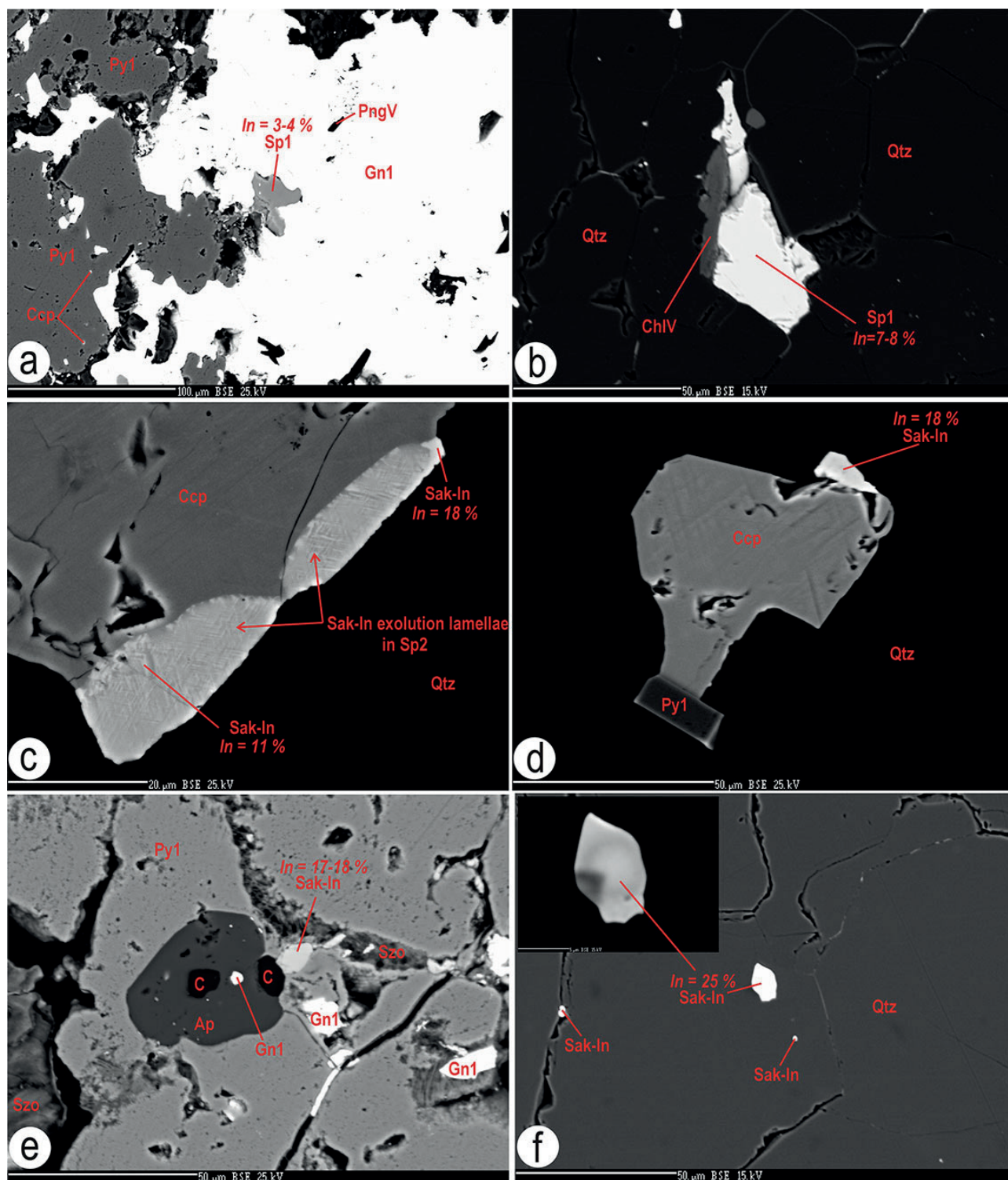
**Fig. 16.** The formation and occurrence of In-rich sulfides. *a, b* – In-rich sphalerite 1 originated and belongs to the mineral assemblage of the stratiform SedEx sulfidic mineralization. The In content in sphalerite 1 ranges from 3 to 8 wt. %. This sphalerite 1 is accompanied by pyrite 1 (Py1) with the chalcopyrite (Ccp) inclusions, by the V-rich mica (PngV), galena 1(Gn1), V-rich chlorite (ChlV) and by the quartz (Qtz). *c* – The In-rich sphalerite 1 (Sp1) decomposition caused the formation of In sakuraiite (InSak) lamellae in the indium-free sphalerite 2 (Sp2) according to reaction 16, see text. *d* – Homogeneous In-rich sakuraiite was formed on the rim of chalcopyrite. *e* – Host pyrite 1 (Py1) encloses graphite (C), fluorapatite (Ap), galena 1, szomolnokite (Szo) and In-rich sakuraiite there contains indium from 17 to 18 wt. %. *f* – In-rich sakuraiite with indium content of 25 wt. % in the quartz matrix. BSE images of mineral assemblages.

entire area in the Gemeric unit and this area of occurrence with Permian metamorphism shows release of $CO_2$ and elements into the fluid phase during the considerable regional extent of Variscan orogeny (Figs. 1–3).

The released fluid phase decomposed and oxidized the original stratiform SedEx sulfides in the chlorite-apatite zone, which partially coincides with the epidote-amphibolite facies (500–600 °C; 526–546 °C; 3–7 kbar) in the Bystrý potok locality. That chlorite-apatite zone is identical to the P-T conditions of the chlorite-apatite zone (420–540 °C) found throughout the Gemeric unit (Radvanec & Gonda, 2019, 2020).

The fluid phase that formed at these P-T conditions consists of $CO_2$, $O_2$, $H_2O$, $H_3PO_4$, obtained from Holec Beds and moreover from $H_2S$ and HF after enrichment of the fluid phase due to decomposition and oxidation of the SedEx sulfides according to 22 empirical reactions. All

reactions are derived from the relationships between the reactants and the newly formed mineral associations based on their relationships confirmed by BSE images (Figs. 4, 6–8, 11, 13–16, 18, 19). The resulting reactions explain the formation of new cassiterite, valentinite, anglesite, schreyerite, szomolnokite, goethite, V-rich mica, V-rich chlorite, Fe-Mn-Pb carbonates, and new generation of In-Sn-Ag-Sb-Pb-Bi-Zn-Fe-As-Cu-Ni-Co sulfides at the expense of the original SedEx mineralization in the crystallization systems were the oxidation is the main process formed those new minerals in situ (Figs. 5, 12, 17, 21).

The present study and previously published data point to oxidation as the main decomposition process of Lower Paleozoic rocks by fluid phase originated in Permian metamorphism. The epidote-amphibolite facies with a related chlorite-apatite zone represent the lower
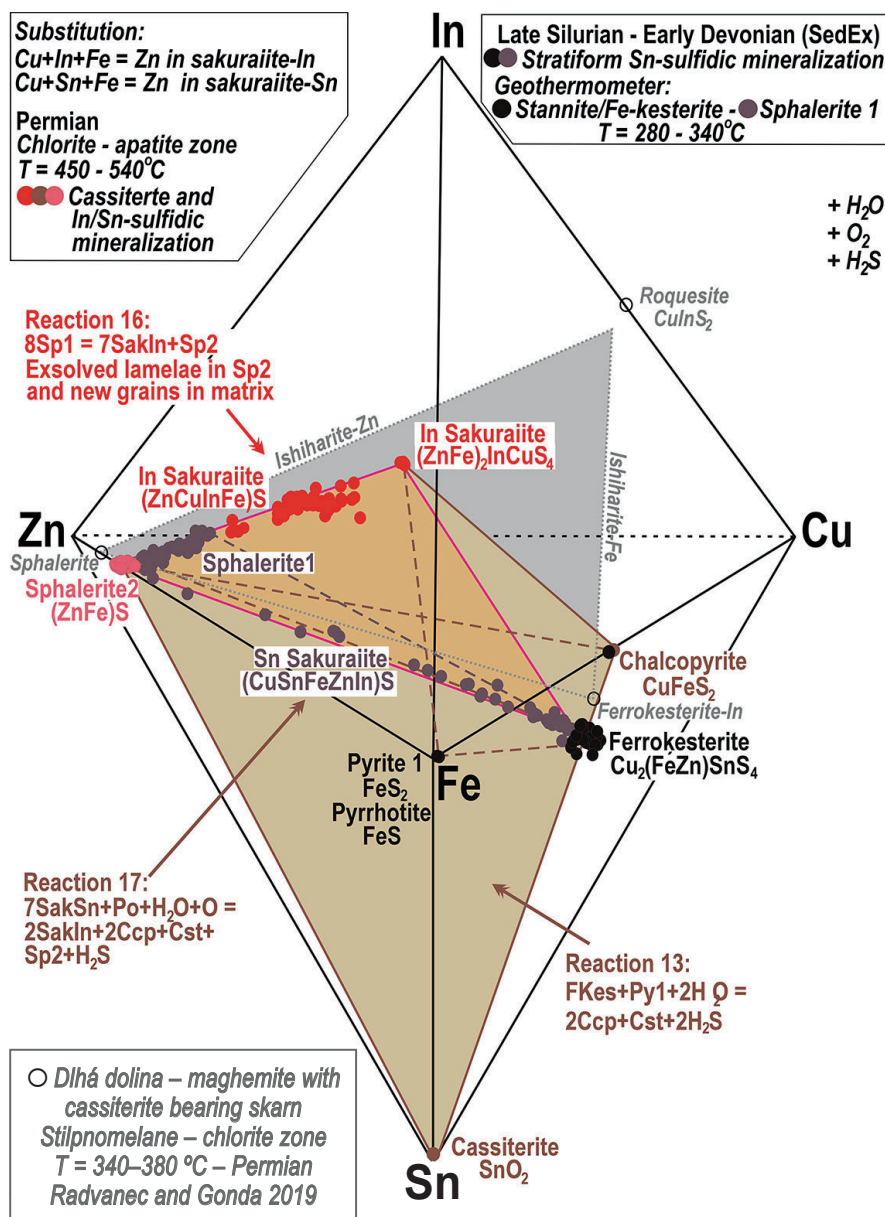


**Fig. 17.** Two interconnected tetrahedral phase diagrams for the system ZnFeCuSnIn, showing the plotting positions of the sphalerite 1 (Sp1), sphalerite 2 (Sp2), Sn-rich sakuraiite (SakSn), In-rich sakuraiite (SakIn), chalcopyrite (Ccp), ferrokesterite (FKes), pyrite 1 (Py1), pyrrhotite (Po), and cassiterite (Cst). The composition planes showing reactions 13, 16 and 17 see the text. The studied In-Sn mineralization is compared with sphalerite, ishiharaite-*Zn*, ishiharaite-*Fe*, roquesite and In-rich ferrokesterite-*In* mineralization from the maghemite-cassiterite skarn at the Dlhá dolina locality described by Radvanec & Gonda (2019).

temperature limit (420–540 °C) for the presence of in situ oxidation. Not only the epidote-amphibolite facies and the related chlorite-apatite zone, but also the temperature 600–650 °C of the amphibolite facies and/or the biotite zone show the oxidation as the main decomposition process of the source minerals, as evidenced by the formation of Fe-Mn skarns with Fe-Mn oxides at the Čučma locality (Radvanec & Gonda, 2020).

The upper temperature part of the amphibolite facies in the Gemeric unit, with above 650 °C, caused anatectic melting of all Lower Paleozoic rocks on two Permian metamorphic hot lines. Anatectic melting on the hot lines produced granitic magma and part of it also differentiated to form varieties of S-type granites with $^{87}Sr/^{86}Sr$ ratios ranging from 0.7110 to 0.7142 (Radvanec et al., 2004, 2007, 2009; Grecula et al., 2009, 2011).

Based on this study and published data, the chlorite-apatite zone, epidote-amphibolite facies and biotite zone with proven anatectic melting are those facies in the Gemeric unit, where oxidation in the Permian is the main decomposition process of minerals found in the Lover Paleozoic rocks, including the Late Silurian-Devonian stratiform SedEx sulfidic mineralization (Radvanec et al., 2004, 2010; Radvanec & Gonda, 2019, 2020).

Within the Holec Beds of Gemerc unit, the stratiform SedEx sulfide mineralization represents a significant occurrence (Figs. 1, 2) and its decomposition owing to its metamorphic overprint in zones and facies mentioned above, including its anatectic melting, released Fe, Cu, Sb, Ag, Pb, Zn, In, Bi As, Ni, Co, V, Ca and Sn into the fluid phase. The same elements, as well as B, F, Sn, Mo, K and Li were released into the fluid phase from SedEx mineralization in the Smolnik locality (Radvanec & Gonda, 2019). These elements were transported by the complex fluid phase rich in $CO_2$, $O_2$, $H_2O$, $H_3PO_4$, HS and $H_2S$ to newly developed Variscan structures, ranging from greisen derivated by the granite magma in the amphibolite facies, skarns and stockwors in the epidote-amphibolite facies and/or in the chlorite-apatite zone to veins located in the greenschist facies. The Variscan structures are filled with oxides, sulfides and Fe-Mn-Mg carbonates, depending on the zones and/or conditions of the metamorphic facies in which the structure has formed (Radvanec et al., 2007, 2010; Radvanec & Gonda, 2019, 2020).

Concerning the sequence of Variscan tectonometamorphic events in papers referred above (l.c.), there were distinguished the Carboniferous-Lower Permian metamorphism **M1a** of Variscan **VD1** convergent / collisional phase (348–275 Ma) and (2) Middle-Upper Permian metamorphic overprint **M1b** (275–262 Ma; monazite and uraninite ages – Konečný in Radvanec et al., 2007) produced by the heat imput from the hot line and causing the active metamorphic core complex formation and related **VD2** uplift in the axial zone of collisional belt as well as related synmetamorphic and ongoing unroofing processes. In present concept of "XD labelling" (Németh, 2021) for better unification and understandability, the Carboniferous **VD1** related metamorphism **M1a** is designated **MV1 (348–275 Ma)** and Permian **VD2** related metamorphism

**M1b** is designated **MV2 (275–262 Ma)**. This new designation is used also in this paper.

The **MV2** thermal processes and later Permian evolution contributed markedly to origin of orogen-parallel extensional fan-like structures with input of fluids, producing Permian mineralized veins.

The cassiterite is the index oxide in the metallogeny of the Gemeric unit. The main occurrence of cassiterite is related to cassiterite bearing greisen with the topaz, tourmaline, löllingite, fluorapatite, white mica, biotite, Bi-rich minerals, margarite, fluorite, molybdenite, uraninite Fe-Mn carbonates and siderite formation in the epidote-amphibolite facies and/or in the biotite zone (Hnilec locality) were the Re-Os age of molybdenite is ~ 263 Ma (Kohút & Stein, 2005). Less cassiterite occurs in the cassiterite-tourmaline-Fe carbonates bearing greisen of the chlorite-apatite zone (Dlhá dolina locality) and least in the maghemite-cassiterite-Fe carbonate/siderite-FeZnCuBiTeIn sulfides skarn formed in the stilpnomelane-chlorite zone (Dlhá dolina locality). The relationship and abundance of cassiterite formation show its consistently decreasing abundance in metamorphic facies and zones from greisen to skarn. The formation of cassiterite covers a temperature range from about 500–600 °C in greisen to 300–370 °C in skarn (Radvanec & Gonda, 2019). However, the data from present study explain the formation of cassiterite by oxidation of Sn-rich source sulfides in-situ under P-T conditions of the chlorite-apatite zone (420–540 °C) without the evidence of the greisen formation in the host stratiform SedEx mineralization. The oxidation of Sn-rich sulfides in the epidote-amphibolite phase or decomposition of Sn-rich sulfides during anatectic melting in the amphibolite facies leads to the formation of cassiterite in situ, or cassiterite is formed in greisens as a part of granite apophyses or near the granite, or cassiterite is formed in skarn with maghemite. Data from this study confirm that the source of tin for cassiterite formation in greisen and skarn is Sn-rich sulfides from the Late Silurian-Devonian SedEx mineralization.

In addition to greisen and skarn mineralization, the short quartz veins and stockwork occurring near porphyritic, medium-grained S-type granites and in P-enriched leucogranites, originating at the Hnilec and Dlhá dolina localities, are considered to represent a root zone of the vein formation and the initial hydrothermal activity related to and dated to the Permian as well. Veins are generally up to 15 cm thick and up to 5 m long. They contain variable amounts of albite, muscovite, Li-bearing micas, chlorites, biotite, tourmaline, rutile, fluorite, polycrase-*(Y)* to uranopolycrase, uraninite, columbite-*(Mn,Ta,Fe)*, bastnäsite-*(Ce)*, carbonates (Mn-rich siderite, rhodochrosite, calcite and dolomite), phosphates (fluorapatite, triplite, xenotime, goyazite-*(REE)*, fluorarrojadite-*(Ba,Na)*, fluorarrojadite-*(Ba,Fe)*, fluordickinsonite-*(Ba,Na)*, viitaniemiite), molybdenite, tungstene, topaz, Bi, Bi-Te, Pb-Bi, Pb-Sb, Sb, As-Co-Ni sulfides and sulfides like pyrite, arsenopyrite, sphalerite, chalcopyrite, tetrahedrite, galena, etc. (Grecula et. al., 1995; Radvanec et al., 2019; Števko & Sejkora, 2021).
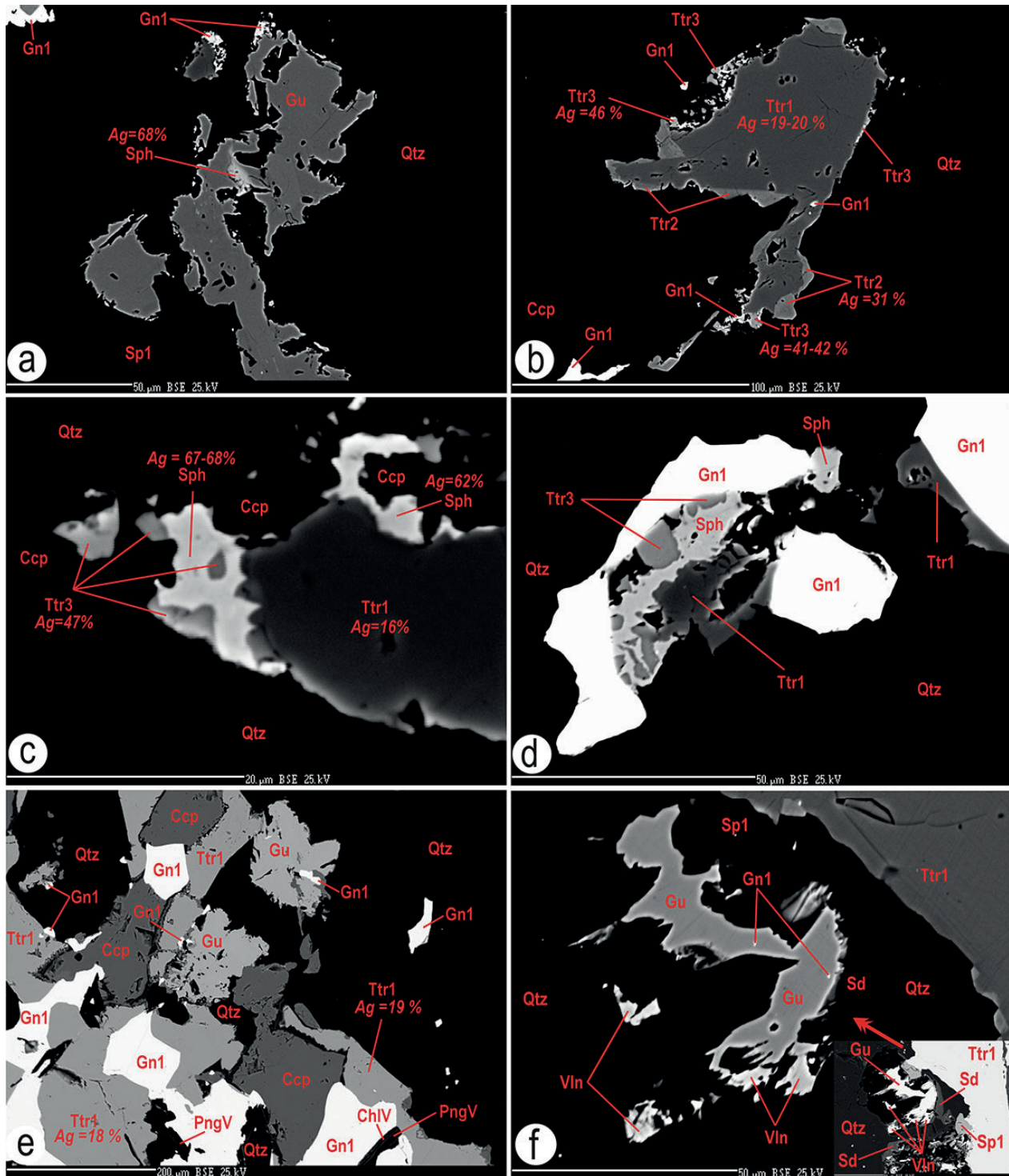
**Fig. 18.** The successive formation of Ag-rich sulfides. *a* – The corroded remnants of stephanite (Sph), gudmundite (Gu) and galena 1 (Gn1) occur in the matrix of quartz (Qtz). *b* – The gradual formation of tetrahedrites from tetrahedrite 1 (Tth1) in the core through tetrahedrite 2 (Tth2) at the rim 1 and final formation of tetrahedrite 3 (Tth3) at rim 2, showing a gradual increase in Ag content from core to the rim 2. The matrix consists of chalcopyrite (Ccp), quartz and galena 1. Zonal tetrahedrites were formed according to reaction 18, see text and Fig. 21. *c, d* – The relationship between stephanite, tetrahedrite 1 and tetrahedrite 3 in the quartz and chalcopyrite matrix. *e* – The corroded grains of gudmundite and their relationship to the quartz, galena 1, tetrahedrite 1, chalcopyrite, V-rich mica (PngV) and V-rich chlorite (ChlV). *f* – Gudmundite partially oxidized to valentinite (Vln) and siderite according to the reaction 15, see text. This gudmundite occurs in the association of tetrahedrite 1 (Tth1), sphalerite 1 (Sp1) and quartz (Qtz). BSE images of mineral assemblages.

The In-rich sakuraite is another index mineral occurring with cassiterite outside the greisen formation. In-rich sulfides associated with coexisting maghemite and cassiterite were formed in the stilpnomelane-chlorite zone in maghemite-cassiterite-Fe carbonate/siderite-FeZnCu-BiTeIn sulfides skarn in the Dlhá dolina locality (Radvanec & Gonda, 2019). There, in the immediate skarn contact with the calcite-ankerite-dolomite lens (former Silurian limestone), the chalcopyrite contains inclusions of ishiharaite-*(Fe)*, sakuraiite and sakuraiite-*(Zn)*. Inclusions of these In-rich sulfides are in chalcopyrite inhomogeneous and often form a mixture of In-rich sphalerite, sakuraiite and stilpnomelane or it is the mixture of In-rich sphalerite, sakuraiite-*(Zn)* and roquesite. Rarely the ishiharaite-*(Fe)* forms individual inclusions in host chalcopyrite (l.c.). These In-rich sulfides, coexisting with chalcopyrite and sphalerite, show crystallization from the fluid phase along with a maghemite-cassiterite-siderite matrix. In the Zn-FeCuInSn system, the In-rich sulfides exhibit a complete substitution series between the sphalerite-roquesite-In-rich ferrokesterite end-members, leading to the formation of ishiharaite-*(Zn)*, ishiharaite-*(Fe)* and/or sakuraiite in the host chalcopyrite. All In-rich sulfides formed in the stilpnomelane-chlorite zone, where T = 300–370 °C and P = 4.3–5.7 kbar (Fig. 17; Radvanec & Gonda, 2019).

This study qualifies the formation of coexisting sphalerite 2 and In-rich sakuraiite in the chlorite-apatite zone with 520–540 °C at higher temperature. The sphalerite 2 and In-rich sakuraiite assemblage originated at the expense of the original In-rich sphalerite 1, Sn (± In) sakuraiite and In-rich ferrokesterite formed in stratiform SedEx mineralization (Figs. 9, 10 and 17). The formation of sphalerite 2 and In sakuraiite is accompanied by the formation of coexisting cassiterite and siderite as it is also in the stilpnomelane-chlorite zone. The different thermal formation of In-rich sulfides are also indicated by the Fe content in sphalerites where the Fe content ranges from 0.97 to 3.62 wt. % in sphalerite of the stilpnomelane-chlorite zone and sphalerite 2 formed at a higher temperature in the chlorite-apatite zone contains Fe ranging from 6.25 to 6.68 wt. % (Radvanec & Gonda, 2019; Tab. 10). The different temperatures of the chlorite-apatite and stilpnomelane-chlorite zones are also manifested by parallel projection planes between the end-members in the ZnFeCuInSn system (Fig. 17).

In addition to the stratiform SedEx sulfide mineralization, greisen, skarn, Mg-Fe-Mn metasomatic mineralization and stockwork mineralization, the siderite-sulfide veins represent the typical and predominant form of mineralization in the Gemeric unit, of which about 1 200 were verified, being located in greeschis facies (Grecula et al., 1995). The mineralization of the veins consists of siderite, ankerite, baryte, chalcopyrite, pyrite, quartz, as well as tetrahedrite, stibnite and sulfides rich in As, Sb, Pb, Bi, Co, Ni and others minerals. Present study data reveal a process whereby the fluid phase of the chlorite-apatite zone oxidized the original stratiform SedEx sulphide mineralization and its decomposition released elements that were subsequently locally transported. The higher temperature of the ore-bearing fluid associated with the amphibolite facies transported the released elements into the vein structures and caused vertical zonation from the quartz- and sulfide-dominated root zone to the siderite- and barite-dominated main vein structure (Grecula et al., 1995; Radvanec et al., 2004). The siderite always forms the central part and baryte only the upper part of vein mineralization in the Gemeric unit (Grecula et al., 1995). In the baryte the $^{87}Sr/^{86}Sr$ ratio ranges from 0.7104 to 0.7154 (Radvanec et al., 1990, 2004). At the Gemerská Poloma locality the magnesite has a ratio of $^{87}Sr/^{86}Sr = 0.71124 – 0.71148$. The $^{87}Sr/^{86}Sr$ data in baryte and magnesite agree well with the $^{87}Sr/^{86}Sr$ ratio ranges from 0.7119 to 0.7144 in the S-type Permian granite reflecting their simultaneous generation in the Variscan MV2 metamorphic-magmatic-hydrothermal (MMH) cycle (Radvanec et al., 2004, 2010; Žák et al., 2005; Radvanec & Gonda, 2019).

The siderite veins are dissected by faults and fissures and the individual vein segments often changed from E-W to NW-SE directions due to Alpine tectonic overprint (Radvanec et al., 1988). The vein structures were locally re-metamorphosed at most in greenschist facies which has rejuvenated the former mineralization. At the Gemerská Poloma locality a part of the magnesite body was converted to talk by a $SiO_2$-rich fluid phase in the Alpine ApD2 unroofing structures (Radvanec et al., 2010; Smolárik & Németh, 2015). At the Rudňany locality the celestine nests located in cracks in the momomineralic baryte and celestine found in cracks from the baryte and ankerite matrix have a ratio of $^{87}Sr/^{86}Sr = 0.721757–0.721893$. Also strontianite hemispheres with $^{87}Sr/^{86}Sr = 0.718536$ at a fracture in the host rock of the siderite-sulfide vein have $^{87}Sr/^{86}Sr$ values compared to these data in the celestine. The $^{87}Sr/^{86}Sr$ data for late-stage Sr minerals from siderite-sulfide veins are significantly higher than the range obtained by Radvanec et al. (1990, 2004) for main-stage baryte. The data on the formation of strontianite, celestine and talc, together with tectonic evolution, reflect a younger and rejuvenating hydrothermal phase of the Alpine metamorphism MAp2, which applies only locally, while the data on baryte, magnesite and granite reflect the main Variscan magmatic-metamorphic-hydrothermal (MMH) cycle in the Paleo-Gemeric domain (Radvanec et al., 2004).

The data from this study complete the genetic relationship between source Late Silurian-Devonian stratiform SedEx sulfidic mineralization and greisen-stockwork-skarns and siderite-sulfide mineralization localized in veins summarized the Permian (MMH) cycle in the Paleo-Gemeric domain (Grecula et al., 1995; Radvanec et al., 2010; Radvanec & Gonda, 2019, 2020). The genetic relationship between the source SedEx stratiform sulphide mineralization and the siderite-sulphide mineralization in veins is supported also by stable isotope data (Radvanec et al., 2004; Žák et al., 2005). The MMH cycle summarizes the genetic connection between mineralization, anatectic melting with the formation of S-type granites in the amphibolite facies and metamorphic facies ranging from epidote-amphibolite facies, biotite zone, chlorite-apatite zone, chlorite-stilpnomelane zone to chlo-
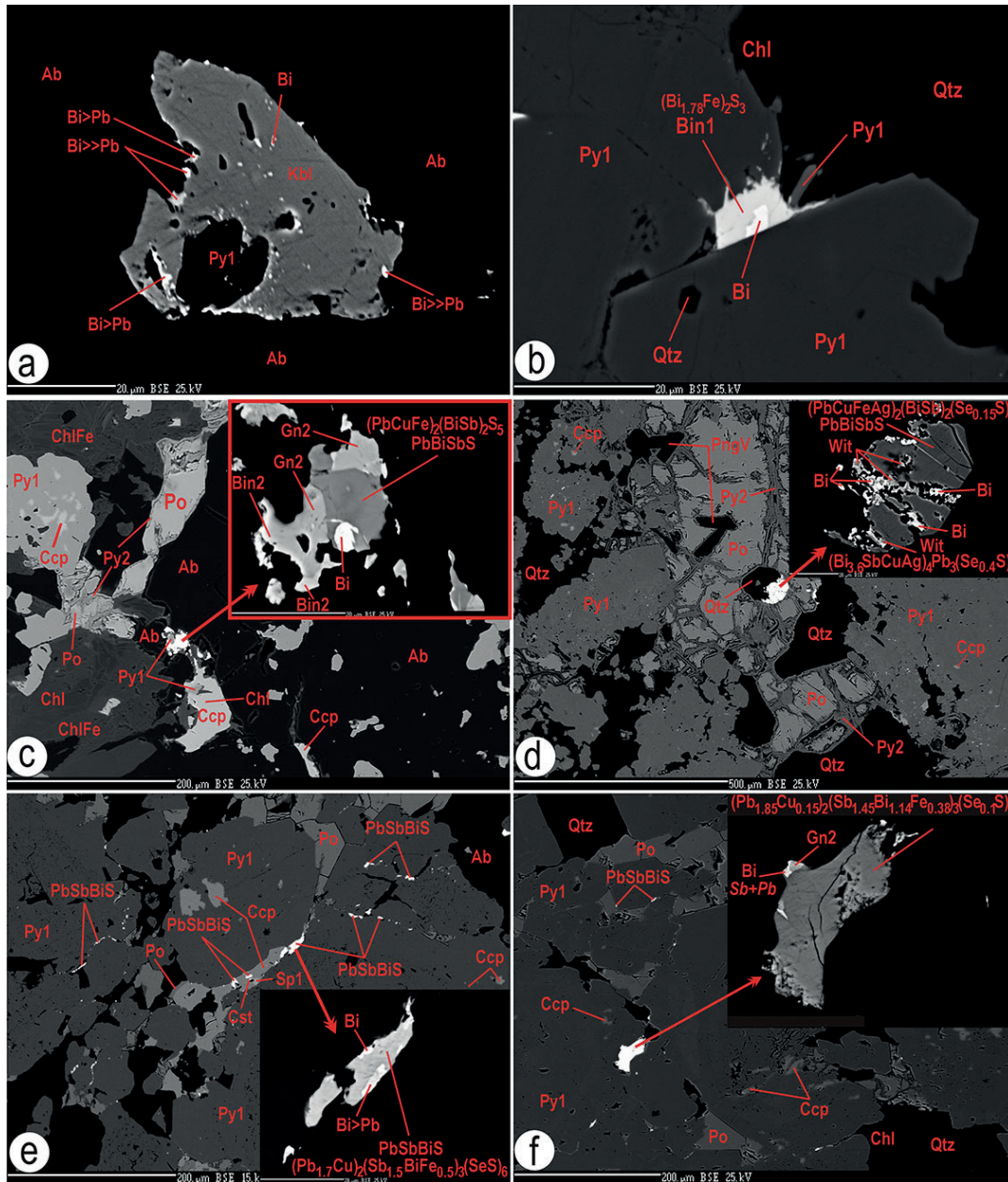
**Fig. 19.** The PbBiSb-rich and PbSbBi-rich sufides, bismuthinite, galena 2 and native Bi relationships in the Bystrý potok locality. ***a*** – Kobellite (Kbl) contains a number of native Bi (Bi) inclusions, and its rim was decomposed by oxidation in the chlorite-apatite zone into a mixture of native Bi-Pb-rich phase (Bi > Pb) with varying residual sulphur content. Kobellite was formed by the SedEx process together with pyrite 1 (Py1) in the albite (Ab) matrix. ***b*** – Bi bearing aggregate composed of bismuthinite 1 (Bin1) and native Bi in the pyrite 1, are regarded to be the SedEx mineral assemblage. ***c*** – Bi-rich sulfide aggregate in albite and the accompanying SedEx mineralization of the matrix consisting of chlorite (Chl), Fe-rich chlorite (FeChl), pyrite 1 with chalcopyrite (Ccp) inclusions. The pyrrhotite (Po) is replaced by pyrite 2 (Py2). The detail shows a composition of the aggregate, where the PbBiSb-rich sulfide with native Bi inclusions is replaced by selenium-rich galena 2 (Gn2) and bismuthinite 2 (Bin2) formed in the chlorite-apatite zone. ***d*** – The Bi-rich aggregate formed by the SedEx process closes the pyrrhotite. The matrix consists of pyrite 1 with chalcopyrite inclusions. In the pyrrhotite the V-rich mica (PngV) and quartz (Qtz) was formed and the rim of the pyrrhotite that is replaced by pyrite 2. The detail shows the decomposition of PbBiSb-rich sulfide (PbBiSbS) by chlorite-apatite zone into a mixture of wittite (Wit) and native Bi. ***e*** – Occurrence of chalcopyrite, cassiterite (Cst), sphalerite 1 (Sp1) pyrrhotite, albite and pyrite 1, where cracks in pyrite 1 are filled by new PbSbBi-rich sulfide (PbSbBiS). The detail shows the composition of the PbSbBi-rich sulfide, which is replaced by the native Bi at the rim and also by a mixture of BiPb-rich native phase (Bi > Pb) with different residual sulphur content. ***f*** – In crack of pyrite 1 the new PbSbBi-rich sulfide is accompanied by galena 2 and native Bi containing Pb and Sb (Sb + Pb). BSE images of mineral assemblages.

147

rite zone in the Permian regional metamorphism of the paleo-Gemeric unit (Grecula et al., 2009, 2011; Radvanec & Gonda, 2019, 2020). These facies and zones produced a fluid phase that contained and transported $CO_2$, $O_2$, $H_2S$, $H_2O$, HF, $BO_3$, HCl, $H_3PO_4$, K, Na, Ca, Al, Si, Fe, Mg, Mn, Sn, F, V, REE, U, Ti, Y, Cu, Sb, Te, Bi, Ag, Zn, In, Ta, Nb,

Pb, Ni, Co and As into the structures, where, depending on where these structures originated, different mineralization has formed, ranging from high-temperature greisen and skarns in the amphibolite or in epidote-amphibolite facies to low-temperature veins in the chlorite zone (Radvanec & Gonda, 2019, 2020). The heat source for the Permian metamorphism and related mineralization was provided by the Variscan subduction zone, which created two hot lines in the upper crust of the Paleo-Gemeric unit. Anatectic melting of the upper crust and the formation of S-type granites with accompanying cassiterite mineralization in greisens and Mn skarns occurred in the amphibolite facies on these hot lines (Radvanec & Gonda, 2019, 2020). In addition to the formation of the S-type anatectic granite from melting of the upper crust in the amphibolite facies above the hot lines, this anatectic melting also gave rise to interconnected andesite-rhyolite volcanism on the surface. The andesite-rhyolite volcanism has the island-arc geochemical characteristics and occurs in a belt arrangement in the northern part of Gemeric unit. Andesite has the characteristics of upper crust and rhyolite characteristics of the mantle (Radvanec & Gonda, 2019). Basalts form separate outflows and occur outside the Gemeric unit (Vozárová & Vozár, 1988). The formation of S-type granitic melt together with the formation of magmatic chambers of Permian calc-alkaline / K-calc-alkaline volcanism (andesite, rhyolite,
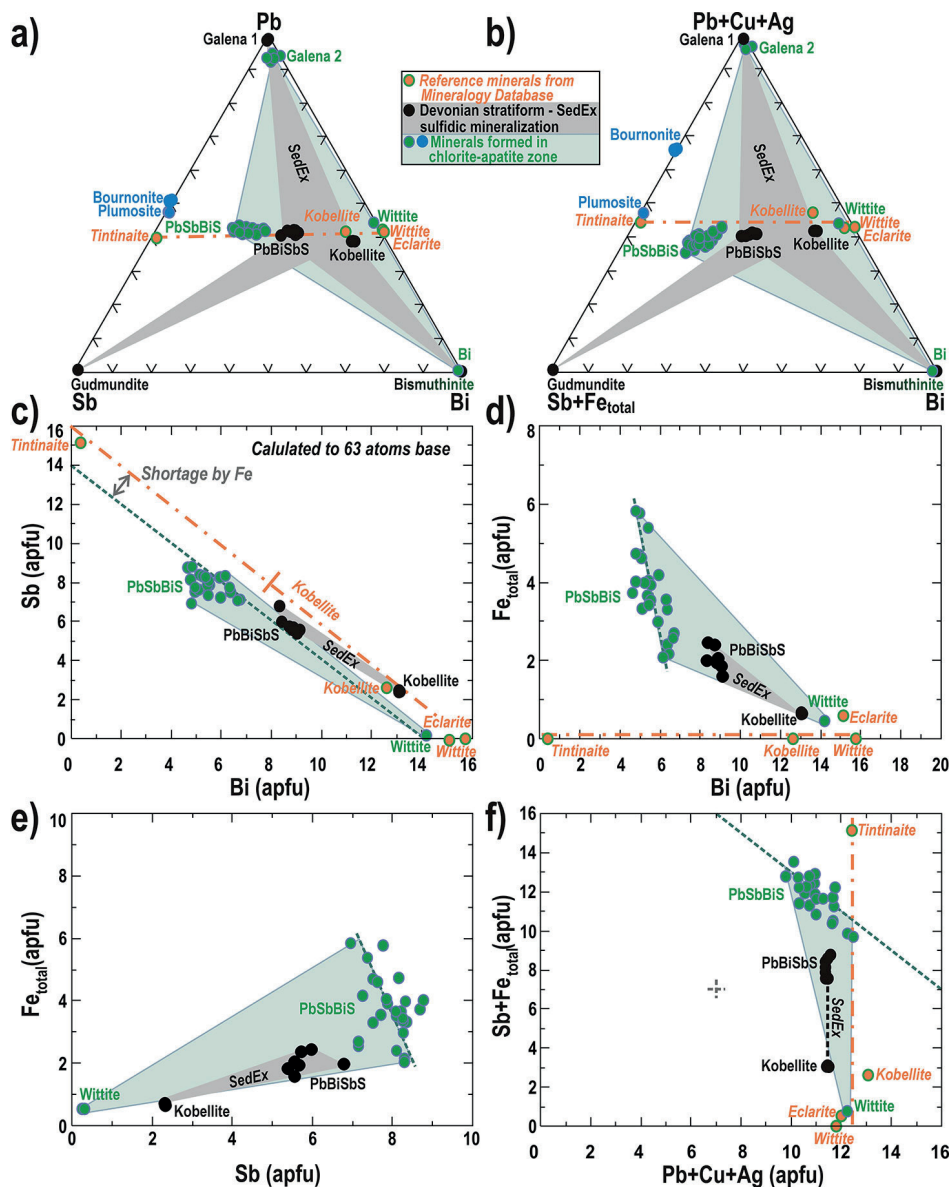


Fig. 20. Chemical classification of stratiform PbBiSb-rich sulfides formed by the SedEx process in the Late Silurian–Early Devonian and their comparison with the new PbSbBi-rich sulfides formed by the chlorite-apatite zone in the diagrams. *a* – Composition of sulfides formed by SedEx in the Sb-Bi-Pb system and their comparison to the new sulfides generation show a rough approximation of Pb-Bi-Sb and Pb-Sb-Bi-rich sulfides from the wittite/eclarite end member to tintinaite in the triangle diagram. *b* – The triangle diagram Sb + Fe$_{total}$ – Bi – Pb + Cu + Ag shows a more accurate sulfides classification of both generations and shows the effect of FeSbS molecule in PbSbBi-rich sulfides being formed in the chlorite-apatite zone. *c* – Substitution of Bi versus Sb, with the exception of kobellite, shows a shortage in the new sulfides of chlorite-apatite zone studied when compared them with ideal Bi and Sb contents of the end-members betwen the wittite/eclarite to tintinaite. *d* – Bi versus Fe$_{total}$ shows trends in the correlation beyond the wittite/eclarite – tintinaite end-members and demonstrates the relationship between sulfides formed by the SedEx process and new sulfides formed in the chlorite-apatite zone. *e* – Relationship of the two sulfide generations in the Fe$_{total}$ versus Sb diagram with their correlation trends. *f* – The sum of Pb + Cu + Ag contents versus Sb + Fe$_{total}$ shows the constant distribution of Pb + Cu + Ag contents in sulfides formed by the SedEx process in contrast to PbSbBi-rich sulfides where the sum of Pb + Cu + Ag substituted the sum of Sb + Fe$_{Total}$.
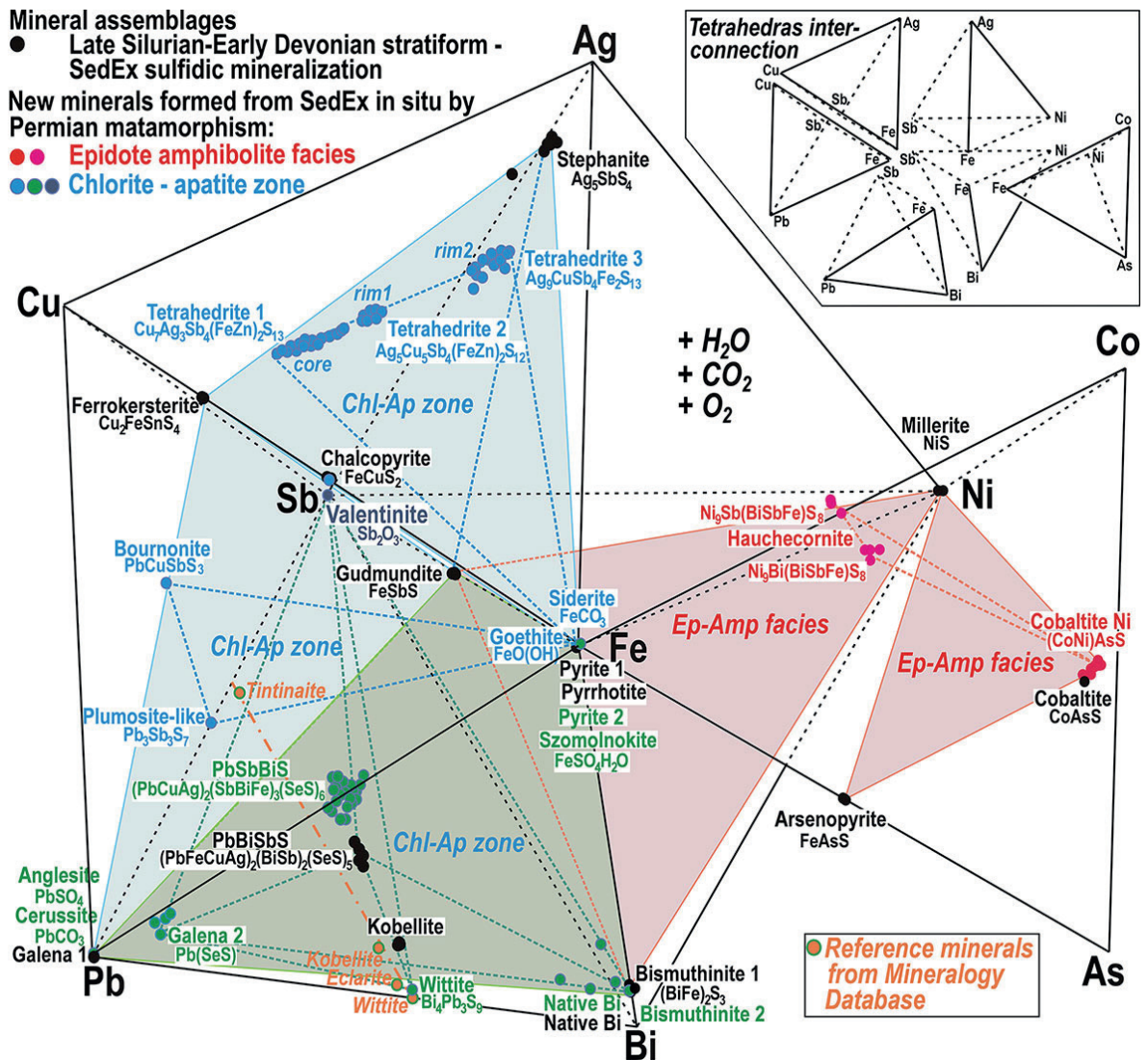
**Fig. 21.** Projections of mineral chemical formulas in the individual tetrahedral phase diagrams linked in the CuAgSbFePbBiAsCoNi system show a relationship between the source Late Silurian-Early Devonian stratiform SedEx sulfidic mineralization and new mineral assemblages formed in Permian epidote-amphibolite facies and related Permian chlorite-apatite zone including the reaction planes.

dacite) in the island arc magmatism caused the bulging of the upper crust above the hot line, which is considered by some authors to be a manifestation of extension related to the Permian rift (Vozárová et al., 2009, 2009a, 2012, 2013, 2015).

### Acknowledgements

### References

BARTALSKÝ, J., ILAVSKÝ, J., BARTALSKÝ, B., ČIŠKO, V., GRECULA, P., HOCK, M., KELLNER, M., KLADIVÍK, E., MAGULA, R., NÁVESŇÁK, D., POPREŇÁK, J., RADVANEC, M., SZABÓ, R. & ŽIFČÁK, F., 1993: Smolník – mesto medenorudných baní. Geológia ložiska polymetalických rúd, ich využitie a vplyv na mesto a okolie. *Bratislava, Miner. Slov., ISBN 80-967010-0-0.*

BIAGIONI, C., GEORGE L. L., COOK, N. J., MAKOVICKY, E., MOËLO, Y., PASERO, M., SEJKORA, J., STANLEY, C. J., MARK, D., WELCH, M. D. & BOSI, F., 2020: The tetrahedrite group: Nomenclature and classification. *Amer. Mineralogist, 105, 109–122.*

BUERGER, M. J., 1939: The crystal structure of gudmundite (FeSbS) and its bearing on the existence field of the arsenopyrite structural type. *Z. Kristallogr. Crystall. Mater., 101, 1–6, 290–316.*

FARYAD, S. W. & PETEREC, D., 1987: Manifestations of skarn mineralization in the eastern part of the Spišsko-gemerské rudohorie Mts. *Geol. Carpath., 38, 111–128.*

FLEET, M. E., 2003: Sheet silicates: Micas, Rock forming minerals. *Volume 3A Sec. ed.*

GRECULA, P., 1982: Gemericum – segment of the Paleotethyan riftogenous basin. *Bratislava, Miner. Slov – Monogr., Alfa, 1–263.*

GRECULA, P., ABONYI, A., ABONYIOVÁ, M., ANTAŠ, J., BARTALSKÝ, B., BARTALSKÝ, J., DIANIŠKA, I., DRNZÍK, E., ĎUĎA, R., GARGULÁK, M., GAZDAČKO, Ľ., HUDÁČEK, J., KOBULSKÝ, J., LÖRINCZ, L., MACKO, J., NÁVESŇÁK, D., NÉMETH, Z., NOVOTNÝ, L., RADVANEC, M., ROJKOVIČ, L., ROZLOŽNÍK, O., VARČEK, C. & ZLOCHA, J., 1995: Mineral deposit of the Slovak Ore Mountains. Vol. 1. *Bratislava, Miner. Slov. – Monogr., 1–834.*

GRECULA, P. (ed.), KOBULSKÝ, J., GAZDAČKO, Ľ., NÉMETH, Z., HRAŠKO, Ľ., NOVOTNÝ, L. & MAGLAY, J., 2009: Geologická mapa Spišsko-gemerského rudohoria 1 : 50 000. *Bratislava, Ministerstvo život. prostr. Slovenskej republiky – Št. Geol. Úst. D. Štúra.*

GRECULA, P., KOBULSKÝ, J., GAZDAČKO, Ľ., NÉMETH, Z., HRAŠKO, Ľ., NOVOTNÝ, L., MAGLAY, J., PRAMUKA, S., RADVANEC, M., KUCHARIČ, Ľ., BAJTOŠ, P. & ZÁHOROVÁ, Ľ., 2011: Vysvetlivky ku geologickej mape Spišsko-gemerského rudohoria 1 : 50 000. *Bratislava, Št. Geol. Úst. D. Štúra (in Slovak).*

ILAVSKÝ, J., 1961: Výhľadová štúdia o Cu rudách do roku 1980. Centrálna časť gemeríd. Kýzové a impregnačné polymetalické typy zrudnení. *Manuscript. Bratislava, archive St. Geol. Inst. D. Štúr.*

KANTOR, J. & FUSÁN, O., 1952: Pyritové ložisko v Bystrom potoku. *Manuscript. Bratislava, archive St. Geol. Inst. D. Štúr (3495).*

KISSIN, S. A. & OVENS, D. R., 1986: The crystallography of sakuraiite. *Canad. Mineralogist, 24, 679–683.*

KOHÚT, M. & STEIN, H., 2005: Re-Os molybdenite dating of granite-related Sn-W-Mo mineralization at Hnilec, Gemeric Superunit, Slovakia. *Mineral. Petrol., 85, 117–129.*

MORAD, V. J., 1990: High chromium and vanadium in andalusite, phengite and retrogressive margarite in contact metamorphosed Ba-rich slate from the Abercrombie Beds, New South Wales, Austria. *Min. Mag., 54, 381–391.*

NAVESŇÁK, D., 1994: Izotopické zloženie olova galenitov Spišsko-gemerského rudohoria a interpretácia. *Manuscript. Bratislava, archive St. Geol. Inst. D. Štúr.*

NAKAMURA, Y. & SHIMA, H., 1982: Fe and Zn partitioning between sphalerite and stannite. In: Proceedings of the Joint Meeting of Society of Mining Geologists of Japan; The Japanese Association of Mineralogists, Petrologists and Economic Geologists and the Mineralogical Society of Japan, *Sendai, Japan* (in Japanese).

NÉMETH, Z., 2021: Lithotectonic units of the Western Carpathians: Suggestion of simple methodology for lithotectonic units defining, applicable for orogenic belts world-wide. *Miner. Slov., 53, 2, 81–91.*

RADVANEC, M., PIOVARCSY, K. & BÖHMOVÁ, I., 1988: Vzťah slovinskej Hrubej, Gelnickej a Krížovej žily v slovinsko-gelnickom rudnom poli. *Miner. Slov.,20, 239–248.*

RADVANEC, M., ŽÁK, K. & GRECULA, P., 1990: Izotopický pomer ⁸⁷Sr/ ⁸⁶Sr v baryte gemerika. *Miner. Slov.,22, 219–224.*

RADVANEC, M., GRECULA, P., NÁVESŇÁK, D. & KOBULSKÝ, J., 1993: Zonálnosť submarinno-exhalačnej mineralizácie v oblasti Mníška nad Hnilcom a Prakoviec, staršie paleozoikum gemerika. *Miner. Slov., 25, 249–262.*

RADVANEC, M., GRECULA, P. & ŽÁK, K., 2004: Siderite mineralization of the Gemericum superunit (Western Carpathians, Slovakia): review and revised genetic model. *Ore. Geol. Rev., 24, 3–4, 267–298.*

RADVANEC, M., KONEČNÝ, P., NÉMETH, Z. & GRECULA, P., 2007: P-T-t path and local anatectic melting of the Lower Paleozoic metapelite with the admixture of psammitic quartz in Variscan metamorphism in Gemericum. *Miner. Slov. 39, 1–44* (in Slovak with English resume).

RADVANEC, M., KONEČNÝ, P., ONDREJKA, M., PUTIŠ, M., UHER, P. & NÉMETH, Z., 2009: Granity gemerika ako indikátor extenzie kôry nad neskorovariskou subdukčnou zónou a pri ranoalpínskej riftogenéze (Západné Karpaty): interpretácia podľa veku monazitu a zirkónu datovaného metódou CHIME a SHRIMP. *Miner. Slov., 41, 381–394.*

RADVANEC, M., NÉMETH, Z. & BAJTOŠ, P. (eds.), KODĚRA, P., PROCHASKA, W., RODA, Š., TRÉGER, M., BALÁŽ, P., GRECULA, P., CICMANOVÁ, S., KRÁĽ, J. & ŽÁK, K., 2010: Magnesite and Talc in Slovakia – Genetic and Geoenvironmental Models. *Bratislava, Št. Geol. Úst. D. Štúra, 189 p. ISBN 978-80-89343-31-7.*

RADVANEC, M. & GRECULA, P., 2016: Geotectonic and metallogenetic evolution of Gemericum (Inner Western Carpathians) from Ordovician to Jurassic. *Miner. Slov., 48, 104–118.*

RADVANEC, M., NÉMETH. Z., KRÁĽ, J. & PRAMUKA, S., 2017: Variscan dismembered metaophiolite suite fragments of Paleo-Thetys in Gemeric unit, Western Carpathians. *Miner. Slov., 49, 1–48.*

RADVANEC, M. & GONDA, S., 2019: Genetic model of Permian hydrothermal mineralization in Gemeric unit (Western Carpathians) from the deep-seated zone of anatectic melting to volcanic-exhalative SedEx mineralization on the surface. *Miner. Slov., 52, 109–156.*

RADVANEC, M. & GONDA, S., 2020: Successive formation of Fe and Mn skarns in the Čučma locality (Gemeric unit, W. Carpathians): from metasomatic stage through the amphibolite facies overprint with Ti-rich tephroite to retrograde stilpnomelane-chlorite zone. *Miner. Slov., 52, 2, 103–132.*

RAVNA, K., 2000: The garnet-clinopyroxene $Fe^{2+}$-Mg geothermometer: an updated calibration. *J. Metamorp. Geol., 18, 2, 211–219,* doi:10.1046/j.1525-1314.2000.00247.x.

SPEAR, F. S., 1995: Metamorphic Phase Equilibria and Pressure-Temperature-Time Paths. Monogr. *Mineral. Soc. Amer.*

SMOLÁRIK, M. & NÉMETH, Z., 2015: Talc genesis related on tectonometamorphic evolution: Preliminary results from the Gemerská Poloma deposit (Gemericum, Western Carpathians). Mineralogicko-petrologická konferencia Petros 20105. Zborník recenzovaných abstratkov a príspevkov. *Bratislava, Univ. Komenského, Prírodoved. fakulta, 54–57.*

ŠTEVKO, M. & SEJKORA, J., 2021: Bismuth, lead-bismuth and lead-antimony sulfosalts from the granite-hosted hydrothermal quartz veins at the Elisabeth mine, Gemerská Poloma, Spišsko-gemerské rudohorie Mts., Slovakia. *J. Geosci., 66, 157–173.*

VOZÁROVÁ, A. & VOZÁR, J., 1988: Late Paleozoic in West Carpathians. *Bratislava, Geol. Úst. D. Štúra, 1–314.*

VOZÁROVÁ, A., ŠMELKO, M. & PADERIN, I., 2009: Permian single crystal U-Pb zircon ages of the Rožňava Formation volcanites (Southern Gemeric Unit, Western Carpathians, Slovakia). *Geol. Carpath., 60, 6, 439–448.*

VOZÁROVÁ, A., EBNER, F., KOVÁCS, S., KRÄUTNER, H.-G., SZEDERKENYI, T., KRSTIĆ, B., SREMAC, J., ALJINOVIĆ, D., NOVAK, M. & SKABERNE, D., 2009a: Late Variscan (Carboniferous to Permian) environments in the Circum Pannonian Region. *Geol. Carpath., 60, 71–104.*

Vozárová, A., Šmelko, M., Paderin, I. & Larionov, A., 2012: Permian volcanics in Northern Gemericum and Bôrka Nappe system: U-Pb zircon dating and implication to geodynamic evolution (Western Carpathians, Slovakia). *Geol. Carpath., 63, 191–200.*

Vozárová, A., Laurinc, D., Šarinová, K., Larionov, A., Presnyakov, S., Rodionov, N. & Paderin, I., 2013: Pb ages of detrital zircons in relation to geodynamic evolution: Paleozoic of the Northern Gemericum (Western Carpathians, Slovakia). *J. Sed. Res., 83, 915–927.*

Vozárová, A., Presnyakov, S., Šarinová, K. & Šmelko, M., 2015: First evidence for Permian-Triassic boundary volcanism in the Northern Gemericum: geochemistry and U-Pb zircon geochronology. *Geol. Carpath., 66, 5, 375–391.*

Žák, K., Radvanec, M. & Grecula, P., 2005: Siderite mineralization of the Gemericum Superunit (Western Carpathians, Slovakia): review and a revised genetic model [Ore Geology Reviews, 24, 267–298] – a reply. *Ore Geol. Rev., 26, 173–180.*

**Tab. 1**
Representative analyses of millerite, cobaltite and hauchecornite.

| Mineral | Millerite | Cobaltite 1 | Cobaltite 2 | Cobaltite 2 | Cobaltite 2 | Hauchecornite | Hauchecornite-(Sb) | Hauchecornite-(Sb) |
|---|---|---|---|---|---|---|---|---|
| Enriched | | | Ni | Ni | Ni | Bi | Bi. Sb | Sb |
| Process | SedEx | SedEx | Ep-Amp | Ep-Amp | Ep-Amp | Ep-Amp | Ep-Amp | Ep-Amp |
| S | 35.65 | 20.26 | 19.87 | 20.42 | 20.24 | 22.62 | 24.35 | 25.60 |
| Fe | 0.67 | 1.67 | 1.50 | 2.64 | 1.51 | 1.42 | 1.13 | 2.12 |
| Co | 0.29 | 32.73 | 25.78 | 27.49 | 32.49 | 1.97 | 2.96 | 2.89 |
| Ni | 64.18 | 0.98 | 7.81 | 4.94 | 3.09 | 44.62 | 46.92 | 47.65 |
| Cu | 0.09 | 0.00 | 0.01 | 0.02 | 0.00 | 0.03 | 0.08 | 0.06 |
| Sb | 0.00 | 0.36 | 0.25 | 0.74 | 0.53 | 5.06 | 16.72 | 20.41 |
| As | 0.02 | 42.87 | 43.85 | 42.07 | 42.79 | 0.00 | 0.00 | 0.05 |
| Pb | 0.10 | 0.06 | 0.01 | 1.48 | 0.00 | 0.22 | 0.34 | 0.34 |
| Se | 0.00 | 0.00 | 0.00 | 0.00 | 0.00 | 0.07 | 0.00 | 0.01 |
| Bi | 0.00 | 0.03 | 0.01 | 0.02 | 0.04 | 24.94 | 8.27 | 1.55 |
| Total (wt %) | 101.00 | 98.96 | 99.09 | 99.82 | 100.69 | 100.95 | 100.77 | 100.68 |
| S | 1.000 | 1.047 | 1.030 | 1.055 | 1.030 | 7.940 | 7.975 | 8.086 |
| Se | 0.000 | 0.000 | 0.000 | 0.000 | 0.000 | 0.010 | 0.000 | 0.001 |
| *X group* | *1.000* | *1.047* | *1.030* | *1.055* | *1.030* | *7.950* | *7.975* | *8.087* |
| Cu | 0.001 | 0.000 | 0.000 | 0.001 | 0.000 | 0.005 | 0.013 | 0.010 |
| Co | 0.004 | 0.921 | 0.727 | 0.773 | 0.900 | 0.376 | 0.528 | 0.497 |
| Ni | 0.983 | 0.028 | 0.221 | 0.140 | 0.086 | 8.559 | 8.397 | 8.225 |
| Pb | 0.000 | 0.000 | 0.000 | 0.012 | 0.000 | 0.012 | 0.017 | 0.017 |
| $Fe^{2+}$ | 0.011 | 0.050 | 0.045 | 0.078 | 0.044 | 0.048 | 0.045 | 0.251 |
| *A group* | *0.999* | *0.999* | *0.993* | *1.004* | *1.030* | *9.000* | *9.000* | *9.000* |
| Sb | 0.000 | 0.005 | 0.003 | 0.010 | 0.007 | 0.468 | 1.442 | 1.698 |
| As | 0.000 | 0.949 | 0.973 | 0.931 | 0.932 | 0.000 | 0.000 | 0.007 |
| Bi | 0.000 | 0.000 | 0.000 | 0.000 | 0.000 | 1.343 | 0.416 | 0.075 |
| $Fe^{3+}$ | 0.000 | 0.000 | 0.000 | 0.000 | 0.000 | 0.238 | 0.168 | 0.134 |
| *B group* | *0.000* | *0.954* | *0.976* | *0.941* | *0.939* | *2.049* | *2.026* | *1.914* |
| Sum (atom.) | 1.999 | 3.000 | 2.999 | 3.000 | 2.999 | 18.999 | 19.001 | 19.001 |
| Fe (Sum) | 0.011 | 0.05 | 0.045 | 0.078 | 0.044 | 0.286 | 0.213 | 0.385 |

**Tab. 2**
Representative analyses of garnet pyroxene (hedenbergite), epidote, actinolite, chlorite, titanite and apatite in the skarn.

| Mineral | Garnet | Pyroxene | Pyroxene | Epidote | Actinolite | Chlorite | Titanite-F | Apatite-F |
|---|---|---|---|---|---|---|---|---|
| Rock | Skarn | Skarn | Skarn | Skarn | Skarn | Skarn | Skarn | Skarn |
| Process | Ep-Amp.f. | Ep-Amp.f. | Ep-Amp.f. | Ep-Amp.f. | Ep-Amp.f. | Ep-Amp.f. | Chl-Ap | Chl-Ap |
| $SiO_2$ | 37.85 | 50.77 | 49.21 | 38.02 | 52.35 | 31.96 | 31.32 | 0.00 |
| $TiO_2$ | 0.33 | 0.07 | 0.04 | 0.04 | 0.02 | 0.00 | 33.44 | 0.00 |
| $Al_2O_3$ | 20.71 | 0.29 | 0.53 | 24.92 | 1.28 | 9.31 | 4.46 | 0.00 |
| $Cr_2O_3$ | 0.01 | 0.00 | 0.00 | 0.01 | 0.00 | 0.00 | 0.00 | 0.00 |
| $Fe_2O_3$ | 0.00 | 0.00 | 0.00 | 11.58 | 0.00 | 0.00 | 0.00 | 0.00 |
| FeO | 8.85 | 18.22 | 16.42 | 0.00 | 21.84 | 31.83 | 1.36 | 0.01 |
| MnO | 13.02 | 3.55 | 6.02 | 0.34 | 1.51 | 0.74 | 0.03 | 0.04 |
| MgO | 0.03 | 4.95 | 4.32 | 0.00 | 8.99 | 12.98 | 0.03 | 0.01 |
| CaO | 19.28 | 22.40 | 22.52 | 23.06 | 12.12 | 0.56 | 29.43 | 56.22 |
| SrO | 0.00 | 0.00 | 0.00 | 0.00 | 0.00 | 0.00 | 0.00 | 0.21 |
| $Na_2O$ | 0.00 | 0.26 | 0.11 | 0.00 | 0.22 | 0.03 | 0.04 | 0.00 |
| $K_2O$ | 0.00 | 0.00 | 0.00 | 0.00 | 0.11 | 0.03 | 0.00 | 0.00 |
| $P_2O_5$ | 0.00 | 0.00 | 0.00 | 0.00 | 0.00 | 0.00 | 0.00 | 41.37 |
| F | 0.24 | 0.00 | 0.00 | 0.00 | 0.00 | 0.03 | 1.31 | 4.47 |
| Cl | 0.01 | 0.00 | 0.00 | 0.00 | 0.01 | 0.00 | 0.02 | 0.01 |
| Total | 100.32 | 100.51 | 99.17 | 97.97 | 98.45 | 87.47 | 100.82 | 100.46 |
| Si | 2.980 | 2.004 | 1.979 | 3.003 | 7.834 | 7.012 | 1.019 | 0.000 |
| $Al^{IV}$ | 0.020 | 0.000 | 0.021 | 0.000 | 0.166 | 0.988 | 0.000 | 0.000 |
| Sum_T | 3.000 | 2.004 | 2.000 | 3.003 | 8.000 | 8.000 | 1.019 | 0.000 |
| $Al^{VI}$ | 1.899 | 0.013 | 0.004 | 2.318 | 0.060 | 1.417 | 0.171 | 0.000 |
| $Fe^{3+}$ | 0.000 | 0.000 | 0.023 | 0.688 | 0.144 | 0.000 | 0.000 | 0.000 |
| Ti | 0.020 | 0.002 | 0.001 | 0.002 | 0.002 | 0.000 | 0.819 | 0.000 |
| Cr | 0.001 | 0.000 | 0.000 | 0.001 | 0.000 | 0.000 | 0.000 | 0.000 |
| $Fe^{2+}$ | 0.583 | 0.601 | 0.529 | 0.000 | 2.590 | 5.840 | 0.037 | 0.001 |
| Mg | 0.004 | 0.291 | 0.259 | 0.000 | 2.006 | 4.245 | 0.002 | 0.001 |
| Mn | 0.868 | 0.119 | 0.205 | 0.023 | 0.191 | 0.138 | 0.001 | 0.003 |
| Ca | 1.626 | 0.947 | 0.970 | 1.952 | 1.943 | 0.132 | 1.026 | 5.088 |
| Sr | 0.000 | 0.000 | 0.000 | 0.000 | 0.000 | 0.000 | 0.000 | 0.01 |
| Na | 0.000 | 0.020 | 0.009 | 0.000 | 0.064 | 0.013 | 0.003 | 0.000 |
| K | 0.000 | 0.000 | 0.000 | 0.000 | 0.021 | 0.008 | 0.000 | 0.000 |
| P | 0.000 | 0.000 | 0.000 | 0.000 | 0.000 | 0.000 | 0.000 | 2.959 |
| Sum | 8.000 | 4.000 | 4.000 | 7.987 | 15.021 | 19.793 | 3.078 | 8.062 |
| O | 12 | 6 | 6 | 13 | 23 | 36 | 5 | 13 |
| O-F-Cl | 0.00 | 0.00 | 0.00 | 0.00 | 0.00 | 0.00 | 0.56 | 1.88 |

**Tab. 3**
Representative analyses of pyrite generations, chalcopyrite, arsenopyrite, galena, stephanite and gudmundite.

| Mineral | Pyrite 1 | Pyrite 1 | Pyrrhotite | Chalcopyrite | Arsenopyrite | Gudmundite | Galena 1 | Stephanite | Pyrite 2 |
|---|---|---|---|---|---|---|---|---|---|
| Process | SedEx | SedEx | SedEx | SedEx | SedEx | Sedex | SedEx | SedEx | Chl-Ap |
| S | 52.88 | 52.77 | 38.83 | 34.81 | 19.98 | 15.65 | 13.63 | 15.93 | 53.82 |
| Cd | 0.00 | 0.00 | 0.00 | 0.00 | 0.00 | 0.01 | 0.00 | 0.00 | 0.00 |
| Ag | 0.02 | 0.07 | 0.04 | 0.05 | 0.00 | 0.03 | 0.05 | 66.72 | 0.00 |
| Zn | 0.00 | 0.00 | 0.00 | 0.05 | 0.18 | 0.04 | 0.44 | 0.02 | 0.00 |
| Fe | 47.14 | 46.80 | 60.07 | 30.65 | 34.50 | 26.68 | 0.00 | 0.08 | 45.58 |
| Co | 0.00 | 0.13 | 0.00 | 0.00 | 0.00 | 0.00 | 0.00 | 0.00 | 0.00 |
| Au | 0.00 | 0.12 | 0.13 | 0.00 | 0.00 | 0.00 | 0.00 | 0.00 | 0.00 |
| Cu | 0.04 | 0.00 | 0.00 | 33.84 | 0.00 | 0.10 | 0.00 | 0.16 | 0.00 |
| In | 0.00 | 0.00 | 0.00 | 0.16 | 0.00 | 0.00 | 0.00 | 0.12 | 0.00 |
| Sn | 0.00 | 0.00 | 0.00 | 0.06 | 0.00 | 0.00 | 0.00 | 0.00 | 0.00 |
| Sb | 0.07 | 0.05 | 0.00 | 0.00 | 0.00 | 57.83 | 0.17 | 15.47 | 0.00 |
| As | 0.05 | 0.08 | 0.09 | 0.04 | 44.43 | 0.00 | 0.00 | 0.00 | 0.00 |
| Pb | 0.00 | 0.00 | 0.00 | 0.00 | 0.00 | 0.09 | 85.22 | 0.67 | 0.00 |
| Bi | 0.05 | 0.00 | 0.14 | 0.00 | 0.00 | 0.08 | 0.25 | 0.04 | 0.00 |
| Total (wt %) | 100.25 | 100.02 | 99.30 | 99.66 | 99.09 | 100.51 | 99.76 | 99.21 | 99.4 |
| S | 1.982 | 1.984 | 1.058 | 2.000 | 1.018 | 1.014 | 1.005 | 3.970 | 2.018 |
| Cd | 0.000 | 0.000 | 0.000 | 0.000 | 0.000 | 0.000 | 0.000 | 0.000 | 0.00 |
| Ag | 0.000 | 0.001 | 0.000 | 0.001 | 0.000 | 0.001 | 0.001 | 4.944 | 0.00 |
| Sn | 0.000 | 0.000 | 0.000 | 0.001 | 0.000 | 0.000 | 0.000 | 0.000 | 0.00 |
| Cu | 0.001 | 0.000 | 0.000 | 0.981 | 0.000 | 0.003 | 0.000 | 0.020 | 0.00 |
| Zn | 0.000 | 0.000 | 0.000 | 0.001 | 0.004 | 0.001 | 0.016 | 0.002 | 0.00 |
| Fe | 1.015 | 1.010 | 0.940 | 1.011 | *1.009 | *0.992 | 0.000 | 0.011 | 0.982 |
| In | 0.000 | 0.000 | 0.000 | 0.003 | 0.000 | 0.000 | 0.000 | 0.008 | 0.00 |
| Sb | 0.001 | 0.000 | 0.000 | 0.000 | 0.000 | 0.987 | 0.003 | 1.016 | 0.00 |
| As | SedEx | 0.001 | SedEx | 0.001 | 0.969 | 0.000 | SedEx | 0.000 | Chl-Ap |
| Pb | 0.000 | 0.000 | 0.000 | 0.000 | 0.000 | 0.001 | 0.972 | 0.026 | 0.00 |
| Bi | 0.000 | 0.000 | 0.001 | 0.000 | 0.000 | 0.001 | 0.003 | 0.002 | 0.00 |
| Co | 0.000 | 0.003 | 0.000 | 0.000 | 0.000 | 0.000 | 0.000 | 0.000 | 0.00 |
| Au | 0.000 | 0.001 | 0.001 | 0.000 | 0.000 | 0.000 | 0.000 | 0.000 | 0.00 |
| Sum (atom.) | 3 | 3 | 2 | 4 | 3 | 3 | 2 | 10 | 3 |
| Fe/S | 0.51 | 0.51 | | | | | | | 0.49 |

(*) – $Fe^{3+}$

**Tab. 4**
Representative analyses of kobellite, PbBiSb-sulfide, bismuthinite, native Bi, wittite,
PbSbBi-sulfide and Se-rich galena.

| Mineral | Kobellite | Kobellite | PbBiSbS | PbBiSbS | PbBiSbS | Bismuthinite 1 | Bismuthinite 2 | native Bi 1 | Wittite | PbSbBiS | PbSbBiS | PbSbBiS | PbSbBiS | PbSbBiS | native Bi 2 | Galena 2 | Galena 2 |
|---|---|---|---|---|---|---|---|---|---|---|---|---|---|---|---|---|---|
| Enriched | | | Se | Se | Se | | | | Se | Fe. Se | Fe. Se | Fe. Se | Fe. Se | Fe. Se | | Se | Se |
| Process | SedEx | SedEx | SedEx | SedEx | SedEx | SedEx | Chl-Ap | Chl-Ap | Chl-Ap | Chl-Ap | Chl-Ap | Chl-Ap | Chl-Ap | Chl-Ap | Chl-Ap | Chl-Ap | Chl-Ap |
| S | 17.49 | 17.56 | 18.38 | 18.47 | 18.58 | 19.39 | 19.59 | 0.62 | 16.24 | 18.41 | 19.13 | 19.78 | 19.85 | 20.31 | 3.86 | 13.88 | 12.63 |
| Se | 0.13 | 0.15 | 0.68 | 0.72 | 0.58 | 0.18 | 0.00 | 0.00 | 1.87 | 0.73 | 1.00 | 0.94 | 0.77 | 0.73 | 0.04 | 1.13 | 3.41 |
| Te | 0.00 | 0 | 0.00 | 0.08 | 0.00 | 0.00 | 0.00 | 0.00 | 0.00 | 0.00 | 0.02 | 0.03 | 0.00 | 0.00 | 0.00 | 0.00 | 0.09 |
| Cd | 0.06 | 0.04 | 0.07 | 0.00 | 0.02 | 0.02 | 0.04 | 0.08 | 0.02 | 0.10 | 0.08 | 0.06 | 0.07 | 0.08 | 0.10 | 0.01 | 0.00 |
| Ag | 0.52 | 0.52 | 0.45 | 0.36 | 0.35 | 0.02 | 0.00 | 0.07 | 0.24 | 0.33 | 0.36 | 0.30 | 0.31 | 0.25 | 0.03 | 0.37 | 0.12 |
| Zn | 0.02 | 0.02 | 0.00 | 0.02 | 0.03 | 0.00 | 0.00 | 0.00 | 0.00 | 0.00 | 0.00 | 0.00 | 0.04 | 0.00 | 0.00 | 0.00 | 0.00 |
| Fe | 0.59 | 0.54 | 2.21 | 1.90 | 2.28 | 2.57 | 1.76 | 1.32 | 0.47 | 2.03 | 3.50 | 4.06 | 5.48 | 6.02 | 2.56 | 2.37 | 2.06 |
| Mn | 0.00 | 0 | 0.00 | 0.00 | 0.00 | 0.01 | 0.00 | 0.00 | 0.00 | 0.00 | 0.00 | 0.00 | 0.00 | 0.00 | 0.00 | 0.00 | 0.00 |
| Cu | 1.03 | 1.11 | 0.84 | 0.82 | 0.82 | 0.14 | 0.18 | 0.19 | 0.22 | 0.95 | 0.95 | 1.00 | 0.86 | 1.21 | 0.49 | 0.15 | 0.34 |
| In | 0.00 | 0 | 0.00 | 0.00 | 0.00 | 0.02 | 0.02 | 0.00 | 0.00 | 0.00 | 0.03 | 0.00 | 0.03 | 0.04 | 0.00 | 0.00 | 0.00 |
| Sn | 0.00 | 0 | 0.00 | 0.00 | 0.00 | 0.05 | 0.10 | 0.04 | 0.04 | 0.00 | 0.08 | 0.00 | 0.00 | 0.00 | 0.00 | 0.00 | 0.00 |
| Sb | 4.54 | 4.57 | 11.64 | 11.28 | 12.25 | 0.13 | 0.63 | 3.05 | 0.52 | 17.17 | 16.55 | 19.39 | 16.37 | 17.67 | 7.10 | 1.28 | 0.08 |
| Pb | 32.79 | 32.93 | 35.54 | 35.75 | 35.78 | 0.75 | 0.90 | 1.78 | 36.51 | 37.37 | 35.27 | 36.57 | 35.55 | 34.65 | 10.87 | 76.36 | 76.71 |
| Bi | 42.83 | 43.01 | 30.29 | 30.98 | 29.42 | 76.55 | 76.53 | 92.97 | 44.13 | 23.07 | 23.24 | 18.29 | 20.72 | 19.38 | 75.94 | 3.67 | 4.51 |
| Total (wt. %) | 100.00 | 100.45 | 100.10 | 100.37 | 100.11 | 99.84 | 99.79 | 100.14 | 100.27 | 100.16 | 100.22 | 100.41 | 100.05 | 100.33 | 101.00 | 99.22 | 99.95 |
| S | 69.567 | 69.533 | 4.906 | 4.939 | 4.927 | 2.943 | 2.986 | 0.037 | 8.652 | 5.900 | 5.915 | 5.931 | 5.921 | 5.915 | 0.185 | 0.970 | 0.902 |
| Se | 0.210 | 0.241 | 0.073 | 0.079 | 0.062 | 0.011 | 0.000 | 0.000 | 0.405 | 0.095 | 0.125 | 0.114 | 0.094 | 0.086 | 0.001 | 0.032 | 0.099 |
| Te | 0.000 | 0.000 | 0.000 | 0.005 | 0.000 | 0.000 | 0.000 | 0.000 | 0.000 | 0.000 | 0.002 | 0.002 | 0.000 | 0.000 | 0.000 | 0.000 | 0.002 |
| *group X* | 69.777 | 69.774 | 4.979 | 5.023 | 4.989 | 2.954 | 2.986 | – | 9.057 | 5.995 | 6.042 | 6.047 | 6.015 | 6.001 | – | 1.002 | 1.003 |
| Cd | 0.068 | 0.045 | 0.005 | 0.000 | 0.002 | 0.001 | 0.002 | 0.001 | 0.003 | 0.009 | 0.007 | 0.005 | 0.006 | 0.007 | 0.001 | 0.000 | 0.000 |
| Ag | 0.615 | 0.612 | 0.036 | 0.028 | 0.027 | 0.001 | 0.000 | 0.001 | 0.038 | 0.031 | 0.033 | 0.027 | 0.027 | 0.022 | 0.000 | 0.008 | 0.003 |
| Cu | 2.068 | 2.218 | 0.113 | 0.110 | 0.110 | 0.011 | 0.014 | 0.006 | 0.058 | 0.154 | 0.149 | 0.151 | 0.129 | 0.177 | 0.012 | 0.005 | 0.012 |
| Zn | 0.039 | 0.039 | 0.000 | 0.003 | 0.004 | 0.000 | 0.003 | 0.000 | 0.005 | 0.000 | 0.000 | 0.000 | 0.006 | 0.000 | 0.000 | 0.000 | 0.000 |
| Mn | 0.000 | 0 | 0.000 | 0.000 | 0.000 | 0.001 | 0.000 | 0.000 | 0.000 | 0.000 | 0.000 | 0.000 | 0.000 | 0.000 | 0.000 | 0.000 | 0.000 |
| In | 0.000 | 0 | 0.000 | 0.000 | 0.000 | 0.001 | 0.001 | 0.000 | 0.000 | 0.000 | 0.003 | 0.000 | 0.003 | 0.003 | 0.000 | 0.000 | 0.000 |
| Pb | 20.187 | 20.182 | 1.468 | 1.479 | 1.468 | 0.018 | 0.021 | 0.016 | 3.010 | 1.854 | 1.688 | 1.698 | 1.641 | 1.562 | 0.081 | 0.826 | 0.848 |
| $Fe^{2+}$ | 1.348 | 1.228 | 0.339 | 0.291 | 0.347 | 0.000 | 0.000 | 0.045 | 0.142 | 0.000 | 0.075 | 0.075 | 0.173 | 0.228 | 0.071 | 0.095 | 0.084 |
| *grupe A* | – | – | 1.961 | 1.911 | 1.958 | 0.033 | 0.041 | – | – | 2.048 | 1.955 | 1.956 | 1.985 | 1.999 | – | – | – |
| $Fe^{3+}$ | – | – | – | – | – | 0.224 | 0.154 | – | – | 0.374 | 0.547 | 0.624 | 0.766 | 0.778 | – | – | – |
| Sb | 4.757 | 4.767 | 0.819 | 0.794 | 0.855 | 0.005 | 0.025 | 0.048 | 0.073 | 1.449 | 1.348 | 1.532 | 1.286 | 1.356 | 0.090 | 0.024 | 0.002 |
| Sn | 0.000 | 0 | 0.000 | 0.000 | 0.000 | 0.002 | 0.004 | 0.001 | 0.006 | 0.000 | 0.007 | 0.000 | 0.000 | 0.000 | 0.000 | 0.000 | 0.000 |
| Bi | 26.143 | 26.135 | 1.241 | 1.271 | 1.197 | 1.782 | 1.790 | 0.845 | 3.607 | 1.135 | 1.103 | 0.842 | 0.948 | 0.866 | 0.559 | 0.039 | 0.049 |
| *grupe B* | – | – | 2.060 | 2.065 | 2.052 | 2.013 | 1.973 | – | – | 2.958 | 3.005 | 2.998 | 3.000 | 3.000 | – | – | – |
| Sum (atom.) | 125 | 125 | 9 | 9 | 9 | 5 | 5 | 1 | 16 | 11 | 11 | 11 | 11 | 11 | 1 | 2 | 2 |
| Fe sum-at. | 1.348 | 1.228 | 0.339 | 0.291 | 0.347 | 0.224 | 0.154 | 0.045 | 0.142 | 0.374 | 0.622 | 0.699 | 0.939 | 1.006 | | | |

The balance of $Fe^{2+}$ and $Fe^{3+}$ calculated according to element substitutions (Fig. 20) and according to chemical formulae divided into groups A. B. X

**Tab. 5**
Representative analyses of In-rich sphalerite 1, ferrokesterite and Sn-rich sakuraiite.

| Mineral | Sphalerite 1 | Sphalerite 1 | Sphalerite 1 | Sphalerite 1 | Fe-kesterite | Fe-kesterite | Fe-kesterite | Fe-kesterite | Fe-kesterite | Fe-kesterite | Sn sakuraiite | Sn sakuraiite | Sn sakuraiite | Sn sakuraiite | Sn sakuraiite | Sn sakuraiite | Sn sakuraiite | Sn sakuraiite |
|---|---|---|---|---|---|---|---|---|---|---|---|---|---|---|---|---|---|---|
| Enriched | | | | | Zn | Zn | In | In | In | In | In | In | Sn | Sn | In | In | In | In |
| Process | SedEx | SedEx | SedEx | SedEx | SedEx | SedEx | SedEx | SedEx | SedEx | SedEx | SedEx | SedEx | SedEx | SedEx | SedEx | SedEx | SedEx | SedEx |
| S | 34.01 | 32.74 | 32.78 | 31.84 | 30.01 | 29.45 | 30.03 | 29.41 | 29.99 | 29.96 | 29.36 | 30.19 | 30.12 | 32.30 | 29.82 | 30.46 | 30.11 | 31.41 |
| Cd | 0.26 | 0.39 | 0.49 | 0.00 | 0.03 | 0.00 | 0.03 | 0.00 | 0.00 | 0.00 | 0.00 | 0.03 | 0.00 | 0.13 | 0.03 | 0.04 | 0.00 | 0.00 |
| Ag | 0.04 | 0.01 | 0.01 | 0.04 | 0.02 | 0.03 | 0.05 | 0.00 | 0.00 | 0.12 | 0.09 | 0.12 | 0.05 | 0.05 | 0.04 | 0.06 | 0.07 | 0.08 |
| Zn | 57.64 | 55.12 | 49.87 | 46.21 | 3.86 | 7.26 | 4.03 | 2.05 | 6.66 | 3.61 | 3.46 | 9.28 | 9.17 | 40.62 | 11.61 | 14.53 | 15.63 | 30.17 |
| Fe | 6.67 | 7.19 | 7.85 | 6.94 | 12.11 | 11.90 | 12.11 | 12.71 | 13.35 | 13.05 | 13.56 | 12.08 | 11.55 | 8.21 | 12.01 | 11.55 | 11.76 | 10.04 |
| Mn | 0.01 | 0.00 | 0.02 | 0.00 | 0.04 | 0.00 | 0.00 | 0.00 | 0.00 | 0.00 | 0.00 | 0.00 | 0.00 | 0.01 | 0.00 | 0.01 | 0.00 | 0.00 |
| Cu | 0.33 | 1.46 | 2.95 | 4.98 | 28.59 | 26.18 | 27.53 | 27.60 | 25.85 | 26.61 | 26.10 | 24.23 | 24.98 | 9.51 | 23.25 | 21.54 | 20.33 | 12.78 |
| In | 0.63 | 2.82 | 5.63 | 8.78 | 0.00 | 0.00 | 0.54 | 2.34 | 3.36 | 4.06 | 4.31 | 3.07 | 0.00 | 0.00 | 1.95 | 1.87 | 5.03 | 5.91 |
| Sn | 0.00 | 0.00 | 0.00 | 0.00 | 25.23 | 24.91 | 26.12 | 25.09 | 21.12 | 22.51 | 23.00 | 20.87 | 23.86 | 8.81 | 21.49 | 19.90 | 16.91 | 9.44 |
| Pb | 0.00 | 0.00 | 0.61 | 0.21 | 0.00 | 0.00 | 0.00 | 0.00 | 0.00 | 0.00 | 0.00 | 0.06 | 0.04 | 0.00 | 0.41 | 0.38 | 0.00 | 0.00 |
| Se | 0.00 | 0.00 | 0.00 | 0.00 | 0.00 | 0.00 | 0.00 | 0.00 | 0.00 | 0.00 | 0.00 | 0.11 | 0.00 | 0.00 | 0.00 | 0.00 | 0.00 | 0.00 |
| Bi | 0.03 | 0.00 | 0.03 | 0.00 | 0.03 | 0.04 | 0.00 | 0.00 | 0.00 | 0.00 | 0.00 | 0.00 | 0.00 | 0.05 | 0.00 | 0.00 | 0.00 | 0.00 |
| Total (wt %) | 99.68 | 99.73 | 100.24 | 99.00 | 99.92 | 99.77 | 100.44 | 99.20 | 100.33 | 99.92 | 99.89 | 100.08 | 99.77 | 99.69 | 100.61 | 100.34 | 99.84 | 99.83 |
| S | 1.022 | 0.999 | 1.008 | 1.003 | 0.998 | 0.985 | 0.999 | 0.996 | 0.990 | 1.000 | 0.987 | 0.998 | 0.999 | 1.006 | 0.984 | 0.997 | 0.991 | 1.003 |
| Cd | 0.002 | 0.003 | 0.004 | 0.000 | 0.000 | 0.000 | 0.000 | 0.000 | 0.000 | 0.000 | 0.000 | 0.000 | 0.000 | 0.001 | 0.000 | 0.000 | 0.000 | 0.000 |
| Ag | 0.000 | 0.000 | 0.000 | 0.000 | 0.000 | 0.000 | 0.000 | 0.000 | 0.000 | 0.001 | 0.001 | 0.001 | 0.000 | 0.000 | 0.000 | 0.001 | 0.001 | 0.001 |
| Sn | 0.000 | 0.000 | 0.000 | 0.000 | 0.227 | 0.225 | 0.235 | 0.229 | 0.188 | 0.203 | 0.209 | 0.186 | 0.214 | 0.074 | 0.192 | 0.176 | 0.150 | 0.081 |
| Cu | 0.005 | 0.022 | 0.046 | 0.079 | 0.480 | 0.442 | 0.462 | 0.472 | 0.430 | 0.448 | 0.443 | 0.404 | 0.418 | 0.150 | 0.387 | 0.356 | 0.338 | 0.206 |
| Zn | 0.849 | 0.825 | 0.752 | 0.714 | 0.063 | 0.119 | 0.066 | 0.034 | 0.108 | 0.059 | 0.057 | 0.150 | 0.149 | 0.621 | 0.188 | 0.233 | 0.252 | 0.472 |
| Mn | 0.000 | 0.000 | 0.000 | 0.000 | 0.001 | 0.000 | 0.000 | 0.000 | 0.000 | 0.000 | 0.000 | 0.000 | 0.000 | 0.000 | 0.000 | 0.000 | 0.000 | 0.000 |
| Fe | 0.115 | 0.126 | 0.139 | 0.126 | 0.231 | 0.229 | 0.231 | 0.247 | 0.253 | 0.250 | 0.262 | 0.229 | 0.220 | 0.147 | 0.228 | 0.217 | 0.222 | 0.184 |
| In | 0.005 | 0.024 | 0.048 | 0.077 | 0.000 | 0.000 | 0.005 | 0.022 | 0.031 | 0.038 | 0.040 | 0.028 | 0.000 | 0.000 | 0.018 | 0.017 | 0.046 | 0.053 |
| Pb | 0.000 | 0.000 | 0.003 | 0.001 | 0.000 | 0.000 | 0.000 | 0.000 | 0.000 | 0.000 | 0.000 | 0.000 | 0.000 | 0.000 | 0.002 | 0.002 | 0.000 | 0.000 |
| Se | 0.000 | 0.000 | 0.000 | 0.000 | 0.000 | 0.000 | 0.000 | 0.000 | 0.000 | 0.000 | 0.000 | 0.001 | 0.000 | 0.000 | 0.000 | 0.000 | 0.000 | 0.000 |
| Bi | 0.000 | 0.000 | 0.000 | 0.000 | 0.000 | 0.000 | 0.000 | 0.000 | 0.000 | 0.000 | 0.000 | 0.000 | 0.000 | 0.000 | 0.000 | 0.000 | 0.000 | 0.000 |
| Sum (atom.) | 1.998 | 1.999 | 2.000 | 2.000 | 2.000 | 2.000 | 1.998 | 2.000 | 2.000 | 1.999 | 1.999 | 1.997 | 2.000 | 1.999 | 1.999 | 1.999 | 2.000 | 2.000 |
| Sphalerite | 84.9 | 82.5 | 75.2 | 71.4 | | | | | | | | | | | | | | |
| Pyrrhotite | 11.5 | 12.6 | 13.9 | 12.6 | | | | | | | | | | | | | | |
| Roquesite | 1 | 4.6 | 9.4 | 15.6 | | | | | | | | | | | | | | |

**Tab. 6**
Representative analyses of Ag-rich tetrehedrite, bournonite, plumosite-like, valentinite and anglesite.

| Mineral | Tetrahedrite 1 | Tetrahedrite 1 | Tetrahedrite 1 | Tetrahedrite 2 | Tetrahedrite 2 | Tetrahedrite 3 | Tetrahedrite 3 | Tetrahedrite 3 | Bournonite | Plumosite-like | Valentinite | Anglesite |
|---|---|---|---|---|---|---|---|---|---|---|---|---|
| | Tetrahedrite-*(Fe)* | | | Kenoargento-tetrahedrite-*(Fe)* | | Rozhdestvenskayite-*(Fe)* | | | | | | |
| Process | Chl-Ap | Chl-Ap | Chl-Ap | Chl-Ap | Chl-Ap | Chl-Ap | Chl-Ap | Chl-Ap | Chl-Ap | Chl-Ap | Chl-Ap | Chl-Ap |
| S | 23.40 | 23.40 | 22.90 | 21.08 | 20.65 | 20.17 | 20.00 | 20.17 | 19.80 | 18.86 | 0.08 | 8.91 |
| Cd | 0.00 | 0.00 | 0.00 | 0.00 | 0.00 | 0.00 | 0.00 | 0.00 | 0.00 | 0.00 | 0.04 | 0.00 |
| Ag | 16.26 | 18.51 | 20.90 | 29.05 | 31.60 | 43.86 | 46.78 | 48.59 | 0.00 | 0.12 | 0.02 | 0.00 |
| Zn | 1.16 | 1.33 | 1.06 | 0.74 | 0.86 | 0.81 | 0.96 | 0.93 | 0.00 | 0.00 | 0.01 | 0.01 |
| Fe | 5.38 | 5.19 | 5.59 | 5.63 | 5.67 | 5.25 | 4.57 | 5.13 | 0.65 | 0.27 | 0.48 | 0.00 |
| Mn | 0.01 | 0.00 | 0.00 | 0.00 | 0.00 | 0.00 | 0.00 | 0.00 | 0.00 | 0.00 | 0.00 | 0.00 |
| Cu | 26.20 | 24.19 | 22.25 | 17.00 | 15.01 | 5.35 | 2.68 | 2.15 | 13.00 | 0.00 | 0.08 | 0.00 |
| In | 0.04 | 0.05 | 0.02 | 0.06 | 0.10 | 0.05 | 0.07 | 0.08 | 0.00 | 0.00 | 0.00 | 0.00 |
| Sn | 0.00 | 0.00 | 0.05 | 0.00 | 0.04 | 0.00 | 0.00 | 0.00 | 0.00 | 0.00 | 0.00 | 0.00 |
| Sb | 27.09 | 27.41 | 27.29 | 27.03 | 26.59 | 24.02 | 23.48 | 24.12 | 23.61 | 31.78 | 83.93 | 0.00 |
| As | 0.00 | 0.00 | 0.00 | 0.00 | 0.00 | 0.00 | 0.00 | 0.00 | 0.67 | 0.52 | 0.00 | 0.00 |
| Pb | 0.08 | 0.13 | 0.00 | 0.00 | 0.00 | 0.28 | 0.73 | 0.08 | 42.26 | 48.67 | 0.03 | 70.22 |
| Bi | 0.00 | 0.00 | 0.00 | 0.00 | 0.00 | 0.00 | 0.05 | 0.12 | 0.21 | 0.33 | 0.06 | 0.08 |
| O | 0.00 | 0.00 | 0.00 | 0.00 | 0.00 | 0.00 | 0.00 | 0.00 | 0.00 | 0.00 | 16.00 | 20.23 |
| Total (wt %) | 99.62 | 100.21 | 100.06 | 100.59 | 100.52 | 99.79 | 99.32 | 101.37 | 100.20 | 100.55 | 100.73 | 99.45 |
| S | 12.980 | 13.050 | 12.951 | 12.039 | 11.961 | 12.798 | 12.981 | 12.853 | 2.984 | 6.958 | 0.007 | 0.886 |
| Cd | 0.000 | 0.000 | 0.000 | 0.000 | 0.000 | 0.000 | 0.000 | 0.000 | 0.000 | 0.000 | 0.001 | 0.000 |
| Ag | 2.682 | 3.069 | 3.514 | 4.932 | 5.442 | 8.274 | 9.027 | 9.205 | 0.000 | 0.013 | 0.001 | 0.000 |
| Sn | 0.000 | 0.000 | 0.008 | 0.000 | 0.006 | 0.000 | 0.000 | 0.000 | 0.000 | 0.000 | 0.000 | 0.000 |
| Cu | 7.335 | 6.809 | 6.349 | 4.900 | 4.388 | 1.713 | 0.878 | 0.691 | 0.989 | 0.000 | 0.004 | 0.000 |
| Zn | 0.316 | 0.364 | 0.294 | 0.207 | 0.244 | 0.252 | 0.306 | 0.291 | 0.000 | 0.000 | 0.000 | 0.001 |
| Mn | 0.003 | 0.000 | 0.000 | 0.000 | 0.000 | 0.000 | 0.000 | 0.000 | 0.000 | 0.000 | 0.000 | 0.000 |
| Fe | 1.714 | 1.662 | 1.817 | 1.846 | 1.886 | 1.913 | 1.703 | 1.877 | 0.056 | 0.059 | 0.025 | 0.000 |
| In | 0.006 | 0.008 | 0.003 | 0.010 | 0.016 | 0.009 | 0.013 | 0.014 | 0.000 | 0.000 | 0.000 | 0.000 |
| Sb | 3.958 | 4.027 | 4.065 | 4.066 | 4.057 | 4.014 | 4.014 | 4.049 | 0.937 | 3.091 | 2.024 | 0.000 |
| Te | 0.000 | 0.000 | 0.000 | 0.000 | 0.000 | 0.000 | 0.000 | 0.000 | 0.000 | 0.000 | 0.000 | 0.000 |
| As | 0.000 | 0.000 | 0.000 | 0.000 | 0.000 | 0.000 | 0.000 | 0.000 | 0.043 | 0.081 | 0.000 | 0.000 |
| Pb | 0.007 | 0.011 | 0.000 | 0.000 | 0.000 | 0.027 | 0.073 | 0.008 | 0.986 | 2.779 | 0.000 | 1.080 |
| Bi | 0.000 | 0.000 | 0.000 | 0.000 | 0.000 | 0.000 | 0.005 | 0.012 | 0.005 | 0.020 | 0.001 | 0.075 |
| O | – | – | – | – | – | – | – | – | – | – | 3 | 4 |
| Sum (atom.) | 29 | 29 | 29 | 28 | 28 | 29 | 29 | 29 | 6 | 13 | 5 | 6 |
| *Other elements analysed: Se, Te* | | | | | | | | | | | | |

**Tab. 6** – Continuation.

| Mineral | Tetrahedrite 1 | Tetrahedrite 1 | Tetrahedrite 1 | Tetrahedrite 2 | Tetrahedrite 2 | Tetrahedrite 3 | Tetrahedrite 3 | Tetrahedrite 3 |
|---|---|---|---|---|---|---|---|---|
| | Tetrahedrite-*(Fe)* | | | Kenoargento--tetrahedrite-*(Fe)* | | Rozhdestvenskayite-*(Fe)* | | |
| Process | Chl-Ap | Chl-Ap | Chl-Ap | Chl-Ap | Chl-Ap | Chl-Ap | Chl-Ap | Chl-Ap |
| Ag | 0.000 | 0.000 | 0.000 | 4.932 | 5.442 | 6.000 | 6.000 | 6.000 |
| Cu | 6.000 | 6.000 | 6.000 | 1.068 | 0.558 | 0.000 | 0.000 | 0.000 |
| *A group* | *6.000* | *6.000* | *6.000* | *6.000* | *6.000* | *6.000* | *6.000* | *6.000* |
| Cu (B group) | 1.335 | 0.809 | 0.349 | 3.832 | 3.830 | 1.713 | 0.878 | 0.691 |
| Ag (B group) | 2.682 | 3.069 | 3.514 | 0.000 | 0.000 | 2.274 | 3.027 | 3.205 |
| Pb | 0.007 | 0.011 | 0.000 | 0.000 | 0.000 | 0.027 | 0.073 | 0.008 |
| Sn | 0.000 | 0.000 | 0.008 | 0.000 | 0.006 | 0.000 | 0.000 | 0.000 |
| In | 0.006 | 0.008 | 0.003 | 0.010 | 0.016 | 0.009 | 0.013 | 0.014 |
| $Mn^{2+}$ (C group) | 0.003 | 0.000 | 0.000 | 0.000 | 0.000 | 0.000 | 0.000 | 0.000 |
| $Fe^{3+}$ (C group) | 0.030 | 0.026 | 0.111 | 0.053 | 0.130 | 0.165 | 0.009 | 0.168 |
| $Fe^{2+}$ (C group) | 1.684 | 1.636 | 1.706 | 1.793 | 1.756 | 1.748 | 1.694 | 1.709 |
| Zn (C group) | 0.316 | 0.364 | 0.294 | 0.207 | 0.244 | 0.252 | 0.306 | 0.291 |
| *B+C group* | *6.063* | *5.923* | *5.985* | *5.934* | *5.982* | *6.188* | *6.000* | *6.086* |
| *Zn+Fe$^{2+}$* | *2.000* | *2.000* | *2.000* | *2.000* | *2.000* | *2.000* | *2.000* | *2.000* |
| $Sb^{3+}$ (D group) | 3.958 | 4.027 | 4.065 | 4.066 | 4.057 | 4.014 | 4.014 | 4.049 |
| $Bi^{3+}$ (D group) | 0.000 | 0.000 | 0.000 | 0.000 | 0.000 | 0.000 | 0.005 | 0.012 |
| *D group* | *3.958* | *4.027* | *4.065* | *4.066* | *4.057* | *4.014* | *4.019* | *4.061* |
| S (Y.Z group) | 12.980 | 13.050 | 12.951 | 12.039 | 11.961 | 12.798 | 12.981 | 12.853 |
| Sum (atom.) | 29 | 29 | 29 | 28 | 28 | 29 | 29 | 29 |

**Tab. 7**
Representative analyses of dolomite, ankerite, siderite, cerussite and Mn-rich calcite.

| Mineral | Dolomite | Dolomite | Ankerite | Ankerite | Siderite | Siderite | Siderite | Siderite | Cerussite | Calcite Mn | Calcite Mn |
|---|---|---|---|---|---|---|---|---|---|---|---|
| Process | Limestone | Limestone | Chl-Ap | Chl-Ap | Chl-Ap | Chl-Ap | Chl-Ap | Chl-Ap | Chl-Ap | Chl-Ap | Chl-Ap |
| FeO | 5.24 | 4.97 | 9.01 | 17.62 | 61.16 | 58.57 | 59.77 | 52.37 | 2.58 | 2.06 | 0.81 |
| MnO | 3.28 | 2.46 | 3.71 | 1.34 | 0.29 | 2.23 | 0.44 | 2.35 | 0 | 8.2 | 6.71 |
| MgO | 16.82 | 17.72 | 13.66 | 9.5 | 0.29 | 0.1 | 0 | 1.19 | 0 | 0.44 | 0.07 |
| CaO | 28.48 | 28.9 | 28.32 | 27.75 | 0.25 | 0.77 | 1.79 | 5.09 | 0 | 45.81 | 49.08 |
| SrO | 0.09 | 0.07 | 0.08 | 0.14 | 0.01 | 0.02 | 0.02 | 0 | 0 | 0.09 | 0.04 |
| PbO | 0 | 0 | 0 | 0 | 0 | 0 | 0 | 0 | 79.65 | 0 | 0 |
| $CO_2$ | 45.99 | 46.65 | 44.97 | 43.84 | 38.13 | 37.96 | 38.31 | 38.82 | 17.27 | 42.82 | 43.26 |
| Total | 99.9 | 100.77 | 99.75 | 100.2 | 100.12 | 99.65 | 100.34 | 99.82 | 99.5 | 99.42 | 99.97 |
| Fe | 0.070 | 0.065 | 0.123 | 0.246 | 0.982 | 0.945 | 0.956 | 0.826 | 0.092 | 0.029 | 0.011 |
| Mn | 0.044 | 0.033 | 0.051 | 0.019 | 0.005 | 0.036 | 0.007 | 0.038 | 0.000 | 0.119 | 0.096 |
| Mg | 0.399 | 0.415 | 0.332 | 0.237 | 0.008 | 0.003 | 0.000 | 0.033 | 0.000 | 0.011 | 0.002 |
| Ca | 0.486 | 0.486 | 0.494 | 0.497 | 0.005 | 0.016 | 0.037 | 0.103 | 0.000 | 0.840 | 0.890 |
| Pb | 0.000 | 0.000 | 0.000 | 0.000 | 0.000 | 0.000 | 0.000 | 0.000 | 0.979 | 0.000 | 0.000 |
| Sr | 0.001 | 0.001 | 0.001 | 0.001 | 0.000 | 0.000 | 0.000 | 0.000 | 0.000 | 0.001 | 0.000 |
| Cations | 1.000 | 1.000 | 1.001 | 1.000 | 1.000 | 1.000 | 1.000 | 1.000 | 1.071 | 1.000 | 0.999 |
| $CO_3$ | 1.045 | 1.060 | 1.003 | 0.972 | 0.839 | 0.841 | 0.850 | 0.870 | 0.380 | 0.973 | 0.983 |
| $CaCO_3$ | 48.6 | 48.6 | 49.4 | 49.7 | 0.5 | 1.6 | 3.7 | 10.3 | 0.0 | 84.0 | 89.1 |
| $MgCO_3$ | 39.9 | 41.5 | 33.2 | 23.7 | 0.8 | 0.3 | 0.0 | 3.3 | 0.0 | 1.1 | 0.2 |
| $FeCO_3$ | 7.0 | 6.5 | 12.3 | 24.6 | 98.2 | 94.5 | 95.6 | 82.6 | 8.6 | 2.9 | 1.1 |
| $MnCO_3$ | 4.4 | 3.3 | 5.1 | 1.9 | 0.5 | 3.6 | 0.7 | 3.8 | 0.0 | 11.9 | 9.6 |
| $PbCO_3$ | 0.0 | 0.0 | 0.0 | 0.0 | 0.0 | 0.0 | 0.0 | 0.0 | 91.4 | 0.0 | 0.0 |
| $SrCO_3$ | 0.1 | 0.1 | 0.1 | 0.1 | 0.0 | 0.0 | 0.0 | 0.0 | 0.0 | 0.1 | 0.0 |
| Total | 99.9 | 99.9 | 99.9 | 99.9 | 100.0 | 100.0 | 100.0 | 100.0 | 100.0 | 99.9 | 100.0 |

**Tab. 8**

Representative analyses of schreyerite, cassiterite, goethite, pyrochroite and szomolnokite.

| Mineral | Schreyerite | Cassiterite | Goethite | Pyrochroite | Szomolnokite |
|---|---|---|---|---|---|
| Process | Chl-Ap | Chl-Ap | Chl-Ap | Chl-Ap | Chl-Ap |
| $SiO_2$ | 0.08 | 0.00 | 0.70 | 0.11 | 0.00 |
| $TiO_2$ | 48.80 | 0.04 | 0.00 | 0.00 | 0.00 |
| $Al_2O_3$ | 0.21 | 0.00 | 0.22 | 0.13 | 0.00 |
| $Cr_2O_3$ | 3.71 | 0.00 | 0.00 | 0.00 | 0.00 |
| $SnO_2$ | 1.07 | 100.37 | 0.00 | 0.00 | 0.00 |
| $FeO$ | 0.00 | 0.14 | 0.00 | 1.46 | 48.83 |
| $Fe_2O_3$ | 9.37 | 0.00 | 80.35 | 0.00 | 0.00 |
| $Sc_2O_3$ | 0.71 | 0.00 | 0.00 | 0.00 | 0.00 |
| $V_2O_3$ | 20.14 | 0.00 | 0.00 | 0.00 | 0.00 |
| $Mn_2O_3$ | 1.54 | 0.00 | 0.00 | 0.00 | 0.00 |
| $ZnO$ | 0.61 | 0.00 | 0.00 | 0.00 | 0.00 |
| $MnO$ | 0.00 | 0.00 | 0.01 | 65.36 | 0.00 |
| $CaO$ | 0.00 | 0.00 | 0.03 | 6.76 | 0.00 |
| $SrO$ | 3.04 | 0.00 | 0.00 | 0.00 | 0.00 |
| $PbO$ | 3.33 | 0.00 | 0.00 | 0.00 | 0.00 |
| $MgO$ | 0.05 | 0.10 | 0.04 | 0.93 | 0.00 |
| $UO_2$ | 5.42 | 0.00 | 0.00 | 0.00 | 0.00 |
| $Na_2O$ | 0.00 | 0.00 | 0.06 | 0.00 | 0.00 |
| $SO_3$ | 0.00 | 0.00 | 0.00 | 0.00 | 47.66 |
| F | 0.00 | 0.00 | 0.24 | 0.00 | 0.00 |
| Cl | 0.00 | 0.00 | 0.01 | 0.00 | 0.00 |
| $H_2O$ | 1.05 | 0.00 | 18.40 | 19.69 | 3.51 |
| Total | 99.13 | 100.67 | 100.06 | 94.44 | 96.49 |
| Si | 0.006 | 0.000 | 0.023 | 0.002 | 0.000 |
| Al | 0.018 | 0.000 | 0.008 | 0.002 | 0.000 |
| V | 1.154 | 0.000 | 0.000 | 0.000 | 0.000 |
| Ti | 2.627 | 0.000 | 0.000 | 0.000 | 0.000 |
| Sn | 0.031 | 0.994 | 0.000 | 0.000 | 0.000 |
| $Fe^{3+}$ | 0.504 | 0.000 | 1.956 | 0.000 | 0.000 |
| $Fe^{2+}$ | 0.000 | 0.003 | 0.000 | 0.019 | 1.103 |
| Cr | 0.210 | 0.000 | 0.000 | 0.000 | 0.000 |
| Sc | 0.044 | 0.000 | 0.000 | 0.000 | 0.000 |
| $Mn^{3+}$ | 0.084 | 0.000 | 0.000 | 0.000 | 0.000 |
| $Mn^{2+}$ | 0.000 | 0.000 | 0.000 | 0.843 | 0.000 |
| Ca | 0.000 | 0.000 | 0.000 | 0.110 | 0.000 |
| Zn | 0.032 | 0.000 | 0.000 | 0.000 | 0.000 |
| Sr | 0.126 | 0.000 | 0.000 | 0.000 | 0.000 |
| Pb | 0.064 | 0.000 | 0.000 | 0.000 | 0.000 |
| Mg | 0.005 | 0.003 | 0.002 | 0.021 | 0.000 |
| U | 0.086 | 0.000 | 0.000 | 0.000 | 0.000 |
| Na | 0.000 | 0.000 | 0.004 | 0.000 | 0.000 |
| S | 0.000 | 0.000 | 0.000 | 0.000 | 0.965 |
| Cations | 4.991 | 1.000 | 1.994 | 0.997 | 2.068 |
| OH | 0.50 | 0.00 | 3.98 | 2.00 | 0.00 |
| O | 9 | 2 | 5 | 2 | 4 |

Mineralia Slovaca, 54, 2 (2022)

**Tab. 9**
Representative analyses of V/Cr-rich muscovite-phengite, V/Cr-rich phengite-illite, V-rich chlorite,
chlorite and kaolinite.

| Mineral | Phengite | Phengite | Phengite | Phengite | Phengite | Phengite | Phengite | Phengite | Phengite-illite | Phengite-illite | Phengite-illite | Phengite-illite | Chlorite | Chlorite | Chlorite | Chlorite | Chlorite | Kaolinite |
|---|---|---|---|---|---|---|---|---|---|---|---|---|---|---|---|---|---|---|
| Enriched | V | V | V/Cr | V/Cr | V/Cr | V/Cr | V/Cr | V/Cr | V/Cr | V/Cr | V/Cr | V/Cr | V | V | | | Fe | |
| Process | Chl-Ap | Chl-Ap | Chl-Ap | Chl-Ap | Chl-Ap | Chl-Ap | Chl-Ap | Chl-Ap | Chl-Ap | Chl-Ap | Chl-Ap | Chl-Ap | Chl-Ap | Chl-Ap | SedEx | SedEx | SedEx | Chl-Ap |
| $SiO_2$ | 48.59 | 48.08 | 48.74 | 47.84 | 46.02 | 46.85 | 45.59 | 45.58 | 50.29 | 50.34 | 50.74 | 51.11 | 24.23 | 24.20 | 25.87 | 26.27 | 24.06 | 47.95 |
| $TiO_2$ | 0.13 | 0.17 | 0.21 | 0.16 | 0.25 | 0.21 | 0.29 | 0.47 | 0.31 | 0.24 | 0.34 | 0.40 | 0.06 | 0.03 | 0.02 | 0.00 | 0.00 | 0.02 |
| $Al_2O_3$ | 33.65 | 29.30 | 28.41 | 28.12 | 24.39 | 23.29 | 22.76 | 22.79 | 30.55 | 27.38 | 26.22 | 28.06 | 19.16 | 17.97 | 22.26 | 22.16 | 19.29 | 36.44 |
| $Cr_2O_3$ | 0.00 | 0.00 | 1.54 | 0.02 | 1.33 | 1.39 | 1.43 | 0.81 | 2.06 | 0.71 | 1.06 | 1.15 | 0.00 | 0.40 | 0.00 | 0.01 | 0.00 | 0.01 |
| FeO | 1.29 | 1.80 | 2.10 | 2.13 | 1.27 | 0.98 | 0.90 | 0.92 | 1.55 | 2.17 | 0.91 | 0.82 | 37.13 | 31.55 | 23.94 | 25.51 | 43.85 | 0.75 |
| $V_2O_3$ | 0.47 | 1.59 | 2.97 | 5.00 | 5.69 | 7.30 | 8.29 | 10.91 | 3.57 | 5.43 | 8.54 | 9.35 | 1.07 | 2.46 | 0.01 | 0.00 | 0.01 | 0.00 |
| MnO | 0.01 | 0.01 | 0.00 | 0.03 | 0.05 | 0.04 | 0.03 | 0.04 | 0.03 | 0.03 | 0.03 | 0.00 | 0.47 | 0.45 | 0.29 | 0.27 | 0.26 | 0.00 |
| MgO | 1.41 | 2.04 | 2.03 | 1.74 | 2.03 | 2.20 | 1.92 | 2.02 | 1.35 | 1.97 | 2.16 | 1.77 | 5.65 | 9.54 | 15.62 | 14.23 | 1.44 | 0.00 |
| CaO | 0.02 | 0.04 | 0.03 | 0.02 | 0.01 | 0.04 | 0.02 | 0.03 | 0.02 | 0.04 | 0.03 | 0.01 | 0.02 | 0.10 | 0.00 | 0.03 | 0.01 | 0.03 |
| $Na_2O$ | 0.55 | 0.25 | 0.33 | 0.32 | 0.30 | 0.26 | 0.20 | 0.22 | 0.24 | 0.22 | 0.10 | 0.08 | 0.00 | 0.00 | 0.01 | 0.01 | 0.03 | 0.01 |
| $K_2O$ | 8.86 | 10.05 | 8.49 | 9.34 | 9.09 | 9.47 | 9.33 | 7.38 | 4.51 | 5.54 | 4.46 | 2.69 | 0.00 | 0.00 | 0.00 | 0.00 | 0.00 | 0.02 |
| Cl | 0.00 | 0.01 | 0.00 | 0.00 | 0.02 | 0.00 | 0.01 | 0.00 | 0.00 | 0.00 | 0.00 | 0.00 | 0.01 | 0.01 | 0.01 | 0.01 | 0.00 | 0.00 |
| $H_2O$ | 4.55 | 4.40 | 4.47 | 4.43 | 4.20 | 4.25 | 4.18 | 4.23 | 4.59 | 4.51 | 4.55 | 4.64 | 10.59 | 10.68 | 11.54 | 11.52 | 10.39 | 13.80 |
| Total | 99.53 | 97.74 | 99.32 | 99.15 | 94.65 | 96.28 | 94.95 | 95.40 | 99.07 | 98.58 | 99.14 | 100.08 | 98.39 | 97.39 | 99.57 | 100.02 | 99.34 | 99.03 |
| Si | 3.204 | 3.277 | 3.270 | 3.241 | 3.283 | 3.302 | 3.271 | 3.234 | 3.288 | 3.348 | 3.345 | 3.304 | 5.489 | 5.432 | 5.377 | 5.467 | 5.553 | 2.084 |
| AlIV | 0.796 | 0.723 | 0.730 | 0.759 | 0.717 | 0.698 | 0.729 | 0.766 | 0.712 | 0.652 | 0.655 | 0.696 | 2.511 | 2.568 | 2.623 | 2.533 | 2.447 | 0.000 |
| Sum_T | 4 | 4 | 4 | 4 | 4 | 4 | 4 | 4 | 4 | 4 | 4 | 4 | 8 | 8 | 8 | 8 | 8 | 2.084 |
| AlVI | 1.817 | 1.629 | 1.514 | 1.484 | 1.332 | 1.235 | 1.194 | 1.139 | 1.640 | 1.492 | 1.381 | 1.440 | 2.600 | 2.182 | 2.826 | 2.898 | 2.796 | 1.865 |
| V | 0.025 | 0.087 | 0.160 | 0.271 | 0.325 | 0.412 | 0.476 | 0.620 | 0.187 | 0.289 | 0.451 | 0.484 | 0.194 | 0.442 | 0.002 | 0.000 | 0.002 | 0.000 |
| Ti | 0.006 | 0.009 | 0.011 | 0.008 | 0.013 | 0.011 | 0.016 | 0.025 | 0.015 | 0.012 | 0.017 | 0.019 | 0.010 | 0.005 | 0.003 | 0.000 | 0.000 | 0.001 |
| $Fe^{2+}$ | 0.071 | 0.103 | 0.118 | 0.121 | 0.076 | 0.058 | 0.054 | 0.055 | 0.085 | 0.121 | 0.050 | 0.044 | 7.034 | 5.922 | 4.162 | 4.439 | 8.464 | 0.027 |
| Cr | 0.000 | 0.000 | 0.082 | 0.001 | 0.075 | 0.077 | 0.081 | 0.045 | 0.106 | 0.037 | 0.055 | 0.059 | 0.000 | 0.071 | 0.000 | 0.002 | 0.000 | 0.000 |
| Mn | 0.001 | 0.001 | 0.000 | 0.002 | 0.003 | 0.002 | 0.002 | 0.002 | 0.002 | 0.002 | 0.002 | 0.000 | 0.090 | 0.086 | 0.051 | 0.048 | 0.051 | 0.000 |
| Mg | 0.139 | 0.207 | 0.203 | 0.176 | 0.216 | 0.231 | 0.205 | 0.214 | 0.132 | 0.195 | 0.212 | 0.171 | 1.908 | 3.192 | 4.840 | 4.414 | 0.495 | 0.000 |
| Ca | 0.001 | 0.003 | 0.002 | 0.001 | 0.001 | 0.003 | 0.002 | 0.002 | 0.001 | 0.003 | 0.002 | 0.001 | 0.005 | 0.024 | 0.000 | 0.007 | 0.002 | 0.001 |
| Na | 0.070 | 0.033 | 0.043 | 0.042 | 0.041 | 0.036 | 0.028 | 0.030 | 0.030 | 0.028 | 0.013 | 0.010 | 0.000 | 0.000 | 0.004 | 0.004 | 0.013 | 0.001 |
| K | 0.745 | 0.874 | 0.727 | 0.807 | 0.827 | 0.851 | 0.854 | 0.668 | 0.376 | 0.470 | 0.375 | 0.222 | 0.000 | 0.000 | 0.000 | 0.000 | 0.000 | 0.001 |
| Cations | 6.875 | 6.946 | 6.860 | 6.913 | 6.909 | 6.916 | 6.912 | 6.800 | 6.574 | 6.649 | 6.558 | 6.450 | 19.841 | 19.924 | 19.888 | 19.812 | 19.823 | 3.980 |
| CCl | 0.000 | 0.002 | 0.000 | 0.000 | 0.005 | 0.000 | 0.002 | 0.000 | 0.000 | 0.000 | 0.000 | 0.000 | 0.008 | 0.008 | 0.007 | 0.007 | 0.000 | 0.000 |
| OH | 2.000 | 1.999 | 2.000 | 2.000 | 1.998 | 2.000 | 1.999 | 2.000 | 2.000 | 2.000 | 2.000 | 2.000 | 15.996 | 15.996 | 15.996 | 15.996 | 16.000 | 4.000 |
| O | 12 | 12 | 12 | 12 | 12 | 12 | 12 | 12 | 12 | 12 | 12 | 12 | 36 | 36 | 36 | 36 | 36 | 9 |

**Tab. 10**
Representative analyses of In-rich sakuraiite and sphalerite 2.

| Mineral | In sakuraiite | In sakuraiite | In sakuraiite | In sakuraiite | In sakuraiite | In sakuraiite | In sakuraiite | Sphalerite 2 |
|---|---|---|---|---|---|---|---|---|
| Process | Chl-Ap | Chl-Ap | Chl-Ap | Chl-Ap | Chl-Ap | Chl-Ap | Chl-Ap | Chl-Ap |
| S | 32.98 | 32.83 | 31.23 | 32.09 | 30.38 | 30.85 | 29.75 | 33.24 |
| Cd | 0.00 | 0.00 | 0.00 | 0.00 | 0.54 | 0.00 | 0.28 | 0.27 |
| Ag | 0.03 | 0.04 | 0.04 | 0.10 | 0.11 | 0.11 | 0.00 | 0.01 |
| Zn | 42.10 | 40.77 | 36.66 | 34.54 | 31.57 | 28.25 | 20.66 | 59.63 |
| Fe | 8.69 | 8.59 | 9.22 | 8.73 | 10.29 | 10.34 | 8.63 | 6.61 |
| Mn | 0.00 | 0.00 | 0.00 | 0.00 | 0.01 | 0.00 | 0.00 | 0.00 |
| Cu | 5.86 | 6.15 | 8.10 | 8.49 | 9.76 | 10.87 | 14.21 | 0.00 |
| In | 10.78 | 11.62 | 14.67 | 15.97 | 18.18 | 19.67 | 25.83 | 0.07 |
| Sn | 0.00 | 0.00 | 0.00 | 0.00 | 0.00 | 0.00 | 0.42 | 0.00 |
| Pb | 0.00 | 0.00 | 0.00 | 0.00 | 0.00 | 0.00 | 0.16 | 0.00 |
| Bi | 0.00 | 0.00 | 0.00 | 0.00 | 0.00 | 0.00 | 0.27 | 0.12 |
| Total (wt %) | 100.44 | 100.00 | 99.91 | 99.92 | 100.85 | 100.09 | 100.20 | 99.95 |
| S | 1.021 | 1.024 | 0.996 | 1.022 | 0.980 | 1.001 | 1.000 | 1.001 |
| Cd | 0.000 | 0.000 | 0.000 | 0.000 | 0.005 | 0.000 | 0.003 | 0.002 |
| Ag | 0.000 | 0.000 | 0.000 | 0.001 | 0.001 | 0.001 | 0.000 | 0.000 |
| Sn | 0.000 | 0.000 | 0.000 | 0.000 | 0.000 | 0.000 | 0.004 | 0.000 |
| Cu | 0.092 | 0.097 | 0.130 | 0.136 | 0.159 | 0.178 | 0.241 | 0.000 |
| Zn | 0.639 | 0.624 | 0.574 | 0.539 | 0.500 | 0.449 | 0.341 | 0.881 |
| Mn | 0.000 | 0.000 | 0.000 | 0.000 | 0.000 | 0.000 | 0.000 | 0.000 |
| Fe | 0.154 | 0.154 | 0.169 | 0.160 | 0.191 | 0.193 | 0.167 | 0.114 |
| In | 0.093 | 0.101 | 0.131 | 0.142 | 0.164 | 0.178 | 0.243 | 0.001 |
| Pb | 0.000 | 0.000 | 0.000 | 0.000 | 0.000 | 0.000 | 0.001 | 0.000 |
| Bi | 0.000 | 0.000 | 0.000 | 0.000 | 0.000 | 0.000 | 0.001 | 0.001 |
| Sum (atom.) | 1.999 | 2.000 | 2.000 | 2.000 | 2.000 | 2.000 | 2.001 | 2.000 |
| Sphalerite | 63.9 | 62.4 | 57.4 | 53.9 | 50 | 44.9 | 34.1 | 88.1 |
| Pyrrhotite | 15.4 | 15.4 | 16.9 | 16 | 19.1 | 19.3 | 16.7 | 11.4 |
| Roquesite | 18.5 | 19.8 | 26.1 | 27.8 | 32.3 | 35.6 | 48.4 | 0.1 |

# Oxidácia a rozpad stratiformnej SedEx sulfidickej mineralizácie v epidotovo-amfibolitovej fácii metamorfózy in situ za vzniku kasiteritu, sľúd bohatých na V, In-Sn-Ag-Sb-Pb-Bi-Zn-Fe-As-Cu-Ni-Co sulfidov a Fe-Ca-Pb karbonátov (lokalita Bystrý potok, gemerikum, Západné Karpaty)

Študované územie lokality Bystrý potok budujú šošovky lyditov, kryštalických vápencov a zriedkavo vápencov s dolomitom, ktoré sú súčasťou grafitických fylitov holeckých vrstiev silúrskeho veku (Grecula et al., 2009, 2011). V stratigrafii spodného paleozoika gemerika holecké vrstvy predstavujú podložie albitovo-kvarcitovo-keratofýrového (trachytového v zmysle klasifikácie IUGS) súvrstvia so stratiformnou sulfidickou mineralizáciou SedEx. Táto SedEx mineralizácia vznikla súčasne s keratofýrovým/ bazaltovým magmatizmom v neskorom silúre až devóne a pochádzala z exhalátov, ktoré vznikli počas magmatizmu na morskom dne v spodnopaleozoickom rifte (obr. 1, 2 a 3; Grecula et al., 1982, 2009, 2011; Radvanec a Grecula, 2016).

Silúrsko-devónske horninové sekvencie boli metamorfované v závere variskej orogenézy v období 281 – 256 mil. rokov. V amfibolitovej fácii táto metamorfóza spôsobila aj lokálne anatektické tavenie so vznikom granitu typu S v dvoch horúcich líniách. Metamorfóza súvisí s prenosom tepla nad subdukujúcou platňou a vrcholí vznikom ostrovnooblúkového andezitovo-dacitovo-ryolitového vulkanizmu v perme (Radvanec et al., 2017; Radvanec a Gonda, 2019).

Vápencové šošovky na lokalite Bystrý potok boli metamorfované a metasomaticky zmenené na skarn v epidotovo-amfibolitovej fácii (526 – 546 °C, 3 – 6 kbar) a v príbuznej chloritovo-apatitovej zóne (420 – 540 °C; obr. 1 – 3). Skarn tvorí granát $Grs_{41.4-60.2}Sps_{19.8-32.8}Alm_{16.7-22.2}Adr_{0-8.5}$, hedenbergit $Wo_{44.5-50.1}Fs_{31.6-38.2}En_{12.7-20.7}$, epidot, aktinolit, titanit, kremeň, zirkón a zvyšky kalcitu. Pukliny v skarne sú vyplnené krátkymi žilkami pyrochroitu a kalcitu bohatého na Mn (obr. 4, tab. 2). Vypočítaná teplota 526 – 546 °C pri P = 3 – 6 kbar z granátovo-klinopyroxénového geotermometra (Ravna, 2000) a minerálna asociácia skarnu určujú P-T podmienky epidotovo-amfibolitovej fácie (Spear, 1995). Pri zistenej teplote 420 – 540 °C chloritovo-apatitovej zóny vznikol v skarne aj fluórapatit a chlorit, pričom P-T podmienky chloritovo-apatitovej zóny sa čiastočne prekrývajú s P-T podmienkami epidotovo-amfibolitovej fácie (obr. 5). V týchto P-T podmienkach vznikli v matrixe silikátov skarnu aj sulfidy. V skarne vznikol kobaltit a millerit bol čiastočne nahradený zonálnym hauchecornitom a hauchecornitom-(Sb) (obr. 4, 21, tab. 1). Stabilné relikty dolomitu z holeckých vrstiev boli postupne zatláčané ankeritom, goethitom a sideritom (obr. 11d, f).

Premenou organickej substancie na grafit v epidotovo-amfibolitovej fácii sa z holeckých vrstiev do nadložia s keratofýrmi a primárnou stratiformnou SedEx sulfidickou mineralizáciou uvoľnila fluidná fáza s obsahom $O_2$, $H_2O$, $CO_2$, $H_3PO_4$, $H_2S$, HF a V, kde vznikli impregnácie schreyeritu, bielej sľudy-fengitu a chloritu v matrixe s obsahom zmesi pôvodných SedEx sulfidov (obr. 5 a 13, tab. 1, 8). Primárna stratiformná SedEx sulfidická mineralizácia, zložená prevažne z pyritu 1, menej pyrotínu, chalkopyritu, sfaleritu 1, galenitu 1, arzenopyritu, ferrokesteritu, stefanitu, gudmunditu, bizmutinitu 1, sulfidu bohatého na PbBiSb (typ $A_2B_2S_5$) a kobellitu, bola oxidovaná a rozložená touto fluidnou fázou za vzniku novej metamorfogénnej minerálnej asociácie in situ (obr. 6, 7a, 8, 15 – 19, tab. 3). Pôvodný SedEx pyrotín sa rozpadol na asociáciu szomolnokit, pyrit 2, goethit a siderit (obr. 11a – b, tab. 8). Agregáty galenitu 1 oxidovali a rozkladali sa na zmes anglesit a ceruzit (obr. 11c, tab. 6 a 7). Pôvodná SedEx asociácia ferrokesterit s obsahom In, sakuraiit s obsahom Sn ± In a sfalerit 1 obsahujúci In a molekulu roquesitu oxidovala, rozpadla sa a zreagovala na kasiterit, chalkopyrit, sakuraiit s obsahom In a na sfalerit 2 (obr. 9, 10, 14 – 17, tab. 5). Lokálne a vzácne vznikol aj agregát zmesi allanit-(Ce), galenit 1, fluórapatit a kasiterit v matrixe zmesi dolomitu, sideritu a kremeňa. Vzácny je aj vznik agregátu siderit a bastnäsit-(Ce) v matrixe kremeňa (obr. 7b, 11f). Siderit je na skúmanej lokalite bežný minerál. Sulfid PbSbBi (typ $A_2B_3S_6$), wittit s obsahom S, bizmutinit 2, rýdzi Bi a galenit 2 s obsahom Se sú nové minerály, ktoré vznikli z rozpadu sulfidu PbBiSb (typ $A_2B_2S_5$), kobellitu a bizmutinitu 1 (obr. 19, 20, 21, tab. 4). Tri zóny tetraedritov od tetraedritu-(Fe) cez kenoargentotetraedrit-(Fe) až po rozhdestvenskayait-(Fe) ukazujú postupné usporiadanie tetraedritov v troch oddelených zónach riadených medzerami nemiešateľnosti v Cu-Ag substitúcii. Tetraedrity 1 – 3 vznikli rozkladom pôvodného ferrokesteritu, stephanitu a gudmunditu (obr. 18, 21, tab. 6). Gudmundit tiež oxidoval na valentinit (obr. 18e – f, 21, tab. 6). Aj bournonit a sulfid podobný plumositu vznikli rozkladom pôvodnej SedEx asociácie ferrokesterit, galenit 1 a gudmundit (obr. 11e, 14c, 21, tab. 6). Celkovo 22 reakcií opisuje vzťah medzi zdrojovou SedEx mineralizáciou a novými metamorfogénnymi minerálmi, ktoré vznikli na úkor pôvodnej stratiformnej SedEx sulfidickej mineralizácie in situ. Chemické zloženie oxidov, sulfidov, sulfátov a Fe-Ca-Pb karbonátov sú vizualizované v tetraédroch, diagramoch a trojuholníkových diagramoch (obr. 5, 9, 10, 12, 17, 20, 21).

Metamorfogénna fluidná fáza uvoľnená z holeckých vrstiev bola obohatená o ďalšie prvky v stratigrafickom horizonte stratiformnej SedEx sulfidickej mineralizácie. V tomto SedEx horizonte boli pôvodné sulfidy v chloritovo-apatitovej zóne oxidované a rozložené 22 reakciami. Pôvodná fluidná fáza z holeckých vrstiev bola takto obohatená a mala nasledujúce zloženie: $O_2$, $H_2S$, $H_2O$, $CO_2$, HF, $H_3PO_4$, K, Na, Ca, Al, Si, Fe, Mg, Mn, Sn, V, REE, U, Ti, Y, Cu, Sb, Bi, Ag, Zn, In, Pb, Ni, Co a As. Geneticky je súčasťou permského matamorfno-magmaticko-hydrotermálneho (MMH) cyklu (Radvanec a Gonda, 2019). Fluidná fáza generovaná v tomto MMH cykle migrovala do štruktúr, kde sa v závislosti od polohy, v ktorej tieto štruktúry vznikli, vytvorili rôzne typy mineralizácie od greisenov a skarnov, ktoré sa nachádzajú v amfibolitovej alebo v epidotovo-amfibolitovej fácii, až po žily v chloritovej zóne gemerika (Grecula et al., 1995; Radvanec a Gonda, 2019).

# Comparison of morphology of quartz crystals – "Marmarosh diamonds" – from Paleogene Flysch sequences of Krosno (Silesian) Zone, Dukla Zone in Ukrainian Carpathians, and Intra-Carpathian sequences of Western Carpathians

OLEKSANDR VOVK[1], IHOR NAUMKO[2], HALYNA ZANKOVYCH[2] and YAROSLAV KUZEMKO[3]

[1]Lesya Ukrainka Volyn National University 13, Voli Av., Lutsk, Ukraine, 43025; vovk.oleksandr@vnu.edu.ua
[2]Institute of Geology and Geochemistry of Combustible Minerals of the NAS of Ukraine
3-a, Naukova Str., Lviv, Ukraine, 79060; naumko@ukr.net, zankovuch@gmail.com
[3]CJSC «Interbudtunnel»

**Abstract:** Quartz crystals of "Marmarosh diamonds" type were goniometrically studied in Ukrainian Carpathians from the veins in flysch deposits of Krosno (Silesian) unit (137 crystals, locality 1 – New Beskydy Tunnel) and the Oligocene sediments of the Dukla Zone (77 crystals; loc. 2 – Pryslip pass). They were compared with quartz crystals from intra-Carpathian Paleogene sequences of the Western Carpathians in Slovakia (175 crystals; loc. 3 – Šoltysa stream). The analysis of the obtained results allows to state that the "Marmarosh diamonds" from the studied Ukrainian and Slovak localities are generally similar. The main simple forms represent the hexagonal prism m $\{10\bar{1}0\}$ and the rhombohedra r $\{10\bar{1}1\}$ and z $\{01\bar{1}1\}$. The following types of crystal habit have been identified: hexagonal-dipyramidal, pseudocubic, hexagonal-prismatic, trigonal-prismatic. For the polyhedra from the Ukrainian Carpathians, minor forms are less typical, such as the trigonal dipyramid s $\{11\bar{2}1\}$ and the trapezoid x $\{51\bar{6}1\}$. Statistically, the shape of "Marmarosh diamond" crystals from the Ukrainian Carpathians is closer to isometric. For them, elongation along the main crystallographic axis is even less typical than for polyhedra from the Slovak localities. In addition, "Marmarosh diamonds" from the W. Carpathians in Slovakia are more often flattened at $\{10\bar{1}0\}$. In the process of crystal growth with decreasing temperature, the habit changes from hexagonal-dipyramidal to trigonal-prismatic. Quartz from Krosno (Silesian) zone of Ukrainian Carpathians was found in the association with calcite. There are numerous hydrocarbon inclusions in both minerals. The mineralogical crystallographic and geochemical investigations (especially of the migrating hydrocarbon fluids), are important for oil and gas geology of the Carpathian oil and gas-bearing province.

**Key words:** quartz crystal morphology, hydrocarbon inclusions, "Marmarosh diamonds", Carpathians

**Graphical abstract**
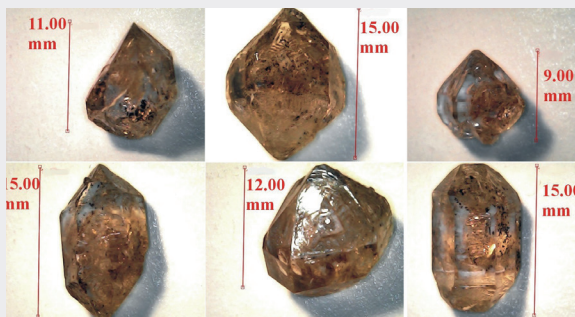


**Highlights**

- Quartz crystals of "Marmarosh diamonds" type from Paleogene sequences of W. and E. Carpathians in Slovak and Ukrainian territories were studied goniometrically. Obtained results indicate their general similarity.
- Numerous hydrocarbon inclusions in these crystals indicate the importance of crystallographic and geochemical investigations for oil and gas geology of the Carpathians.

## Introduction

Quartz crystals of "Marmarosh diamonds" type can be found in many regions of the world (Alps, Carpathians, Crimea, Donbas, Caucasus, etc.). They were first discovered within the Marmarosh massif of the Eastern Carpathians. The perfection of the morphology of the "Marmarosh diamonds", for which they got their name, has attracted the attention of researchers since the first mention of their findings (Fichtel, 1791; Zipser, 1817; Tokarski, 1905; etc.). The first crystal morphological description of this quartz was made by Leidolt in 1885. Later it was supplemented by research by Arkhipova (1951, 1961), Lazarenko et al. (1963) and Vozniak et al. (1974).

"Marmarosh diamonds" are widespread in carbonate-quartz veins in flysch deposits of the Carpathian

thrust-fault structure of the ages from the Cretaceous to Paleogene and Neogene (Kolodii, 2004). In Slovakia "Marmaros diamonds" occur in the vicinity of Ulič, Veľký Lipník, and Starina localities. The best known occurrences in the Ukrainian Carpathians are found in the surroundings of Kobylets'ka Polyana, Pidpolozzya, Nyzhni Vorota, Mizhgirya, Volovets' and Byckiv (Udubasa et al., 2002). These are transparent colorless quartz crystals with a typical glass luster. The size of the crystals along the main crystallographic axis is usually from the first millimeters to 1.0 cm, occasionally up to 3.0 cm. Quartz fills fractured zones in sedimentary rocks, being in paragenesis with calcite and close association with bitumen of different composition. Goniometric studies have shown that the main habitual forms of such quartz are the hexagonal prism $\{10\bar{1}0\}$, rhombohedra $\{10\bar{1}1\}$, $\{01\bar{1}1\}$, less often usually poorly developed trigonal dipyramid $\{11\bar{2}1\}$.

The first complete crystal morphological description of "Marmarosh diamonds" from the Ukrainian Carpathians was done by Matkovskiy (1961). As a result of goniometric studies of many crystals, the scientist identified two main types of habitus:

- columnar-prismatic with predominant development of prism faces (characteristic of "Marmarosh diamonds" from Eocene deposits of the Pidpolozzia village area);
- dipyramidal with predominant development of rhombohedral faces (characteristic of "Marmarosh diamonds" from flysch deposits of the Chivchyn Mountains area).

Vozniak et al. (1974) in the Ukrainian Carpathians identified three types of habitus of "Marmarosh diamonds" (Fig. 1):

- prismatic with the predominant development of the faces of the prism;
- rhombohedral with predominant development of rhombohedral faces;
- pseudocubic with a sharp predominance of positive rhombohedron faces and without or with weak prism face development.

Zatsikha et al. (1984) in the Ukrainian Carpathians identified dipyramidal and dipyramidal-prismatic types of habitus of "Marmarosh diamonds".

Kvasnytsia (2016) described rare form – rhombohedron $\{01\bar{1}2\}$, being established for the first time not only for the "Marmarosh diamonds" but also for quartz crystals from various hydrothermal mineralizations of Ukraine.

Typical representatives of "Marmarosh diamonds" are crystals of rhombohedral and pseudocubic habit. Information on the shape, habit and morphology of all these species are summarized in Matkovskyi (2011).

In addition to the habit of crystals, an important typomorphic feature of "Marmarosh diamonds" is the presence of different hydrocarbon inclusions. They are indicators of the sequence of growth of individuals, changes in the chemical composition of the mineral-forming fluid (from high-density hydrocarbon-water in the initial stages to oil-water, and sometimes with significant impurities of carbon dioxide in the final). Accordingly, this testifies to the important role of "Marmarosh diamonds" in the reproduction of hydrocarbon migration processes during the formation of industrial accumulations of oil and gas condensates in oil and gas provinces. Therefore, "Marmarosh diamonds", as a new genetic type of quartz – skeletal crystals with hydrocarbon inclusions (Vozniak et al., 1978), are of fundamental importance as fixers of chemical composition and PT parameters of migration processes of hydrocarbon compounds and direct connection with oil and gas, as well as the evidence of a detailed PT history of the Folded Carpathians (Vityk et al., 1996).

The hydrocarbon inclusions in the crystals "Marmarosh diamonds" from the Western Carpathians on Slovak territory (in further text Slovak Carpathians) are described by Hurai et al. (1995). The morphology of "Marmarosh diamonds" polyhedra from the Veľký Lipník locality is described by Fulín (1997).

In current paper we present morphology of "Mararosh diamonds" in three localities. Two of them (Krosno zone and Veľký Lipník area) were already described (Dudok et
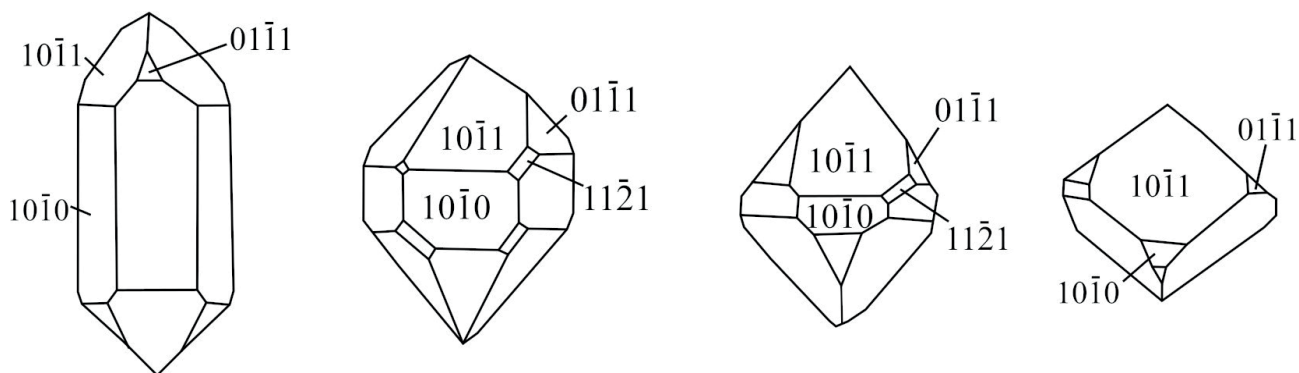


**Fig. 1.** Types of habit of "Marmarosh diamonds" (Vozniak et al., 1974).

al., 2002; Vovk et al., 2018; a.o.), but the New Beskydy Tunnel was only recently built, and all presented research results from there are new and less known to the scientific community. Obviously, the comparison of new results with data obtained earlier allows to present wide spectra of "Marmarosh diamonds" morphology and their genesis from different localities. Therefore, the main focus is on the new studied locality of the Krosno (Silesian) structural-facial unit of the Ukrainian Carpathians in the area of the New Beskydy Tunnel. We will consider only the peculiarities of the crystal morphology and genesis of "Marmarosh diamonds" from the Ukrainian Carpathians and compare them with individuals from the Slovak Carpathians, which are described mainly in (Dudok et al., 2002).

**Methodology**

As it was mentioned above, the investigated crystals were selected in three localities. The first of them is located in the Krosno (Silesian) zone of the Ukrainian Carpathians, in the area of the New Beskydy Tunnel. Field geological studies were carried out during the construction of the tunnel, if possible, directly with the geological service of the tunnel. They included the selection and description of stuffs, macroscopic analysis of structural and textural features of the veinlet-impregnated mineralization and host rocks.

Altogether 137 crystals of "Marmarosh diamonds" were selected for goniometric research from the veinlet-impregnated mineralization in the flysch deposits of the Krosno (Silesian) structural-facial unit of the Ukrainian Carpathians in the area of the New Beskydy Tunnel (Figs. 2 and 3). Samples were taken from observation points along the tunnel recorded at a distance of 1 247.6 m, 1 435 m, 1 445 m, 1 464 m, 1 505 m, 1 508 m, 1 522 m, 1 544 m and 1 612 m.

General mineralogical approaches were used to provide mineralogical studies. Determination of the composition of volatiles, relative gas saturation as well as water saturation of fluid inclusions was performed by the mass spectrometry on the MX-3A mass spectrometer (IGGC of the National Academy of Sciences of Ukraine, analyst B. Sakhno). A mineral (rock) sample weighing 200 mg of the +1–2 fraction was crushed in a specially designed mortar; before analysis, the inlet system of the mass spectrometer was vacuumed to values of the order of $1.10^{-3}$ Pa. Relative gas saturation $\Delta P$, Pa – pressure increase in the inlet system of the mass spectrometer (relative to the residual pressure of the order of $1.10^{-3}$ Pa in it), which is created as a result of the release of volatile components (without taking into account the water vapor sorbed on $P_2O_5$, placed in the inlet system) from inclusions and closed pores when grinding the sample. It can represent a comparative value for the same weights. The chemical composition of minerals of the veinlet-impregnated mineralization was determined using



**Fig. 2.** The map with position of sampling localities: 1 – veins in the flysch deposits of the Krosno (Silesian) structural-facial unit of the Ukrainian Carpathians in the area of the New Beskydy Tunnel; 2 – Oligocene deposits of the Dukla zone (observation point 1 502, Pryslip pass); 3 – the Inner-Carpathian Paleogene (observation point 1 527, Veľký Lipník area, Šoltysa stream).

scanning electron microscopy and X-ray microanalysis based on the PEMMA-102-02 raster electron microscope – microanalyser (analyst R. Serkis).

The crystals were measured on a two-circle goniometer GD-1 (analyst O. Vovk). Gnomostereographic projections were built on the basis of research materials, based on which the axonometric projections of polyhedra were drawn. All axonometric projections of quartz crystals constructed using the Shape program (demo version) are made at the position of the projection pole φ = 71.5° and ρ = 80°.

The second locality represents the Oligocene deposits of the Dukla zone (observation point 1 502, Pryslip pass; Figs. 2 and 3). Altogether 77 quartz crystals of the "Marmarosh diamond" type were selected from cracking zones in the relevant rocks, represented by sandstones and siltstones. At the observation point 1 502 the azimuth of the dip of the host rocks is 140°, the angle of dip is 70–80° (140/70–80°); concerning cracks – the dip azimuth is 190–200°, angle of dip 70–80° (190–200/70–80°). At observation point 1 527 in the host rocks it is 150/30°; 125/80–90° and 185/80–90°. The thickness of the cracks varies from the first millimeters to 3.0 cm.

The third locality occurs in the Inner Carpathian Paleogene in Slovakia (observation point 1 527, Veľký Lipník area, Šoltysa stream; Figs. 2 and 3). Altogether 175 quartz crystals of the "Marmarosh diamond" type were goniometrically studied. According to Fulín (1997) "Marmarosh diamonds": are found in the grey-blue sandstones, in weathered samples having yellowish brown colour. Sandstones are characterized by the presence of NW-SE trending cracks with a dip of 70–90° to SE. The "Marmarosh diamonds" from the W. Carpathians are typical with all types of hydrocarbon inclusions described for similar quartz from the Ukrainian and Polish Carpathians (Dudok, 2000; Kalyuzhnyi et al., 1998).



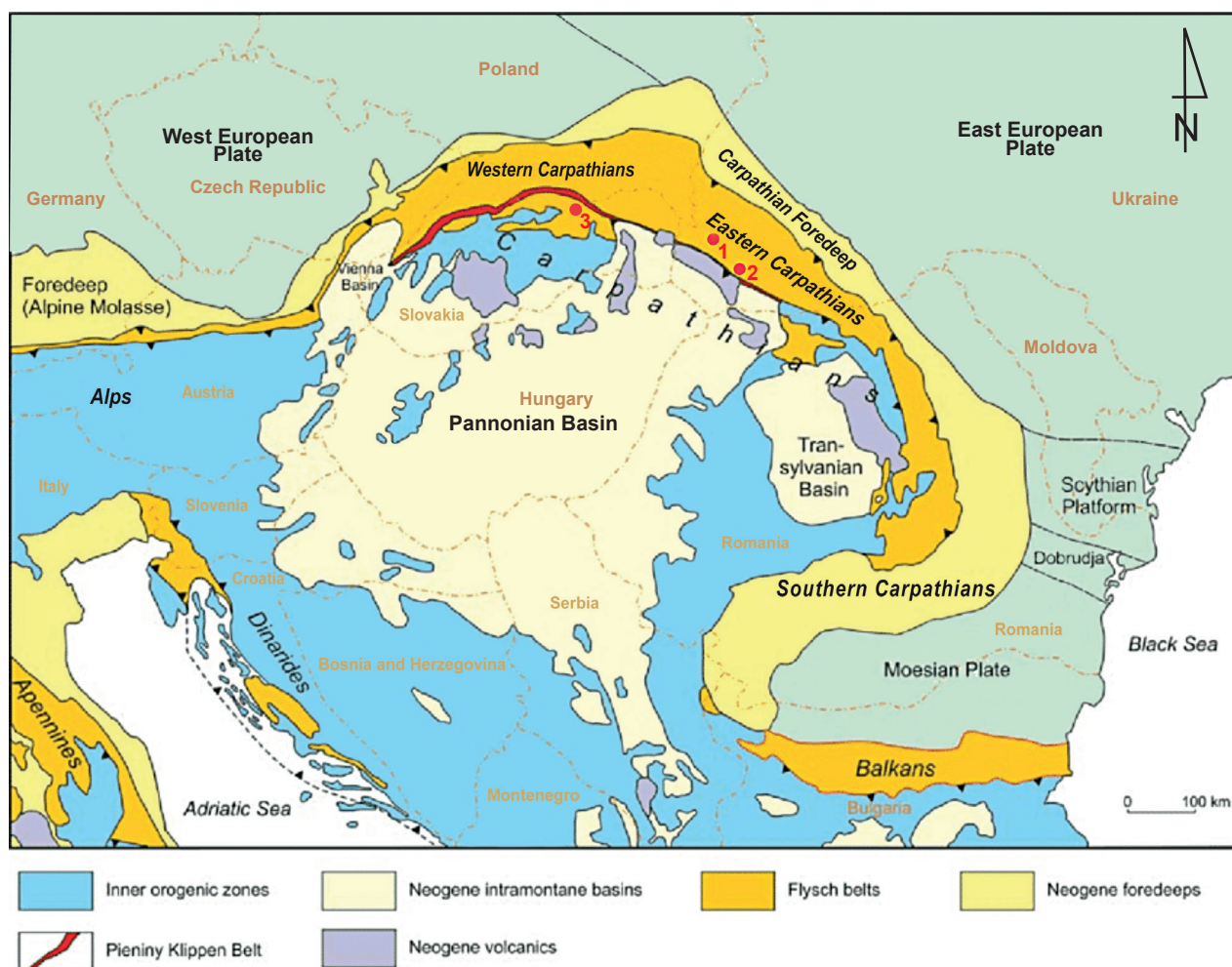**Fig. 3.** Tectonic map (Birkenmajer & Gedl, 2017) with position of sampling points: 1 – veins in the flysch deposits of the Krosno (Silesian) structural-facial unit of the Ukrainian Carpathians in the area of the New Beskydy Tunnel; 2 – Oligocene deposits of the Dukla zone (observation point 1 502, Pryslip pass); 3 – the Inner-Carpathian Paleogene (observation point 1 527, Veľký Lipník area, Šoltysa stream).

## Results and discussion
### Crystal morphology and habits

Polyhedra of "Marmarosh diamonds" from both – the Ukrainian and Slovak parts of Carpathians are two-headed, their size is up to 1 cm, rarely up to 3 cm along the main crystallographic axis $L_3$. The faces of the hexagonal prism m $\{10\overline{1}0\}$ and the rhombohedra r $\{10\overline{1}1\}$ and z $\{01\overline{1}1\}$ are present on all crystals. The development of these faces determines the crystals habit. In addition, a trigonal dipyramid s $\{11\overline{2}1\}$ was found on about a third of individuals from the Dukla zone and on 13 % of crystals from the Inner Carpathian Paleogene. This form was not detected on the studied polyhedra from the Ukrainian Carpathians. Acute rhombohedra are rare. All these forms are described in the special literature, in particular in Goldschmidt (1922).

The habitus of the crystals is isometric or short-column, rarely columnar. There are several types of individuals by habit (see Tab. 1).

Hexagonal-dipyramidal habit with approximately equal development of the faces of rhombohedra r $\{10\overline{1}1\}$ and z $\{01\overline{1}1\}$ and underdeveloped faces or without faces of the prism m $\{10\overline{1}0\}$ (Fig. 11.1). Crystals of this habit are quite common in the Slovak part of Carpathians, almost half of them have dipyramids. In the Ukrainian Carpathians, in particular in the flysch deposits of the Krosno (Silesian) structural-facial zone, this type is also manifested (Vovk et al., 2018, 2019), but less frequently.

Pseudocubic (Fig. 11.2) crystals are characterized by well-developed faces of one of the rhombohedra (positive or negative) and small faces of the prism and the other rhombohedron. Such individuals are rare in both the Ukrainian and Slovak Carpathians. Crystals of transitional habit between hexagonal-dipyramidal and pseudocubic are more typical for the Slovak Carpathians (Fig. 11.3). Dipyramide was found in only 5 % of the total number of crystals.

Hexagonal-prismatic. This type is divided into two subtypes:

I. – Short-prismatic. Crystals of this subtype are characterized by uniform development of three main forms: hexagonal prism, positive and negative rhombohedrons (Fig. 11.4). Such individuals in the Slovak Carpathians make up 18 % of the total number of crystals. Dipyramide was found in a third of them (Fig. 11.5). Such polyhedra are even more typical of the Krosno (Silesian) structural-facial zone. Their frequency is 30 %.

II. – Actually prismatic (Fig. 11.6). The main form is a prism, rhombohedra are evenly developed, but are of secondary importance. Such individuals are very rare for both the Ukrainian and Slovak Carpathians, no dipyramid has been found in them.
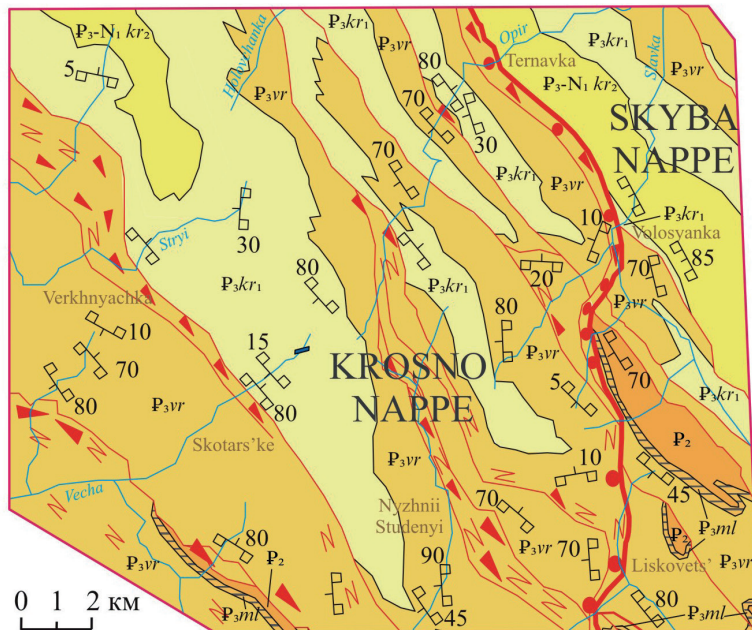


**Fig. 4.** Geological map of the eastern part of the Krosno Nappe and the adjacent segment of the Skyba Nappe in the basins of the upper reaches of the Stryi, Opir, Vecha, Rika rivers: 1 – Research area; 2 – Eocene flysch; 3 – Menilite Fm.; 4 – Verets (Transitional) Fm.; 5 – Lower Krosno Fm. (sandstones); 6 – Middle Krosno Fm. (bedded flysh); 7 – strike, dip angle and position of the bed bottom; 8 – tectonic breccia; 9 – tectonic mélange; 10 – intensively folded deposits; 11 – tectonic boundary between the Krosno and Skyba nappes; 12 – secondary faults; 13 – geological boundaries.
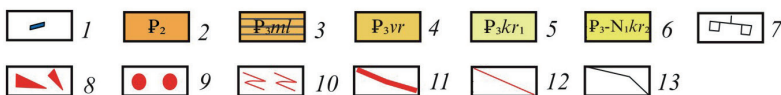
## Lithostratigraphy of the Silesian Nappe
## of the Turka Subnappe



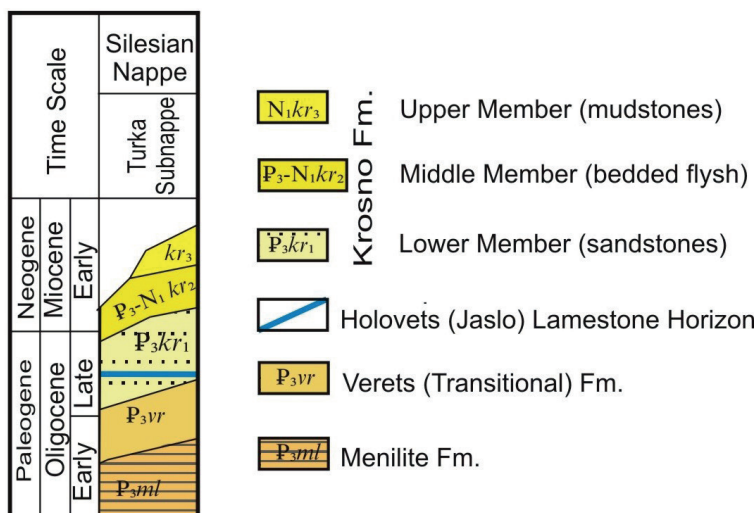| | Upper Member (mudstones) |
| --- | --- |
| N₁*kr₃* | |
| P₃-N₁*kr₂* | Middle Member (bedded flysh) |
| P₃*kr₁* | Lower Member (sandstones) |
| | Holovets (Jaslo) Lamestone Horizon |
| P₃*vr* | Verets (Transitional) Fm. |
| P₃*ml* | Menilite Fm. |

**Fig. 5.** Lithostratigraphic column of the flysch zone with depicted Krosno (Silesian) zone (Hnylko et al., 2021). The samples of quartz crystals were taken from Lower Member P₃*kr₁*.
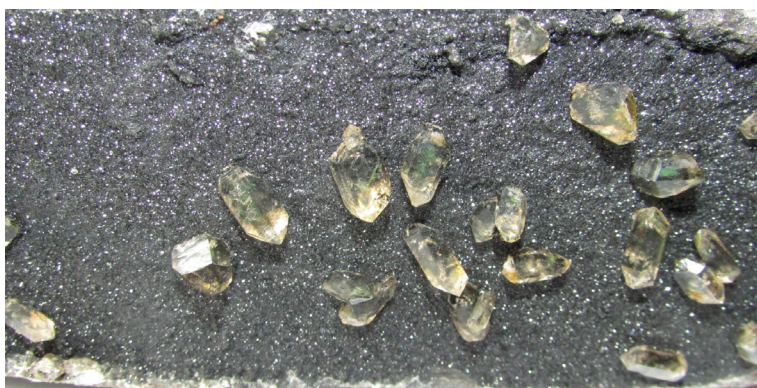


**Fig. 6.** The New Beskydy Tunnel.



**Fig. 7.** The outcrop with crystals of "Marmarosh diamonds" in the area of the New Beskydy Tunnel.

Trigonal-prismatic is also divided into two subtypes:

I. – Short-prismatic. The prism and one of the rhombohedra are well developed, the other rhombohedron is of secondary importance (Fig. 11.7). Such crystals are rare in Slovak Carpathians, dipyramid was found in one of them. Such polyhedra are very typical for the Krosno (Silesian) structural-facial zone of the Ukrainian Carpathians, their frequency is 54 %;

II. – Actually prismatic. The hexagonal prism dominates the rhombohedra of different sizes (Fig. 11.8). Individuals of this type represent 2 % (Inner Carpathian Paleogene) and 9 % (Dukla zone) of the total number of crystals. Dipyramid was found on two of them. In the Krosno (Silesian) zone of the Ukrainian Carpathians, the frequency of such polyhedra is slightly higher – 9 %.

According to the analysis of statistical data it can be concluded that in the process of growth (i.e. with decreasing temperature), the habit of crystals changes from hexagonal-dipyramidal to trigonal-prismatic. The presence of dipyramid is typical for individuals of hexagonal-dipyramidal and hexagonal-prismatic (short-prismatic) habit from the Slovak Carpathians.

In addition to the crystals described above, which are close to ideal, the distorted individuals are quite common. The macroscopic symmetry of real crystals may differ from the true one both in the direction of decrease and in the direction of increase. The greatest symmetry is in individuals of hexagonal-dipyramidal and hexagonal-prismatic habit. The appearance of the sixth-order pseudoaxis is due to the equal development of positive and negative rhombohedra, and the pseudoplanes arose in the absence of the faces of the dipyramid s $\{11\bar{2}1\}$ and the trapezoid x $\{51\bar{6}1\}$. Such highly symmetric crystals are formed under conditions of chaotic rotation of the crystal in a medium with maximum symmetry $\infty L \infty \infty PC$ (symmetry of a sphere) or $L \infty \infty PPS$ (symmetry of a stationary cylinder), provided that the axis of infinite order of the medium coincides with the axis of third order quartz. The flow of matter to all faces of the crystal is uniform. In nature, under such conditions, crystals grow that rotate continuously in the melt or in solution. Therefore, dipyramidal crystals are charac-

teristic with paramorphoses of trigonal quartz on hexagonal quartz in quartz porphyries and for late hydrothemal quartz of ore and quartz-carbonate veins. Crystals of prismatic habit grew under conditions of more intense influx of matter to the faces of the prism. Such conditions can occur if the crystal is attached to the head of the rock. Individuals grow under the condition of a homogeneous liquid slick with the symmetry of a circle, in the case of identical sides of the slick - with the symmetry of the cylinder. The second head of such crystals is often regenerated due to the fact that the crystal broke off from the attachment.

There are several degrees of elongation of the crystals in the ratio of sizes along the $L_3$ axis to the $L_2$ axis: short-prismatic (elongation 2.5); long-prismatic (~ 4); needle (> 6); very shortened (< 1.5). The studied crystals from the Slovak Carpathians are strongly shortened or short-prismatic. Long-prismatic individuals are extremely rare, and no needles are present. Polyhedra from the Ukrainian Carpathians are strongly shortened (over 90 %), or short prismatic (up to 10 %), long prismatic and needle-shaped among the studied individuals are not detected (Fig. 9).

Crystals with reduced visible symmetry were also found: flattened prisms and rhombohedra (with visible $L_2$ symmetry), wedge-shaped and pseudotriclinic.

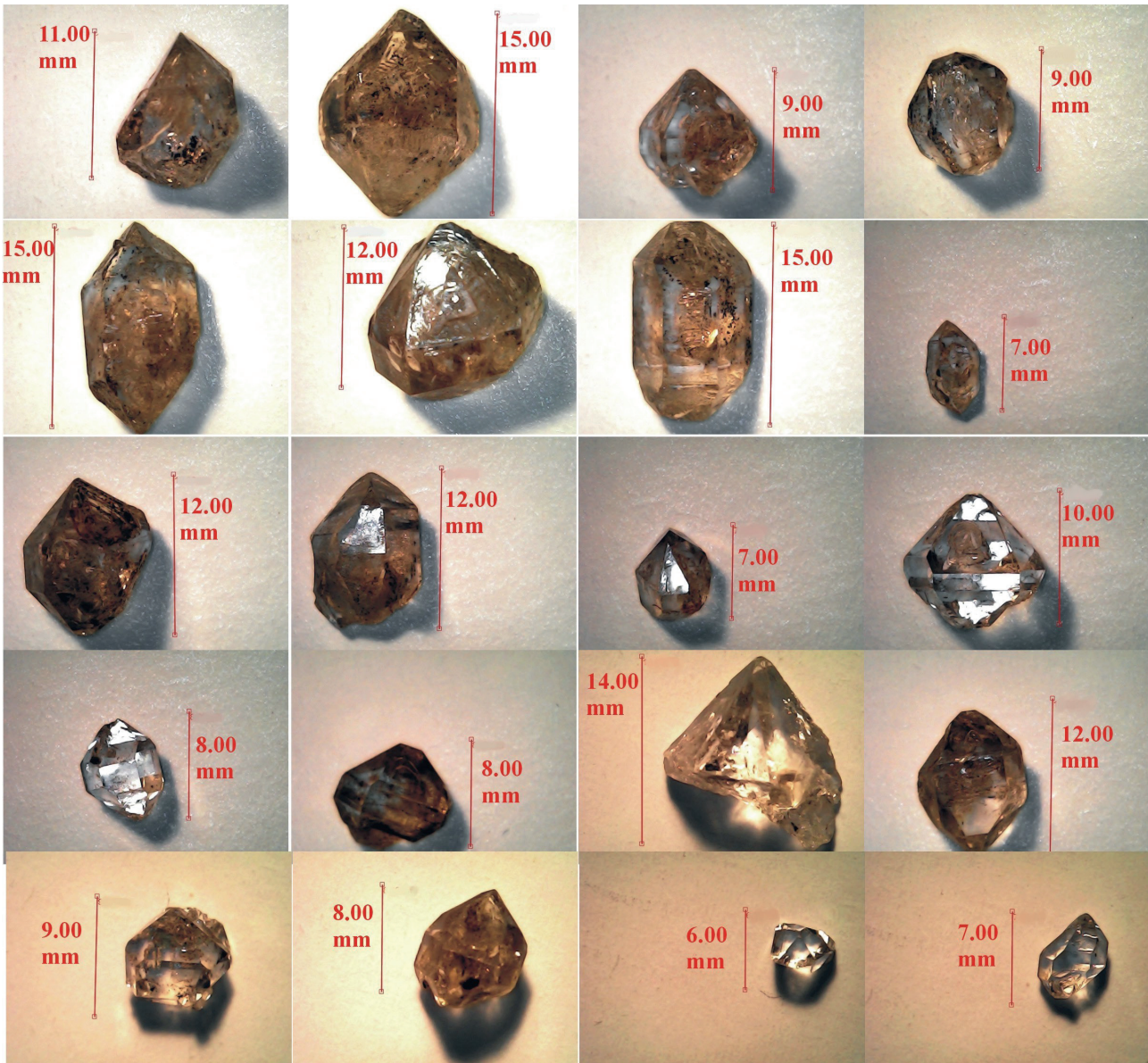Crystal morphological studies of quartz also determined the flattening size of crystals n, i.e. the ratio of



**Fig. 8.** The crystals of "Marmarosh diamonds" from the Krosno (Silesian) structural unit of Ukrainian Carpathians (the area of the New Beskydy Tunnel).

crystal sizes in $L_3$ to the distance between opposite faces $\{10\bar{1}0\}$ perpendicular to the flattening direction. In our case, the value of n ranges from 1 : 1 to 1 : 3 for individuals from the Slovak Carpathians and up to 1 : 2 for polyhedra from the Ukrainian Carpathians. Individuals are flattened on the faces $\{10\bar{1}0\}$ or $\{01\bar{1}0\}$. The macrosymmetry of such crystals is pseudorhombic, individuals were attached to the prism face to the rock wall, which caused a more intense influx of matter to the two opposite faces of the prism. Crystals flattened on a rhombohedron grew in the conditions of a bilateral slick with symmetry of the cylinder. The axis of infinite order of the medium coincided with $L_2$ in the crystal, so the symmetry of individuals is monoclinic. Wedge-shaped crystals with symmetry P grew under conditions close to those in which pseudorhombic individuals flattened by $\{10\bar{1}0\}$ grew. They were also attached to the face $\{10\bar{1}0\}$ to the rock wall, but the symmetry of the medium was less. Mineral-forming fluids moved along the crystal in the direction from the more developed crystal top to the less developed one. Due to the unilateral direction of flows on individuals of all elements of symmetry, only the pseudoplane is preserved. Wedge-shaped crystals are very valuable genetically, because they contain information about the directions of migration of mineral-forming fluids.

Pseudotriclinic crystals indicate that the symmetry of the medium was not maximal, and the elements of symmetry of the crystal did not coincide with the elements of symmetry of the medium. That is, individuals grew obliquely in relation to the directions of migration of mineral-forming fluids.

As a result, the analysis of literature data (Vozniak et al., 1974; Lazarenko et al., 1963; Matkovskiy, 1961) and own goniometric studies of crystal morphology of "Marmarosh diamonds" from the deposits of the Ukrainian (Krosno, now Silesian and Dukla zones) and Slovak Carpathians (Dukla zone and Intra-Carpathian Paleogene zone) allowed to state that in general that the "Marmarosh diamonds" from the Slovak and Ukrainian Carpathians are similar. However, in (Dudok et al., 2002) it is said that the described individuals from the Slovak Carpathians are less characterized by polyhedra of prismatic habit. Our studies of

"Marmarosh diamonds" and the Krosno (Silesian) zone of the Ukrainian Carpathians show that prismatic individuals are even rarer than in the Slovak Carpathians.

Anyway, there is the conclusion about the evolution of habit from hexagonal-dipyramidal to trigonal-prismatic by decreasing of the temperature during growth (Vovk et al., 2019).

### Inclusions in quartz in "Marmarosh diamonds" from the Krosno zone

The polyhedra of rhombohedral and pseudocubic habit with a strong lustre of the "Marmarosh diamond" type were formed in a hydrocarbon-saturated (oil-saturated) fluid medium in a calm tectonic situation, when the tectonic overprint had already ended, creating a system of fractured
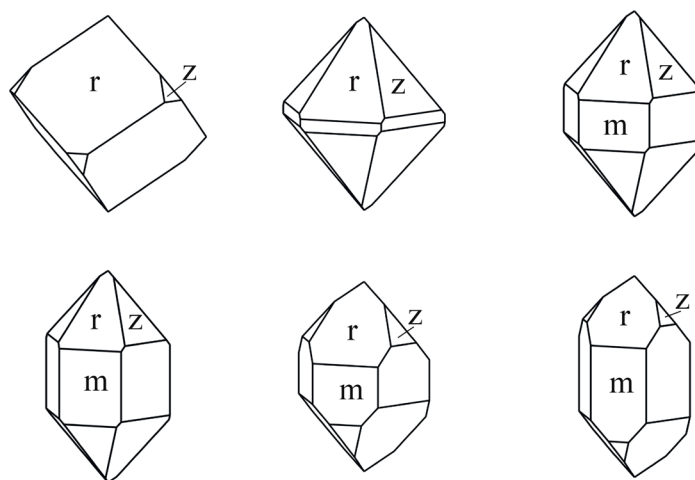


**Fig. 9.** Crystal types of "Marmarosh diamonds" from the Krosno (Silesian) structural unit of Ukrainian Carpathians (Vovk et al., 2018). Simple forms m $\{10\bar{1}0\}$, r $\{10\bar{1}1\}$ and z $\{01\bar{1}1\}$.
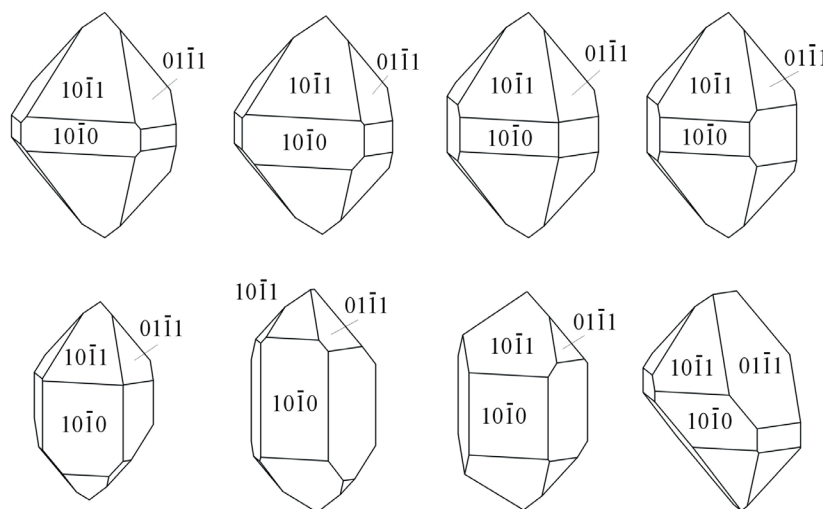


**Fig. 10.** Crystal habit of "Marmarosh diamonds" from the Krosno (Silesian) structural unit of Ukrainian Carpathians (the area of the New Beskydy Tunnel).
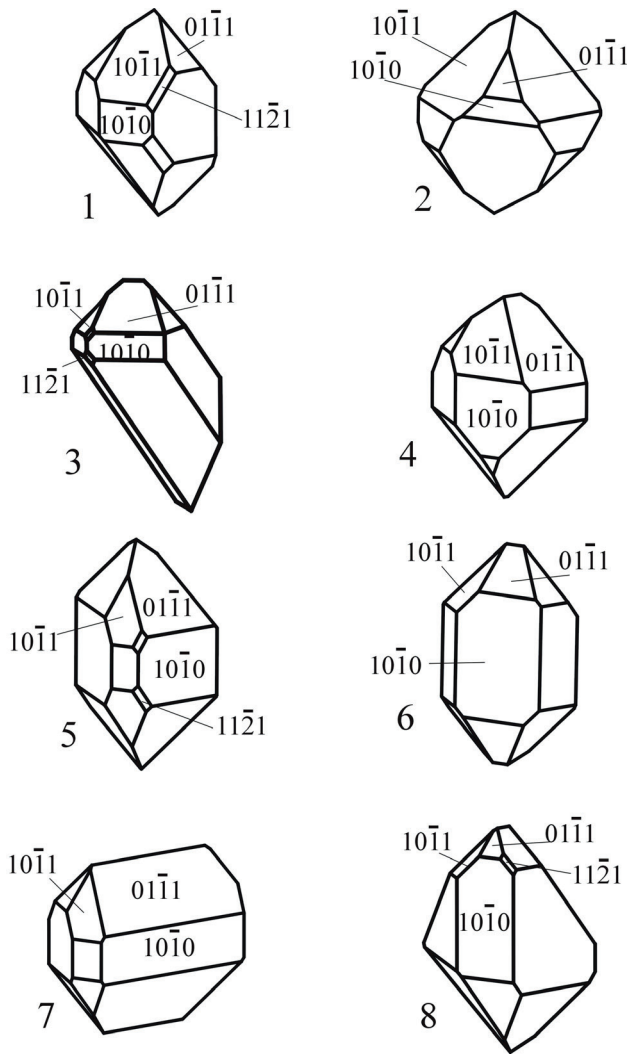
**Fig. 11.** Crystal habit of "Marmarosh diamonds" from Slovak Carpathians (Dudok et al., 2002).

zones. The healing of the formed cracks contributed to the crystallization of perfect crystals of typical rhombohedral and pseudocubic habit, which by their defects-inclusions in the process of growth-synthesis captured and preserved hydrocarbons of various aggregate and phase states (Naumko et al., 2004, 2014, 2017).

Quartz of the "Marmarosh diamond" type in the Krosno (Silesian) zone is associated with calcite. Calcite forms mottled veins (up to 55 mm) of various shapes, the thickness of which varies from microscopic to 2–3 cm and more. Veins with partially or completely leached calcite and traces of sliding are often observed. It is represented by crystalline-granular varieties, mainly fine-grained (0.1 mm) and coarse-grained (over 0.1 mm). Large-crystalline varieties predominate. Large calcite grains reach 4–6 mm. Dense aggregates, druses, and sometimes well-cut crystals are often found (Zankovych, 2016). The chemical composition of calcite of the veinlet-impregnated mineralization

of the rock complexes in the area of the New Beskydy Tunnel, is close to the theoretical one. Contains significant impurities of magnesium (0.00–0.37 wt. %), manganese (0.02–0.52 wt. %) and iron (0.06–0.87 wt. %).

Impurities in the chemical composition of quartz were not detected, because their content are near the detection limit. Numerous fluid inclusions of hydrocarbons were found in the investigated crystals of "Marmarosh diamonds" and calcite from the Krosno (Silesian) zone in the area of the New Beskydy tunnel (Naumko et al., 2017). According to mass spectrometry, the composition and ratio of volatiles in them is characterized only by the presence of hydrocarbons, mainly methane and the firsts members of its homologous series (see Tab. 2). In particular, all analysed samples are strongly dominated by methane (87.6–97.3 vol. %). In addition, in quartz crystal (sample NBT-1) there is homologous series of methane to propane (up to 2.9 vol. %), in another quartz crystal (sample NBT-7) – to butane with traces of heavier hydrocarbons, probably of the methane series (12.4 vol. %). It should be emphasized the high weight concentration of hydrocarbon components in the fluid (up to $392.236.10^{-6}$ g per g of the sample), which determines the possibility of its transfer of mineral substances (and hydrocarbons) and crystallization of parageneses with "Marmarosh diamonds" from such a hydrocarbon-containing fluid. The given data indicate the hydrocarbon orientation of upward migrating paleo-fluids (Naumko et al., 2022).

## Conclusions

Common and distinctive features of the morphology of quartz crystals of the "Marmarosh diamonds" type from the Slovak and Ukrainian Carpathians have been revealed.

Common in the "Marmarosh diamonds" from the Slovak and Ukrainian Carpathians are:
1. Presence of basic simple forms of hexagonal prism m $\{10\bar{1}0\}$ and rhombohedra r $\{10\bar{1}1\}$ and z $\{01\bar{1}1\}$.
2. Types of crystal habitus: hexagonal-dipyramidal, pseudocubic, hexagonal-prismatic, trigonal-prismatic.
3. Elongation of the crystals in the ratio of the dimensions along the $L_3$ axis to the $L_2$ axis is preferably < 1.5.

The differences in the polyhedra of "Marmarosh diamonds" from the Ukrainian and Slovak Carpathians are as follows:
1. On polyhedra from the Slovak Carpathians, less important simple forms are more common: the trigonal dipyramid s $\{11\bar{2}1\}$ and the trapezoid x $\{51\bar{6}1\}$.
2. In the Krosno (Silesian) zone of the Ukrainian Carpathians, greatly shortened individuals appear even more often.
3. Crystals flattened on $\{10\bar{1}0\}$ are more characteristic of the Slovak Carpathians.

Fluid inclusions of hydrocarbons are present in all

**Tab. 1**
Habit of "Marmarosh crystals" from Ukrainian Carpathians and Western Carpathians.

| Habit | The area of the New Beskydy tunnel crystals % | Dukla zone | Intra-Carpathian Paleogene |
|---|---|---|---|
| Hexagonal-dipyramidal | 7 | 35 | 31 |
| Pseudocubic | 1 | 24 | 23 |
| Hexagonal-prismatic (short-prismatic) | 30 | 18 | 18 |
| Hexagonal-prismatic (actually prismatic) | 1 | 7 | 3 |
| Trigonal-prismatic (short-prismatic) | 52 | 7 | 23 |
| Trigonal-prismatic (actually prismatic) | 9 | 9 | 2 |

**Tab. 2**
The composition of volatiles of fluid inclusions in "Marmarosh diamonds" and calcite of the veinlet-impregnated mineralization and closed pores of host rocks of the Krosno (Silesian) zone in the area of the New Beskydy tunnel) (Naumko et al., 2022).

| Number of the sample | Interval of selection [m] | Mineral (sample mass) | Components: volume share, % weight concentrations, $n.10^{-6}$ g/g of the sample[2] | | | Relative gas saturation $\Delta P$, Pa | Total weight concentration, $n.10^{-6}$ g/g of the sample[1] |
|---|---|---|---|---|---|---|---|
| | | | $CO_2$ | $CH_4$ | $C_nH_{2n+2}$ | | |
| NBT-1 | 1 247.6 | "Marmarosh diamond" crystal (0.16 g) | – | $\dfrac{97.3}{248.430}$ | $\dfrac{2.7^{[3]}}{0.370}$ | 36.0 | 248.800/311.000[2] |
| NBT-2 | 1 435 | The same (0.19 g) | – | $\dfrac{97.1}{61.530}$ | $\dfrac{2.9^{[3]}}{0.140}$ | 10.8 | 61.670/64.916[2] |
| NBT-3 | 1 445 | The same (0.32 g) | – | $\dfrac{97.1}{113.560}$ | $\dfrac{2,9^{[3]}}{0.250}$ | 33.3 | 113.81/71.130[2] |
| NBT-4 | – | Calcite crystal (0.43 g) | – | $\dfrac{99.0}{8.420}$ | $\dfrac{1.0^{[3]}}{0.002}$ | 3.2 | 8.422/3.817[2] |
| NBT-7 | 1 464 | "Marmarosh diamond" crystal (0.16 g) | – | $\dfrac{87.6}{204.100}$ | $\dfrac{12.4^{[3]}}{11.630}$ | 25.3 | 215.730/392.236[2] |

Notes:

1) – the total weight concentration in samples NBT-1–NBT-4 and NBT-1–NBT-7 was determined relative to the mass of the crystal;

2) – the total weight concentration is reduced to the standard amount of weight – 200 mg;

3) – in samples NBT-1–NBT-4 in the composition $C_nH_{2n+2}$ $n$ = 2, 3, in sample NBT-7 – n = 2–4 (up to 6).

calcite and quartz crystals of the "Marmarosh diamonds" type. By the chemical composition data, it is methane with impurities of higher hydrocarbons (up to hexane). The high weight concentration of hydrocarbon components in the fluid determines the possibility of its transfer of mineral substances (and hydrocarbons) and crystallization of parageneses with "Marmarosh diamonds" from such a hydrocarbon-containing fluid.

Detailed studies of the vein mineralization of the rock complexes of the Krosno (Silesian) zone of the Ukrainian Carpathians, exposed by the New Beskydy tunnel, make it possible to obtain important genetic information about the composition and distribution of hydrocarbons in fluid inclusions in non-ore minerals of the veinlet-impregnated mineralization as relics of migrating hydrocarbon fluids within the flysch formation of the region. Therefore, further mineralogical research will contribute not only to obtaining new results from mineralogy, geochemistry and crystallography, but also important data from the oil and gas geology of the Carpathian oil and gas-bearing province.

## Acknowledgement:

## References

Arkhipova, L. D., 1951: To the mineralogy of Kobyletska Polyana in Transcarpathia. *Mineral. Collection, 5, 243–252* (in Russian).

Birkenmajer, K. & Gedl, P., 2017: The Grajcarek succession (Lower Jurassic–Mid Paleocene) in the Pieniny Klippen Belt, West Carpathians, Poland: a stratigraphic synthesis. *Ann. Soc. geol. Pol., 87, 55–88.* doi: http://dx.doi.org/10.14241/asgp.2017.003.

Dudok, I. V., 2001: Peculiarities of hydrocarbon composition of inclusions in "Marmarosh diamonds" of the Ukrainian Carpathians. *Geol. geochem. comb. miner., 2, 51–62* (in Ukrainian).

Dudok, I. V., Vovk, O. P. & Karoli, S., 2002: Peculiarities of crystal morphology of "Marmarosh diamonds" from the Slovak Carpathians. *Mineral. Collection, 52, 2, 96–101* (in Ukrainian).

Dudok, I. V. & Yarmolovich-Shults, K., 2000: Possibilities of using fluid inclusions in the study of hydrocarbon migration processes ("Marmarosh diamonds"). *Prace Inst. Gór. naft. Gazow., 110, 447–450* (in Russian).

Fulín, M., 1997: Marmarošský diamant pri Veľkom Lipníku. *Minerál – Svět nerostů a drahých kamenů, 5, 1, 42–43.*

Goldschmidt, V., 1922: Atlas der Krystallformen. Band 7. *Heidelberg, Verlag Winters, Taf. 55–108.*

Hnylko, O., 2010: On the north-eastern boundary of the Krosno tectonic zone in the Ukrainian Carpathians. *Geol. geochem. comb. miner., 2, 151, 44–57* (in Ukrainian).

Hnylko, O., Hnylko, S., Heneralova, L. & Tsar, M., 2021: An Oligocene olistostrome with exotic clasts in the Silesian Nappe (Outer Ukrainian Carpathians, Uzh River Basin). *Geol. Quart., 65, 47, 1–18.*

Hurai, V., Širáňová, V., Marko, F. & Soták, J., 1995. Hydrocarbons in fluid inclusions from quartz-calcite veins hosted in Paleogene flysch sediments of the Central Western Carpathians. *Miner. Slov., 27, 383–396.*

Kalyuzhnyi, V. A. & Sakhno, B. E., 1998: Prospects for forecasting minerals by typomorphic features of fluid inclusions of hydrocarbons and carbon dioxide (Transcarpathian Basin, Folded Carpathians. Ukraine). *Geol. geochem. comb. miner., 3, 104, 133–147* (in Ukrainian).

Kolodii, V. V. (ed.), 2004: Carpathian oil and gas province. *Lviv – Kyiv, Ukrainian Publ. Center LLC, 1 – 390* (in Ukrainian).

Kvasnytsia, I. V., 2016: Rhombohedron {0112} on crystals of "Marmarosh diamonds" (Ukrainian Carpathians). *Notes Ukrainian Miner. Soc., 13, 32–35* (in Ukrainian).

Lazarenko, E. K. & Lazarenko, E. A., Baryshnikov, E. K. & Malygina, O. A., 1963: Mineralogy of Transcarpathia. *Lvov, 1–380* (in Russian).

Matkovskyi, O. (ed.), 2011: Minerals of the Ukrainian Carpathians. Silicates. *Lviv, Ivan Franko Lviv Nat. Univ., 1– 520* (in Ukrainian).

Matkovskiy, O. I., 1961: On the so-called "Marmarosh diamonds". *Mater. commiss. miner. geochem., 1, 149–158* (in Russian).

Naumko, I., Bratus, M., Dudok, I., Kalyuzhnyi, V., Kovalyshyn, Z., Sakhno, B., Svoren, Yo. & Telepko, L., 2004: Fluid regime of catagen-hydrothermal process of the period of formation of vein and vein-interspersed mineralization In: Kolodii, V. V. et al.: Carpathian oil and gas province. *Lviv – Kyiv, Ukrainian Publ. Center LLC, 308 – 345* (in Ukrainian).

Naumko, I. & Zankovych, H., 2014: Hydrocarbons of fluid inclusions in minerals of oil and gas rock complexes of the Krosno zone of the Ukrainian Carpathians (state and research priorities). *Miner. collection, 64, 1, 134–154* (in Ukrainian.)

Naumko, I. M., Zankovych, G. O., Kuzemko, Ya. D., Dyakiv, V. O. & Sakhno, B. E., 2017: Hydrocarbon gases of fluid inclusions in "Marmarosh diamonds" from veins in deposits of the flysch formation in the area of the New Beskydy tunnel (Krosno zone of the Ukrainian Carpathians). *Reports. NAS Ukraine, 10, 70–77.* DOI: https://doi.org//10.15407 dopovidi2017.10.070 (in Ukrainian).

Naumko, I., Zankovych, G., Kokhan, O., Vovk, O., Kuzemko, Ya., Sakhno, B. & Serkiz, R., 2022: Non-ore minerals of the veinlet-impregnated mineralization in the sediments of the Krosno zone of the Ukrainian Carpathians. *Geol. geochem. comb. miner., 1–2* (*187–188*), *103–114.* https://doi.org//10.15407/ggcm.2022.01-02.103 (in Ukrainian).

Udubasa, G., Ďuda, R., Szakáll, S., Kvasnytsya, V., Koszowska, E. & Novák, M., 2002: Minerals of the Carpathians. Ed. by Sándor Szakáll. *Prague, Granite, 479 p.*

Vityk, M. O., Bondar, R. J. & Dudok, I. V., 1996: Fluid inclusions in "Marmarosh diamonds": evidence for tectonic history of the Folded Carpathian Mountains, Ukraine. *Tectonophysics, 255, 163–174.*

Vovk, O., Zankovych, G. & Naumko, I., 2018: Peculiarities of crystal morphology of "Marmarosh diamonds" from veins in flysch deposits of the Krosno structural-facial unit of the

Ukrainian Carpathians (area of the New Beskydy Tunnel). *Miner. collection, 68, 1, 72–75* (in Ukrainian).

Vovk, O. P., Zankovich, G. O. & Naumko, I. M., 2019: Materials for the comparative characterization of crystal morphology of "Marmarosh diamonds" of the Ukrainian and Slovak Carpathians. Achievements and prospects of geological science in Ukraine. *Proc. sci. conf. dedic. 50th anniv. Inst. Geochem., Miner. Ore Form. M. P. Semenenko Nat. Acad. Sci. Ukr. (Kyiv, May 14–16, 2019). 2 vol. Kyiv, IGMO Ukr., 1, 130–131* (in Ukrainian).

Vozniak, D. K., Lazarenko, E. K. & Pavlyshyn, V. I., 1978: A new genetic type of quartz – skeletal crystals with inclusions of hydrocarbons. *Region. Genetic Miner., 2, 15–26* (In Russian).

Vozniak, D. K., Kvasnitsa, V. N. & Galaburda, Yu. A., 1974: Typomorphic features of "Marmarosh diamonds". *In: Typomorphism of Ukrainian quartz, Kyiv, 79–82* (in Russian).

Zatsikha, B. V., Kvasnitsa, V. N., Galiy, S. A. & Matkovskiy, O. I., 1984: Typomorphism of minerals from polymetallic and mercury deposits in Transcarpathia. *Kyiv, Naukova Dumka, 1–168* (in Russian).

Zankovych, H., 2016: Geochemistry of fluids of veinlet-impregnated mineralization of promising oil- and gas-bearing complexes of the north-western part of the Krosno zone of Ukrainian Carpathians. (Extended abstract of candidate thesis). *Lviv, Ukraine, Inst. Geol. Geochem. Comb. Miner. NAS Ukr* (in Ukrainian).

# Porovnanie morfológie kryštálov kremeňa – „marmarošských diamantov" – zo sekvencií paleogénneho flyšu krosnianskej (sliezskej) a duklianskej zóny v Karpatoch na Ukrajine a vnútrokarpatských paleogénnych sekvencií Západných Karpát

Na komparatívny goniometrický výskum kryštálov kremeňa, tzv. marmarošských diamantov, boli použité vzorky z reprezentatívnych výskytov vo Východných Karpatoch na území Ukrajiny – kryštálov v žilách vo flyšových sedimentoch krosnianskej (sliezskej) jednotky (137 kryštálov; lokalita 1 – nový Beskydský tunel; obr. 2 – 7) a tiež v oligocénnych sedimentoch duklianskej zóny (77 kryštálov, lokalita 2 – priesmyk Pryslip; obr. 2 a 3). „Marmarošské diamanty" v Západných Karpatoch na území Slovenska zastupovali výskyty vo vnútrokarpatských paleogénnych sekvenciách na lokalite 3 – Veľký Lipník, vodný tok Šoltysa (175 kryštálov; obr. 2 a 3 ).

Získané výsledky potvrdzujú, že „marmarošské diamanty" zo študovaných lokalít oboch štátov vykazujú podobné charakteristiky. Dominantne sú zastúpené jednoduché kryštály hexagonálneho prizmatického tvaru $m$ $\{10\overline{1}0\}$ a tiež romboédre $r$ $\{10\overline{1}1\}$ a $z$ $\{01\overline{1}1\}$. Identifikované boli aj nasledujúce polyhedrálne kryštálové tvary: hexagonálno-dipyramidálny, pseudokubický, hexagonálno-prizmatický a trigonálno-prizmatický. Predĺženie kryštálov vyjadruje pomer rozmerov pozdĺž osi $L_3$ k osi $L_2$, ktorý vykazuje hlavne hodnoty < 1,5.

V prípade výskytov v Ukrajinských Karpatoch sú trigonálno-dipyramidálny tvar $s$ $\{11\overline{2}1\}$ a trapezoidný tvar $x$ $\{51\overline{6}1\}$ menej typické. Štatisticky sa kryštálový tvar „marmarošských diamantov" z Ukrajinských Karpát prejavuje ako viac izometrický. Ich predĺženie pozdĺž hlavných kryštalografických osí je menej typické ako v prípade polyhedrálnych tvarov zo slovenských lokalít. Navyše, „marmarošské diamanty" zo slovenského územia Západných Karpát sú častejšie splošteného tvaru $v$ $\{10\overline{1}0\}$. V procese rastu kryštálu sa pri poklesávajúcej teplote tvar mení z hexagonálno-dipyramidálneho na trigonálno-prizmatický.

Kremeň z krosnianskej (sliezskej) zóny Ukrajinských Karpát sa zistil v asociácii s kalcitom. V oboch mineráloch sa vyskytujú početné inklúzie.

Vo všetkých kryštáloch kalcitu a kremeňa „marmarošských diamantov" sú prítomné inklúzie uhľovodíkov. Podľa údajov o chemickom zložení ide o metán s nečistotami vyšších uhľovodíkov (až po hexán). Vysoká hmotnostná koncentrácia uhľovodíkových zložiek vo fluide určuje možnosť prenosu minerálnych látok (a uhľovodíkov) a kryštalizáciu paragenéz s „marmarošskými diamantmi" z tzv. fluíd obsahujúcich uhľovodíky. Podrobné štúdie žilnej mineralizácie horninových komplexov krosnianskej (sliezskej) zóny Ukrajinských Karpát odkrytých novým Beskydským tunelom umožňujú získať dôležité genetické informácie o zložení a distribúcii uhľovodíkov v kvapaline inklúzie v nerudných mineráloch žily, ktorá reprezentuje relikty migrujúcich uhľovodíkových tekutín v rámci flyšovej formácie regiónu. Ďalší mineralogický výskum prispeje nielen k získavaniu nových výsledkov z mineralógie, geochémie a kryštalografie, ale aj dôležité údaje z karpatského ložiska ropy a plynu.

Mineralogicko-kryštalografický a geochemický výskum (so zameraním na migráciu hydrokarbonátových fluíd) poskytuje podstatné informácie pri vyhľadávaní a prieskume výskytov ropy a zemného plynu v karpatskej roponosnej a plynonosnej provincii.

# Comparison of two model environmental burdens with massive light non-aqueous phases liquids (LNAPL) pollution – the extent of pollution identified by geological survey vs. reality uncovered by remediation

JURAJ MACEK[1, 2], ĽUBOMÍR JURKOVIČ[1], JÁN MILIČKA[1], ROMAN TÓTH[1, 2]
and HANA HORVÁTHOVÁ[1]

[1]Comenius University in Bratislava, Faculty of Natural Sciences, Department of Geochemistry,
Ilkovičova 6, 842 15 Bratislava 4, Slovak Republic; juraj.macek@uniba.sk
[2]The Centre of Environmental Services, Ltd., Kutlíkova 17, 852 50 Bratislava, Slovak Republic

**Abstract:** The paper deals with the results of exploration and remediation in two railway operations. Locomotive depots in Štúrovo and Leopoldov belonged to heavily polluted sites with the occurrence of light non-aqueous phases liquids (LNAPL) on the groundwater table. Remediation began on the sites in 2018. The results of the pre-remediation surveys did not indicate the presence of large volumes of pollution in the form of free phase, however, during the remediation LNAPL flowed into new wells. At the same time, the spreading of LNAPL accumulations and the progressing of pollution in dissolved form by groundwater has not been confirmed. Comparison of surveys and remediation points to various facts that must be considered when evaluating the degree of pollution of the site. It is necessary to perceive the whole space of the railyard as possible source of pollution. Remediation project should not be based solely on the presence of LNAPL. Its presence and the risk it poses must be verified. Outcomes of activities, based on limited data, may in that case differ from the remediation goals.

**Key words:** remediation, light non-aqueous phases liquids, locomotive depot, environmental burden
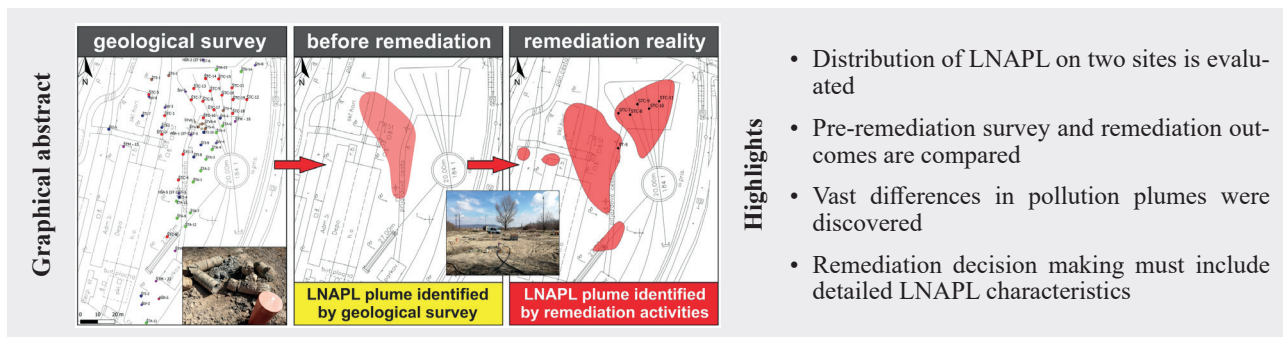
## Introduction

The basis for planning of a remediation is usually a detailed site survey. It mostly results in accurate information on the nature and spatial distribution of the pollution. Selected sites, locomotive depots in Leopoldov and Štúrovo (Fig. 1), have a long history of repairs of traction rolling stock. Both were already in operation in the 1950s. During transition from steam to diesel traction, both depots switched to maintenance of diesel locomotives.

During operations, leakage of oil-based operating fluids (diesel, lubricants) may have occurred, either due to leaks from single walled tanks and fittings or improper handling. Both sites have been examined in detail in the past (Štúrovo depot – Polák, 1987; Solymosiová et al., 1988; Leopoldov depot – Vrana, 2008) and since 2008 groundwater monitoring has been carried out on both sites.

In Štúrovo, four boreholes in the vicinity of underground storage tanks were identified, in which light non-aqueous phases liquids (LNAPL) thicknesses up to 870 mm were present for a long time (Kostolanský et al., 2017a). In Leopoldov, LNAPL was observed only in one borehole located near the fuel dispensing point (LEV-1 borehole). The assumed sources of pollution were fuel pipelines or leaks from pumping fuel (Kostolanský et al., 2017b). In 2017, both sites were included in the group of 14 railway sites where the Ministry of Environment of Slovak Republic was approved for the implementation of remediation. In the information system of environmental burdens, the sites were registered as confirmed environmental burdens – NZ (029) / Štúrovo-Rušňové depo, Cargo, a. s. (SK/EZ/NZ/601) and HC (1844) /
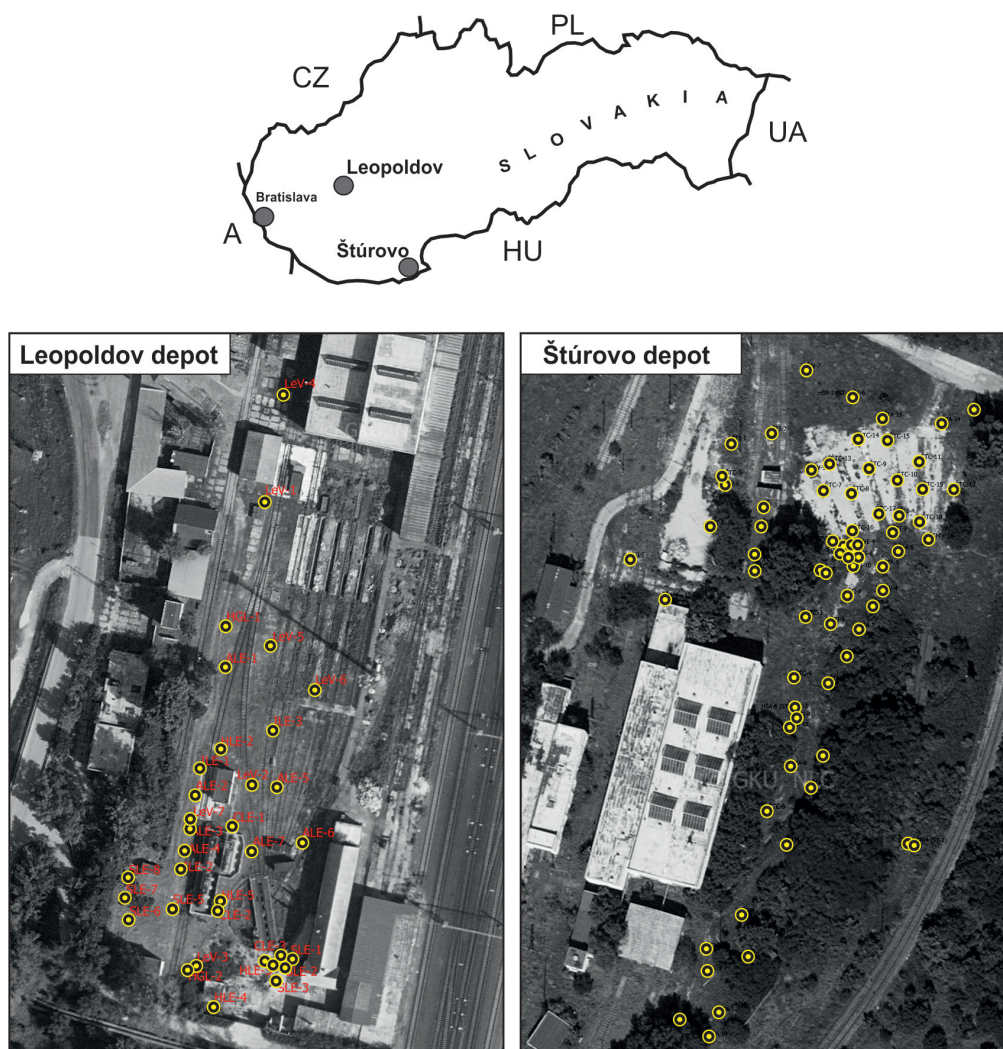
**Fig. 1.** Schematic map of model locomotive depots with the location of realized geological and remediation objects

Leopoldov-Rušňové depo, Cargo, a. s. (SK/EZ/HC/1844). The depot in Štúrovo has been out of operation since 2008, operation in Leopoldov is limited at present.

The first step of remediation was the pre-remediation survey which led to update of the risk assessment. Atmogeochemical measurements (detection of VOC´s in soil vapor) were carried out as a part of the survey, which primary focused on the drilling of soil probes and hydrogeological wells from which soil and groundwater samples were collected. Primary concentrations of organic substances – NEL-IR (non-polar extractable substances – infrared spectrum), NEL-UV (non-polar extractable substances – ultraviolet spectrum), $C_{10}$–$C_{40}$ (total petroleum hydrocarbons via GC-FID), BTEX (benzene, toluene, ethylbenzene, xylenes), CAH (chlorinated aliphatic hydrocarbons), PAH (polycyclic aromatic hydrocarbons), and PCB (polychlorinated biphenyls) – were determined in the samples and the extent of contamination was continuously adapted based on the new information obtained during the geological survey. Concentrations of

BTEXs, CAHs, PAHs and PCBs were low, or under the laboratory detection limit.

The results of the survey in Leopoldov identified extensive soil pollution in the vadose zone (0.0–1.0 m below ground surface (bgs) at max. 2 320 mg.kg$^{-1}$ $C_{10}$–$C_{40}$, 3.0–5.0 m bgs max. 6 160 mg.kg$^{-1}$ $C_{10}$–$C_{40}$) and in the saturation zone (5.0–7.0 m bgs up to 5 690 mg.kg$^{-1}$ $C_{10}$–$C_{40}$) and in groundwater (up to 6.76 mg.l$^{-1}$ $C_{10}$–$C_{40}$). Pollution consisted of oil substances (diesel), identified mainly in the area under the turntable and under the above-ground fuel tanks. The occurrence of LNAPL was confirmed during the survey only in the original LEV-1 well (Tupý et al., 2019). In the newly built wells only an oil sheen was observed at the groundwater head. The assumed sources of pollution were handling areas of filling and discharging of fuel, operating place of oil-mill and above-ground fuel tanks.

Survey in Štúrovo depot identified very extensive soil contamination at the top of the saturation zone with the content of $C_{10}$–$C_{40}$ in soils up to 17 200 mg.kg$^{-1}$. The

maximum concentration of $C_{10}$–$C_{40}$ in groundwater was up to 7.71 mg.l$^{-1}$. The occurrence of LNAPL was observed only in old wells on area of about 700 m$^2$. The assumed source of pollution were three underground single walled fuel storage tanks – USTs (Urban et al., 2019).

Based on the results of pre-remediation survey, the main planned remediation operations focused to the pumping and treatment of groundwater in oil separators and the pumping of LNAPL out from the created hydraulic depressions. In Leopoldov, the removal 2 000 m$^3$ of polluted soils was also planned. The paper deals with the results of exploration and remediation activities on above mentioned sites. Other techniques used for LNAPL plume estimation are described in case studies in papers by Dippenaar et al. (2005), Steyl et al. (2012) or Mineo et al. (2022).

### Geological situation at model sites

#### *Leopoldov*

According to Vass (2014) the investigated territory belongs to the Danube Basin, Blatné Depression, belonging to the Váh river floodplain and lies on Quaternary fluvial sediments. Lithofacially it is built by undivided fluvial loams or sandy to gravel loams. More lithological and lithofacial information are presented by Maglay et al. (2005) and Maglay et al. (in press).

Alluvial sediments of the Váh river in broader area reach a thickness of 7–10 m. On the surface, there are clays and sands of variable thickness (1–4 m), below them there is a continuous layer of gravel and sand (Valušiak, 1987). Exploration works (wells LEV-1 to LEV-7) verified the lithological conditions in the area of the locomotive depot up to a depth of 12 m below ground level (Vrana, 2008). Below the backfill layer, 0.5 m thick, locally up to 2.8 m, there is a clay-sandy layer (sandy clay, loamy sand) 1.6 to 1.8 m thick. Below is developed a sandy layer with an admixture of gravel to a depth of approx. 4.5–5 m, below which sandy gravels occur.

The Neogene sediments do not outcrop to the surface anywhere within the Quaternary alluvial basement in the immediate vicinity. The underlying Neogene is built of Pontian sediments with a predominance of variegated clays with positions of fine, medium, loamy-clay sands and locally with gravel lenses (Valušiak, 1987). The basement of the gravel-sand layer is formed by impermeable clay and was verified in the area of the locomotive depot at a depth of 10 to 11 m below the ground. Representative geological profile of locality Leopoldov with massive contamination is presented in Fig. 2.

#### *Štúrovo*

The area of interest is located on the eastern edge of the Štúrovo-Mužla Terrace with poorly divided terrain between the valley floodplains of the Hron and the Danube rivers. The terrace is built of Quaternary sediments – gravel-sand facies approx. 3–4 m thick, with well-worked layers of all
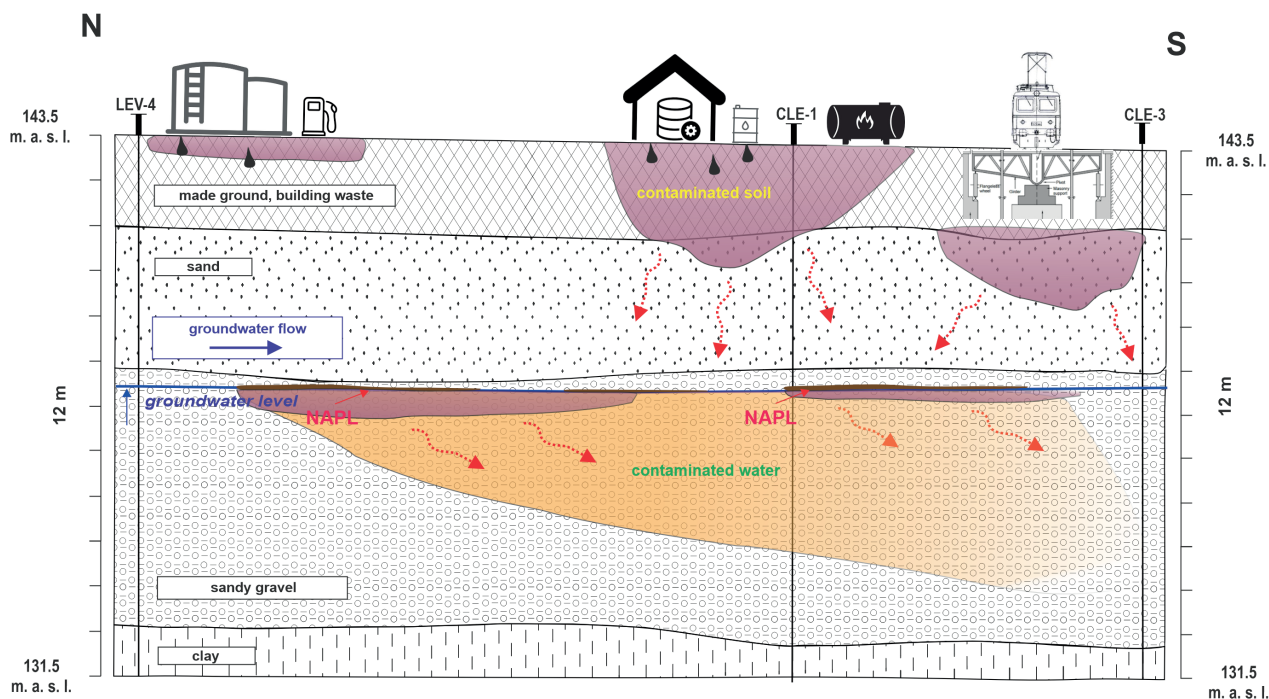


**Fig. 2.** Leopoldov depot – geological situation at model site in cross section with contamination.

grain size categories. Pebbles consist of quartz, quartzite, more rarely of granitic rocks. The occurrence of the sandy fraction is variable in percentage content and grain size. In the overburden of sandy gravels, the loess, loess clays and clays of considerable thickness occur, approx. 8–10 m thick. The base of the terrace consists of clayey-sandy sediments of the Neogene and Paleogene. More detailed lithological and lithofacial information are presented by Nagy et al. (1998). Representative geological profile of locality Štúrovo with massive contamination is on the Fig. 3.

From a geological point of view, the localities differ considerably. In Leopoldov, under a layer of material accumulation up to 3.0 m thick, a great water bearing gravel layer occurs. The Váh floodplains in the wider area reach a thickness of 7–10 m. The survey verified the lithological conditions of the area up to a depth of 12 m below the ground surface in the locomotive depot. Below the 0.5 m thick bacfill layer (locally up to 2.8 m) a clayey-sandy layer (sandy clay, loamy sand) with thickness of 1.6 to 1.8 m is located. Below is a sandy layer with gravels up to a depth of ca. 4.5–5 m, below this layer sandy gravels occur (Tupý et al., 2019).

The base of gravel-sandy layer is built by impermeable clays and was verified in the locomotive depot at a depth of 10 to 11 m below the ground surface. The main collectors of groundwater are Quaternary gravel-sandy sediments, which reach a thickness of about 10–15 m in the studied area (Tupý et al., 2019).

The coefficient of hydraulic conductivity of gravel sandy sediments ranges from 1 to $2.10^{-3}$ m.s$^{-1}$. From a hydraulic point of view, the groundwater in the Quaternary sediments is unconfined. General direction of groundwater flow is from north to south.

The situation is considerably different in Štúrovo. Geological conditions in the locomotive depot were verified by new wells to the depth of 15 m below ground surface. Below the top 0.5–3.8 m thick backfill layer, there is an impermeable layer consisting of silty clay and silt. Under these, from a depth of 7.8–9.8 m sandy gravels 1.7–4.0 m thick (in average about 2.5 m) occur. Below the impermeable clays occur (Auxt et al., 2009; Urban et al., 2019). Groundwater at the site of interest is in sandy gravels of fluvial origin. It is filled up with infiltrated rainwater. The height of the water column is very variable and depends not only on the infiltrated amount of precipitation, but also on the character of the bedrock and the overall natural conditions. Transmissivity also varies, hydraulic conductivity coefficient ranges inbetween $10^{-4}$ to $10^{-5}$ m.s$^{-1}$, aquifer is confined.

## Methods

The removal of pollution from both sites was based on a similar principle. The pumping and infiltration wells with a diameter of 200 mm were drilled and the groundwater pumping started. After groundwater treatment in the oil separator, it was infiltered via several wells back into the aquifer. In Štúrovo, it was enough to pump water of
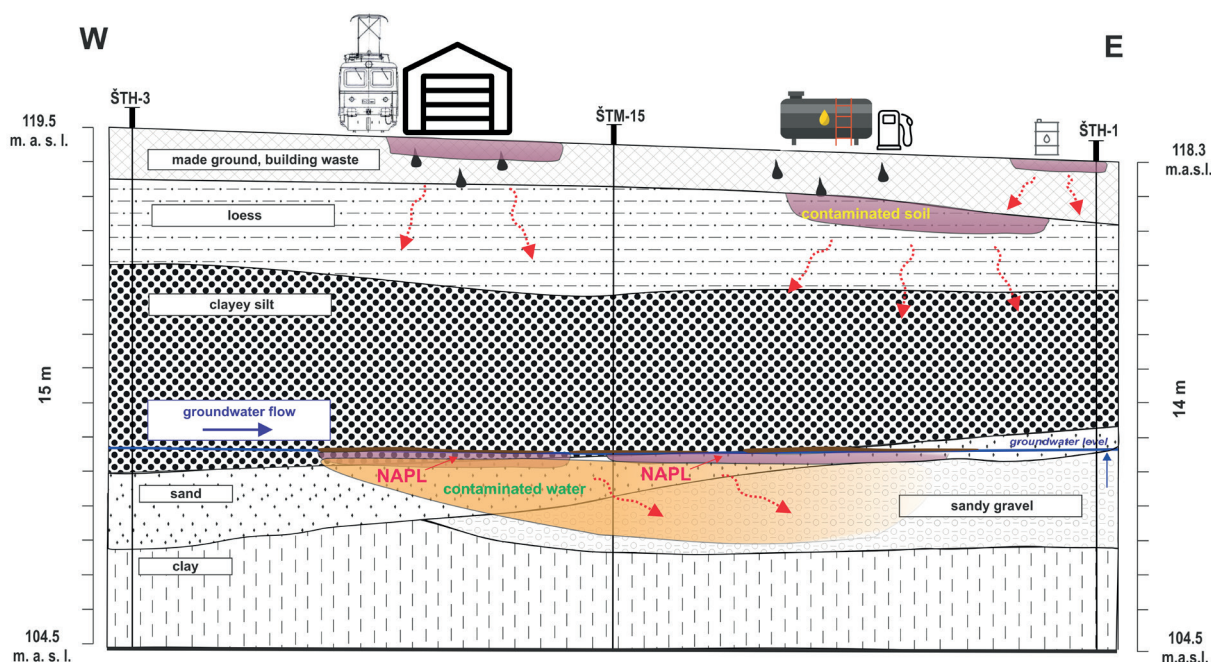


**Fig. 3.** Štúrovo depot – geological situation at model site in cross section with contamination.

about 0.5–1.0 l.s$^{-1}$ to create optimal depression cones, into which pollution flowed. On the contrary, in Leopoldov, the lowering of groundwater levels in the wells was achieved by pumping more than 3.0 l.s$^{-1}$. In addition, in Štúrovo there was not sufficient groundwater inflow into the pumped wells, and therefore it was necessary to gradually reduce the pumping capacity.

Remediation was carried out for approximately 2 years at both sites. These included supplementary methods to remove residual pollution such as air-sparging, soil washing and enhanced biodegradation by bacterial strains isolated from the contaminated soil in Štúrovo. In 2021, the turntable and the polluted soils below it were removed in Leopoldov (Fig. 4). The excavation was carried out about 2 m below groundwater level. Subsequently, LNAPL was skimmed from the water table. Groundwater samples were analysed at the accredited laboratory ALS Czech Republic, s. r. o., Na Harfě 336/9, Praha 9, Czech Republic. The "CZ_SOP_D06_03_151 (ČSN EN ISO 9377-2)" method for detection of extractable compunds in the hydrocarbon range C10–C40 (gas chromatography with flame ionisation detector) was utilized.



**Fig. 4.** LNAPL in excavation pit at locality Leopoldov depot.

## Results and discussion

### *Štúrovo*

To start the remediation, the pumping out of LNAPL from the existing wells was realized. Almost 150 l of pollution was pumped from the ST-5 well at once. The initial step of remediation at both sites was to build a network of new wells. In Štúrovo, the drilling was carried out stepwise in 5 stages. In Leopoldov, the remediation wells were drilled in one stage (except for airsparging wells).

During drilling works in Štúrovo, spontaneous LNAPL inflows into new wells were observed. During the realization of wells (07/2019) at the margin of the assumed pollution cloud (identified in Urban et al., 2019), a relatively fast inflow of LNAPL into two new wells was observed.

In the next phase of drilling works (07/2020), a large area with another source of pollution at the site was identified. This source of LNAPL pollution was more quantitatively abundant as in the area around the underground storage tanks. The presence of pollution in the form of a mobile LNAPL was confirmed in the track area in front of the former roundhouse, that no longer exists today. The high degree of soil saturation by pollution was also confirmed by the immediate occurrence of LNAPL in new wells (up to a thickness of almost 1 000 mm). LNAPL was first pumped without supporting groundwater pumping (in several wells on the site, after the initial volume of the LNAPL was pumped out, it has not immediately inflowed again). High inflows of LNAPL in several new wells (STC-8, STC-10) were the impulse for starting groundwater pumping in adjacent wells (STC-7, STC-9, STC-11). Subsequently, LNAPL with a thickness of almost 1500 mm (STC-9) appeared in these wells (except STC-11). Approximately 2 m$^3$ of pollution was pumped from wells in the vicinity of underground reservoirs and more than 4 m$^3$ from wells in the railyard area. Thus, the source of pollution identified during the remediation (trailyard in front of the former depot building) was double abundant in terms of extracted LNAPL as the originally considered source of pollution (underground fuel tanks). In addition to the two main pollution sources, two smaller sources (fuel pipeline and repair pit) were identified at the site (Urban et al., 2021).

The remediation thus verified the pollution by LNAPL on an area approximately three times larger than originally expected (Fig. 5). The work of Macek and Milička (2021) evaluates the nature of pollution regarding its degradation and the result is the conclusion that the pollution comes from several different sources. Despite the fact, that the depot has been out of operation for more than 10 years, one of the collected LNAPL samples showed no obvious signs of degradation.

**Fig. 5.** LNAPL plume at model localities identified by remediation activities – a) Leopoldov depot (Tupý et al., 2022), b) Štúrovo depot (Urban et al., 2021).

The estimated age of pollution at the site is from 8 to 48 years.

### Leopoldov

In Leopoldov, the remediation wells were drilled in one stage (except for airsparging wells). No significant spontaneous infiltrations of LNAPL were observed in the newly built wells (07/2019). Free phase was observed in 08/2019 in 9 wells (of 13) with a maximum layer thickness of 40 mm. After the start of remediation and the start of groundwater pumping in August 2019, significant inflows of pollution in the form of LNAPL were observed in the CLE-1 and CLE-2 wells. LNAPL flowed into the CLE-2 well immediately after it was pumped, reaching a thickness of almost 80 cm (approx. 25 l), which was the highest volume of all wells. Gradually, after the groundwater pumping from new drilled wells, LNAPL inflow was also observed in wells CLE-3, ALE-4, ALE-7, HLE-2 and ILE-2. The area around the turntable and above-ground fuel tanks thus proved to be much more polluted than originally expected. In total, more than 5 m³ of LNAPL, and of LNAPL and groundwater mixtures, with high contents of emulsified petroleum substances, were pumped exclusively from boreholes in the turntable area and fuel tanks.

The distribution of the pollution identified during the remediation corresponds to the area identified by the pre-remediation survey. However, the concentration of pollution highly exceeds the original assumptions. The occurrence of LNAPL also in the area around the CLE-3 well behind the turntable (downgradient from the source) proved the high degree of soil and groundwater pollution in the studied area (Fig. 6). This fact was not discovered either by long-term monitoring work in the years 2008–2017 (Kostolanský et al., 2017b) or by the pre-remediation survey (Tupý et al., 2019). It should be noted that the monitoring wells (Kostolanský et al., 2017b) are located mainly in the railyard area, upgradient from turntable and UST. In the originally assumed pollution center, the situation was exactly reverse. Pollution was pumped out from the LEV-1 well (units of liters) and no repeated inflow was observed.

The aim of the paper is to point out the different pollution conditions at the sites, which were found before and during the remediation. During the surveys, no LNAPL was observed in the newly built wells; according to LSPA (2008), the presence of LNAPL in mobile form should by indicated by high levels of pollution in some soil samples (more than 10,000 mg.kg$^{-1}$ C$_{10}$–C$_{40}$). Nevertheless, during remediation of both sites, large volumes of pollution were pumped out of the wells (in Leopoldov approx. 5 m³, in Štúrovo approx. 6.5 m³). The high degree of pollution was evident in Štúrovo already at the beginning of the drilling works during the remediation. LNAPL flowed into some remediation wells spontaneously immediately after drilling.

During the remediation, several facts were observed, which were inconsistent with theoretical assumptions, based on the characteristics of pollutants and the properties of the geological environment. Laboratory analyses of groundwater samples from Leopoldov collected prior remediation (August 2019), showed low pollution concentrations in the CLE-2 well (compared to the results of other samples). They achieved approximately double IT criteria for NEL-IR and C$_{10}$–C$_{40}$, and the concentrations in samples from other wells (ALE-4, ALE7, ILE-1) exceed these values up to 20 times (Tab. 1). In the sample from the CLE-1 well, the concentrations of both parameters were below the ID criterion. However, the highest amount of LNAPL was during the remediation extracted from wells CLE-1 and CLE-2.

**Fig. 6.** LNAPL plume at model sites (Leopoldov depot) – a) identified by geological survey, b) identified by re-mediation activities (Tupý et al., 2022).

**Tab. 1**

Evaluation of groundwater contamination in Leopoldov – selected parameters and wells (Tupý et al., 2022; *ID/IT Criterion from Directive of Ministry of Environment of the Slovak Republic No. 1/2015-7, Anon, 2015).

| Well | NEL-IR [mg.l$^{-1}$] | C$_{10}$–C$_{40}$ [µg.l$^{-1}$] |
|---|---|---|
| CLE-1 | 0.119 | 216 |
| CLE-2 | 2.22 | 1 230 |
| ALE-4 | 2.33 | 5 600 |
| ALE-7 | 8.67 | 7 060 |
| ILE-1 | 5.05 | 11 700 |
| ID Criterion* | 0.5 | 250 |
| IT Criterion* | 1 | 500 |

In Štúrovo the inflow of LNAPL was observed into wells outside the two main contamination clouds, probably due to preferential pathways and the realization of remediation pumping of groundwater from the wells. On the other hand, the inflow of LNAPL into the well in the assumed center of the pollution (under removed USTs) did not occur after its drilling, neither after the start of groundwater pumping and the subsequent depression of its level. LNAPL appeared in this well spontaneously about half a year after its completion despite the fact, that there was no pumping of groundwater from other wells in its vicinity. This may be the result of natural changes in the groundwater level within the changes of the seasons. The volume of LNAPL calculated according to the Directive of the Ministry of Environment of the Slovak Republic No. 1/2015-7 (Anon, 2015) was significantly overestimated for Štúrovo (10.5 m$^3$ of pollution on an area of 700 m$^2$). The formula used does not contain any correction in terms

of soil or free product properties (Hall et al., 1984; de Pastrovich et al., 1979); moreover, due to the confined aquifer, the values measured in the field do not correspond to reality, but are highly overestimated (Hawthorne et al., 2011). Also, the soil pores are not completely saturated with pollution. According to API (1998), the pores in coarse-grained materials as sandy gravels in both localities are saturated with pollution in the range of 10–56 %. Considering 270 measurements carried out in the research, only in 17 % of the samples was observed the pore saturation by more than 10 %.

Generally, we can say that despite the large volume of pollution that was found in the porous media, there was no spread of the LNAPL, nor contamination dissolved in groundwater. This is consistent with the research of Rice et al. (1995). The authors examined LNAPL contamination clouds at 271 sites with underground storage tanks; their spreading was demonstrated in only 8 % of examined cases. Similarly, no spread of pollution in dissolved form in groundwater has been reported. During the long-term monitoring of both sites no increased values of oil sub-stances dissolved in groundwater were observed. The reason may be the out washing of more soluble parts of groundwater pollution in the past (Kostolanský et al., 2017a, b). In groundwater samples from wells located approximately 10 m (or even less) from the LNAPL clouddowngradient, only minimal pollution concentra-tions were observed during the remediation. Pollution in dissolved form was identified only in wells where LNAPL was observed (thickness in order of mm to cm). A more detailed analysis of these samples (treatment of the sam-ples with non-polar silica gel) revealed that part of the con-taminant identified by laboratory analyses as petroleum, refers not to petroleum hydrocarbons. These results are likely influenced by pollution degradation products (polar

substances) preferentially dissolved in groundwater and detected by $C_{10}$–$C_{40}$ analysis (Lang et al., 2009; Zemo et al., 2017; Bruckberger et al., 2018).

## Conclusion

The distribution of pollution found in the pre-remediation survey at both sites was significantly different from the findings obtained by the remediation. New abundant sources of pollution have been identified at both sites. During the remediation, more than 1 m³ of pollution was extracted from the newly drilled wells. Pollution in the vicinity of above-ground storage tanks in Leopoldov can be attributed to leakage from them or to the leakage from the diesel pipeline. The occurrence of pollution in Štúrovo is discontinuous, therefore its probable source are not only USTs, but also massive leaks in the railyard during the operation of the depot. The extracted volume of pollution, as well as the rate of spontaneous re-inflow of LNAPL into the boreholes, suggests the local high degree of saturation of the rock pores by the pollution.

In the case of historic railway sites, it is therefore necessary to consider not only well-defined sources of pollution e.g. such as oil and fuel housekeeping and distribution, but also the whole space of the railyard as possible source. Pollution at examined sites is of different nature (diesel, lubricating oil) as well as different degrees of degradation. This fact indicates continuous leaks during the active period of operation. The suggestion for the implementation of remediation should not be based solely on the identification of LNAPL in wells on the site, as it is in accordance with the Directive of the Ministry of Environment of the Slovak Republic no. 1/2015-7. The assessment of the contamination degree must be verified, for example, based on experimental extraction of LNAPL from wells and the continuity of repeated inflow, and (or) on long term evaluation of LNAPL thickness in wells. Costs and duration of remediation activities, projected based on limited data, are thus very hard to estimate and contain high risk of discovering important new facts related to site contamination.

## Acknowledgement

## References

Anon, 2015: Directive of Ministry of Environment of the Slovak Republic No. 1/2015 – 7 for the elaboration of risk assessment analysis of contaminated sites. *Bratislava, Ministry Environ. Slovak Rep., 1–96* (in Slovak).

API (American Petroleum Institute), 1998: Recommended Practices for Core Analysis. 2nd Ed. *Washington*, *Amer. Petroleum Inst., 1–200.*

Auxt, A. & Ingár, K., 2009: Vypracovanie programov opatrení v rámci prípravy plánov manažmentu oblastí povodí v súlade s požiadavkami vodného zákona a Rámcovej smernice o vode pre prevádzky ZSSK CARGO a. s. – III. etapa prác – Doplnkový prieskum životného prostredia vo vybraných prevádzkach ZSSK Cargo Slovakia, a. s. Záver. správa. *Manuskript. Bratislava, Cenvis*.

Bruckberger, M. C., Bastow, T. P., Morgan, M. J., Gleeson, D., Banning, N., Davis, G. & Puzon, G. J., 2018: Biodegradability of polar compounds formed from weathered diesel. *Biodegradation, 29, 443–461.*

De Pastrovich, T. L., Baradat, Y., Barthel, R., Chiarelli, A. & Fussell, D. R., 1979: Protection of ground waterfrom oil pollution. *The Hague, Netherlands, CONCAWE report, 3/79, 1–61.*

Dippenaar, M. A., Sole, M. D., Van Rooy, J. L., du Toit, G. J. & Reynecke, J. L., 2005: Determining actual LNAPL plume thickness: review and case study in a fractured aquifer. *Bull. Eng. Geol. Environ., 64, 347–360.*

Hall, R. A., Blake, S. B. & Champlin Jr., S. C., 1984: Determination of hydrocarbon thickness in sediments using borehole data. Proceeding of the 4th National Symposium on Aquifer Restoration and Ground Water Monitoring. *National Water Well Assoc., 300–304.*

Hawthorne, J. M., Adamski, M., Garg, S. & Kirkman, A., 2011: Confined LNAPL. Definition, Conditions and Terminology. *Applied NAPL Sci. Rev., 1, 5* (available from http://naplansr. com/confined-lnapl-volume-1-issue-5-may-2011/).

Kostolanský, M., Macek, J., Auxt, A., Benko, J., Drábik, A., Urgela, P. & Šuchová, M., 2017a: Monitoring geologických faktorov životného prostredia a udržiavanie geologických diel – rušňové depo Štúrovo. Záverečná správa. *Manuskript. Bratislava*, *Cenvis*.

Kostolanský, M., Macek, J., Auxt, A., Benko, J., Drábik, A., Urgela, P. & Šuchová, M., 2017b: Monitoring geologických faktorov životného prostredia a udržiavanie geologických diel – rušňové depo Leopoldov. Záverečná správa. *Manuskript. Bratislava, Cenvis.*

Lang, D. A., Bastow, T. P., Van Aarssen, B. G. K., Warton, B., Davis, G. B. & Johnson, C. D., 2009: Polar compounds from the dissolution of weathered diesel. *Ground Water Monitoring Remediation, 29, 4, 85–93.*

LSPA (Licensed Site Professionals Association), 2008: LNAPL and The Massachusetts Contingency Plan, Part II. LSPA Technical Practices Committee, July 2008, 47 p.

Macek, J. & Milička, J., 2021: Light non-aqueous phase liquids distribution and weathering in former railyard; SE Danube Basin, Slovakia. *Acta Geol. Slov., 13, 1–12.*

Maglay, J., Pristaš, J., Nagy, A., Fordinál, K., Buček, S., Havrila, M., Kováčik, M., Elečko, M. & Baráth, I., 2005: Geologická mapa regiónu Trnavská pahorkatina 1 : 50 000. *Bratislava, Št. Geol. Úst. D. Štúra.*

Maglay, J., Fordinál, K., Nagy, A., Kováčik, M. Šefčík, P., Vlačiky, M., Šimon, L., Moravcová, M., Zlocha, M., Zlinská, A., Fričovská, J., Žecová, K., Baráth, I., Liščák, P., Ondrášiková, B., Gluch, A., Kucharič, Ľ.†, Zeman, I., Kubeš, P., Benková, K., Bottlik, F., Marcin, D., Michalko, J., Baláž, P., Stupák, J. & Tuček, Ľ., (in press): Vysvetlivky ku geologickej mape regiónu Podunajská

nížina – Podunajská rovina v mierke 1 : 50 000. *Bratislava, Št. Geol. Úst. D. Štúra.*

MINEO, S., DELL'AERA, F. M. L. & RIZZOTTO, M., 2022: Evolution of LNAPL contamination plume in fractured aquifers. *Bull. Eng. Geol. Environ.,* 81, 134.

NAGY, A. (ed.), HALOUZKA, R., KONEČNÝ, V., LEXA, J., FORDINÁL, K., HAVRILA, M., VOZÁR, J. KUBEŠ, P., LIŠČÁK, P., STOLÁR, M. & DULOVIČOVÁ, K., 1998: Vysvetlivky ku geologickej mape Podunajskej nížiny – východná časť 1 : 50 000. *Bratislava, GS SR, Vyd. D. Štúra,* 187 s.

POLÁK, R., BUKVOVÁ, J., VARGA, F. & ŠUPOLÍKOVÁ, M., 1987: Štúrovo anilín. Havária podzemných vôd. Záverečná správa. *Manuskript. Bratislava, Vodné zdroje.*

RICE, D. W., GROSE, R. D., MICHAELSEN, J. C., DOOHER, B., MACQUEEN, D. H., CULLEN, S. J., KASTENBERG, W. E., EVERETT, L. G. & MARINO, M. A., 1995: California leaking underground fuel tank (LUFT) historical case analyses. *Environ. Protect. Depart., Environ. Restor. Divis.* Report UCRL-AR-122207, *Sacramento, CA,* 1–65.

SOLYMOSIOVÁ, E., KOSŤOV, K., BUKVOVÁ, J. & SITÁR, J., 1988: Štúrovo – znečistenie podzemných vôd ropnými látkami. Záverečná správa o hydrogeologickom prieskume. *Manuskript. Bratislava, Vodné zdroje,* 21 s.

STEYL, G., GOMO, M., VERMAAK, K., BOTHWELL, G., VAN TONDER, G. J., SURRIDGE, K., LORENTZ, S., NGALEKA, J., SIKOSANA, S., DLAMINI, M., ZONDI, N. & REVIL-BOURDARD, S., 2012: Field Investigations to Study the Fate and Transport of Light Non-Aqueous Phase Liquids (LNAPLs) in Groundwater. Final Report No. 1766/1/12. *Pretoria, Water Res. Commission,* 134 p.

TUPÝ, P., SCHWARZ, J., ANTAL, J., MASIAR, R., FILO, J., JASOVSKÝ, Z., MORAVČÍK, D., FICKULIAKOVÁ, M., DRÁBIK, A., BÁGELOVÁ, A., MACEK, J., URGELA, P., BENKO, J., KOSTOLANSKÝ, M. & JURKOVIČ, Ľ., 2019: Sanácia environmentálnej záťaže HC (1844) / Leopoldov – Rušňové depo, Cargo a.s. (SK/EZ/HC/1844). Čiastková záver. správa s aktualizovanou analýzou rizika znečisteného územia. *Manuskript. EBA_ODOS_ENVIGEO,* 112 s.

TUPÝ, P., SCHWARZ, J., ANTAL, J., MASIAR, R., FILO, J., JASOVSKÝ, Z., MORAVČÍK, D., FICKULIAKOVÁ, M., DRÁBIK, A., BRUTENIČ, M., MACEK, J., TÓTH, R., BENKO, J., KOSTOLANSKÝ,

M., JURKOVIČ, Ľ., KRAVČENKO, D. & MALÝ, V., 2022: Sanácia environmentálnej záťaže HC (1844) / Leopoldov – Rušňové depo, Cargo a.s. (SK/EZ/HC/1844). Záverečná správa s posanačnou analýzou rizika znečisteného územia. *Manuskript. EBA_ODOS_ENVIGEO.*

URBAN, O., CHOVANEC, J., KEKLÁK, V., MACHLICA, A., ŠMIDOVIČOVÁ, S., SERES, Z., ŠTEFÁNEK, J., DEMKO, M., BEDNÁRIK, M., GREGOR, T., KOLÁŘOVÁ, J., POLÁK, M., ZAVADIAK, R., FAJČÍKOVÁ, K., BOROŠOVÁ, M., KOLESÁR, M., HORVÁTHOVÁ, M., VYBÍRAL, V., ČOPAN, J., DRÁBIK, A., MACEK, J., BÁGELOVÁ, A., JURKOVIČ, Ľ., KOSTOLANSKÝ, M., BENKO, J. & URGELA, P., 2019: Sanácia environmentálnej záťaže NZ (029) / Štúrovo – Rušňové depo, Cargo a.s. (SK/EZ/NZ/601). Čiastková záver. správa s aktualizovanou analýzou rizika znečisteného územia. *Manuskript. DEKONTA,* 89 s.

URBAN, O., CHOVANEC, J., KEKLÁK, V., GREGOR, T., KOLÁŘOVÁ, J., VYBÍRAL, V., ŠKARVAN, A., ČOPAN, J., DRÁBIK, A., MACEK, J., JURKOVIČ, Ľ., KOSTOLANSKÝ, M., BENKO, J., MALÝ, V., KRAVČENKO, D., TÓTH, R. & BRUTENIČ, M., 2021: Sanácia environmentálnej záťaže NZ (029) / Štúrovo – Rušňové depo, Cargo a.s. (SK/EZ/NZ/601). Záver. správa s posanačnou analýzou rizika znečisteného územnia. *Manuskript. Dekonta.*

VALUŠIAK, I., 1987: VNS Leopoldov – výstavba obilného sila, návrh na odvodnenie – zníženie hladiny podzemnej vody, podrobný HGP. JRD 1. Máj, Kočín. *Manuskript. Bratislava, archív Št. Geol. Úst. D. Štúra* (67403), 1–5.

VASS, D., 2014: Regionálne geologické členenie Slovenska [online]. *Bratislava, Št. Geol. Úst. D.* Štúra. Dostupné na: http://apl.geology.sk/temapy.

VRANA, K., 2008: Vypracovanie programov opatrení v rámci prípravy plánov manažmentu oblastí povodí v súlade s požiadavkami vodného zákona a Rámcovej smernice o vode pre prevádzky ZSSK CARGO a.s. – I. etapa prác za lokalitu Čierna nad Tisou – prekladisko. Záver. správa. *Manuskript. Bratislava, HYDEKO – KV.*

ZEMO, D. A., O'REILLY, K. T., MOHLER, R. E., MAGAW, R. I., DEVINE, C. E., AHN, S. & TIWARY, A. K., 2017: Life cycle of petroleum biodegradation metabolite plumes, and implications for risk management at fuel release sites. *Integr. Environ. Assess. Management,* 13, 4, 714–727.

# Porovnanie dvoch modelových environmentálnych záťaží s rozsiahlym znečistením fázou ropných látok – rozsah znečistenia identifikovaný geologickým prieskumom vs. sanačná realita

Prezentovaná štúdia sa zaoberá výsledkami geologických prác v dvoch modelových železničných prevádzkach. Pre tento typ lokalít je charakteristický častý výskyt znečistenia vo forme voľnej fázy ropných látok (VFRL) na hladine podzemnej vody. Je to výsledok únikov veľkého objemu znečistenia (najčastejšie nafty) do životného prostredia.

Vybrané lokality, železničné depá v Leopoldove a Štúrove, majú dlhodobú históriu opráv hnacích koľajových vozidiel. Obe boli v prevádzke už v 50. rokoch 20. storočia a patrili k silne znečisteným prevádzkam s výskytom VFRL na hladine podzemnej vody. Lokality boli v minulosti podrobne preskúmané a od roku 2008 sa na oboch vykonávalo monitorovanie podzemnej vody. V Štúrove boli

v okolí podzemných nádrží na pohonné hmoty (PHM), predpokladaného zdroja znečistenia, identifikované 4 vrty, v ktorých sa dlhodobo vyskytovala VFRL s hrúbkou až 870 mm (Kostolanský et al., 2017a). V Leopoldove bola VFRL pozorovaná iba v jednom vrte, ktorý sa nachádza v blízkosti výdajného miesta na PHM (vrt LEV-1). Predpokladaným zdrojom znečistenia boli potrubné rozvody na PHM, resp. úniky pri prečerpávaní PHM (Kostolanský et al., 2017b). Obe lokality boli v roku 2017 zaradené medzi 14 železničných lokalít, na ktorých Ministerstvo životného prostredia Slovenskej republiky (MŽP SR) schválilo realizáciu sanačných prác. Cieľom článku je poukázať na rozdielne stavy znečistenia lokalít, ktoré sa zistili pred sanáciou a počas sanácie.

V roku 2018 sa začali realizovať geologické práce na oboch lokalitách. Prvým krokom bolo uskutočnenie predsanačného prieskumu s aktualizovanou analýzou rizika znečisteného územia. Ťažiskom prác bola realizácia prieskumných a hydrogeologických vrtov, z ktorých sa odoberali vzorky zemín a podzemnej vody. Výsledky predsanačných prieskumov nepoukazovali na prítomnosť veľkého objemu znečistenia vo forme voľnej fázy, no počas realizácie sanačných prác dochádzalo k natekaniu menšieho objemu VFRL do vrtov (hrúbka vrstvy v jednotkách centimetrov). Zároveň sa nepotvrdilo rozširovanie mrakov VFRL a šírenie znečistenia v rozpustenej forme podzemnou vodou.

Výsledky prieskumu v Leopoldove identifikovali rozsiahle znečistenie zemín v pásme prevzdušnenia a nasýtenia, ako aj podzemnej vody ropnými látkami (naftou). Znečistenie bolo identifikované hlavne v priestore pod točňou a pri nadzemných nádržiach na PHM. Výskyt VFRL sa počas prieskumu potvrdil iba v pôvodnom vrte LEV-1 (Tupý et al., 2019). Prieskum v štúrovskom depe identifikoval plošne rozsiahle a výrazné znečistenie zemín pásma nasýtenia a podzemnej vody. Výskyt VFRL bol pozorovaný iba v starých vrtoch na ploche približne 700 m$^2$. Predpokladaným zdrojom znečistenia boli podzemné jednoplášťové nádrže na PHM (Urban et al., 2019).

V roku 2019 sa začala na oboch lokalitách sanačná etapa geologických prác. V Leopoldove neboli pozorované výrazné samovoľné nátoky VFRL do novovybudovaných vrtov. Znečistenie vo forme fázy bolo pozorované v 9 vrtoch (celkovo z 13 novovybudovaných) s maximálnou hrúbkou vrstvy 40 mm. Po začatí sanačných prác a spustení sanačného čerpania podzemnej vody boli pozorované výrazné prítoky znečistenia vo forme VFRL, ktoré natekalo okamžite po odčerpaní, pričom hrúbka vrstvy VFRL dosahovala takmer 80 cm (pri vrte s priemerom pažnenia 200 mm ide o zhruba 25 l znečistenia). Bolo to najviac zo všetkých vrtov. Postupne, po realizácii overovacích čerpaní podzemnej vody z novovybudovaných vrtov, bolo natekanie VFRL pozorované aj v ďalších vrtoch. Oblasť okolo točne a nadzemných nádrží na PHM sa tak ukázala ako oveľa viac znečistená, ako boli pôvodné predpoklady. Spolu bolo v rámci sanačných prác odčerpaných a likvidovaných viac ako 5 m$^3$ VFRL, resp. zmesi VFRL a podzemnej vody s vysokým obsahom emulgovaných ropných látok, a to výhradne z vrtov v priestore pri točni a nádržiach na PHM (Tupý et al., 2022).

V Štúrove v niektorých novovybudovaných vrtoch boli pozorované okamžité samovoľné nátoky VFRL. V priestore koľajiska pred dnes už neexistujúcou budovou depa sa potvrdila prítomnosť znečistenia vo forme mobilnej VFRL. Vysoký stupeň nasýtenia horninového prostredia znečistením sa potvrdil aj okamžitým (jednotky dní) objavením VFRL v nových vrtoch (do hrúbky takmer 1 000 mm). VFRL sa odčerpávala najskôr bez podporného čerpania podzemnej vody (vo viacerých vrtoch na lokalite po odčerpaní prvotného objemu VFRL už nedošlo k jej ďalšiemu dotekaniu). Z vrtov v okolí podzemných nádrží boli

odčerpané zhruba 2 m$^3$ znečistenia, z vrtov v priestore koľajiska viac ako 4 m$^3$ (Urban et al., 2021). Zdroj znečistenia identifikovaný počas sanačných prác (koľajisko pred bývalou budovou depa) bol teda dvojnásobne výdatnejší z hľadiska odčerpanej VFRL ako pôvodne uvažovaný zdroj znečistenia (podzemné nádrže na PHM). Okrem uvedených dvoch hlavných zdrojov znečistenia boli na lokalite identifikované aj dva menšie zdroje (produktovod PHM a opravárenská jama). Sanačnými prácami sa tak overilo znečistenie VFRL na približne trojnásobne väčšej ploche, ako sa pôvodne predpokladalo. V práci Maceka a Miličku (2021) je vyhodnotený charakter znečistenia z hľadiska jeho degradácie. Výsledkom je zistenie, že znečistenie pochádza v viacerých rôznych zdrojov. Napriek tomu, že depo je viac ako 10 rokov mimo prevádzky, bola na lokalite odobraná vzorka VFRL bez zjavných známok degradácie. Odhadovaný vek znečistenia na lokalite je od 8 do 48 rokov.

Rozšírenie znečistenia identifikované v priebehu sanačných prác z hľadiska priestoru zodpovedá ploche identifikovanej predsanačnými prieskumami. Koncentrácia znečistenia však vysoko prekračuje pôvodné predpoklady. Počas prieskumov sa nezistila VFRL v novovybudovaných vrtoch (resp. v Leopoldove iba vo forme filmu), prítomnosť VFRL v mobilnej forme mohol podľa LSPA (2008) naznačovať iba vysoký obsah znečistenia v niektorých vzorkách zemín (viac ako 10 000 mg . kg$^{-1}$ C$_{10}$ – C$_{40}$). Napriek tomu bol na oboch lokalitách počas sanačných prác z vrtov odčerpaný veľký objem znečistenia vo forme VFRL. V rámci realizácie prác sa ukázali aj viaceré skutočnosti, ktoré boli v nesúlade s teoretickými predpokladmi založenými na charakteristikách znečisťujúcich látok a vlastnostiach geologického prostredia. V Leopoldove bola pred sanáciou koncentrácia znečistenia rozpusteného v podzemnej vode vo vrtoch CLE-1 a CLE-2 relatívne nízka (v CLE-1 nižšia ako ID kritérium smernice MŽP SR č. 1/2015-7), z týchto vrtov sa však počas sanácie odčerpal najväčší objem VFRL. V Štúrove bolo pozorované natekanie VFRL aj do vrtov mimo dvoch hlavných kontaminačných mrakov, pravdepodobne v dôsledku preferenčných miest a realizácie sanačného čerpanie podzemnej vody z vrtov. Natekanie VFRL do vrtu v centre znečistenia sa ale nezistilo po jeho odvŕtaní ani po spustení čerpania podzemnej vody a následnom znižovaní jej hladiny. VFRL sa v tomto vrte objavila samovoľne asi pol roka po jeho realizácii napriek tomu, že v jeho okolí sa nečerpala podzemná voda z iných vrtov. Porovnanie prieskumov a sanačných prác poukazuje na rôzne druhy neistôt, ktoré je nutné brať do úvahy pri vyhodnocovaní stupňa znečistenia lokality a plánovaní sanačných prác.

# Inštrukcie autorom

## Etika publikovania, záväzná pri publikovaní v časopise Mineralia Slovaca:
### www.geology.sk/mineralia *položka* **Publikačná etika**

**1.** Geovedný časopis Mineralia Slovaca publikuje scientometricky hodnotné recenzované pôvodné vedecké články s vysokým citačným potenciálom. V úvode príspevku musí autor jasne deklarovať, čím konkrétnym je jeho príspevok prínosný pre rozvoj geovied. Rešeršné štúdie sa publikujú len ojedinele.

**2.** Články na publikovanie (manuskripty) sa do redakcie zasielajú poštou (dva vytlačené exempláre a CD so všetkými súbormi v editovateľnej podobe) alebo e-mailom (editovateľné súbory a kompletná verzia vo formáte PDF).

**3.** Súčasne s článkom je potrebné redakcii poslať autorské vyhlásenie o originalite textu a obrázkov. Kópie obrázkov z iných publikácií musia byť legalizované získaním práva na publikovanie. Vyhlásenie musí obsahovať meno autora (autorov), akademický titul a trvalé bydlisko.

**4.** Rozsah manuskriptu na publikovanie je najviac 25 rukopisných strán (MS Word, Times New Roman, veľkosť písmen 12 bodov, riadkovanie 1,5) vrátane literatúry, obrázkov a vysvetliviek. V prípade veľkého odborného prínosu sú v ojedinelých prípadoch povolené aj dlhšie články.

**5.** Články sú publikované v angličtine alebo v slovenčine. Články v slovenčine musia obsahovať anglický preklad názvu, abstraktu, kľúčových slov, resumé a popisov k obrázkom a tabuľkám. Články písané v angličtine musia obsahovať slovenské resumé.

### Text

**1.** Abstrakt stručne sumarizuje článok. Môže mať najviac 200 slov a nemá obsahovať citácie. Počet kľúčových slov je maximálne 6. Text má mať úvod, charakteristiku (stav) skúmaného problému, použitú metodiku, nové zistenia, ich interpretáciu, diskusiu, záver a zoznam literatúry. Východiskové údaje musia byť zreteľne odlíšené od interpretácií. V texte musia byť odvolávky na všetky použité obrázky a tabuľky.

**2.** Hierarchiu nadpisov v texte je potrebné vyznačiť ceruzkou na ľavom okraji strany manuskriptu: 1 – najvyššia, 2 – nižšia, 3 – najnižšia.

**3.** V texte sa uprednostňuje citácia v zátvorke, napr. (Dubčák, 1987; Hrubý et al., 1988), pred formou ... podľa Dubčáka (1987).

**4.** Pozícia obrázkov a tabuliek v texte sa označí. Nie je vhodné, aby text v editore MS Word obsahoval vložené obrázky, ale náhľadová verzia v pdf ich má obsahovať.

**5.** Grécke písmená treba identifikovať na ľavom okraji slovom (napr. sigma). Potrebné je odlišovať pomlčku od spojovníka. Symboly, matematické značky, názvy skamenelín a pod., ktoré sa majú vysádzať kurzívou, autor v rukopise podčiarkne vlnovkou.

### Obrázky a tabuľky

**1.** Ilustrácie a tabuľky vysokej kvality bývajú publikované buď **na šírku stĺpca (81 mm), alebo strany (170 mm).** Optimálna veľkosť písma a čísel v publikovaných obrázkoch je 2 mm. Články v slovenčine musia mať popisy v obrázkoch a tabuľkách v slovenčine, záhlavie tabuliek a texty pod obrázkami a tabuľkami sú v slovenčine a angličtine. Články v angličtine majú všetky texty v angličtine. **Maximálny rozmer ilustrácie a tabuľky vytlačený v časopise je 170 x 230 mm.** Väčšie (skladané) ilustrácie sú publikované len v ojedinelých prípadoch.

**2.** Pri počítačovej tvorbe obrázkov odporúčame používať programy **s vektorovým zobrazením (Corel Draw, Adobe Illustrator a pod.). Čiary tzv. vlasovej hrúbky, softvérová alebo rastrová výplň plôch (napr. v Corel Draw) nie sú prípustné.** Výplne v obrázkoch musia pozostávať zo samostatne vysádzaných objektov.

**3.** Ilustrácie vrátane fotografií musia obsahovať **grafickú mierku** v centimetrovej či metrovej škále, prípadne sa rozmer zobrazených objektov vyjadrí v popise obrázka. Mapy a profily musia mať aj **azimutálnu orientáciu** a jednotné vysvetlivky, ktoré sa uvedú pri prvom obrázku. Zoskupené obrázky, napr. fotografie a diagramy, sa uvádzajú ako jeden obrázok s jednotlivými časťami označenými písmenami (a, b, c atď.).

**4.** Pri zasielaní fotografií vo forme počítačových súborov (formáty JPG alebo TIF) sa požaduje rozlíšenie minimálne 600 DPI. Publikovanie farebných ilustrácií môže byť spoplatnené.

### Literatúra

**1.** Minimálne 50 % citácií musí reprezentovať publikácie od roku 2000. V zozname literatúry sa v abecednom poradí uvádza len literatúra citovaná v danom článku.

**2. Spôsob uvádzania literatúry v zozname literatúry**

*Knižná publikácia:* Gazda, L. & Čech, M., 1988: Paleozoikum medzevského príkrovu. *Bratislava, Alfa,* 155 s.

*Časopis:* Vrba, P., 1989: Strižné zóny v metapelitoch. *Miner. Slov., 21,* 135 – 142.

*Zborník:* Návesný, D., 1987: Vysokodraselné ryolity. *In: Romanov, V. (ed.): Stratiformné ložiská gemerika. Špec. publ. Košice, Slov. geol. spol.,* 203 – 215.

*Manuskript:* Radvanský, F., Slivka, B., Viktor, J. & Srnka, T., 1985: Žilné ložiská jedľoveckého príkrovu gemerika. Záverečná správa z úlohy SGR-geofyzika. *Manuskript. Spišská Nová Ves, archív Št. Geol. Úst. D. Štúra,* 28 s.

**3.** Pri článku viac ako dvoch autorov sa v texte cituje iba prvý autor s dodatkom et al., ale v zozname literatúry sa uvádzajú všetci.

# Instructions to authors

## Publication ethics, being obligatory for publishing in the journal Mineralia Slovaca:
### www.geology.sk/mineralia *item* **Publication ethics**

**1.** Geoscientific journal Mineralia Slovaca publishes scientometrically valuable original peer-reviewed scientific articles with a high citation potential. In the introduction of each article the author(s) must clearly declare, which innovative data the paper brings for the development of geosciences. The retrieval studies are published only exceptionally.

**2.** The articles for publishing (manuscripts) must be sent to Editorial Office by post (two printed copies and CD with editable files), or by e-mail (editable files plus complete preview version in PDF format).

**3.** Simultaneously with the article the Editorial Office must receive the author´s proclamation that no part of the manuscript was already published and figures and tables are original as well. Copied illustrations from other publications must contain a copyright.

**4.** The extent of the manuscript for publishing is limited to 25 manuscript pages (MS Word, 12 points Times New Roman, line spacing 1.5) including figures, tables, explanations and references. In the case of contribution with a high scientific value, the longer manuscripts for publishing are exceptionally permitted.

**5.** Articles can be published in Slovak or English languages. The title, abstract, key words, shortened text (resumé), as well as description to figures and tables in Slovak articles are published also in English. Articles published in English contain Slovak resumé.

### Text

**1.** Abstract briefly summarizing the article is limited to 200 words, no references are allowed. The maximum number of key words is 6. Text of the article has to contain the introduction, characterization (state) of investigated problem, applied methodology, obtained new data, discussion, conclusion and references. The obtained data must be distinctly separated from interpretations. All applied figures and tables must be referred in the text.

**2.** The hierarchy of headings in the manuscript must be indicated by a pencil note: 1 – highest level, 2 – lower, 3 – lowermost level.

**3.** The references in the text prefer parentheses, e.g. (Dubčák, 1987; Hrubý et al., 1988). The form "according to Dubčák (1987)" should be used only exceptionally.

**4.** Position of figures and tables must be indicated in the manuscript. Editable text of manuscript sent to editorial office must be without figures and tables, though the preview PDF has to contain them in a correct position.

**5.** Greek letter in the text must be identified at the left margin of the text (e.g. sigma). The text should strictly distinguish the dash from hyphen. Symbols, mathematic signs, names of fossils, etc., which should be printed in italics, must be underlined by the wavy line in the manuscript.

### Figures and tables

**1.** The high quality figures and tables can be published either in **maximum width of column (81 mm) or page (170 mm).** The optimum size of letters and numbers in the camera-ready figure is 2 mm. Articles published in Slovak contain the Slovak descriptions in figures and tables, the tables headings and descriptions beneath figures and tables are in Slovak and English. English articles contain all texts in English. **Maximum dimension of figures and tables in the journal is 170 x 230 mm. Larger (fanfolded)** illustrations are published only exceptionally.

**2.** For figures drawing the editorial office recommends the vector graphics editors (Corel Draw, Adobe Illustrator, etc.). **The very thin lines (hair lines), the pre-defined software or raster fillings of polygons (e.g. in Corel Draw) are not allowed.** The filling must consist from separately set objects.

**3.** Each illustration including photographs must contain graphic (metric) scale, eventually the dimensions of visualized objects have to be stated in the describing text to figure. Maps and profiles must contain also the azimuth orientation, their detail explanations are stated at the first figure. Grouped figures, e.g. photographs and diagrams, are compiled as one figure with separate parts designated by letters (a, b, c, etc.).

**4. The photographs sent as JPG of TIF files are required for having minimum 600 DPI resolution.** Publishing of colour illustrations can be charged by a fee.

### References

**1. Minimum 50 % of referred works must represent contemporary publications after 2000.** The references in alphanumeric order encompass only literature cited in the article.

**2. Examples of referring:**

*Book:* Gazda, L. & Čech, M., 1988: Paleozoic of the Medzev nappe. *Bratislava, Alfa,* 155 p.

*Journal:* Vrba, P., 1989: Shear zones in the metapelite complexes. *Miner. Slov., 21,* 135–142.

*Anniversary volume:* Návesný, D., 1987: High-potassium rhyolites. *In: Romanov, V. (ed.): Stratiform deposits of Gemericum. Spec. publ. Košice, Slov. geol. soc.,* 203–215.

*Manuscript:* Radvanský, F., Slivka, B., Viktor, J. & Srnka, T., 1985: Vein deposits of the Jedľovec nappe of Gemericum. Final report from the project SGR-geophysics. *Manuscript. Spišská Nová Ves, Archive Št. Geol. Úst. D. Štúra,* 28 p.

**3.** The article with more than two authors is referred by the name of the first author with the amendment et al., but the list of references contains names of all authors.

# OBSAH – CONTENT

## PÔVODNÉ ČLÁNKY – ORIGINAL PAPERS

**Indexed / Abstracted / Accessed by SCOPUS and EBSCO**
Indexované / abstraktované / sprístupňované databázami SCOPUS a EBSCO

**www.geology.sk/mineralia**